Characterizing and Modeling Elastic Stiffness Variation of Opalinus Clay Based on Laboratory and In-situ Measurements

by

Lang Liu

A thesis submitted in partial fulfillment of the requirements for the degree of

Doctor of Philosophy

in

Geotechnical Engineering

Department of Civil and Environmental Engineering
University of Alberta

Abstract

Opalinus Clay is the designated host rock for future radioactive waste disposal in Switzerland. Characterizing the elastic stiffness of Opalinus Clay and its variation is essential in the ground deformation prediction and geophysical survey during the construction and operation of disposal repositories. In this thesis, an in-situ method, pressuremeter testing (PMT), is employed in three boreholes at the Mont Terri Rock Laboratory to determine the in-situ elastic stiffness of the Opalinus Clay. The shear modulus is measured by PMT in Oplainus Clay using the unloading steps at different expansion pressures, and its dependence on pressure is shown to be significant when the expansion pressure is less than 5 MPa. The interpreted shear modulus values agree with those measured from triaxial tests on core specimens when small-strain nonlinearity, elastic anisotropy, shear mode, and loading path are considered. A representative modulus value of approximately 3 GPa is established for intact Opalinus Clay at the Mont Terri site for the shear strain magnitude at 0.1%. The prediction using the anisotropic elasticity parameters obtained from laboratory tests reasonably agrees with the anisotropic borehole modulus measured in a borehole drilled parallel to bedding planes.

The evolution of elastic properties is measured using an ultrasonic survey during triaxial tests on laboratory specimens. A cycle of triaxial compression and extension under constant mean stress is applied to the specimens to approximate the stress condition during borehole unloading and reloading. The measured evolution of dynamic elastic modulus differs from that obtained from the triaxial tests under constant lateral stress. Compared to the static modulus, the sensitivity of the dynamic modulus to stress is not significant for the applied stress range. The damage initiation threshold is identified from the measured evolution of the elastic properties and can be distinguished for different triaxial shear modes and specimen saturations.

The variation of static elastic modulus during triaxial loading was modeled using three elastic stiffness functions. Isotropic damage and plastic yielding are incorporated in the constitutive formulation. The

model reproduces the nonlinear stress-strain relationship observed in multi-staged triaxial tests. The axisymmetric borehole response in a cycle of drilling unloading and pressuremeter loading is also predicted by implementing the proposed model into a finite element (FE) code. The modeling study demonstrates that the modulus values obtained from pressuremeter tests can be underestimated due to drilling-induced borehole damage even when the stress at the borehole wall is recovered to the initial state.

The borehole damage can be localized by (1) overstressing and/or (2) the instability of geological structures, e.g., bedding planes, after drilling unloading. Identifying the localized BDZ by overstressing may enable the determination of the far-field stress orientation at the borehole cross-section plane. The in-situ methods, including rotational interval velocity measurement (ROT-IVM) and PMT, both show the azimuthal variation of elastic properties in the borehole nearfield. The ROT-IVM data can be further analyzed using tomography inversion, which allows for an estimation of the extent of BDZ. The variations of P-wave velocity and its anisotropy, however, are not likely linked to the estimated variation of the stress field but to the varying saturation of Opalinus Clay at different measurement locations. The anisotropic borehole modulus measured by PMT at a lower pressure range may indicate the orientation of BDZ, but the indication can be complicated by the local pore fluid dissipation in the near-borehole field. Alternatively, using the PMT data after borehole yielding under high expansion pressure is shown to be promising in capturing the far-field stress orientations in the Opalinus Clay, regardless of the initial borehole disturbance.

Preface

This thesis is an original work by Lang Liu. Some chapters of this thesis are submitted/published:

Part of Chapter 2 was published as [Liu, L., Giger, S., Martin, D., Chalaturnyk, R., Deisman, N. 2021. Stress and strain dependencies of shear modulus from pressuremeter tests in Opalinus Clay. *The 6th international conference on geotechnical and geophysical site characterization.*]

Part of Chapter 2 was published as [Liu, L., Giger, S., Martin, D., Chalaturnyk, R., Schuster, K., Deisman, N., Keller, L., 2022. In-situ elastic stiffness characterization by pressuremeter testing in Opalinus Clay and reconciliation with laboratory tests, *Rock Mechanics and Rock Engineering*.]

Part of Chapter 2 was submitted to *International Journal of Rock Mechanics and Mining Sciences* as [Liu, L., Martin, D., Giger, S., Chalaturnyk, R., Assessment of anisotropic elastic parameters using triaxial and pressuremeter tests in Opalinus Clay.]

Part of Chapter 3 was published as [Liu, L., Chalaturnyk, R., Deisman, N., Zambrano, G., 2022. Evolutions of dynamic elastic properties of Opalinus Clay under varying stress paths. *56th U.S. Rock Mechanics/Geomechanics Symposium.*]

Part of Chapter 4 was published as [Liu, L., Chalaturnyk, R., 2020. Modeling borehole expansion in weak rocks using CDM approach. *54th U.S. Rock Mechanics/Geomechanics Symposium.*]

Part of Chapter 4 was published as [Liu, L., Deisman, N., Chalaturnyk, R., 2022. Modelling elastic stiffness evolution of Opalinus Clay based on laboratory measurements with implications for in-situ testing, *Rock Mechanics and Rock Engineering*.]

Acknowledgment

This thesis would not be possible without guidance, suggestions, and resources provided by many people. It is my great privilege to complete this research work under the supervision of Dr. Rick Chalaturnyk, who supports me with his trust, enlightens me with novel ideas, and always inspires me with his expertise and passion in geomechanics, and Dr. Derek Martin, who influences me with his pursuit of scientific rigor, motivates me to read and think critically, and challenges me with his valuable insights. Dr. Silvio Giger from the Swiss National Cooperative for the Disposal of Radioactive Waste (Nagra) is sincerely acknowledged for his coordination of the GC field campaign at the Mont Terri Rock Laboratory and his provision of the drillcores for the laboratory investigation in this thesis. His support with high-quality test data and many fruitful discussions on my research work deepens my understanding of the constitutive behavior of Opalinus Clay. I would also like to acknowledge Dr. Kristof Schuster and Dr. Werner Graesle from German Institute for Geosciences and Natural Resources (BGR) for their generosity in sharing the interval velocity measurement and multi-staged triaxial test results, respectively.

At the Mont Terri site, Dr. Nathan Deisman and Mr. Kevin Wallin from the University of Alberta, Dr. Senecio Schefer from Swisstopo, and the staff from Schützeichel are greatly acknowledged for their on-site help on pressuremeter testing. Suggestions from Mrs. Yasmin Byrne and Mr. Robert Whittle at Cambridge In-situ Ltd. on pressuremeter test data evaluation are also sincerely appreciated. At the University of Alberta, I'm grateful for the support from colleagues in the Reservoir Geomechanics Research Group, including Dr. Deisman, Mr. Jakob Brandl, Mr. Gilbert Wong, Mr. Keivan Khaleghi, Dr. Amir Haghi, Dr. Noga Vaisblat, Dr. Zambrano Gonzalo, and many others, for their support on the laboratory investigation. Mr. Mark Labbe is acknowledged for his help in specimen preparation. Mr. Randy Kofman and Dr. Henry Herrera are acknowledged for their suggestions in the acquisition and analysis of ultrasonic wave signals. Dr. Samer Adeeb is acknowledged for his comments on constitutive modeling. Mr. Caixiang Fan is acknowledged for his help in reviving an obsolete code (*rayinvr*) for tomography inversion analysis. A special thank you goes to my officemate Dr. Haghi for his advice, peer support, and many comforting conversations through the pandemic.

This research work is financially supported by Nagra, Natural Sciences and Engineering Research Council of Canada (NSERC), and Energi Simulation Industrial Research Consortia in Reservoir Geomechanics.

Finally, my deepest gratitude goes to my family who always support and love me, and to God, by whose grace I made it.

Table of Contents

List of Tables

List of Figures

Chapter 1

Introduction

1.1 Research Motivation

Ground deforms when it undergoes a change of stress. The estimation and measurement of ground deformation are critical in rock engineering. For example, it allows for the control of the subsurface subsidence during depletion of the reservoir in oil/gas production and the tunnel convergence during underground excavation.

An important factor that affects the ground deformation prediction is rock stiffness. The rock stiffness varies across the rock types (Kulhawy 1975). Even within the same rock type, the stiffness can vary significantly depending on the factors such as mineralogical composition, porosity, and water content (Sone and Zoback 2013; Rybacki et al. 2015).

At the field scale, the rock stiffness often refers to the deformation modulus of rock mass, which includes the contributions from both intact rocks and discontinuities. To determine this parameter, field methods, such as plate jacking tests, were often conducted on the tunnel surface (Coulson 1979; Hoek and Diederichs 2006). These tests require ample underground space for equipment setup and are time-consuming. Therefore, for the sites where direct measurement is not available, empirical relationships were suggested to estimate rock mass deformation modulus based on intact rock modulus and other parameters quantifying the geological conditions (Hoek and Diederichs 2006). At the laboratory scale, stiffness measurement is often performed on the cylindrical specimens extracted from the rock core. These specimens need to be carefully prepared and are supposed to represent the intact rock modulus. However, the specimens commonly suffer from different degrees of sampling disturbance. The disturbance can reduce the modulus by up to 50% from that of the undisturbed rock when the core is recovered from a highly stressed ground (Martin and Stimpson 1994). Additional disturbance can be induced during core handling and specimen preparation if the rock is sensitive to chemical and environmental alterations (Pei 2003; Corkum and Martin 2007; Ewy and Stankovic 2010; Pineda et al. 2014). Therefore, an accurate determination of the rock stiffness for its in-situ condition remains challenging.

This study is established on a recent geomechanical testing program (GC-Experiment) at the Mont Terri Rock Laboratory in Switzerland to characterize the deformation and strength properties of Opalinus Clay, a weak argillaceous rock. Appropriate guidelines to minimize the sampling disturbance have been adopted by Minardi et al. (2021) in their laboratory measurements of elastic stiffness. These

measurements, however, still require verification from field measurements that are considered to establish in-situ stiffness values. As an in-situ method, pressuremeter (also known as “dilatometer”) testing, is used in this study to determine the elastic stiffness of the Opalinus Clay. By assessing the in-situ testing results with the laboratory measurements, several questions are to be answered in this thesis:

- How should the elastic stiffness be evaluated for this rock type?
- Do the laboratory measurements agree with the in-situ measurements?
- What factors should be considered to reconcile the laboratory measurements with the in-situ measurements for this rock type?
- Is it possible to quantify the laboratory and in-situ measurements using a unified constitutive model, which can then be used to predict the deformation under arbitrary stress/strain paths?
- Are additional tests required to improve the modeling of elastic stiffness for this rock type?

The study aims at providing meaningful guidance regarding the rock elastic stiffness measurement and interpretation to support the deformation prediction of future radioactive waste repositories.

1.2 Research Background

1.2.1 Radioactive Waste Disposal

Radioactivity is a natural phenomenon, and it has many beneficial applications, ranging from power generation to uses in the medical industry. At the same time, the radiation risks to workers, the public, and the environment need to be strictly managed. Disposal of radioactive wastes represents the final step in the management, and it requires disposal facilities that can provide the necessary degree of containment and isolation to ensure safety for the long-term disposal (IAEA 2012). The underground geological repository has been favored for radioactive waste disposal because the ground can act as a natural barrier to the potential leakage of the disposed waste. An example layout of a high-level waste (HLW) repository with its main components is shown in Figure 1-1. The geological formation where the waste is emplaced is called host formation. In the past 40 years, many host formations have been considered for the construction of the future repository, 40% of which are granitic and 60% are sedimentary rocks (Blechschmidt and Vomvoris 2011).

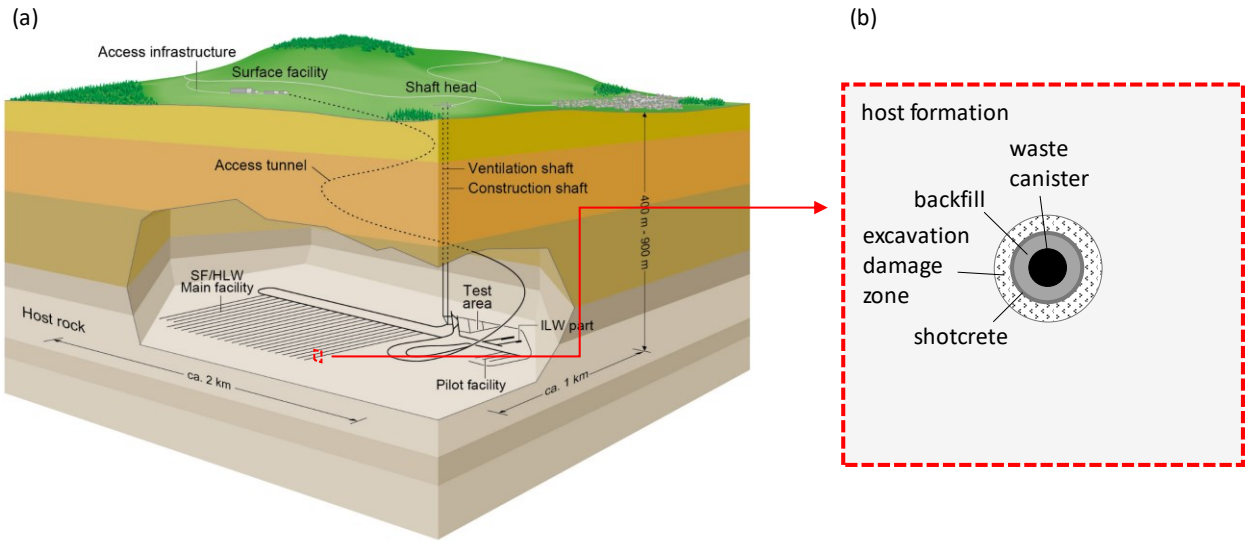

Figure 1-1. (a) Example layout of the high-level waste repository with necessary features (Poller et al. 2014) and (b) cross-section of the waste emplacement layout in an excavated host rock. Drawings on not on the scale.

Shale is a type of fine-grained sedimentary rock with relatively low permeability (< 5e-13 m/s). Opalinus Clay is a shale formation in northern Switzerland selected by Nagra (Swiss Cooperative for the Disposal of Radioactive Waste) as a designated host rock for high-level radioactive waste disposal. To provide the basis for site selection and the safety case for the construction of deep geological repositories, Nagra is currently drilling a series of deep boreholes located within three candidate regions in Northern Switzerland (Figure 1-2). The campaign includes a detailed site investigation with borehole logging, in-situ testing, geological mapping, and laboratory testing on the core samples, aiming to provide accurate measurement on the local stress field, the structural record, and lithofacies distribution not only in the Opalinus Clay Formation but also the overlying and underlying formations.

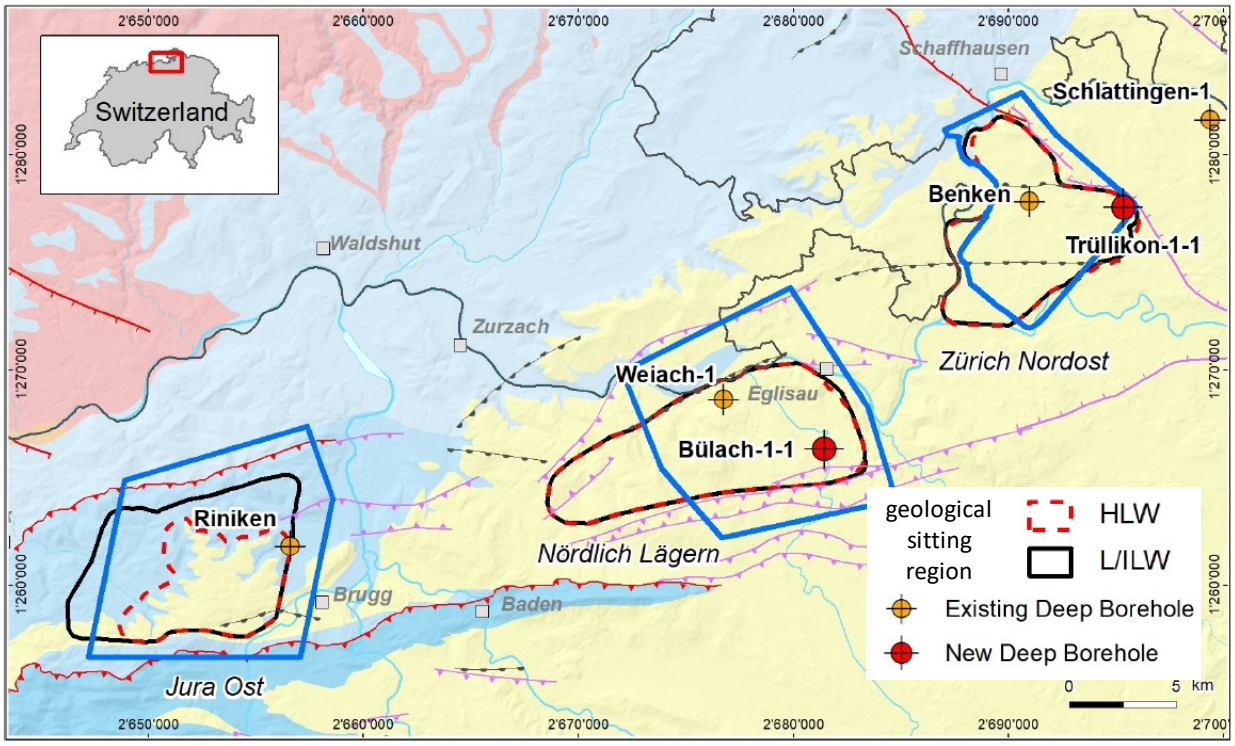

Figure 1-2. Location of the three candidate (geological sitting) regions for radioactive waste repository construction (after (NAGRA 2020))

1.2.2 Opalinus Clay and Mont Terri Rock Laboratory

Lithologically, Opalinus Clay is classified as *argillaceous claystone*. The Opalinus Clay consists of dark grey, silty, micaceous clays, and quartz/carbonate inclusions. According to Hawkins and Pinches' (1992) definition, argillaceous claystone refers to the sedimentary rocks that have more than 40% clay fraction and are dominated by grains with particle size less than 0.06 mm. The grain size analysis conducted by Klinkenberg et al. (2009) using backscattered electron (BSE) images showed that more than 70% of the grains in the Opalinus Clay have sizes smaller than 0.063 mm.

The Opalinus Clay was first deposited about 174 Ma ago in a shallow-marine environment during the early Toarcian to late Aalenian age of the Jurassic period (Hostettler et al. 2017). The typical geological processes after deposition involve burial, compaction, consolidation, and diagenesis, which reduces the porosity and increases the mechanical strength of the Opalinus Clay (Corkum and Martin 2007). These processes also resulted in highly oriented clay fabrics. There are also alterations of the mechanical properties by processes such as unloading, weathering, and tectonic activities, which complicate estimating and predicting the constitutive behavior for argillaceous rocks (Gens 2013).

Mont Terri Rock Laboratory is an underground research facility located inside the Jura Mountains in Northwest Switzerland (Figure 1-3). It was established about two decades and is dedicated to scientific research on the hydrogeological, geochemical, and geomechanical properties of the Opalinus Clay (Thury and Bossart 1999; Bossart et al. 2017).

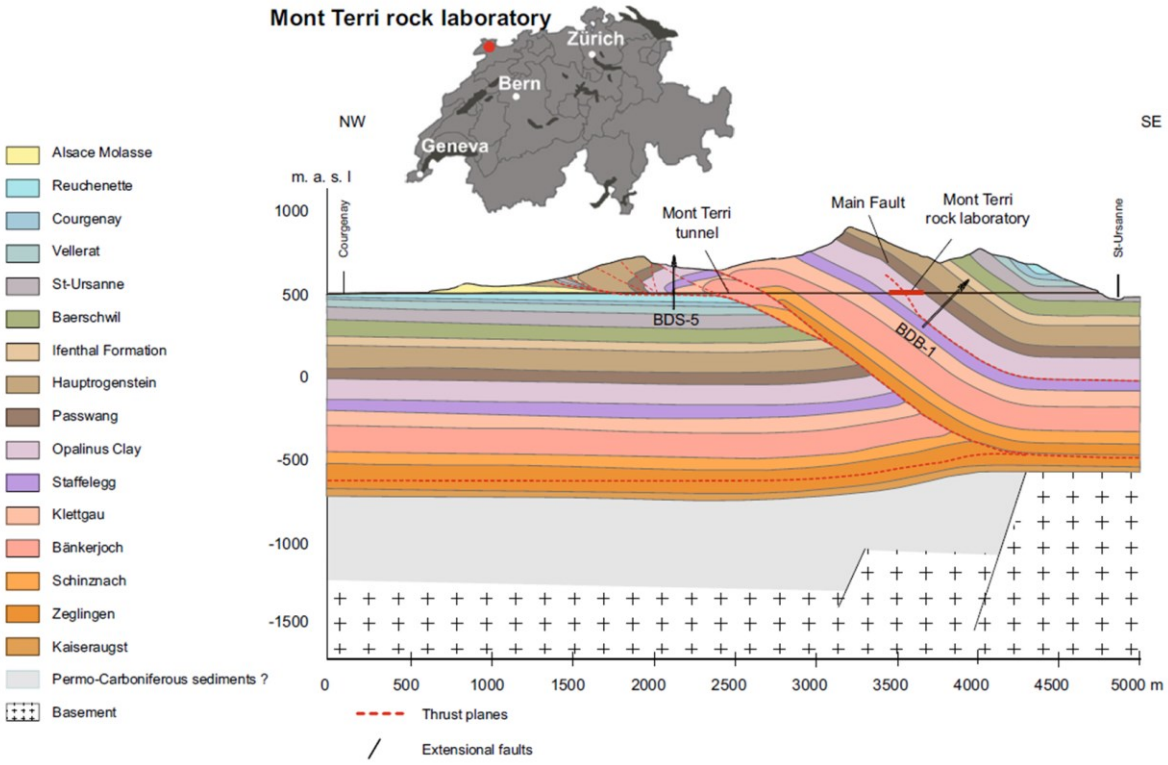

Figure 1-3. Location of the Mont Terri Rock Laboratory with the surrounding geological formations and major tectonic features in the region (Hostettler et al. 2017)

In the Mont Terri region, the Opalinus Clay Formation is overlain by the Passwang Formation and underlain by the Staffelegg Formation (Figure 1-4). The present thickness is about 131 m on average, with the bedding dipping between 30° to 50° towards the SSE. The maximum burial of the Opalinus Clay in its geological history is estimated to have been 1350 m. Given the current overburden of about 280 m in thickness, the overconsolidation ratio of the Opalinus Clay is approximately 5 (Bossart et al. 2017). The Jura Mountains formed during the late Miocene to early Pliocene age due to late alpine thrusting and folding. The Jura thrust-and-fold belt, together with other regional tectonic interferences, led to three major fault systems (Nussbaum et al. 2011) in the rock laboratory, besides the central intersecting "Main Fault" (Figure 1-4).

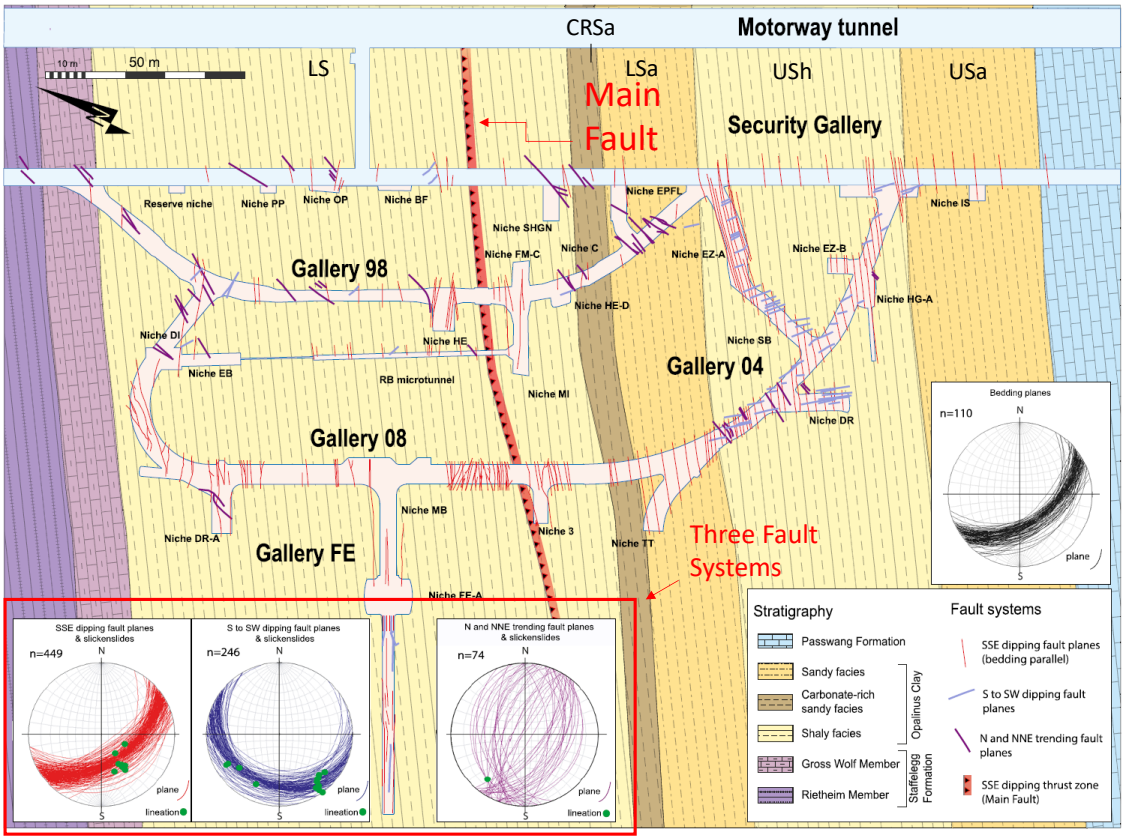

Figure 1-4. Geologic-tectonic map of the Mont Terri Rock Laboratory (Bossart et al. 2017). The abbreviations for lithostratigraphic units are: USa – upper sandy; USh – upper shaly; LSa – lower sandy; CRSa – carbonate-rich sandy; LSh – lower shaly.

Opalinus Clay can be subdivided into three lithofacies using mineral compositions – shaly, sandy, and carbonate-rich sandy facies (Bossart et al. 2017). The three lithofacies of the Opalinus Clay can be subdivided into five local lithostratigraphic units (Hostettler et al. 2017; Lauper et al. 2018), from the bottom to top – lower shaly facies, carbonate-rich sandy facies, lower sandy facies, upper shaly facies, and upper sandy facies (Figure 1-4). Hostettler et al. (2017) summarized some important characteristics of these units: the lower shaly facies consists of mica-bearing marly claystones and has sharp transition to the carbonate-rich sandy facies, which is characterized by quartz-bearing calcareous biodetritic lens; the lower sandy facies is rich in calcareous silty claystones, and overlain by dark grey mica-bearing silty claystones in upper shaly facies; the upper sandy facies consist of light grey silty claystones. Three major mineral components that are found in the Opalinus Clay are calcite, quartz, and clay minerals (including illite, illite–smectite mixed layers, kaolinite, and chlorite). The minor mineral components are mica, feldspar, pyrite, and organic matter. The mineral compositions vary from facies to facies, and the estimates for the three types of lithofacies were summarized by Bossart et al. (2017) in Table 1-1. The representative petrophysical and mechanical properties of the Opalinus Clay are also given in Table 1-1.

Because of its highly laminated structures, the mechanical properties are anisotropic and can be distinguished between the directions normal and parallel to bedding.

Table 1-1. Representative properties of Opalinus Clay reported by Bossart et al. (2017)

Parameters		Lithofacies		
		Shaly	Sandy	Carbonate-rich sandy facies
Mineralogy	Clay Minerals (wt %) (Illite, chlorite, kaolinite)	39-80	29-70	8-45
	Clay Minerals (wt %) (Illite/smectite mixed layers)	5-20	5-15	3-8
	Quartz (wt %)	10-27	22-44	22-36
	Carbonates (wt %)	4-35	11-25	34-57
	Others (wt %)	2-8	1-7	3-12
Petrophysical Properties[a]	Bulk Density (g/cm^3)	2.45	2.52	-
	Total Porosity (%)	18	11.1	-
	Water Content (%)	6.6	4	-
	P-wave Velocity[b] (m/s)	2620 (3410)	3280 (3860)	-
Mechanical Properties[a]	Uniaxial Compressive Strength (MPa) [b]	7 (10.5)	16 (18)	-
	Young's Modulus (GPa) [b]	2.8 (7.2)	6 (13.8)	-

[a] values shown are the best estimates;

[b] values shown are determined normal to bedding (and perpendicular to bedding).

1.3 Reviews of Theories, Hypotheses, and Methodologies

1.3.1 Definition and Determination of Elastic Properties

The deformation of materials under stress that can be recovered once the stress is relieved is defined as elastic deformation. A rigorous definition of elasticity is often associated with strain energy, which is the potential energy a strained body would release after unloading. The relationship between stress and strain can be derived using the strain energy function, which leads to a fourth-order tensor defined as *elastic stiffness*. When the material processes a certain degree of symmetry, the elastic stiffness may be described using a reduced number of stiffness parameters, for example, Young's modulus E and Poisson's ration v for isotropic elastic materials. A simple relation between stress σ and strain ε can be therefore established, for example, for one-dimensional case,

$$\sigma = E\varepsilon \tag{1-1}$$

The elastic parameters are closely linked to the wave velocity, for instance, in an isotropic medium,

$$\begin{aligned} \rho v_p^2 &= \frac{E(1-\nu)}{(1+\nu)(1-2\nu)} \\ \rho v_s^2 &= \frac{E}{2(1+\nu)} \end{aligned} \tag{1-2}$$

where ρ, v_p, and v_s are density, compression (or P-), and shear (or S-) wave velocities, respectively. Determining the wave velocities for geological media is important in the source estimation from the seismograms and the impact analysis in earthquake engineering.

The determination of the elastic stiffness relies on the deformation measurement under a given loading condition. The deformation was categorized into different types depending on the strain amplitude and frequency (Figure 1-5) by Batzle et al. (2006). Wave transmission methods, such as ultrasonic survey, well logging, and seismic exploration, limit the small strain amplitude of the rock to the range of 10^{-7} to 10^{-6} typically. The deformation is generally reversible and therefore elastic within this range. The modulus of rock can be determined using the measured velocity in combination with density (e.g., the reverse form of Eqn. (1-2)), and the determined moduli are termed *dynamic moduli*. Alternatively, the deformation of the rock can be directly measured provided that the instrumentation can resolve the displacement under the imposed loading. This enables the determination of the moduli using the measured strain for a given stress change in the laboratory tests on the core specimens. Since the stress is changed in a pseudo-static

manner at a relatively low rate compared to dynamic methods, the determined moduli are therefore termed *static moduli*.

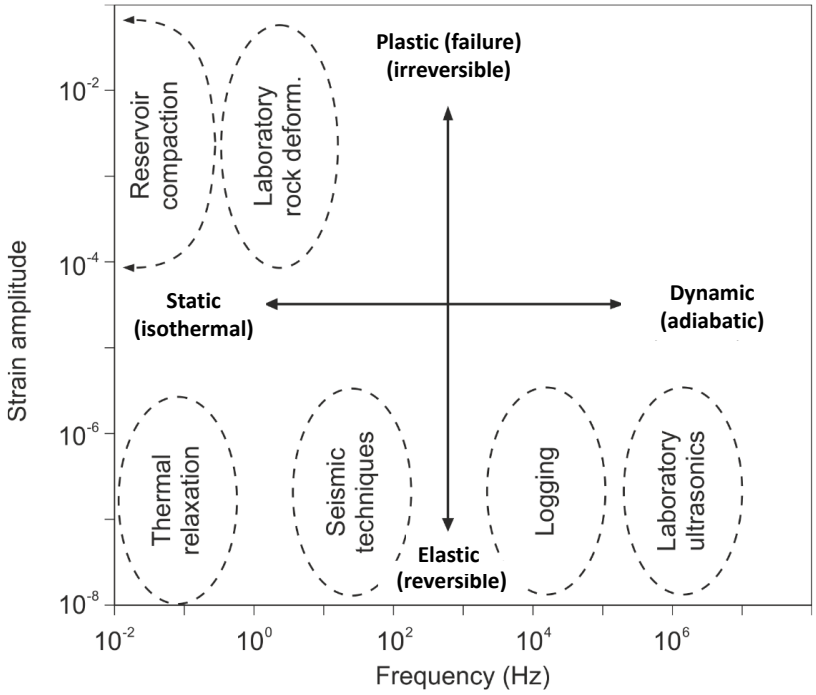

Figure 1-5. Typical deformation process over a wide range of frequencies and amplitude where the moduli of geomaterials are determined (Batzle et al. 2006).

Dynamic moduli of the fluid-saturated rocks were found to depend on the frequency due to the viscous flow (Biot 1956) and/or squirt (Mavko and Jizba 1991) of the unrelaxed fluid in the pore space induced by the passing wave. The dependence of the wave velocity on the frequency is described as *velocity dispersion*. The characteristic frequency value f_c is usually calculated to divide high- and low-frequency behavior. f_c is dependent on multiple factors, including the porosity of the rock and the viscosity of the pore fluid (Mavko et al. 2009). At a sufficiently high frequency f, i.e., $f \gg f_c$, pore fluid motion is dominated by the inertial effect and the wave-induced pore pressure variation causes the rock to be stiffer; therefore, a higher bound of velocity v_∞ (and associate Moduli M_∞) is reached. At a sufficiently low frequency, i.e., $f \ll f_c$, the spatial variation of the wave-induced pore pressure is relaxed over time and a lower bound of moduli M_0 or velocity v_0 is reached. The dispersion may be modelled by a simple relation (Mavko et al. 2009):

$$M(f) = \frac{M_0 M_\infty \left[1 + (f/f_c)^2\right]}{M_\infty + (f/f_c)^2 M_0} \tag{1-3}$$

The dependence of the moduli on frequency can be determined in the laboratory by applying forced oscillation on core specimens. This dynamic technique provides displacement modulation at the end faces of the specimen at a specified frequency, and the modulus can be calculated using the measured force and strain modulation amplitudes. A detailed description of the testing system can be referred to Szewczyk et al. (2016). An example of the elastic modulus measurement using forced oscillation for the Opalinus Clay at varying frequencies is shown in Figure 1-6. It should be noted that only the seismic frequency, i.e., less than about 200Hz, is allowed in this type of measurement. The comparison of the moduli measured across a large span of frequency shows the strong dispersion of the Opalinus Clay. This has been typically seen in the shales rather than sandstones, possibly suggesting an essential role of clay minerals in the dispersion mechanism (Fjær et al. 2013).

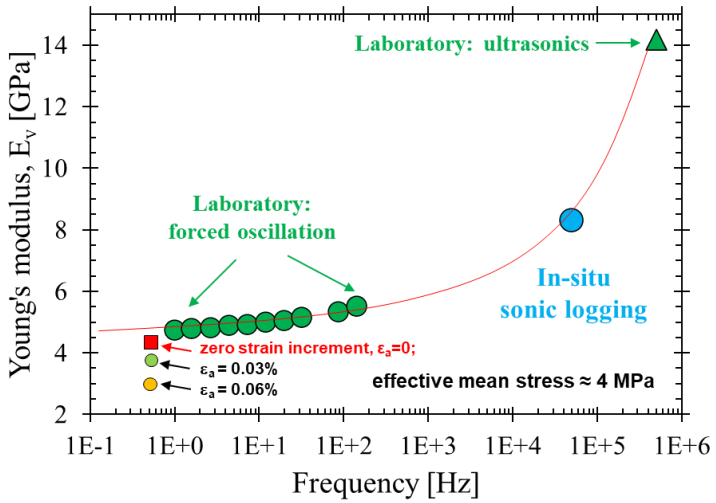

Figure 1-6. Dependence of modulus values on frequency from measurements on Opalinus Clay (Giger et al. 2018b)

The dispersion relation can also be applied to the static measurement on the core specimen. Instead of frequency *f*, strain rate $\dot{\varepsilon}$ is used and compared with the average strain rate derived from elastic wave propagation in a dynamic test (Fjær et al. 2013). If the strain amplitude of an elastic wave is 10^{-7}, a quasi-static loading test with a typical strain rate of 10^{-6} s^{-1} is equivalent to a dynamic test with the frequency at the order of 1Hz, which is in the lower frequency range of dispersion.

The factor that may have the most significant impact on the static modulus measurement is the strain amplitude. For a monotonic loading over a finite strain, deformation at macro-scale may become nonlinear and irreversible when at the micro-scale (a) grain crushing and/or (b) the frictional sliding or opening of the micro-cracks occur. The accumulated inelastic strain for a given stress increment leads to the reduction of the measured modulus. In general, grain crushing is responsible for the inelastic

deformation under a hydrostatic loading, while frictional sliding is dominant under the deviatoric loading, such as in a uniaxial compression test.

Immediately upon the unloading in a compression test, the micro-crack sliding was shown to be inhibited, and the inelastic deformation did not continue until the sliding was reactivated in the reverse direction (Walsh 1965; David et al. 2012). This can be demonstrated using a uniaxially stressed body with a critically aligned microcrack in Figure 1-7(a). This phenomenon motivated using unload-reload cycles (Figure 1-7(b)) in triaxial compression tests for the modulus determination for weak rocks that exhibit strong nonlinearity during the initial loading (e.g., Plona and Cook 1995; Holt et al. 2015; Zhang and Laurich 2020).

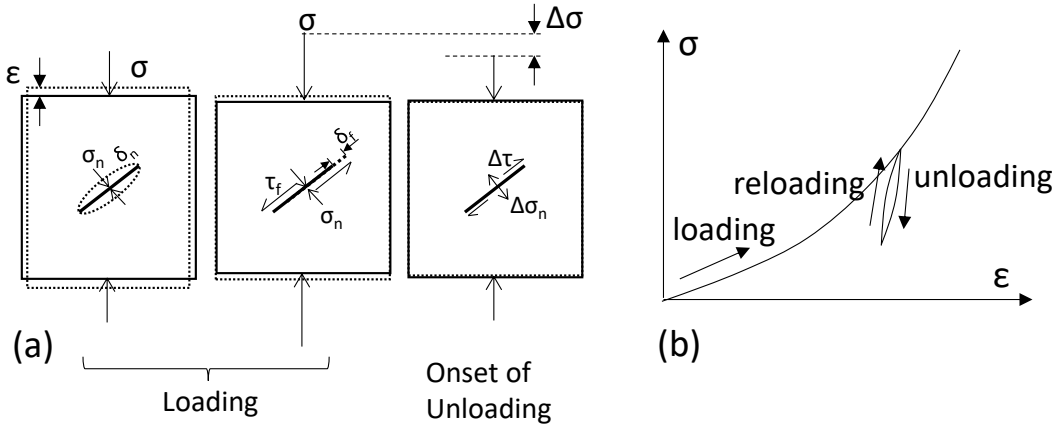

Figure 1-7.(a) Schematic of the stress (σ, τ) and displacement (δ) on a microcrack in a uniaxially stressed body with resultant deformation (ε). (b) typical stress-strain curve for weak rocks under unconfined uniaxial loading.

To further approximate the true elastic moduli and reconcile with the dynamic moduli, Fjær et al. (2013) suggested extrapolating the modulus measurement to the zero strain amplitude in an unloading sequence. A similar technique was applied by Lozovyi and Bauer (2018) for their measurement on the Opalinus Clay. The determined static modulus at zero strain reasonably approached the dynamic modulus obtained from the forced oscillation tests, as shown in Figure 1-6.

The comparison of the static and dynamic moduli of sedimentary rocks is further complicated by the saturation of the specimen, the drainage condition in the static measurement, the loading/probing orientation with respect to the rock anisotropy, and the material heterogeneities (Fjær 2019). For example, the material heterogeneities can play a substantial role primarily when the dynamic and static measurements are conducted at two different scales, respectively – the elastic wave tends to follow the path with the stiffest constituents, whereas static measurement is the response obtained from the entire

volume of the material under the loading. In general, the influence of each factor addressed above may be hard to identify as it can be coupled with other mechanisms.

1.3.2 Dependence of Elastic Properties on Stress/strain Path

Rock is composed of different components, including solid minerals and voids. Its elastic properties depend on the proportion and stiffness of each component and their geometrical distributions in a volume of interest (Fjaer et al. 2008). The proportion of the voids (or porosity) may be the dominant factor in the rock with reasonable homogeneity. The increase of the elastic stiffness is generally associated with the reduction of the voids in the increase of the confining stress. According to an extensive set of laboratory test data on various rock types, the increase of Young's modulus with confining stress could be generally described by an exponential relationship (Kulhawy 1975). It was also found that Young's modulus obtained for competent crystalline rocks with low porosity is less sensitive to the confining stress than more porous clastic rocks.

The impact of the voids on the elastic stiffness (or equivalent wave velocity) of rock has been generally modeled using two micromechanical schemes – *grain packing* and *crack inclusion* (Fjaer et al. 2008). Conceptually speaking, the former reproduces the physical mechanism of grain contacts and rearrangement as expected in the granular rocks (e.g., sandstones). At the same time, the latter can be used to resemble the rocks with strong structural anisotropy by assuming the crack sets with preferential orientations (e.g., in shales). Both schemes can assess the influence of stress on elastic stiffness. For example, regarding the grain packing scheme, Li and Fjaer (2012) studied the interaction of the packed and bonded grains after stress alteration and the resultant change of static and dynamic moduli using discrete element methods. Regarding the crack inclusion scheme, Mukerji and Mavko (1994) introduced a stress-dependent tensor of crack compliance $W_{ijkl}^{(q)}(\boldsymbol{\sigma})$ for the q^{th} crack, and it contributes to the overall compliance of the rock $S_{ijkl}(\boldsymbol{\sigma})$ in the following additive manner,

$$\begin{aligned} \Delta S_{ijkl} &= \sum_{q} \phi^{(q)}(\boldsymbol{\sigma}) W_{ijkl}^{(q)}(\boldsymbol{\sigma}) \\ S_{ijkl} &= S_{ijkl}^{0} + \Delta S_{ijkl} \end{aligned} \tag{1-4}$$

where $\phi^{(q)}(\boldsymbol{\sigma})$ is the porosity of the q^{th} crack that is also stress-dependent, and S_{ijkl}^{0} is the intrinsic compliance of the rock at a crack-free condition, which may be determined at a substantially high confining pressure.

Eqn. (1-4) explains the stiffening effect of crack closure under directional compressive stress, suggesting that the stiffness anisotropy can be induced by stress. For a rock with isotropic intrinsic compliance (or

stiffness) and a random distribution of crack sets with the same geometrical characteristics, Eqn. (1-4) predicts an isotropic stiffening under hydrostatic compression. The crack compliance generalized for all the crack sets in this case may be calibrated if the compressive and shear wave velocity measurements are available (Mavko et al. 1995).

The initiation and/or growth of the cracks in rocks may occur under (a) tensile loading and (b) high deviatoric stress even under compression. For the latter case, cracks oriented at a skew angle relative to the major principal stress may be under tension at the tip and tend to grow if the local tensile stress exceeds the limit. The stress-induced cracking process has been investigated on the core specimen at different scales (Hallbauer et al. 1973; Tapponnier and Brace 1976; Chiarelli et al. 2003; Desbois et al. 2017). Figure 1-8 (a) shows an example of micro-cracks developed subparallel to the axial stress in the specimen after loading. At a larger scale, the axial fracturing that dominates the rock damage under unconfined compression was commonly observed and was reproduced using finite-discrete element modeling (Figure 1-8(b)).

By breaking the diagenetic bonding and creating new voids, the stress-induced cracking process causes the reductions of both static modulus (Niandou et al. 1997; Chiarelli et al. 2003; Heap and Faulkner 2008; Zhang and Laurich 2020) and wave velocity (Sayers 1990; Dewhurst and Siggins 2006; Fjaer 2006; Popp and Salzer 2007). Such alteration to the mechanical properties of rock is generally referred to as damage.

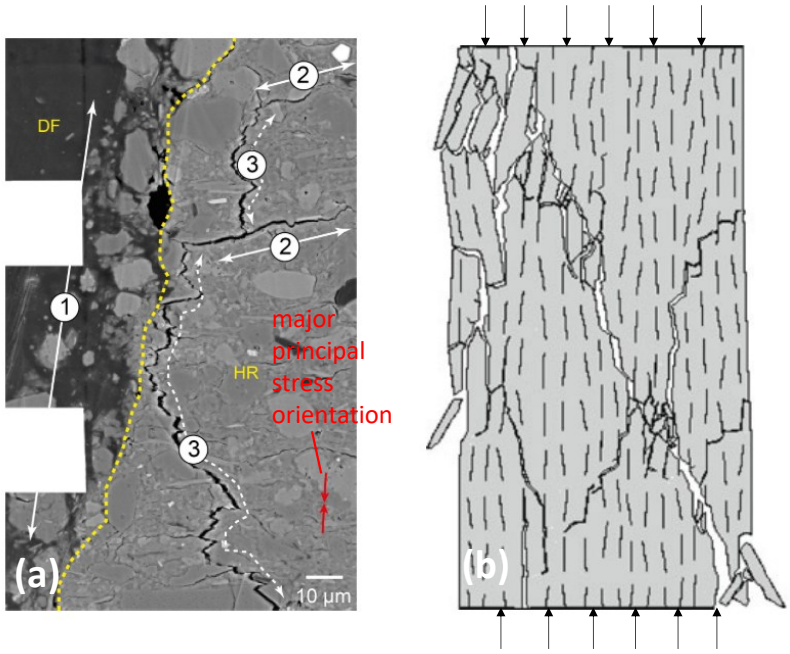

Figure 1-8. Stress-induced cracking in claystones with preferential fracture orientation subparallel to the major principal stress: (a) BSE-SEM micrograph of specimen section after uniaxial loading at 2 MPa confining pressure with (1) damage fabric and (2,3) micro-cracks in Callovo–Oxfordian Clay (Desbois et al. 2017); (b) predicted fracture patterns in Opalinus Clay specimen after unconfined compression test using finite-discrete element method (Lisjak et al. 2014b)

For a standard triaxial compression test, a combination of the mechanisms mentioned above may affect the mechanical properties of the rock. Different stages of deformation were proposed for brittle rocks (Bieniawski 1967; Martin 1997): (1) crack closure, (2) linear deformation, (3) crack initiation and stable growth, and (4) unstable crack growth. The same concept was adopted to investigate the nonlinear behavior of the Opalinus Clay (Corkum and Martin 2007; Popp and Salzer 2007; Amann et al. 2011). The typical stress-strain curve of Opalinus Clay during the phase of uniaxial compression in a triaxial test is shown in Figure 1-9. The initial loading stage is dominated by nonlinear compression when the pre-existing micro-cracks and/or pores are closed, and the specimen appears to be stiffened. New cracks are initiated and growing in the increase of loading. The transition of volumetric strain ε_v from being compressive to dilative is an indication of the cracking process. The dilation of the Opalinus Clay specimen under unconfined compression was identified by Amann et al. (2011) and closely associated with the onset of acoustic emission generated from cracking. They found that micro-cracks developed at a very early stage of loading (about 30% of the peak stress), which suggests that the stage of linear deformation proposed for brittle rocks may not exist for the tests at low confining pressure on the Opalinus Clay specimens. At Stage 2 in Figure 1-9, the increase of the elastic stiffness and wave velocity as a result of crack closure tends to be impeded by ongoing cracking processing (Popp and Salzer 2007;

Zhang and Laurich 2020). Eventually, those mechanical properties will reach their peak values, followed by a sharp reduction. The reduction will reach a limit when the induced cracks are interconnected and finally coalesced into rupture planes.

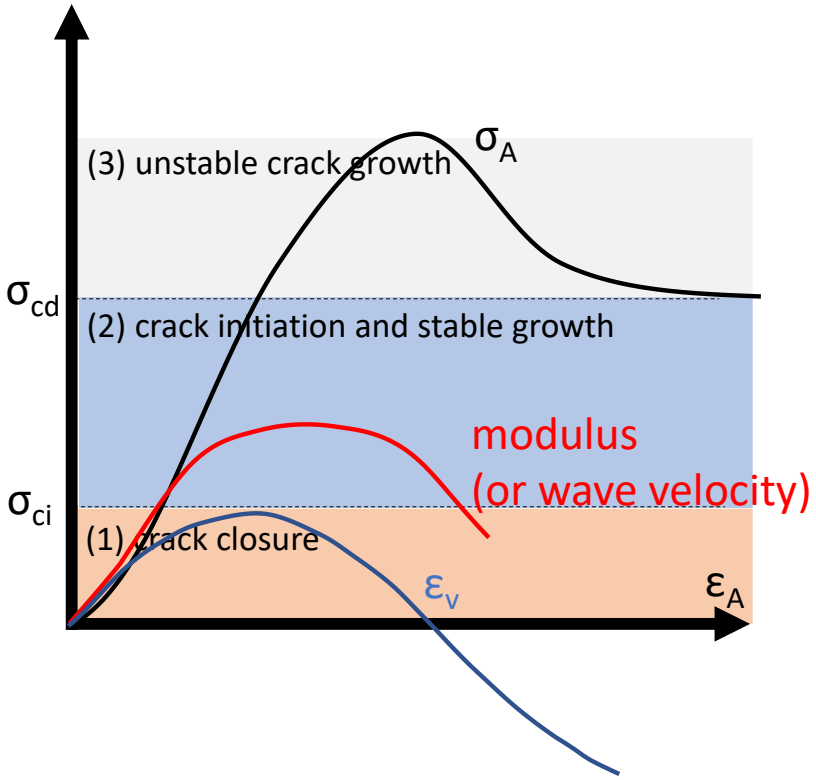

Figure 1-9. Typical deformation of Opalinus Clay at different loading stages during uniaxial compression at low or zero confining pressure. σ_A, ε_A, and ε_v are the axial stress, axial strain, and volumetric strain, respectively. σ_{ci} and σ_{cd} are crack initiation and crack damage stresses, respectively. The evolution of the elastic modulus (or wave velocity) is generalized for the measurements obtained by Popp and Salzer (2007) and Zhang and Laurich (2020)

For saturated rocks, the presence of pore fluid impacts the overall elastic stiffness with lower compressibility than air. At the same time, it resists the compression of voids when being pressurized by an undrained loading. In other words, the stress that acts on the rock skeleton is less than the loading applied externally. Therefore, the concept of effective stress was generally used to describe the variation of the elastic stiffness for tests of the saturated shales. The relationship between Young's modulus and the effective confining or mean stress for Opalinus Clay has been determined in the undrained triaxial test where pore pressure was measured (Giger et al. 2018a; Wild and Amann 2018a; Minardi et al. 2021).

1.3.3 In-situ Stiffness Measurement

The in-situ static stiffness is often assessed by measuring the deformability of the rock in a larger volume than the laboratory specimen. The measurement was conducted in a test borehole using borehole jacking test and/or the pressuremeter (dilatometer) tests. Schematic diagrams of these borehole tests are shown in Figure 1-10. The expansion of the borehole was measured under pressure-controlled inflation. Borehole jack applies the loading diametrically against a portion of the borehole circumference (Goodman et al. 1968). It is mostly used for testing competent rocks as it allows the loading plate to be driven by a hydraulic or mechanical piston under high pressure. Pressuremeter applies the uniform pressure at the borehole wall by inflating a membrane-covered probe. Pressuremeter probes are divided into two categories based on the way the expansion of the borehole is determined. "Menard" type pressuremeter only monitors the volume of fluid injected into the probe. The radial displacement is calculated from the measured volumetric change of the probe. Two guard cells at the end of the probe are often used to prevent the probe from expanding axially. "Cambridge" type pressuremeter measures the radial displacement directly at multiple diametric axes, which is considered more reliable than the conversion from the volume measurement and also allows the anisotropic response of the borehole to be captured (Rocha 1970; Zalesky et al. 2007; Liu et al. 2021a).

For pressuremeter testing in the ground that doesn't exhibit strong anisotropies in in-situ stress and material stiffness, the problem is generally assumed to be axisymmetric in the testing plane. This simplification in the boundary condition allows the analytical solutions used for test data interpretation to derive a broad class of geomaterials and varying drainage conditions. These interpretation methods are generally called *cavity expansion methods* and are summarized by Yu (2000). For an axisymmetric deformation in a linear elastic medium, a simple relationship between pressure p_c and radial displacement u_r at the borehole wall can be derived following Timoshenko and Goodier's (1934) procedure that combines stress equilibrium, compatibility, and stress-strain relations,

$$u_r = \frac{p_c a}{2G} \tag{1-5}$$

where G is the shear modulus of the medium. The pressuremeter test curve of p_c versus u_r allows for the direct determination of the shear modulus.

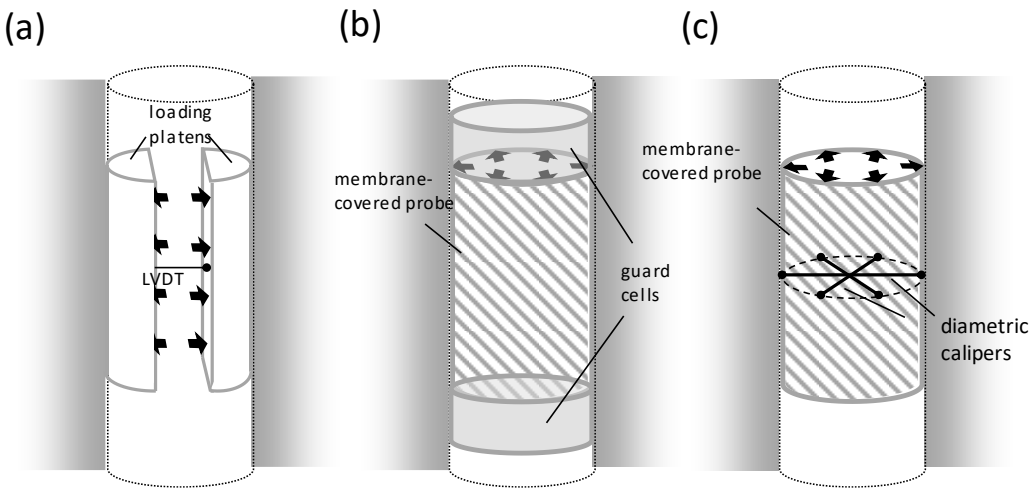

Figure 1-10. Rock deformability measurement in a test borehole by (a) borehole jacking test, (b) "Menard" type pressuremeter test, and (c) "Cambridge" type pressuremeter test.

It should be noted that a in Eqn. (1-5) is the current radius of the borehole rather than the initial radius a_0, which means that u_r is actually in a nonlinear relation with p_c when $a = a_0 + u_r$. However, the deformation of rock in pressuremeter tests is reasonably small, i.e., $u_r/a_0 < 1\%$, so the linear form of Eqn. (1-5) with $a = a_0$ is acceptable. Under the linear elastic assumption, the deformation at the step of pressuremeter loading is independent of the previous step of drilling unloading regardless of the initial stress field.

Pressuremeter testing has been applied in nearly all types of geomaterials. A reliable measurement of the stiffness in rocks requires the high-pressure capacity and displacement resolution of the pressuremeter probe. Another challenge that is often encountered, especially for the testing in weak rocks (with UCS < 25MPa), is the disturbance at the borehole wall induced by stress relief, the erosion of the softer layers, and/or the drilling vibration. The disturbance would place the question of how good the measurement is representative of the undisturbed rocks. In extreme cases, it would cause borehole instability and even the loss of the instrument if the borehole collapse. Therefore, careful design and operation of drilling are important for pressuremeter testing in weak rocks. Self-boring pressuremeters were designed and used to reduce the drilling and installation disturbance. However, because the drill bit attached to the instrument is often oversized to reduce the friction on the instrument during drilling, disturbance by stress relief is also inevitable and should be taken into account for self-boring pressuremeter test in most weak rocks (Clarke and Smith 1992). The mechanical disturbance to rock in the near-borehole field after stress change at the borehole wall will be reviewed in Section 1.3.4.

1.3.4 Borehole Responses under Unloading/Loading

1.3.4.1 In-situ Stress

Any natural materials in the ground are subject to stress. Such a stress state often refers to in-situ stress. At a given point in the solid earth, the in-situ stress is mathematically defined as a second-order tensor in a reference Cartesian coordinate system,

$$\boldsymbol{\sigma} = \begin{bmatrix} \sigma_{xx} & \sigma_{xy} & \sigma_{xz} \\ \sigma_{yx} & \sigma_{yy} & \sigma_{yz} \\ \sigma_{zx} & \sigma_{zy} & \sigma_{zz} \end{bmatrix} \tag{1-6}$$

It can be physically seen as equilibrated forces acting on an infinitesimal cube with normal and shear components,

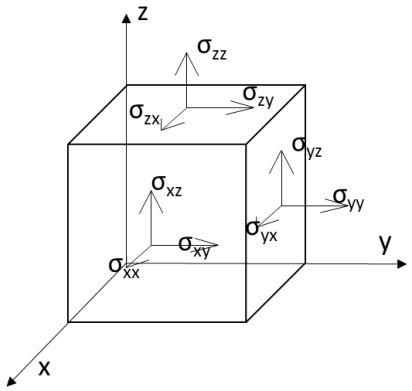

Figure 1-11. Stress on an infinitesimal cube of a solid in the Cartesian coordinate system

With a specific rotation of coordinate frame, the stress state can be expressed with three principal normal stresses in a tensor with other components vanished,

$$\boldsymbol{\sigma} = \begin{bmatrix} \sigma_1 & 0 & 0 \\ 0 & \sigma_2 & 0 \\ 0 & 0 & \sigma_3 \end{bmatrix} \tag{1-7}$$

For the stress tensor in the ground, it is common to assume that one principal stress is vertical and results purely from the gravitation of overburden. At the depth z below the surface, this principal stress is therefore equal to,

$$\sigma_V = -\int_0^z \rho g dz \tag{1-8}$$

where earth density ρ also varies with depth. The other two principal stresses are horizontal and denoted as σ_H and σ_h, representing the maximum and minimum horizontal principal compression, respectively. For simple uniaxial compaction in a homogeneous medium, the horizontal stress is isotropic and can be calculated using Hoek's law with the horizontal deformation constraint (Eaton 1969),

$$\sigma_H = \sigma_h = \frac{\nu}{1-\nu}\sigma_V \tag{1-9}$$

In reality, the complex geological history of the ground, including surface erosion, fluid migration, faulting, and other tectonic activities, can alter the in-situ stress locally and lead to a significant deviation of the horizontal stress from the estimation by Eqn. (1-9).

The orientations and magnitudes of in-situ stresses in a region are usually constrained by seismic and geological observations (Zoback 2010). The local in-situ stress estimate may be refined by conducting measurements in a drilled hole. These stress determination techniques usually include the perturbations to an unloaded borehole (Amadei & Stephasson, 1997), such as 1) borehole *overcoring* and 2) *micro-fracturing* under a controlled hydraulic injection in a test interval. The stress estimation by borehole overcoring uses the strain-induced after the stress relief and requires the prior information of the rock stiffness. It is mainly applied to shallow boreholes where the strain measurement device can be easily installed. The micro-fracturing technique relies on the initiation of fractures that open in the direction of the minimum principal stress and therefore have the most reliable estimation of the minimum principal stresses. An accurate estimation of the in-situ stress by micro-fracturing also relies on the premise that the extent of the fracturing is beyond the stress disturbance zone in the near-borehole field. The quality of the stress estimates suffers from the limitation of each stress determination technique. A considerable uncertainty in the stress estimate has been observed in the challenging ground, for example, in clay shales (Martin and Lanyon 2003; Yuan et al. 2013). However, the uncertainty may be constrained when multiple independent measurements and indirect evidence from on-site observations are carefully assessed and integrated.

1.3.4.2 Drilling Unloading

Stress redistributes around the borehole wall after drilling-induced unloading. The redistributed stress field can be analytically determined according to the solutions derived for a circular opening in an isotropic (Kirsch 1898) or an anisotropic elastic (Amadei 1983) medium. For a vertical borehole with

radius a, three in-plane stresses σ_θ, σ_r and $\sigma_{\theta r}$, and out-plane stress σ_z, in a cylindrical coordinate system from the prediction using Kirsch's solution are,

$$\begin{aligned}
\sigma_r &= \frac{\sigma_H + \sigma_h}{2}\left(1 - \frac{a^2}{r^2}\right) + \frac{\sigma_H - \sigma_h}{2}\left(1 + \frac{3a^4}{r^4} - \frac{4a^2}{r^2}\right)\cos 2\theta + p_c \frac{a^2}{r^2} \\
\sigma_\theta &= \frac{\sigma_H + \sigma_h}{2}\left(1 + \frac{a^2}{r^2}\right) - \frac{\sigma_H - \sigma_h}{2}\left(1 + \frac{3a^4}{r^4}\right)\cos 2\theta - p_c \frac{a^2}{r^2} \\
\sigma_{\theta r} &= -\frac{\sigma_H - \sigma_h}{2}\left(1 - \frac{3a^4}{r^4} + \frac{2a^2}{r^2}\right)\sin 2\theta \\
\sigma_z &= \sigma_V - 2\nu\left(\sigma_H - \sigma_h\right)\frac{a^2}{r^2}\cos 2\theta
\end{aligned} \tag{1-10}$$

where r and θ are the radius and the angle from the axis of σ_H, respectively; ν is the Poisson's ratio of the rock. The internal pressure p_c is equal to 0 for a fully unloaded borehole. The displacement field is also readily derived by invoking the stress-strain relations for a plane-strain condition (Goodman 1989), and at the borehole wall,

$$\begin{aligned}
\frac{u_r}{r_0} &= -\frac{1+\nu}{2E}\left[\left(\sigma_H + \sigma_h\right) + \left(3 - 4\nu\right)\left(\sigma_H - \sigma_h\right)\cos 2\theta\right] + \frac{p_c}{E}\left(1+\nu\right) \\
\frac{u_\theta}{r_0} &= \frac{\left(1+\nu\right)}{2E}\left(3 - 4\nu\right)\left(\sigma_H - \sigma_h\right)\sin 2\theta - \frac{p_c}{E}\left(1+\nu\right)
\end{aligned} \tag{1-11}$$

where θ is the angle clockwise from σ_H and p_c is the borehole pressure. In Eqn. (1-11), borehole convergence is defined as negative. It is treated as the supposition of the displacements due to total stress relief and subsequent borehole loading.

The closed-form solution of the local stress distribution was derived by Amadei (1983) and tailored by Ong (1994) for a borehole drilled with arbitrary orientation in a generally anisotropic medium. Gaede et al. (2012) and Fang (2018) revisited the solution and presented the simplified forms for the cases where the anisotropy of the medium is reduced to transverse isotropy. In Amadei's (1983) thesis, the exact expression of the borehole wall displacement at the azimuth θ for the case with general anisotropy was also provided, but it remained complicated for practical use.

An example of the principal stress trajectory around the borehole in an isotropic elastic medium is shown in Figure 1-12 for the case of $\sigma_H / \sigma_h = 3$, where the tangential stress concentration and relief are predicted for the rock element near borehole wall at θ equal to 90° and 0° respectively.

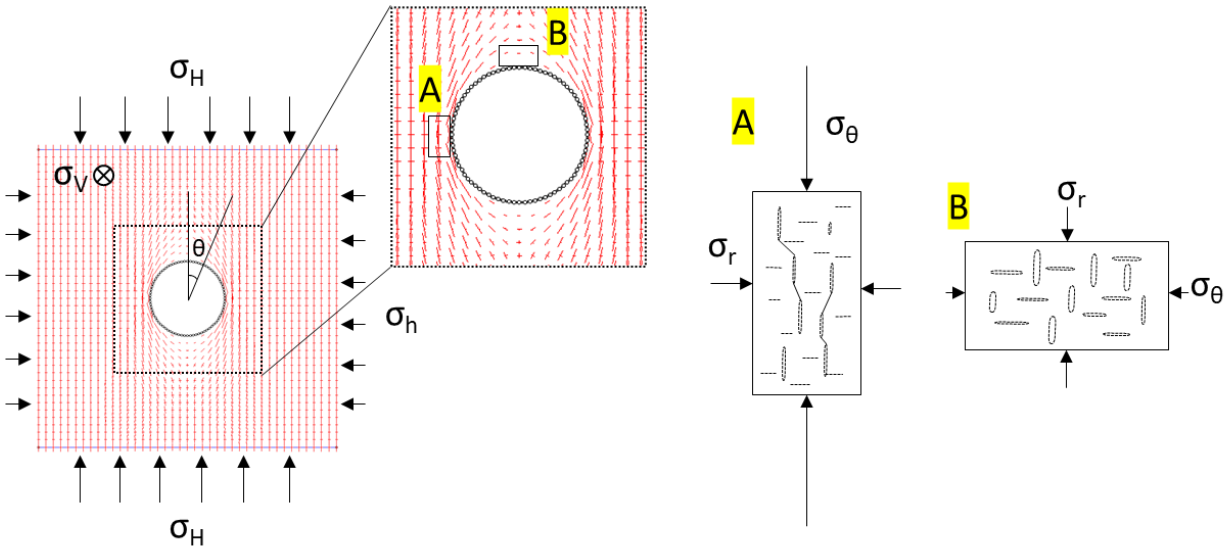

Figure 1-12. Principal stress trajectory around a circular opening predicted using the boundary element method in Examine2D (Rocscience 2006) for the case of $\sigma_H / \sigma_h = 3$. The stress concentration and possible cracking behavior in two elements near the borehole wall at θ=0° and 90° respectively are demonstrated at the right.

The dependence of the elastic properties on the stress as addressed in Section 1.3.2 implies the stress-induced anisotropy in the near-borehole field for the case shown in Figure 1-12. For the simplification, it is intended to use a scalar, mean stress p, to quantify the stress concentration in the medium. Using Eqn. (1-10), the azimuthal variation of p at the borehole wall is,

$$p = \frac{\sigma_V + \sigma_H + \sigma_h}{3} - 2(1+\nu)(\sigma_H - \sigma_h)\cos 2\theta \qquad (1\text{-}12)$$

Eqn. (1-12) indicates higher stress concentration at $\theta = 90^o$ than $\theta = 0^o$ by a magnitude of $4(1+\nu)(\sigma_H-\sigma_h)$. The non-uniform stress concentration around borehole leads to local stiffening of rock with more closure of pre-existing cracks with at $\theta = 90^o$ and less crack closure and even reopening of cracks which lead to local softening of rock at $\theta = 0^o$. The azimuthal variation of the elastic stiffness in the rock surrounding the borehole was identified using ultrasonic surveys (Winkler 1996; Winkler and D'Angelo 2006). Figure 1-13(a) illustrates the block sandstone specimen with a borehole at the center from Winkler's (1996) experiment, where the compressive wave velocity along the borehole axis was measured at varying azimuths using an array of ultrasonic transmitters and receivers. The measurement result under the condition when external uniaxial boundary stress σ_{yy} was equal to 10 MPa is shown in Figure 1-13(b). The lowest velocity, suggesting the least local stress concentration, was identified near the azimuth of the maximum boundary stress, $\sigma_{yy,}$ which agrees with the prediction by Eqn. (1-12). It should be noted that the background velocity (at zero stress) of the Berea sandstone used in this experiment was about 2.54

km/s, even lower than at $\theta = 0^{o}$ where tension at the borehole wall was expected. This might be because the velocity obtained from the ultrasonic survey (e.g., Figure 1-13(b)) likely represents a local region in the medium that extends beyond the borehole wall, as shown by Fang et al. (2013). In another experiment in Hanson sandstone with relatively lower porosity, the measured wave velocity was more sensitive to tensile stress than Berea sandstone and reduced to a magnitude less than the background velocity (about 3.27km/s) at $\theta = 0^{o}$. Therefore, rocks with different initial physical properties may have different responses to stress change.

The local stress concentration near $\theta = 90^{o}$ may also induce additional cracks oriented parallel to the tangential stress, as shown in the conceptual diagram of Figure 1-12. The development of these cracks can be progressive after the tangential stress exceeds the strength limit of the rock. The phenomenon that for a certain circumferential and radial extent near the borehole rock loses its mechanical integrity and starts to spall out from the borehole wall is called *borehole breakout*. Two major mechanisms that trigger the breakout have been identified – (a) slip of fractures under local shearing and (b) detachment of grains under extension. The first mechanism causes the development of the *conjugated fractures* surrounding the borehole as observed by Meier et al. (2013) in the shale with refined and uniformly sorted grains, whereas the second mechanism leads to *splitting-type cracking* as observed in the rocks with coarser and poorly sorted grains (Ewy and Cook 1990a; Haimson 2007).

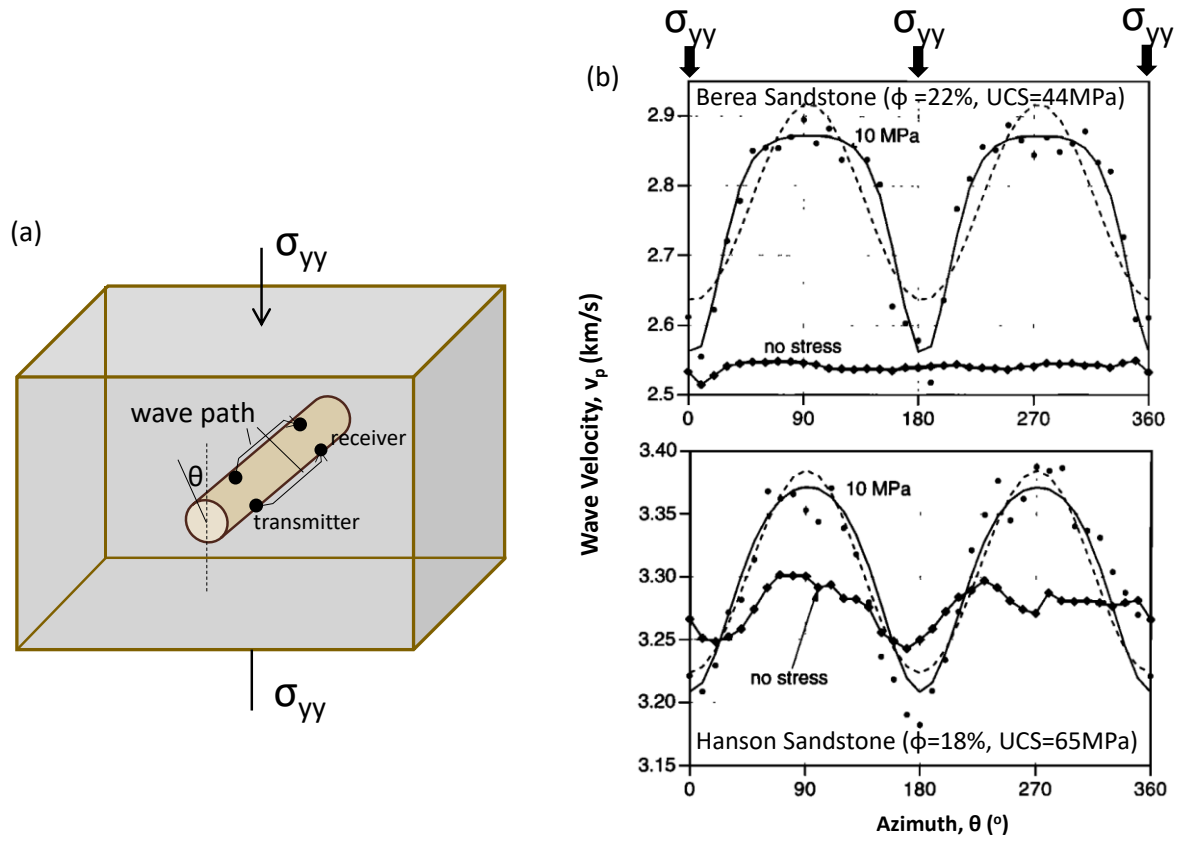

Figure 1-13. (a) Schematic diagram of the experimental setup in Winkler's (1996) investigation of the azimuthal variation of wave velocity around the borehole caused by stress concentration; (b) azimuthal variation of the compressive wave velocity in two sandstones from measurement (dots) and trendline fitting (lines) when σ_{yy}=10 MPa. ϕ: porosity; *UCS*: unconfined compression strength.

Balland and Renaud (2009) applied borehole ultrasonic survey in Callovo-Oxfordian claystone at Meuse-Haute/Marne underground research laboratory. They used an array of transmitters and receivers with different sensor distances. The radial variation of the velocity was interpreted using tomographic inversion of the ultrasonic data (Figure 1-14(a)) and repeated for multiple axes covering the entire 360° plane of borehole cross-section (Figure 1-14(b)). It was found that the P-wave velocity increases from the borehole wall to the far-field within the first ~5cm (0.175 borehole diameter). The low velocity at the borehole wall, especially at the azimuth of the minimum in-plane far-field stress σ_h, is likely the consequence of the borehole damage with potential breakout under high tangential stress (about 36MPa against a *UCS* of 12MPa).

As mentioned before, tensile cracking is also likely at the azimuth $\theta = 0°$ when $\sigma_\theta < 0$ at the borehole wall, according to Eqn. (1-10) when $\sigma_H / \sigma_h > 3$. The development and interaction of the different families of

the cracks around the borehole wall add extra complexity in modeling and quantifying the borehole damage (Carter et al. 1991). The stress-induced change of mechanical properties in the near-borehole field would change the stress distribution in return. The prediction using the linear elastic solution, therefore, becomes inaccurate. The improved prediction has been proposed to account for the reduction of the elastic modulus under stress relief (Santarelli and Brown 1987) and the reduction of the strength after borehole yielding (Reed 1986).

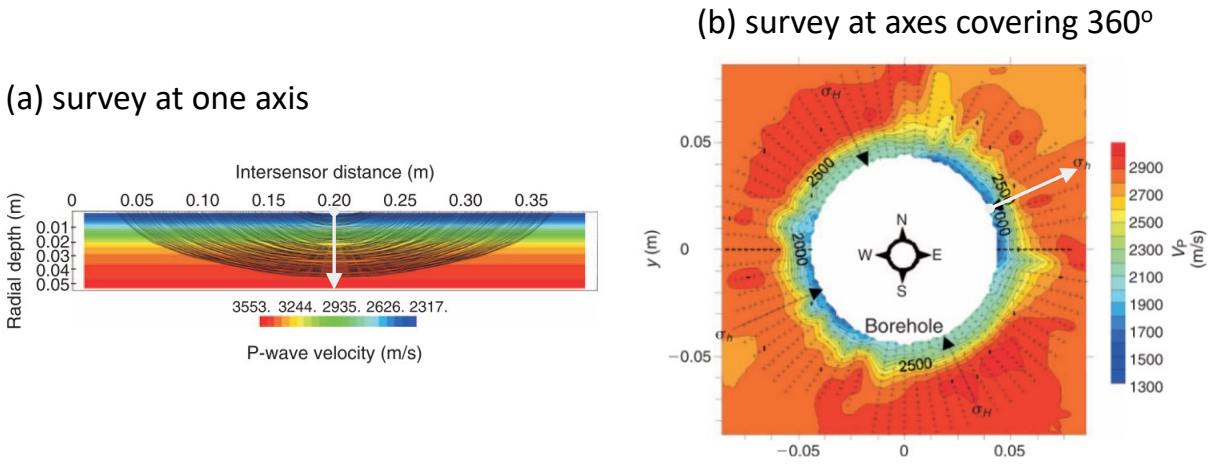

Figure 1-14. Wave velocity field determined by tomography inversion of borehole ultrasonic survey (Balland and Renaud 2009) for (a) one axis and (b) whole borehole cross-section. Reduction of velocity near the borehole, particularly in the direction of the minimum far-field stress σ_h, indicates the damage of rock.

1.3.4.3 Borehole Loading

The stress applied to the borehole wall changes the local stress in the borehole nearfield and expands the borehole. Figure 1-15 shows the stress path under a uniform expansion pressure covering the borehole wall. The increase of the radial stress σ_r tends to reduce the tangential stress σ_θ in the nearfield and, to a certain extent, induces tension at the borehole wall. Employing Kirsch's equation (Eqn. (1-10)) for a vertical borehole predicts that the tensile failure would be initiated when

$$p_c = (\sigma_H + \sigma_h) - 2(\sigma_H - \sigma_h)\cos 2\theta + T \tag{1-13}$$

where T is the tensile strength of the rock. Shear failure is also likely once the in-plane shear stress $(\sigma_r - \sigma_\theta)/2$ exceeds the limit τ_f (Figure 1-15). Combining Eqn. (1-10) leads to the critical expansion pressure for the shear failure to occur at the borehole wall,

$$p_c = \frac{\sigma_H + \sigma_h}{2} - \left(\sigma_H - \sigma_h\right)\cos 2\theta + \tau_f \tag{1-14}$$

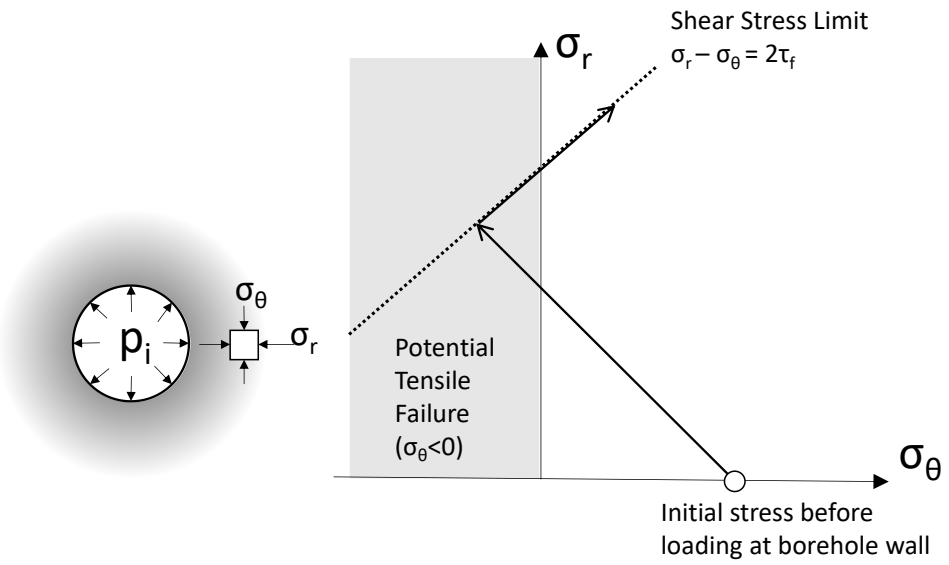

Figure 1-15. Stress state and stress path for a borehole under uniform internal loading

Both Eqns. (1-13) and (1-14) predict that the tensile and shear failures would initially occur at $\theta = 0^o$ in the direction of σ_H. Although azimuthal and radial variations of mean stress are expected in the borehole nearfield for the case of $\sigma_H \neq \sigma_h$, according to Eqn. (1-10), the increase of p_c does not change the mean stress distribution, and therefore neither the mechanical properties associated with the mean stress. However, any nonlinearity and anisotropy introduced in the material models, as shown in later chapters, will change the prediction of local stress and the mechanical properties after borehole loading. Tensile and shear failures would also induce an irrecoverable change in the mechanical properties of rock in the borehole nearfield.

1.4 Thesis Outline

This thesis includes field, laboratory, and modeling assessments of the elastic stiffness of the Opalinus Clay. Chapter 2 describes the GC field experiment at the Mont Terri Rock Laboratory and the evaluation of the pressuremeter test data in comparison with reported laboratory results. Chapter 3 presents the laboratory work on the Opalinus Clay core specimens with the objective of understanding the evolution of the elastic stiffness in a cycle of loading and unloading. Chapter 4 provides a constitutive formulation of the Opalinus Clay based on the laboratory measurement with the special consideration of stress-dependent elastic modulus. The constitutive model is implemented into a finite element code so that the borehole response at the stages of borehole drilling and pressuremeter loading can be predicted. Chapter 5

investigates the localized borehole damage zone induced by drilling unloading and aims to explore its relation to the in-situ stresses. This chapter incorporates the model analysis (both analytical and numerical) and the explanation of the field observations. A robust estimation of the far-field stress orientation in the borehole cross-section plane is provided. Chapter 6 summarizes the findings presented in this thesis and suggests the direction of future research.

Chapter 2

Determination and Assessment of In-situ Elastic Properties at Mont Terri Rock Laboratory[1]

2.1 Site Information

Situated at about 300m below the surface, the Mont Terri Rock Laboratory lies in the Mont Terri anticline. It consists of 1200 m of galleries and niches, which can be accessed through the security gallery of the Mont Terri motorway tunnel. The site of interest is the south side of the laboratory, where a new gallery, Gallery 18, was recently excavated (Figure 2-1). Three boreholes were drilled for pressuremeter tests as part of the Geomechanical In-situ Characterization (GC) GC Experiment. Boreholes BGC-2 and BGC-A4 were oriented normal to bedding, while borehole BGC-A6 was drilled following the bedding strike. It was inferred from regional geological mapping that upper shaly, lower sandy, carbonate-rich sandy, and lower shaly facies were encountered in borehole BGC-2, whereas borehole BGC-A4 encountered the upper sandy and upper shaly facies. Borehole BGC-A6 only encountered the upper sandy facies (Figure 2-1).

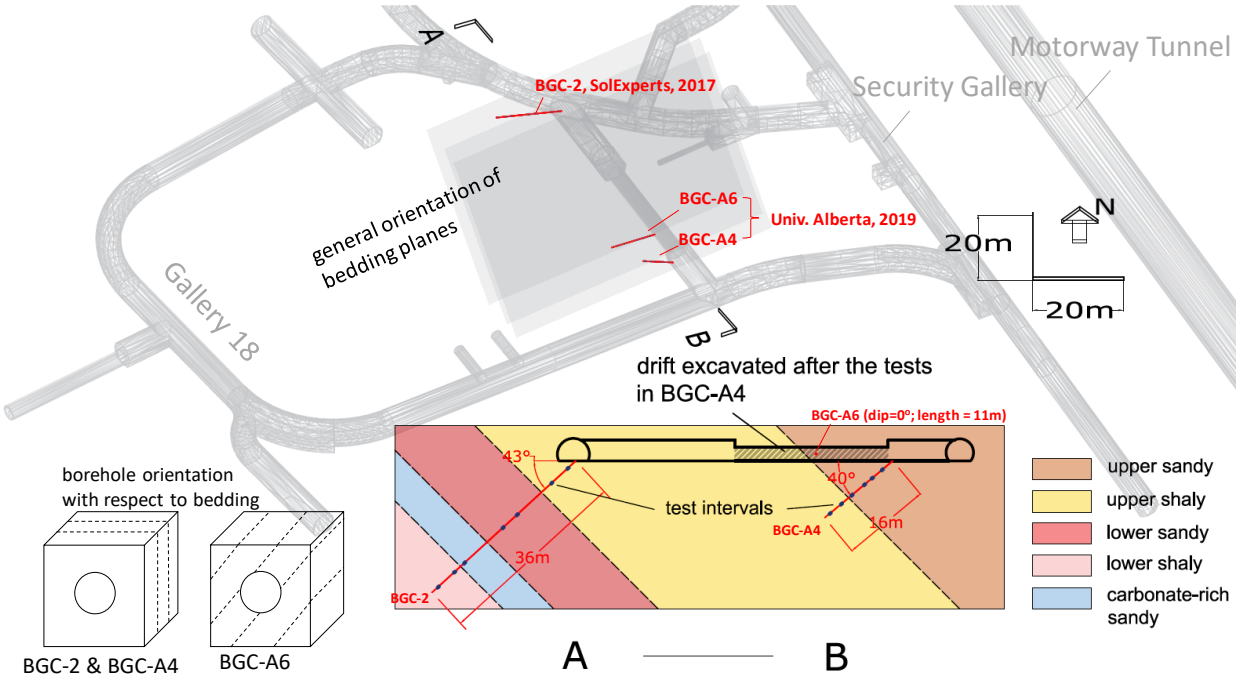

Figure 2-1. Location and orientation of three test boreholes in the Mont Terri Rock Laboratory

[1] A version of this chapter has been published in Rock Mechanics and Rock Engineering

The initial stress field at the laboratory was determined using several techniques, including borehole slotter, undercoring, and hydrofracturing (Bossart and Wermeille 2003; Martin and Lanyon 2003). The in-situ stress estimate suggested by the undercoring method is given in Table 2-1. Although different from the results determined by borehole slotter measurement, the stress tensor obtained by undercoring showed an agreement with that indicated by hydrofracturing. The orientation of its minimum in-situ principal stress could reasonably be explained by a stress-free boundary of the valley to the southwest side of the laboratory. The use of the undercoring stress tensor in the 3D stress modeling of excavation also predicted borehole breakouts observed in the laboratory (Martin and Lanyon 2003). However, the inadequately low minimum principal stress (0.6 MPa) was recognized given measured far-field pore pressure (2.0 MPa). A modified magnitude of 2.2 MPa was then considered by Corkum (2006) and will be used in this study.

Table 2-1. In-situ stress tensor for the Mont Terri Rock Laboratory proposed by Martin and Lanyon (2003)

In-situ Principal Stresses	Magnitude	Trend	Plunge
	(MPa)	(°)	(°)
Maximum	6.5	210	70
Intermediate	4	320	10
Minimum	0.6 (2.2*)	50	15
* modified by Corkum (2006)			

2.2 Borehole Drilling and Logging

For all three test boreholes, drilling was driven by air flush. It has been recognized that drying with the flushed air improves the stability of the borehole. However, once the drilling was completed, the swelling of Opalinus Clay tended to occur under a re-saturation process by pore water seepage/diffusion from the far-field. The unconfined borehole wall would become unstable and deteriorate over time (Labiouse and Vietor 2014; Kupferschmied et al. 2015). This was later confirmed by our observation of the mud-smeared borehole wall after borehole BGC-A4 was left open for about six months.

To minimize the damage from re-saturation, pressuremeter tests started shortly (< 2 days) after drilling completion. However, the damage at the borehole wall after unloading was still evident, especially in borehole BGC-A6. Borehole breakouts were identified at multiple depths and were primarily oriented normal to the bedding plane (e.g., Figure 2-2). This type of damage was triggered by the instability of the bedding structure after unloading, as also observed in the other boreholes drilled parallel to bedding (Labiouse and Vietor 2014; Kupferschmied et al. 2015).

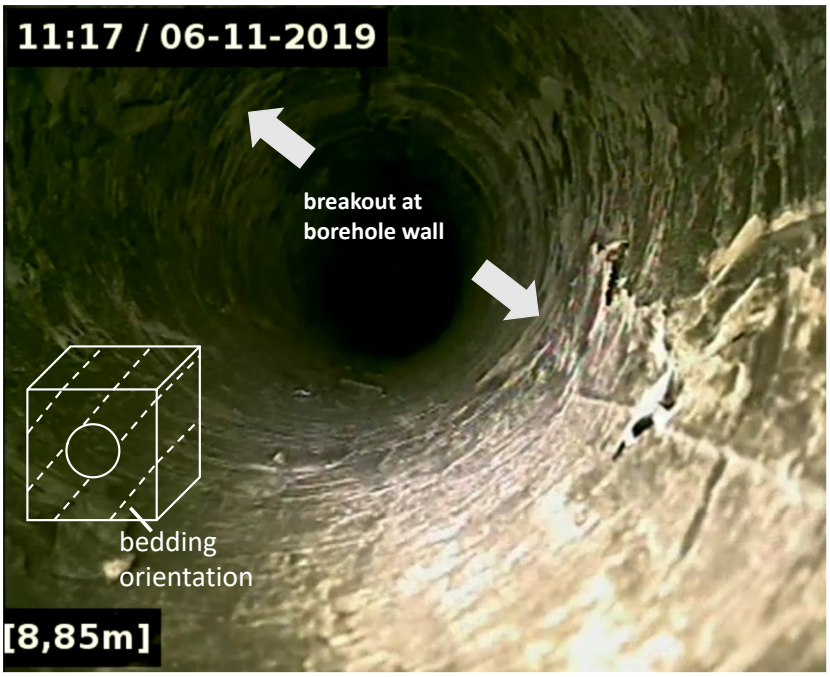

Figure 2-2. Borehole damage captured by borehole camera in borehole BGC-A6 (drilled parallel to bedding) before pressuremeter tests at a depth of 8.85m

To characterize the petrophysical variation along the borehole depth with high resolution, gamma-ray (GR) logging and interval velocity measurement (IVM) were also employed in the boreholes BGC-2 and BGC-A4. The former was conducted in borehole BGC-1 adjacent to the borehole BGC-2 with the same borehole orientation. The latter was conducted in boreholes BGC-2 and BGC-A4 using the ultrasonic borehole probe designed by BGR (Bundesanstalt für Geowissenschaften und Rohstoffe - Federal Institute for Geosciences and Natural Resources) in Germany. The use of the ultrasonic borehole probe in underground laboratories has been well documented by Schuster (2019). The method allows the waves to transmit over the different offsets between the emitter and receivers with one single excitation (Figure 2-3). The transmitting wave has a central frequency of 50 kHz. The wave velocity can be determined apparently using the offset and the travel time determined by picking the first arrival of the corresponding wave phase in the waveforms. Figure 2-4 shows an example of the waveforms obtained at the receiver R2 for the complete coverage of the borehole length as the probe was moved along the borehole at a step of 5cm. Appendix I documents measured v_p determined from the data obtained at two receivers, R1 and R4, with core photos aligned side by side for the boreholes BGC-2 and BGC-A4.

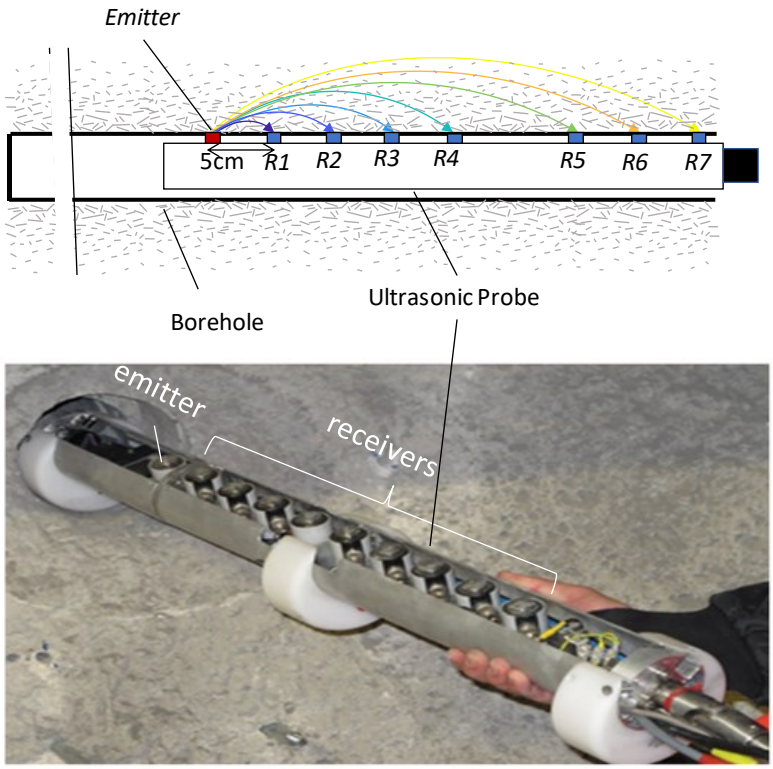

Figure 2-3. BGR 8-channel ultrasonic borehole probe (8KUBS-05) and the schematic diagram of the ray paths propagating between the emitter and an array of receivers with different offsets.

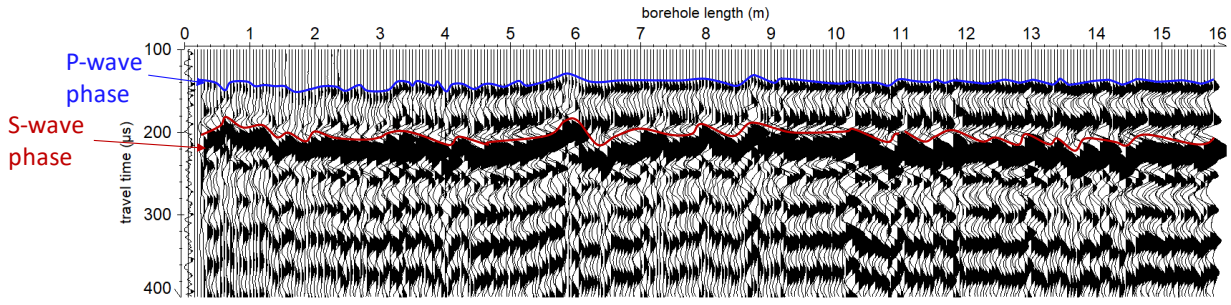

Figure 2-4. An example of the waveforms with identified P- and S-wave arrivals received at R2 along the borehole BGC-A4 at a step of 5cm. The depth refers to the mid-point of the emitter-receiver offset.

The logging results for boreholes BGC-1, BGC-2, and BGC-A4 are shown in Figure 2-5. Apparent P-wave velocity determined from the wave propagation over a 20cm interval (R4) represents the rock properties away from near-borehole disturbance, as will be discussed later. Drilled cores from all three boreholes were examined, and geological features were mapped immediately after the core was retrieved from the core barrel. The core was typically fracture-free but drilling normal to bedding produced core disking parallel to bedding, which was frequently observed on the cores recovered from these boreholes.

These artificial core breaks were distinguished from pre-existing discontinuities, such as the fault planes and fractures. At the Mont Terri Rock Laboratory, a disturbed zone surrounding the excavation with fractures induced by unloading was defined as an excavation damaged zone (EDZ) (Bossart et al. 2002; Marschall et al. 2017). Beyond the EDZ, the ground might also be influenced by the stress perturbation from the excavation. Figure 2-5 also shows the significant mineralogical variability even in one stratigraphic unit, for example, in carbonate-rich sandy facies, as confirmed by both geophysical logging and core mapping.

Siegesmund et al. (2014) showed that the presence of cemented carbonate in the sandy facies led to higher wave velocities than the shaly facies that lacked the cemented carbonate. In this study, the boundary shown in the profile of v_p between sandy and shaly facies is far less clear in borehole BGC-A4 than that in borehole BGC-2. Cores taken from upper sandy facies in borehole BGC-A4 also show a similar lithological appearance with the upper shaly facies and bear less continuous carbonate lens than the lower sandy facies (Appendix I). A mineralogical analysis conducted on the core samples using SEM (Scanning Electron Microscopy)-based methods shows the minor differences in quartz, calcite, and clay contents between these two facies (respectively, 3.5%, 2.8%, and -8.8%). To quantify the longitudinal heterogeneity in each facies, the variogram of v_p obtained for 5cm interval (R1) is calculated (Figure 2-6). According to the variograms, the upper sandy and upper shaly facies can be clearly distinguished. Less variance of v_p is observed in shaly facies than sandy or carbonate-rich sandy facies at all lag distances. Opalinus Clay is therefore seen to be more homogeneous in shaly facies at the pressuremeter test intervals covering the length of 0.5 m to 1 m in these boreholes.

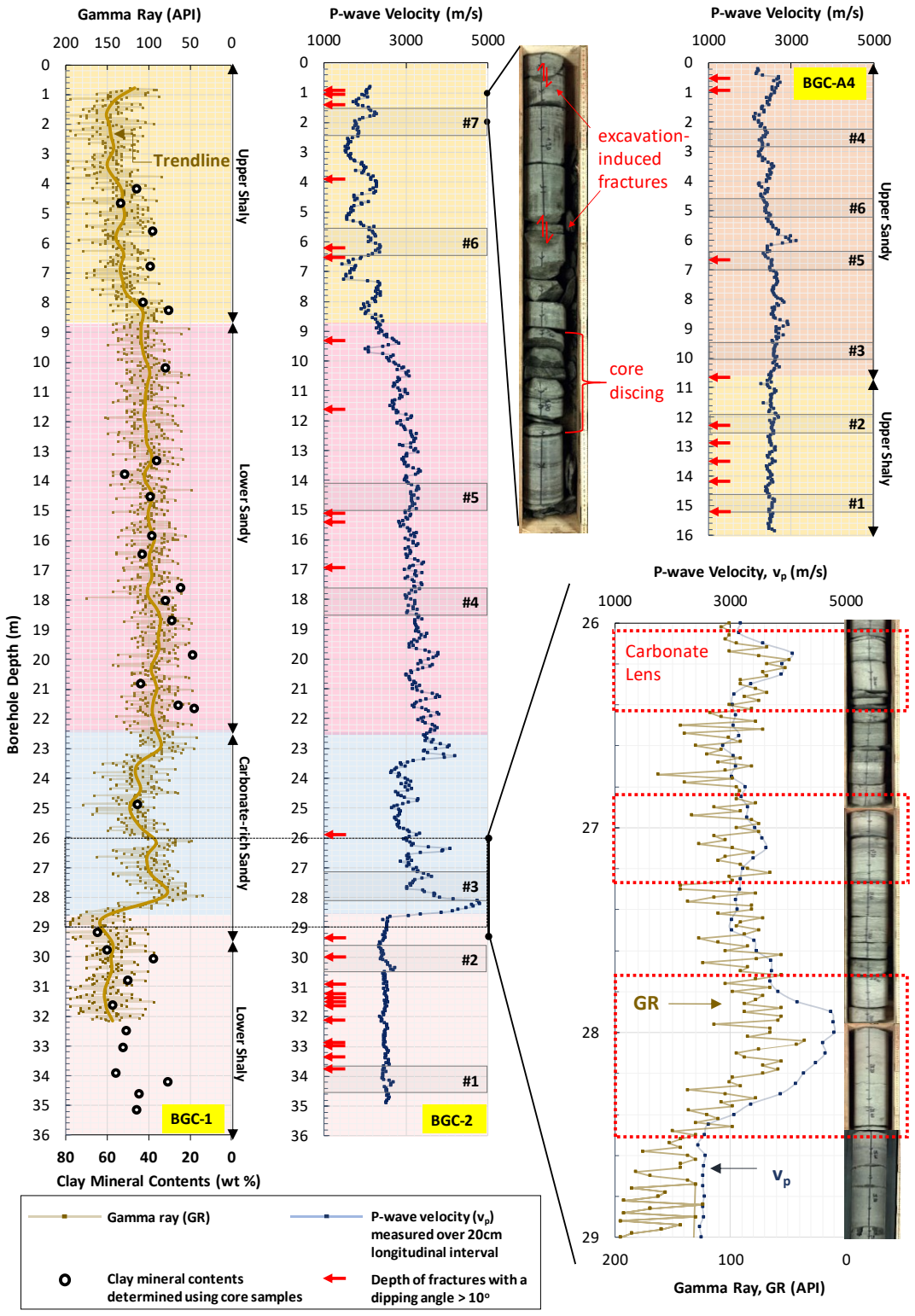

Figure 2-5. Composite plot of core photos and petrophysical properties obtained for borehole BGC-1, BGC-2, and BGC-4. Boreholes BGC-1 and BGC-2 are parallel and about 5 m apart. A blow-up view for a depth interval in borehole BGC-2 compares the heterogeneities shown in the core, gamma-ray, and velocity logs.

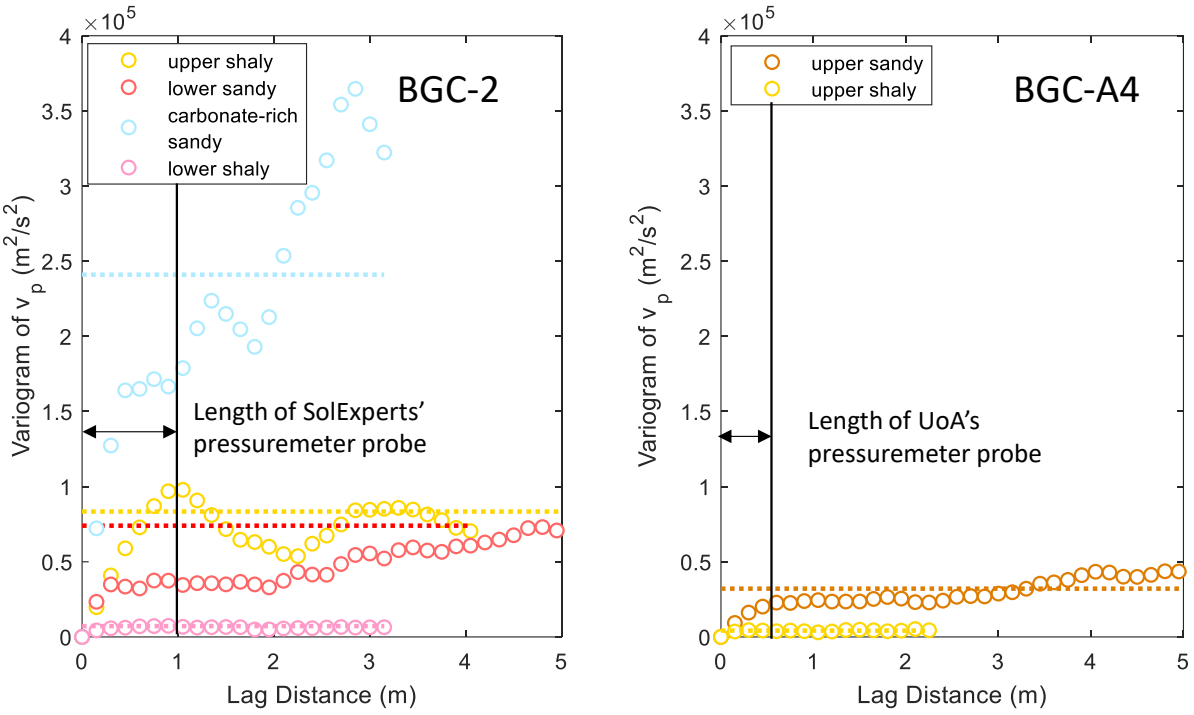

Figure 2-6. Variograms of P-wave velocity v_p. Horizontal dash lines mark the total variance of v_p for each facies. The local heterogeneity within the test interval covered by the pressuremeter probe is indicated by the vertical line intersecting the variograms.

Wave velocity is known to be affected by the fractures the wave propagates through, whereas GR is not sensitive to the mechanical disturbance of the rock and is considered a primary indicator of the mineral compositions at logging depths. A negative correlation between GR and v_p can be recognized over all measured depths. Linear regression is established between v_p and GR using a portion of the data covering the depth range of 20 – 32 m, where the variability of the measured v_p is significant. The regression model is further applied to all the GR readings and predicts the v_p over the entire logging depth. The mismatch between prediction and measurement is evident at the first ~10m. If the GR and the predicted v_p reflect the properties of the intact rock, then the relatively low magnitude of the measured v_p at the first 10m is likely the consequence of the rock mass disturbance by the excavation.

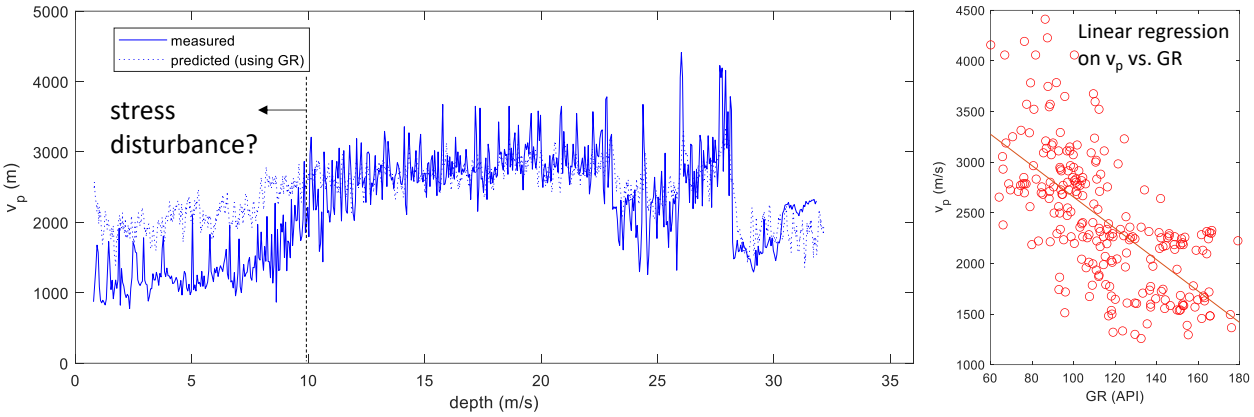

Figure 2-7. Variation of v_p predicted based on the GR against the variation of measured v_p in borehole BGC-1. A portion of the data (>20m) is used for linear regression between v_p and GR.

In the section that is not affected by the rock mass disturbance, the high-resolution wave velocity logs from IVM allow the clear identification of the minerals, e.g., the carbonate lens in the carbonate-rich sandy facies verified with the core photos (Figure 2-8). v_p and v_s determined using the same emitter-receiver offset (R4) in Figure 2-8 show almost the same trend of variation in the selected section, indicating that either of them can be used to identify the mineralogical variation. Compared to velocity obtained by R4 for waves propagating over a 20 cm offset, the P-wave log obtained at R1 for a 5 cm wave propagation offset shows more details of such variation.

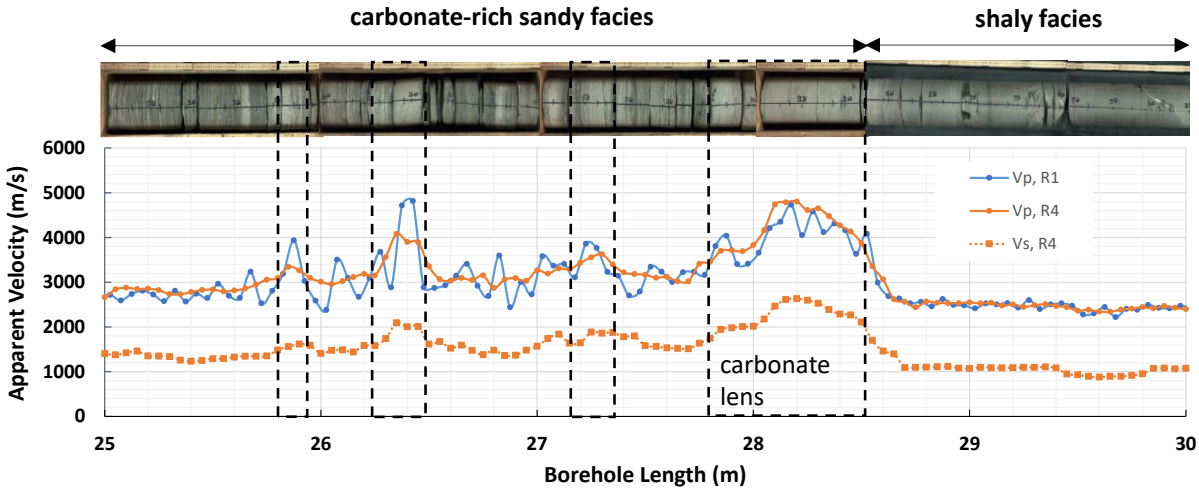

Figure 2-8. Apparent velocity determined using R1 and R4 from IVM in borehole BGC-2 and comparison with core photos.

One purpose of performing IVM with different wave transmission intervals is that the rock at varying depths into the borehole wall can be probed, as illustrated in Figure 2-3. The comparison between the velocity of wave received after short (e.g., at R1) and long transmissions (e.g., at R7) reveals the

information of the velocity change from the borehole surface to the far-field. Three scenarios have been proposed by Schuster et al. (2017) in their evaluation of apparent velocity $v_{p,R1}$, $v_{p,R2}$ and $v_{p,R3}$, respectively from waves received at R1, R2 and R3 (Figure 2-9): (a) $v_{p,R1} = v_{p,R2} = v_{p,R3}$: no radial variation of velocity; (b) $v_{p,R1} > v_{p,R2} > v_{p,R3}$: negative gradient of the velocity from borehole wall to far-field; (c) $v_{p,R1} < v_{p,R2} < v_{p,R3}$: positive gradient of the velocity from borehole wall to far-field.

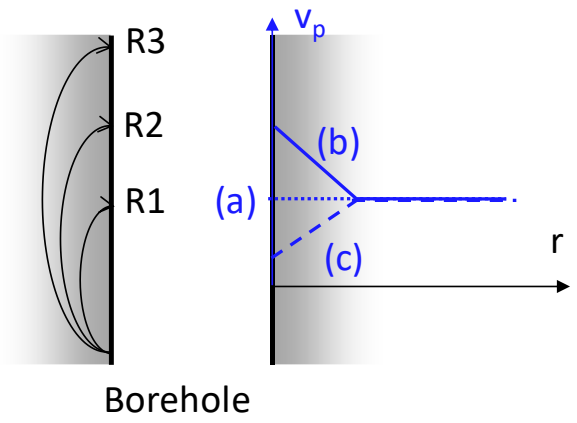

Figure 2-9. Three scenarios of velocity variation in radius of the borehole (after Schuster et al. (2017))

It should be noted that the use of apparent velocity to define these scenarios can only be applied to the case where the velocity variation along the longitudinal direction of the borehole is uniform. For the rock with fine interbedding like in this study, the apparent velocity is primarily governed by the longitudinal heterogeneity, and the difference between the velocities, for example, at R1 and R4 at the common points, is likely the result of the different longitudinal coverages. This is, in fact, the reason why $v_{p,R4}$ appears to be the moving average of the $v_{p,R1}$ in Figure 2-8.

As shown later, an accurate characterization of the velocity variation in both longitudinal and radial directions can be done using tomographic inversion analysis on the IVM data. Alternatively, the apparent velocity averaged for each receiver over a larger span of borehole length may define the scenario of radial variation of velocity qualitatively. In Figure 2-10, the comparison of averaged velocity in three lithofacies in borehole BGC-1 demonstrates a higher v_p for the wave having deeper penetration into the borehole wall (at R7) than the wave having shallower penetration (at R1). This corresponds to scenario (c) in Figure 2-9, where velocity is lower at the borehole near-field than at the far-field. The low P-wave velocity near the borehole wall might be caused by the mechanical damage after unloading and/or the consequence of the non-uniform saturation in radius. The more significant reduction of the $v_{p,R1}$ from $v_{p,R7}$ in lower shaly facies and part (A) of the carbonate-rich sandy facies than that of the lower sandy facies

and part (B) of the carbonate-rich sandy facies implies higher sensitivity of the borehole wall to the stress relief and/or saturation in the Opalinus Clay with higher clay content.

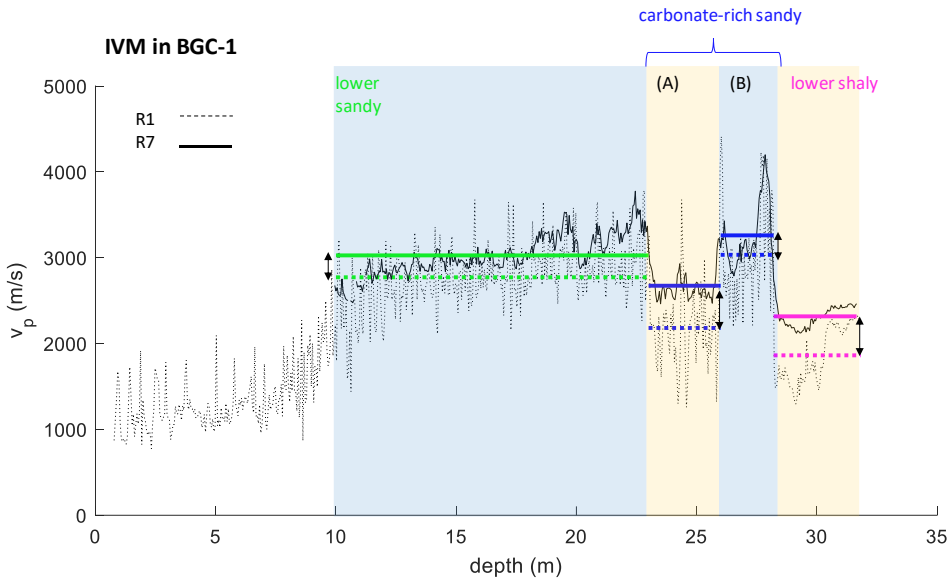

Figure 2-10. Comparison of apparent P-wave velocities v_p received at R1 and R7 with the emitter-receiver offsets of 5cm and 40cm, respectively. The horizontal line marks the v_p averaged for each lithofacies unit. Note that the carbonate-rich sandy facies is divided into two spans (A) and (B) based on their trends.

The velocity variation was also found to be temporal. Figure 2-11 shows the change of the P-wave velocity measured in borehole BGC-A4 over three days. The velocities measured by three different receivers (R1, R4, and R7) had an overall increase, and the most significant increase was in $v_{p,\,R1,}$ particularly near the borehole collar.

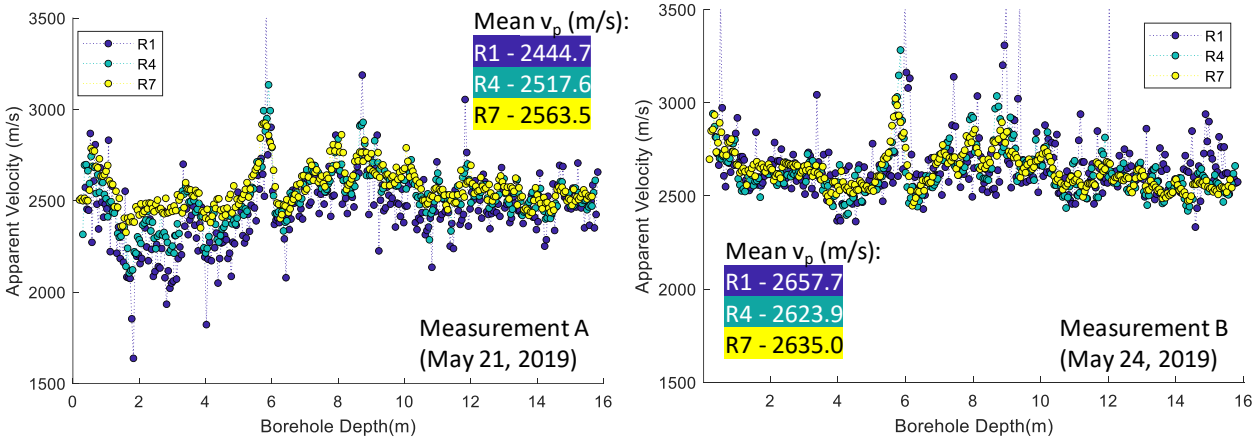

Figure 2-11. Change of the apparent P-wave velocity along borehole length over three days.

The observed velocity change over time could be related to the saturation/desaturation process at the borehole wall. The wave velocity of Opalinus Clay was shown to be influenced by the saturation of the specimen in laboratory investigations (Mitaritonna et al. 2009; Wild et al. 2014). Wild et al. (2014) found that the P-wave velocity in the direction perpendicular to bedding had an initial drop from the virgin saturated state after a slight increase of suction (or decrease of the saturation) to air entry value. By further drying the specimen from an environment with a relative humidity of 99% to 50%, Mitaritonna et al. (2009) observed a continuous increase of both P- and S- wave velocities by almost 30%, and the increase is less significant in the damaged Opalinus Clay.

Given the laboratory findings above, the following processes of saturation/desaturation at the borehole wall may be postulated - a) induced suction immediately after air-flushed drilling stiffens the surface layer (more dominant in the undisturbed rock because unloading-induced cracks may compromise this effect), b) the effect of suction may be soon reduced after a short-time relaxation when the borehole wall is wetted, c) pore fluid diffusion and moisturizing at the borehole wall affect the acoustic properties and borehole stability over a certain period of time but may be impeded by the air ventilation near borehole entry.

At Mont Terri Rock Laboratory, the trend of velocity variation similar to Figure 2-11 was observed by Schuster (2009) in another borehole, where v_p was generally increased between two measurements over a month after the borehole wall was re-saturated. This might imply that re-saturation might happen as quickly as three days as seen in borehole BGC-A4.

2.3 Pressuremeter Test Results

Pressuremeter tests (PMTs) were performed in three drilled holes using two different pressuremeter probes owned by SolExperts and the University of Alberta (UofA), respectively (Figure 2-1). The typical stress state in the ground surrounding a borehole under pressuremeter loading is shown in Figure 2-12. The tests in three boreholes are summarized in Table 2-2[2].

[2] Test data are available at https://doi.org/10.6084/m9.figshare.19607388.v1

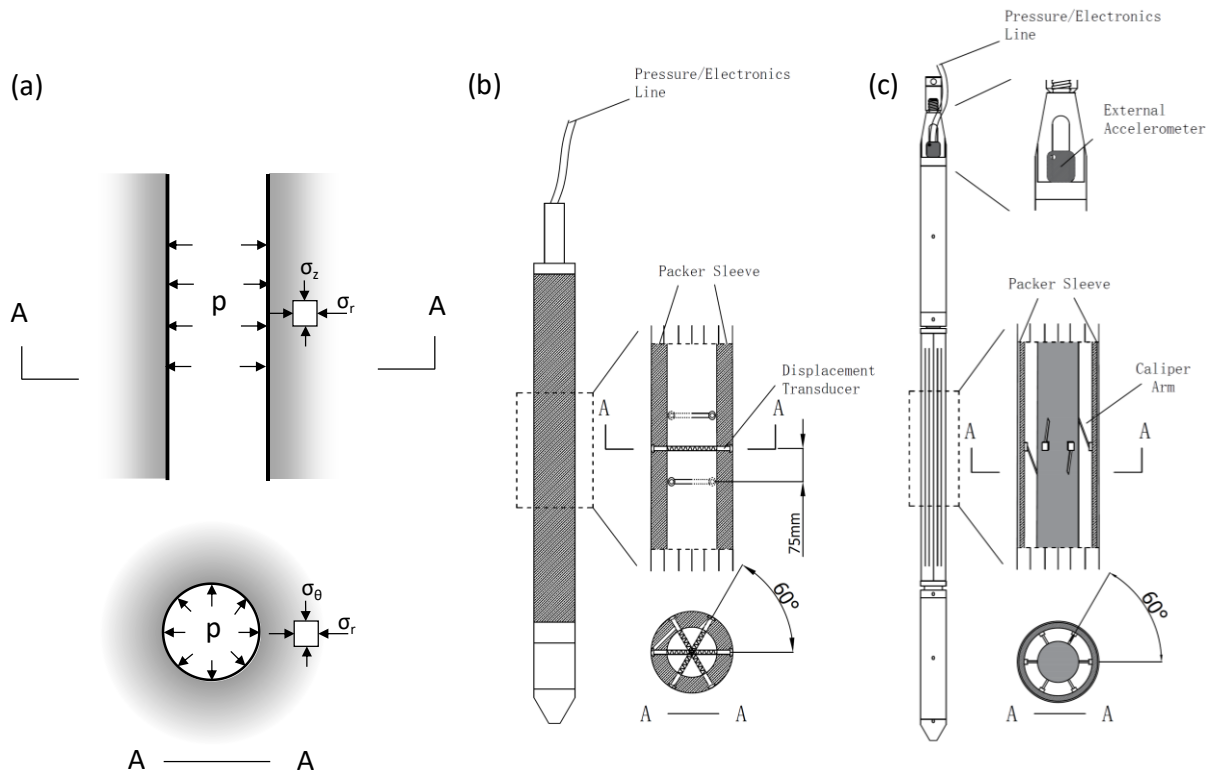

Figure 2-12. Typical stress state in the ground under pressuremeter loading (a) and pressuremeter probes used in this study: SolExperts' (b) (adapted from Zalesky et al. 2007) and UofA's (c).

Table 2-2. Summary of PMTs in GC program at Mont Terri Rock Laboratory

Test Sequence	Test Depth (to the center of probe)	Lithostratigraphic Units	Maximum Test Pressure	Azimuth of Caliper Arm 1 (UofA's pressuremeter only)
Borehole: BGC-2 (normal to the bedding dip) Testing Probe: 118 mm Dilatometer (SolExperts); Drilled Hole Diameter: 131 mm				
#1	34.0 m	Lower Shaly	16.0 MPa	N/A
#2	30.0 m	Lower Shaly	3.5 MPa	N/A
#3	27.5 m	Carbonate Sandy	3.5 MPa	N/A
#4	18.0 m	Lower Sandy	3.5 MPa	N/A
#5	14.5 m	Lower Sandy	3.5 MPa	N/A
#6	6.0 m	Upper Shaly	3.5 MPa	N/A
#7	2.0 m	Upper Shaly	3.5 MPa	N/A
Borehole: BGC-A4 (normal to the bedding dip) Testing Probe: 73 mm High Pressure Dilatometer (UofA); Drilled Hole Diameter: 86 mm				
#1	14.9 m	Upper Shaly	18.0 MPa	82°
#2	12.2 m	Upper Shaly	14.0 MPa	149°
#3	9.7 m	Upper Sandy	13.8 MPa	137°
#4	6.7 m	Upper Sandy	15.5 MPa	124°
#5	4.9 m	Upper Sandy	17.4 MPa	146°
#6	2.5 m	Upper Sandy	13.9 MPa	136°
Borehole: BGC-A6 (parallel to the bedding strike) Testing Probe: 73 mm High Pressure Dilatometer (UofA); Drilled Hole Diameter: 76 mm				
#1	9.4 m	Upper Sandy	16.5 MPa	225°
#2	7.8 m	Upper Sandy	18.2 MPa	219°
#3	4.5 m	Upper Sandy	17.8 MPa	225°
#4	2.9 m	Upper Sandy	17.2 MPa	230°
#5	1.4 m	Upper Sandy	16.3 MPa	213°

SolExperts' pressuremeter probe has three diametric displacement transducers, oriented at an angle of 120º to each other and placed in three planes spaced 75 mm apart (Figure 2-12). The external deformation (at the borehole wall) can be directly measured with the steel pins penetrating through the packer sleeve. The transducers for diametric displacement have a resolution of ±1 μm, allowing the rock stiffness to be determined at small shear strains.

The pressuremeter probe used by UofA was initially designed by Cambridge Insitu, Ltd. It has six independent radial caliper arms with measurement pads sitting on the same plane and 60° apart Figure 2-12). All the caliper arms are mechanically linked to strain gauges resolving displacements of less than ± 0.5 μm. Compliances of the rubber membrane and internal components were carefully calibrated and used for radial displacement correction. To determine the orientation of the probe in the borehole, an external accelerometer was mounted at the tool head. The heading of each caliper arm in the plane perpendicular to the borehole can be determined once the orientation of the probe is known. More information about the calibrations of UofA's pressuremeter and the field testing setup can be found in Appendix II.

In both series of tests, nitrogen was used to inflate the probe, and inflation pressure was logged simultaneously with displacement readings. An initial injection was required to expand the packer and obtain an even contact of the packer sleeve to the borehole wall. For all the tests in BGC-2 except test #1 at 34.0m, the load was increased in 0.2 MPa steps with a 3-minute pressure hold after each step. The unload-reload cycles were executed at specified pressure levels with 0.25 or 0.45 MPa pressure change in a 1-minute step. For tests in BGC-A4 and BGC-A6, a different loading scheme was adopted – the pressure was changed continuously at a rate of about 0.45 MPa/min in both loading and reloading, but with a reduced rate as low as 0.15 MPa/min in unloading. This was intended to yield more data points in evaluating strain-dependent shear modulus, as shown later. The diagrams of pressure control for these two schemes are shown in Figure 2-13.

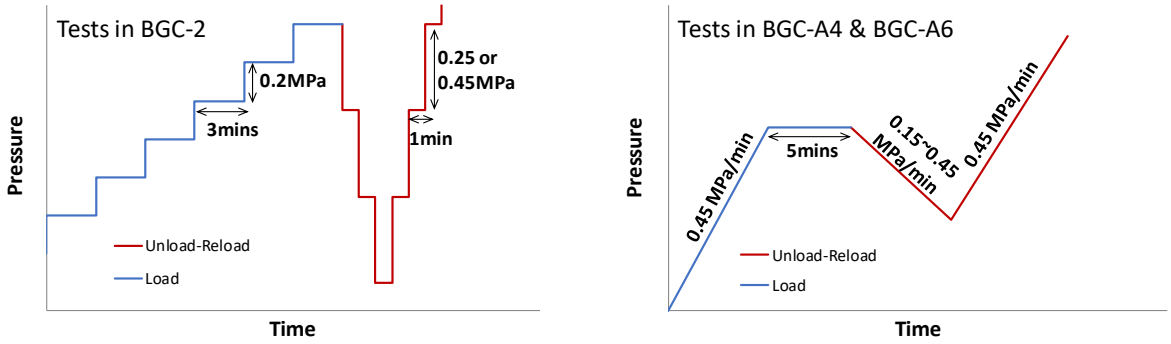

Figure 2-13. Typical pressuremeter loading schemes for tests in three boreholes

2.3.1 Test Data

Pressuremeter tests (PMTs) in borehole BGC-2 are at low pressure except for the first test at 34.0m. Figure 2-14 is an example plot of data obtained from test #2 in borehole BGC-2. The radial displacement was zeroed by the first reading from the transducers so that the actual diametric borehole deformation could be observed. The difference among the three curves reveals the anisotropy of stiffness in the testing plane.

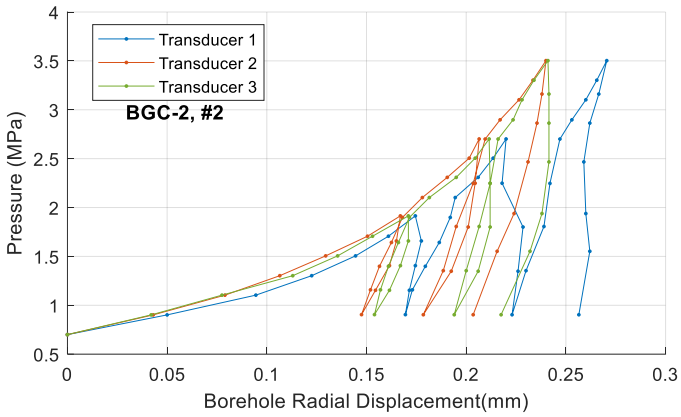

Figure 2-14. Data obtained from test #2 at 30m in borehole BGC-2

In this dataset, transducer 1 captured an unusual borehole deformation during all the unloads and reloads. Geological mapping of the core from the test interval indicated a fault plane dipping through the planes where the transducers were located (Figure 2-15). It is thus speculated that the unusual unload/reload readings from Transducer 1 were influenced by this local geological feature.

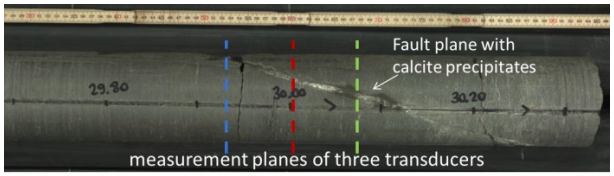

Figure 2-15. Shaly Opalinus Clay core recovered from the test interval of BGC-2, #2 at 30m

An averaging procedure is applied to the measured displacement readings (Figure 2-16). Compared with the curve averaged from all three transducer readings, the curve averaged from only transducers 2 and 3 has a more reasonable unload-reload response and will be used in later analysis.

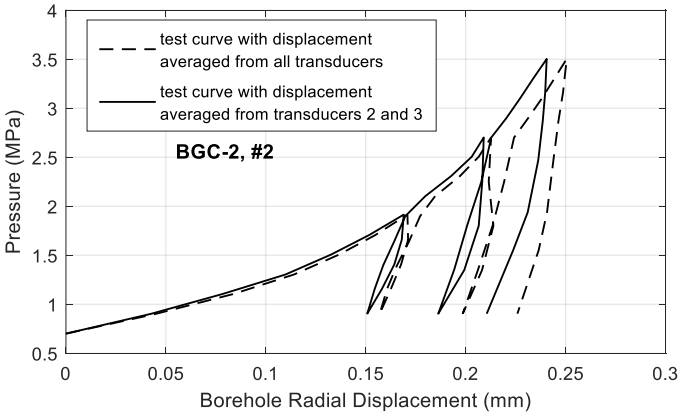

Figure 2-16. Test curves with averaged displacement readings

Displacement measurements by three transducers using SolExperts' probe directly reflect the deformation of the borehole at different diametric axes. When using UofA's pressuremeter, an important step for deriving the true radial displacements is to correct for system compliance. The radial compression of the membrane should be considered in the correction of data obtained by UofA's probe. The membrane compression with expansion pressure is usually treated as a constant system compliance factor that can be calibrated from an inflation test against a stiff hollow cylinder when the pressures are >5 MPa. When the pressures are < 5 MPa, a constant value cannot be used, and the nonlinearity in calibration data should be treated (Figure A- 7). This nonlinearity is caused by the length change of the membrane as the ends of the membrane are forced into the annulus between the probe and cylinder wall (Clarke 1995) and the bending of the steel strips used as protective sheath dressed outside of the membrane (pers. comm., Whittle & Byrne).

A hysteresis from the load to the unload curve observed in Figure A- 7 is a natural response for rubber when stretched, known as Mullin's effect (Bouasse and Career 1903). The stress-strain response of rubber in loading can be partially recovered during the relaxation between tests, whereas the unloading curve seems not dependent on the relaxation time or unloading rate. In this work, unload data was fitted with a piecewise fit function, which was then applied to correct field measurements.

PMTs in boreholes BGC-A4 and BGC-A6 were loaded to high pressures up to 18.2 MPa using UofA's pressuremeter. The typical test curves are shown in Figure 2-17, where displacement readings were obtained from six independent caliper arms. The orientation of the probe was informed from the onboard accelerometer data, and the azimuth of each caliper arm with respect to the borehole top was then determined.

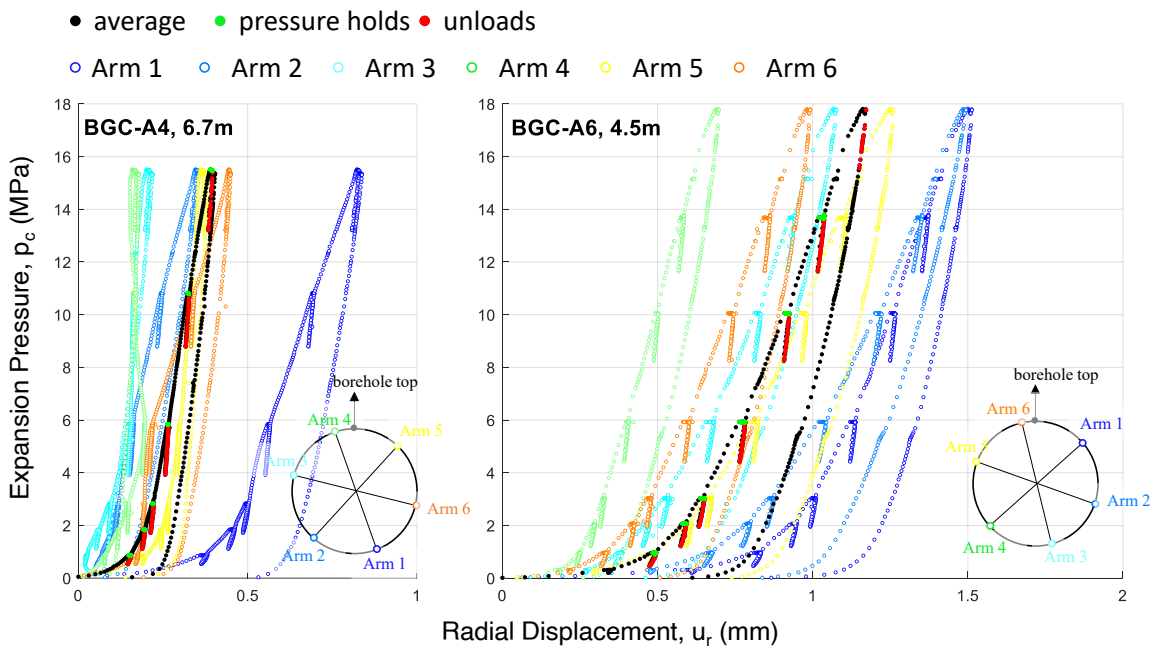

Figure 2-17. Data obtained from tests #4 and #3 in boreholes BGC-A4 and BGC-A6, respectively. Note that the displacement at the borehole lift-off has been subtracted from the caliper displacement.

For the interpretation of isotropic mechanical properties, cylindrical cavity expansion analysis is applied to PMT data, assuming that 1) axial strain is zero and 2) borehole deformation is axisymmetric. Houlsby and Carter (1993) have shown that for the dimension of expansion interval with the length-to-diameter ratio ≥ 4, the first assumption only results in a negligible deviation (< 5%) of the interpreted stiffness from its actual value. The statement underlying the second assumption is that the material is rotationally isotropic in the testing plane. This is an appropriate assumption for tests in boreholes BGC-2 and BGC-A4, even though the stress-induced near-borehole anisotropy might also be present. A curve with the displacement reading averaged from all axes is used in the cavity expansion analysis. At each pressure increment, the ratio of the averaged displacement reading $\overline{u_r}$ to the initial borehole radius a_0 is defined as the cavity strain, ε_c.

2.3.2 Initial Borehole Expansion

The condition of a drilled hole can be indicated from the initial pressuremeter loading. In Figure 2-18, an extended nonlinear expansion in the PMTs in borehole BGC-2 is observed for a pressure increase up to 3.5 MPa. This nonlinearity possibly results from the flattening of borehole wall asperities but more likely the compaction of damaged Opalinus Clay surrounding the borehole under pressuremeter loading. The fact that the borehole expansion in shaly facies is more significant than in sandy/carbonate-rich sandy facies after 3.5 MPa loading implies that the Opalinus Clay might have more significant borehole wall

damage in shaly facies. This is consistent with the conclusion made from IVM after a comparison of apparent v_p calculated for short and long traveling distances (Figure 2-10). Due to the uncertainty in the calibration of the system compliance during the loading stage (Figure A- 7), the test data obtained using UofA's pressuremeter is not used in this analysis.

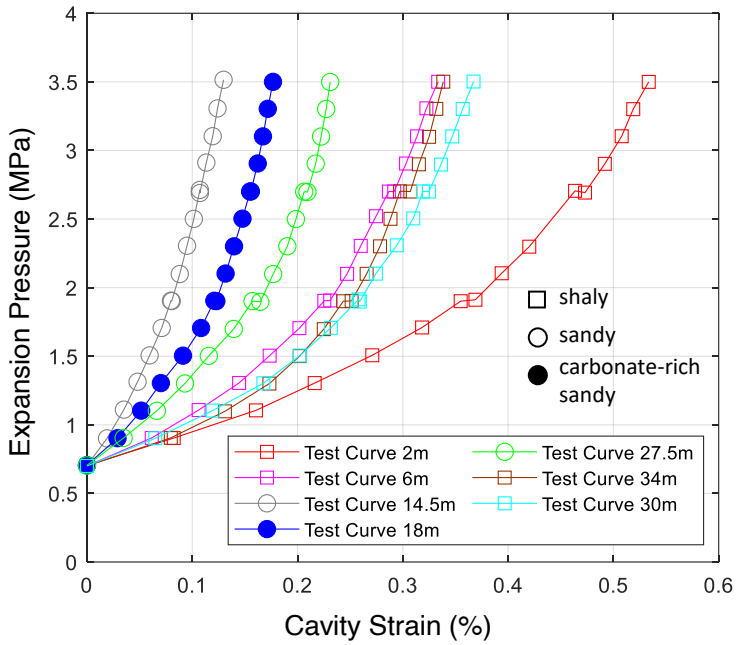

Figure 2-18. Loading portion of the test curves to 3.5 MPa from PMTs in borehole BGC-2

2.3.3 Time-dependent Deformation

The time-dependent response of Opalinus Clay was studied by allowing the borehole to expand under constant pressure for approximately 5 minutes at multiple pressure levels in boreholes BGC-A4 and BGC-A6. Consolidation and creep of the Opalinus Clay in the near borehole might both contribute to the time-dependent expansion. The borehole expanded during pressure hold at a decreasing rate in general (e.g., two cases in Figure 2-19). At lower pressure levels (p_c < 10 MPa), the difference in the measured expansions for 5 minutes was negligible between pressure holds in each test, whereas at higher pressure levels (p_c > 10 MPa), the amount of the cavity expansion increased substantially. The increase might be caused by the yielding of Opalinus Clay at the borehole wall under a large deviator stress (σ_r - σ_θ) expected at the high expansion pressure. The time-dependent expansion appears to be more noticeable when the expansion pressure is higher or when the loading is partially normal to the bedding plane.

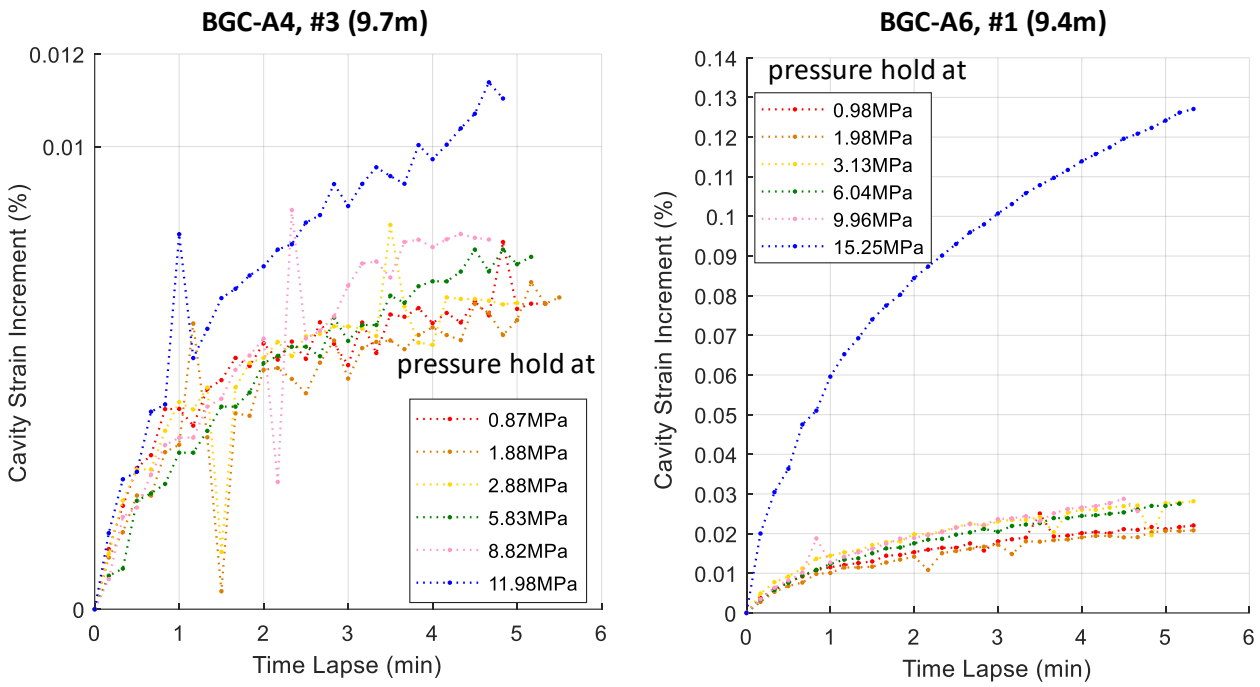

Figure 2-19. Increase of cavity strain during pressure holds at multiple pressure levels. Note different scales at the vertical axis.

2.3.4 Shear Modulus

The relationship between pressure p_c and cavity strain ε_c for borehole expansion in a linearly elastic ground can be derived following Timoshenko and Goodier's (1934) procedure combining stress equilibrium, compatibility, and stress-strain relations. Under the assumption that the expansion is infinitesimal, i.e., $\varepsilon_c << r_0$, a simple relationship is given as,

$$\varepsilon_c = \frac{p_c}{2G} \tag{2-1}$$

With p_c and ε_c measured in a pressuremeter test, the shear modulus G can be determined. The loading curve has an extended nonlinear expansion at the lower pressure range (p_c < 3 MPa), possibly resulting from the flattening of borehole wall asperities and the inelastic behavior of disturbed Opalinus Clay under expansion. For ground that suffers the drilling disturbance, unload-reload cycles were suggested to determine shear modulus (Windle and Wroth 1977; Clarke and Smith 1992) by performing linear regression on the unload data (Figure 2-20). The shear modulus values determined for the unloading steps in all the pressuremeter tests from this field campaign are summarized in Appendix III.

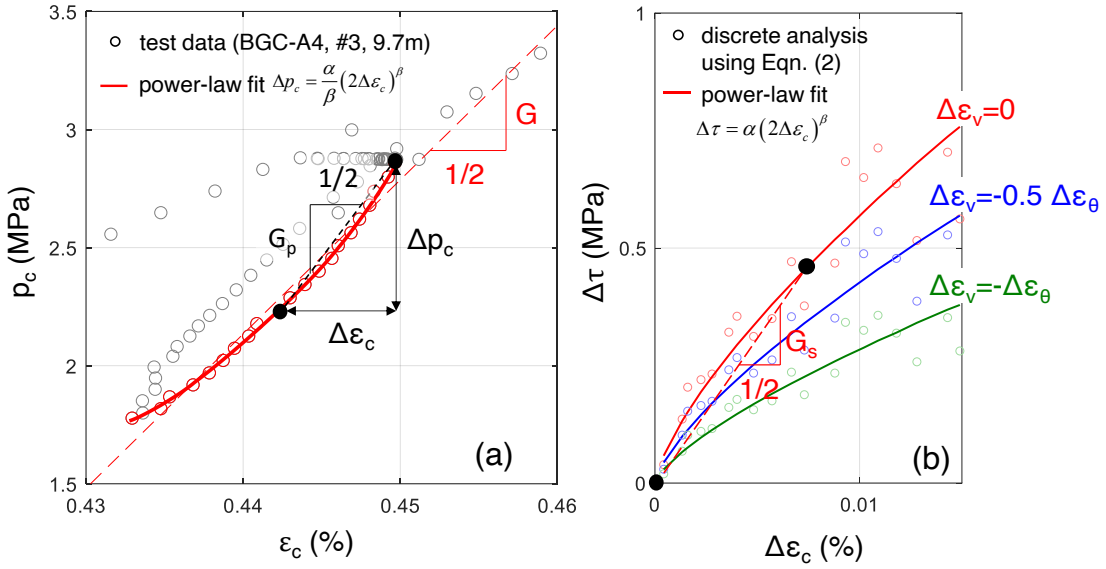

Figure 2-20. Interpretation of unload data: (a) determination of shear modulus G using the best linear fit and the demonstration of pressure and cavity strain increments in unloading (b) interpreted shear stress versus cavity strain assuming varying degrees of volumetric change $\Delta\varepsilon_v$ and the determination of secant shear modulus G_s at a strain increment.

This has advantages over using the loading portion of the test curve because 1) the modulus determination is not affected by any preceding frictional deformation; 2) the stress dependency of elastic stiffness can be assessed with multiple cycles at different pressure levels.

The shear modulus values G obtained using the linear fit of unloading at different pressure levels are shown in Figure 2-21. A similar trend of G with expansion pressure p_c is observed in three boreholes - the modulus initially increases rapidly with p_c and becomes almost independent of p_c once a threshold of approximately 5 MPa is exceeded.

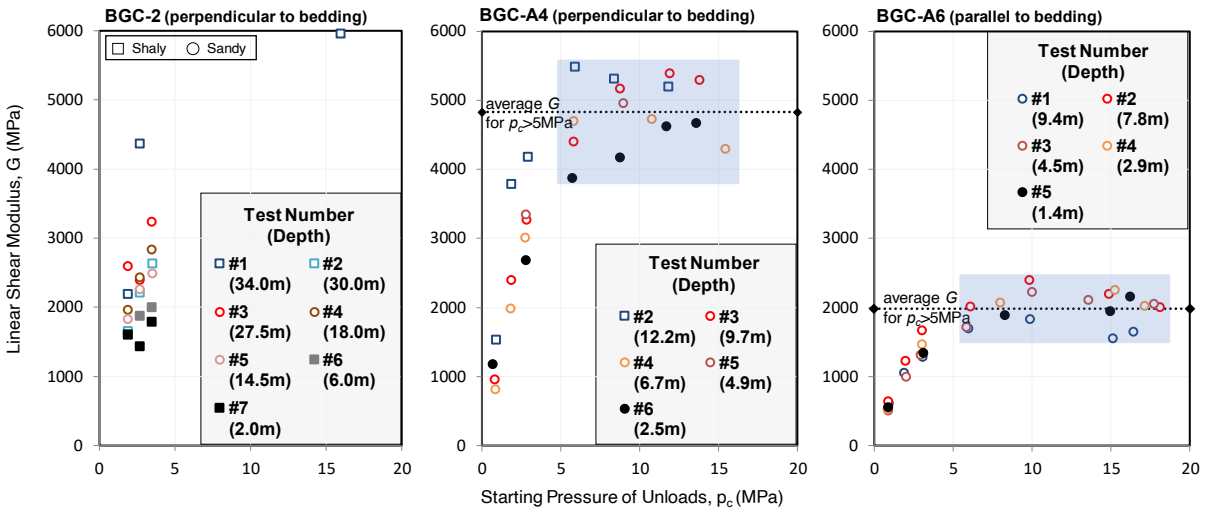

Figure 2-21. Shear modulus determined by linear regression on the unload data from all tests. Solid-filled markers refer to tests within EDZ. *G* in blue shades (p_c > 5 MPa) are plotted with depth in Figure 2-24. Note that test BGC-A4, #1 is not included because the unload-reload cycle was not intended, and the instrument malfunctioned before the final unload.

2.3.5 Anisotropic Moduli

The displacements measured by caliper arms using UofA's probe needs to be corrected because they were affected by the eccentric movement of the instrument core (Liu et al. 2021a). To obtain the true deformation of a borehole at varying axes, two approaches can be employed for each pressure increment: 1) average the pair of displacement measurements on the same axis, or 2) correct the displacements by finding the relative movement of the instrument center with respect to the borehole by fitting the borehole profile with a shape function. The elliptical function was found suitable for this purpose and proved accurate in characterizing a deformed borehole profile (Wagner et al. 2004; Schwerzmann et al. 2006). A linear least square approach was employed in this work to obtain the best elliptical fit. The procedure of the 2nd approach is detailed in Appendix IV.

The test curves corrected for the instrument core's eccentric movement using these two approaches are shown in Figure 2-22. The abnormal response of the displacement reduction in the pressure increase as seen in the Arms 3 & 4 of the test BGC-A4, #4 at 6.7m (Figure 2-17) is eliminated from the corrected test curve.

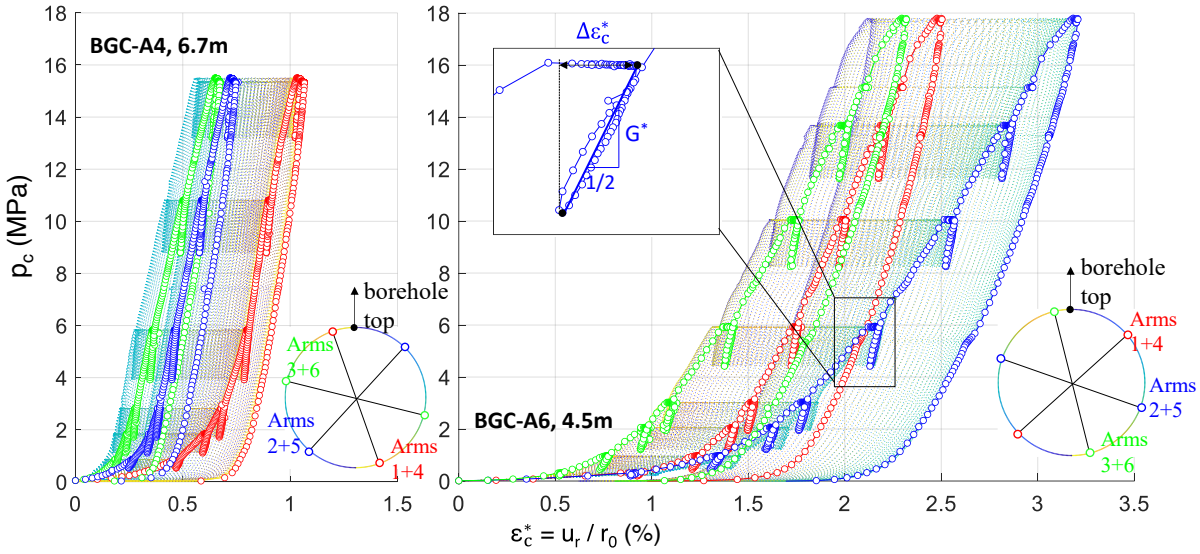

Figure 2-22. Pressuremeter test curves obtained for three caliper axes and derived for a range of borehole azimuths from 0 to 360°. Orientations of the derived curves are referred to as the outside contour of the compass. Determination of anisotropic modulus G^* using unload data is demonstrated.

The anisotropy of Opalinus Clay can be assessed by the elastic stiffness obtained from borehole deformation at varying diametric axes in the testing plane. The cavity expansion analyses performed for an isotropic medium are no longer valid for these anisotropic conditions. Instead, a nominal modulus parameter, anisotropic borehole modulus G^*, can be derived for each diametric axis using unload-reload cycles from either the data obtained from a pair of opposing calipers or the curve reconstructed for a particular orientation using data from six calipers (Figure 2-23). With the primary interest of exploring the azimuthal variation of G^* caused by the elastic anisotropy, a simple procedure was applied using the chord of unload data, and a constant G^* was obtained for each diametric axis.

The azimuthal variations of G^* are shown in Figure 2-23 for unload data obtained at $p_c > 5$ MPa at in the two tests shown in Figure 2-22. For the test in borehole BGC-A4 oriented normal to bedding, the derived G^* is nearly constant at varying azimuths, confirming the isotropic elastic stiffness in the plane parallel to bedding. In contrast, for the test in borehole BGC-A6 oriented parallel to bedding, G^* demonstrates a clear anisotropy with the axis of its maximum magnitude preferentially aligned with the dip of bedding.

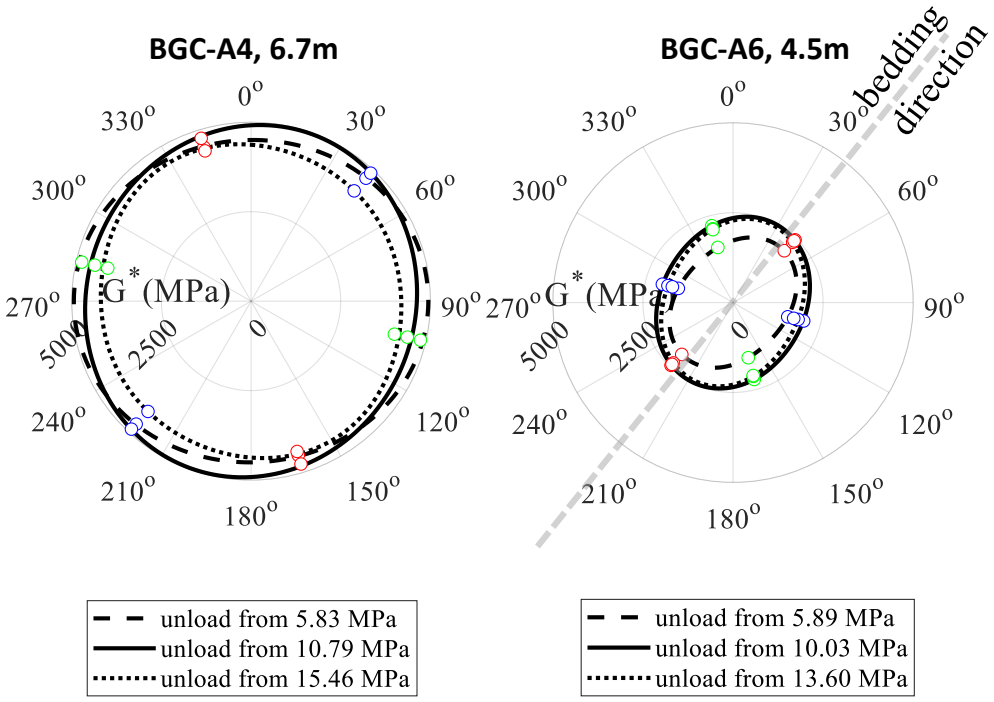

Figure 2-23. Azimuthal variations of derived G^* at multiple pressure levels for two tests in boreholes BGC-A4 and BGC-A6, respectively.

2.4 Discussion

2.4.1 Factors that Influence Shear Modulus

In Figure 2-21, the shear modulus G determined at $p_c > 5$ MPa in borehole BGC-A6 (oriented parallel to bedding) is only half of that determined from tests in borehole BGC-A4 (oriented perpendicular to bedding). This suggests that the measured modulus is substantially affected by the anisotropy of Opalinus Clay. Ideally, the effect of the lithofacies can be analyzed based on the tests in borehole BGC-2, where a distinct difference in mineralogical composition exists between shaly and sandy facies units (Figure 2-5). Figure 2-21 shows that G is not strongly correlated with the lithofacies. However, the insufficient measurements for $p_c > 5$ MPa in this borehole do not permit an unbiased comparison, given that G is very sensitive to p_c and highly variable for $p_c < 5$ MPa. In contrast, the low magnitude of shear modulus is consistently observed for tests at shallow borehole depths in all three boreholes (e.g., 2.0 m and 6.0 m in borehole BGC-2, 2.0 m in borehole BGC-A4, and 1.4 m in borehole BGC-A6), indicating the influence of rock mass disturbance in the EDZ.

Liu et al. (2021b) revealed that the local geological features, such as veins, could affect the displacement measurement at individual axes during the pressuremeter test. It is expected that natural fractures encountered within the pressuremeter test intervals can reduce the measured modulus values. The

influence of these fractures is investigated in Figure 2-24 using G obtained at p_c > 5MPa for two boreholes drilled in the upper sandy and upper shaly facies. In borehole BGC-A6, the shear modulus value is significantly degraded by a steeply dipping fracture at the center of the pressuremeter test interval at 9.4 m, whereas a fracture encountered by the test at 12.2 m of borehole BGC-A4 does not have an evident impact on the measured modulus values compared to those at the intervals without fractures. For the latter case, the fracture only gently dips through the borehole cross-section plane and is located off the interval center where calipers are seated. It, therefore, suggests that the impact of a fracture on the shear modulus measurement can be restricted geometrically by 1) the orientation of the fracture with respect to the pressuremeter loading and/or 2) the proximity of the fracture center to the caliper arms.

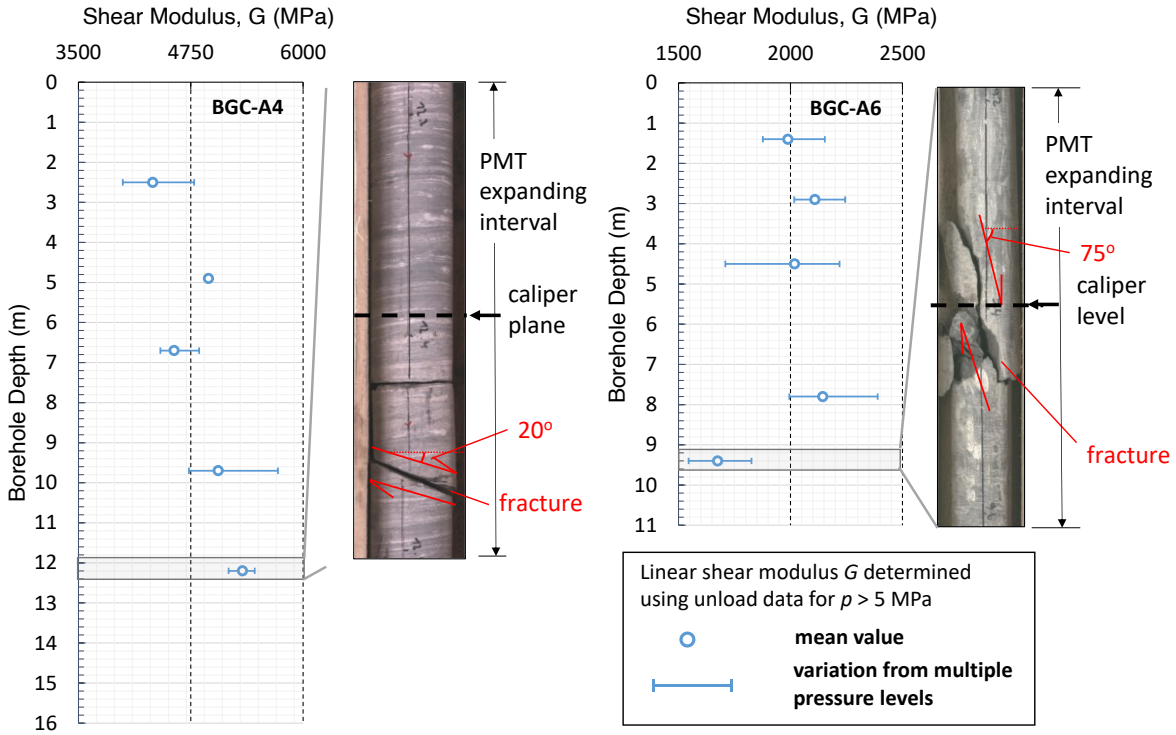

Figure 2-24. Influence of local fractures on the measured pressuremeter modulus values. Note that the x-axis scales are different in the two plots.

2.4.2 Nonlinearity of Shear Modulus at Small Strain

Nonlinear characteristics have also been observed in the unload-reload cycles. To quantify this nonlinearity, incremental analysis is applied to unload data (Figure 2-20). This analysis was suggested by Palmer (1972) so that the relationship between shear stress τ and shear strain γ for a single material point can be derived from the measured pressure-expansion response. It should be noted that the analysis

assumes 1) that the material points along the radius follow the same stress path and 2) that the volumetric deformation is zero. Windle and Wroth (1975) removed the second restriction and allowed the analysis to be made for the case where the volumetric strain was expected. Their solution proposed for a dilative/contractive geomaterial can be written in the incremental form:

$$\Delta\tau = \frac{\left(1+\Delta\varepsilon_c\right)\left(2+\Delta\varepsilon_c - l\right)}{2\left(1+l\Delta\varepsilon_c\right)}\Delta\varepsilon_c \frac{dp_c}{d\varepsilon_c} \tag{2-2}$$

where the coefficient l admits the linear relationship between volumetric strain ε_v and tangential strain ε_θ, i.e., $\Delta\varepsilon_v = -l\Delta\varepsilon_\theta$. The derivative $\frac{dp_c}{d\varepsilon_c}$ is evaluated discretely. For small expansion/contraction, the cavity strain is about half of the shear strain at the borehole surface, i.e., $\Delta\varepsilon_c \approx \Delta\gamma_c / 2$. Eqn. (2-2) indicates that when small-strain nonlinearity is considered, the shear modulus directly derived using the pressuremeter data, i.e., Δp_c vs. $\Delta\varepsilon_c$, differs from the shear modulus that describes the constitutive relationship between $\Delta\tau$ vs. $\Delta\gamma_c$. The former is known as the pressuremeter shear modulus G_p, whereas the latter is regarded as the secant shear modulus G_s representative of a material point (Wood 1990). It was concluded by Favero et al. (2018) in their triaxial tests on Opalinus Clay that the volumetric strain was compressive and could approach the axial strain for shearing under drained condition. In the pressuremeter unloading, the shear strain accumulated during pressuremeter loading is released, and dilation occurs, and hence, l is positive in Eqn. (2-2). Giger et al. (2018) has observed virtually no volume change of Opalinus Clay specimen at the pre-failure stage in triaxial undrained tests. Because of the difference in strain paths, the conclusion from testing on core materials can not be directly used in quantifying the strain rate effect in pressuremeter testing. The strain rate also varies across the medium in the pressuremeter test, making different states of volumetric deformation possible along the radius. In the following analysis, given the measured high cavity strain rate ($> 5.0 \times 10^{-7}\ s^{-1}$) in all the pressuremeter unload-reload cycles, zero volumetric strain ($l = 0$) is assumed for the shear stress-strain analysis. Given that $\Delta\varepsilon_c \rightarrow 0$, Eqn. (2) can be therefore rewritten to determine G_p and G_s in a simple form,

$$\begin{aligned} G_p &= \frac{\Delta p_c}{2\Delta\varepsilon_c} \\ G_s &= \frac{\Delta\tau}{\Delta\gamma_c} = \frac{dp_c}{2d\varepsilon_c} \end{aligned} \tag{2-3}$$

It should be noted, however, that neglecting the possible dilation could result in an overestimation of the shear stress (and therefore the shear modulus), as shown in Figure 2-20(b).

To parametrize the small-strain nonlinearity observed in borehole deformation, a power-law function for shear stress-strain relation, i.e., $\Delta\tau = \alpha\Delta\gamma_c^{\beta}$, was considered by Bolton and Whittle (1999), and a simple relationship between pressure and cavity strain was derived for the case of zero volumetric strain,

$$\Delta p_c = \frac{\alpha}{\beta}\left(\Delta\gamma_c\right)^{\beta} \tag{2-4}$$

The relationship permits a fit of the data and avoids the scatter caused by the process of numerical differentiation in the derivation using Eqn. (2-2). Once fitting parameters α and β are obtained, the relationships between the pressuremter shear modulus G_p or the secant shear modulus G_s and the shear strain increment $\Delta\gamma_c$ is readily expressed by provoking Eqn. (2-3),

$$\begin{aligned} G_p &= \frac{\alpha}{\beta}\Delta\gamma_c^{\beta-1} \\ G_s &= \alpha\Delta\gamma_c^{\beta-1} \end{aligned} \tag{2-5}$$

Based on the derived power-law relationship (Eqn. (2-4)) between pressure and shear strain at the cavity wall, Bolton and Whittle (1999) suggested plotting the unload or reload data in logarithm scales so that the power-law fit parameters (α and β) could be determined from the following linear relationship,

$$\ln\left(\Delta p_c\right) = \ln\left(\frac{\alpha}{\beta}\right) + \beta\ln\left(\Delta\gamma_c\right) \tag{2-6}$$

An example of linear fits on three unloads data from test BGC-A4, #2 is shown in Figure 2-25(a), and the fit parameter values are listed in Table 2-3. Examination of the power-law fits in normal scales reveals a general underfit of the data in the later stage of unloading (e.g., $\Delta\gamma_c > 0.02\%$ for $p_c = 8.4$ MPa in Figure 2-25(b)). At the initial small strains ($\Delta\gamma_c < 0.005\%$), the pressure and displacement readings are sensitive to the electrical noise of the transducers and any hysteresis in instrument response at the onset of unloading. Therefore, the data points in this range appear to be scattered and are not necessarily representative of the actual response of the ground. In the logarithm scales, these scatters tend to be exaggerated and dictate the linear regression, as shown in Figure 2-25.

Table 2-3. Power-law fit results using two fitting approaches

p_c at the Start of Unloading (MPa)	α (MPa)		β		Fit of Δp_c - $\Delta\gamma_c$	
					RMSE (MPa)	
	L	*NL*	*L*	*NL*	*L*	*NL*
0.9	1131	91	0.947	0.700	0.034	0.013
2.91	1270	239	0.849	0.688	0.076	0.044
8.4	284	756	0.682	0.778	0.061	0.035

L: determination using linear regression on the $\ln(\Delta p_c)$ - $\ln(\Delta\gamma_c)$ plot.
NL: determination using nonlinear regression on the Δp_c - $\Delta\gamma_c$ plot.
RMSE: root-mean-square error of Δp_c.

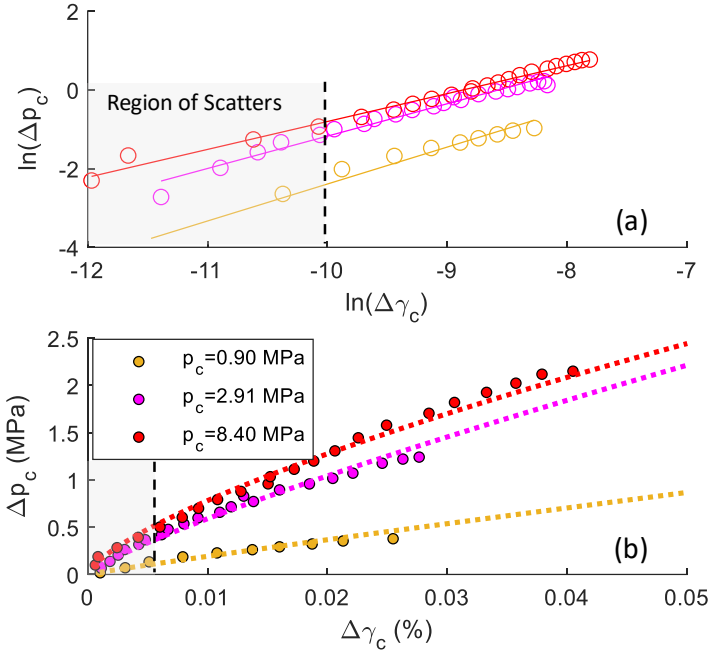

Figure 2-25. (a) Linear regression of the unload data from test BGC-A4, #2 in logarithm scales and (b) comparison between fit curves and the data in normal scales.

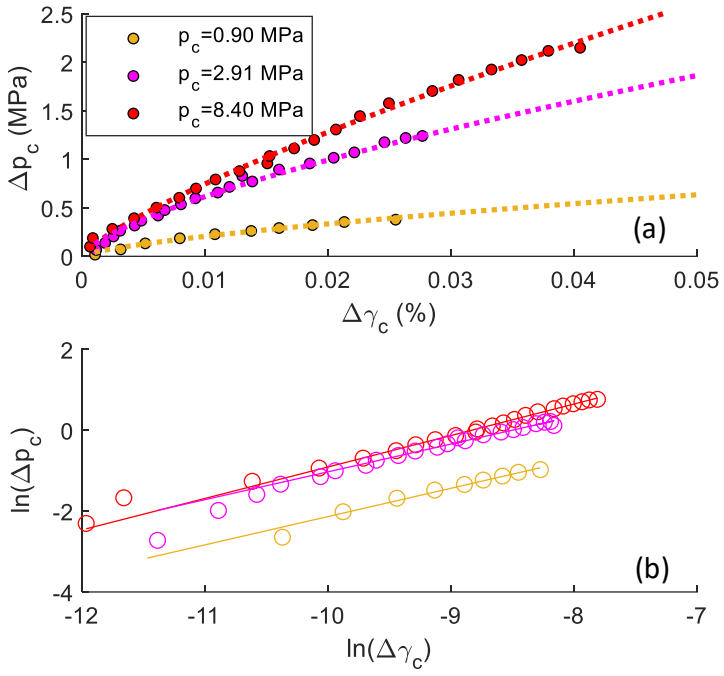

Figure 2-26. (a) Nonlinear regression of the unload data from test BGC-A4, #2 in normal scales and (b) comparison between fit curves and the data in logarithm scales.

The initial scatters may be filtered out before the analysis. Alternatively, nonlinear regression can be applied to all the data points in the normal scales, for example, using a trust-region algorithm available in the MATLAB curve fitting toolbox. Figure 2-26(a) shows the best power-law fits on the three unload data, and their fit parameter values are listed in Table 2-3. The fits in the normal scales are improved with the root-mean-square error (*RMSE*) significantly lower than those determined using the linear regression on the logarithm plots. Their linear expressions in logarithm scales also demonstrate the insensitivity of the fit to the initial scatters at the small strains (Figure 2-26(b)). It should be noted that adopting different fitting approaches can lead to vastly different values of power-law parameters determined, as shown in Table 2-3.

Figure 2-27 demonstrates the power-law fits using the nonlinear regression for three tests. The power-law fit parameters determined for all the unloading steps are summarized in Appendix III and also plotted in Figure 2-28. For the tests carried out in boreholes BGC-A4 and BGC-A6, both α and β demonstrate a clear trend of increase at $p_c < 5$ MPa, but become more or less constant at $p_c > 5$ MPa. The value for α determined for the tests in borehole BGC-A4 is lower than that determined for the tests in borehole BGC-A6 on average, again demonstrating the effect of the stiffness anisotropy caused by bedding orientation. The small-strain nonlinearity is quantified by the parameter β and does not exhibit a clear difference between the tests in these two boreholes. In contrast, for the tests in borehole BGC-2, α and β suffer from

significant scatters at the given pressure levels and are not dependent on p_c. Due to much fewer data points logged by SolExperts' probe, the power-law fits are more susceptible to any possible measurement errors and are generally of less quality (with an average *RMSE* of 0.067 MPa) than the fits for the tests in boreholes BGC-A4 and BGC-A6 (with an average *RMSE* of 0.035 MPa). Therefore, caution must be taken when using the power-law fit of unload data from this borehole in the assessment of the small-strain nonlinearity. Lithofacies again does not appear to affect the values of the fit parameters in this study.

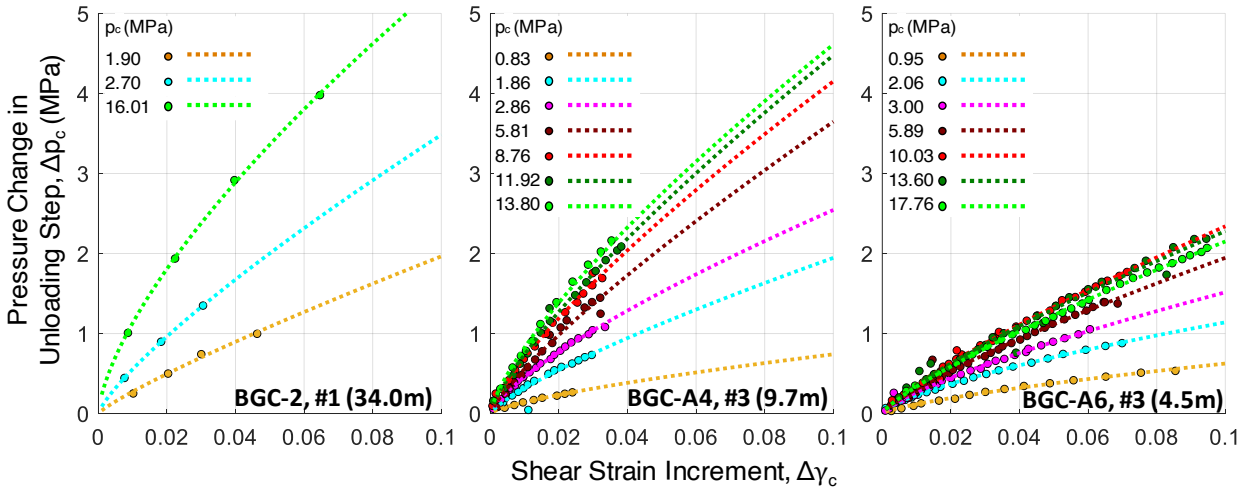

Figure 2-27. Nonlinear relationship between pressuremeter shear modulus G_p and strain increment $\Delta\gamma_c$ in unloading steps at different expansion pressures. Data is fitted by the power-law function.

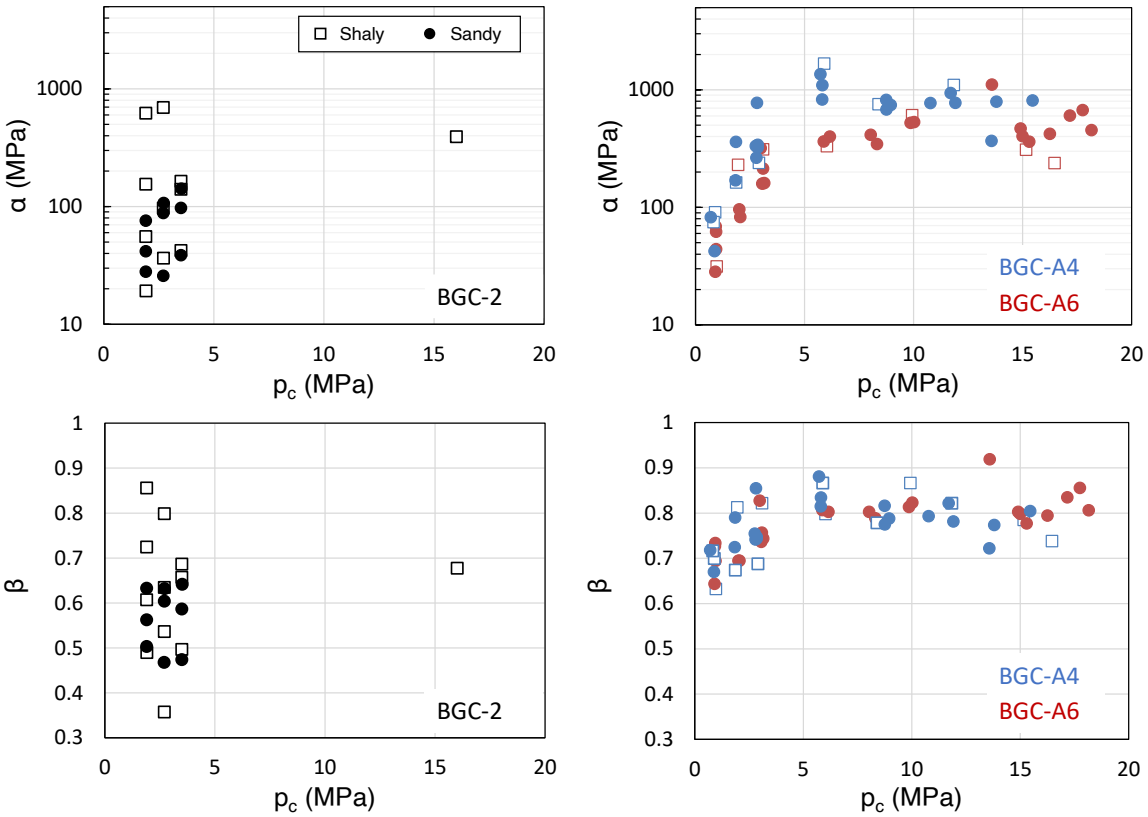

Figure 2-28. Power-law fit parameters determined using the unload data from tests in different boreholes

The small-strain nonlinearity of the Opalinus Clay is compared with other argillaceous sediments in Table 2-4. Since the borehole disturbance affects the unload-reload cycles at the low pressures, only the β values determined for $p_c > 5$ MPa are used. Having a higher β value, the Opalinus Clay exhibits less nonlinearity than London Clay and Gault Clay both classified with high plasticity (Ng et al. 1995; Hight et al. 2003), while it has the same magnitude of β as Westgate Shale evaluated from a pressuremeter test in a deep borehole (Liu et al. 2021a). It was shown by Jardine et al. (1984) that cemented structure in a low or medium plasticity geomaterial, such as the Opalinus Clay in this study, could reduce the nonlinearity of its small-strain stiffness.

Table 2-4. Summary of the nonlinear parameter β for small-strain shear stress-strain analysis and unloading strain rate for pressuremeter tests

Parameters	Argillaceous Soils/Rocks			
	Opalinus Clay (p_c > 5 MPa)	Westgate Shale [c]	London Clay [a]	Gault Clay [b]
Total Number of Unload or Reload Data Evaluated	34	4	3	4
Mean of β	0.81	0.85	0.59	0.58
Standard Deviation of β	0.04	0.08	0.03	0.02

[a.] Reported by Bolton and Whittle (1999).

[b.] Reported by Whittle (1999).

[c.] Reported by Liu et al. (2021a).

The less nonlinear response (i.e., higher β values) may result from the slower unloading rate for these tests. During unloading, the time-dependent expansion as seen from pressure hold might continue and compensate for the contraction resulting from the decrease of expansion pressure. Such an effect can be more evident if a slower unloading rate is applied, so the apparent stiffness derived from the unload data appears to be more linear than that derived from faster unloading. To confirm this, two unloads at different rates were compared in test BGC-A4, #6 (Figure 2-29). After the first regular unload-reload cycle, a second cycle using a fast unload (923 kPa/min) was performed after a 1 min pressure hold. The results shown in Figure 2-29 show that the fast unload tends to promote a stiffer response immediately after the pressure reversal. In fact, the unloading can produce negative stiffness when a significant amount of consolidation/creep is present and/or the unloading occurs at an extremely low rate, as shown by Clarke and Smith (1992) from their tests in mudstones.

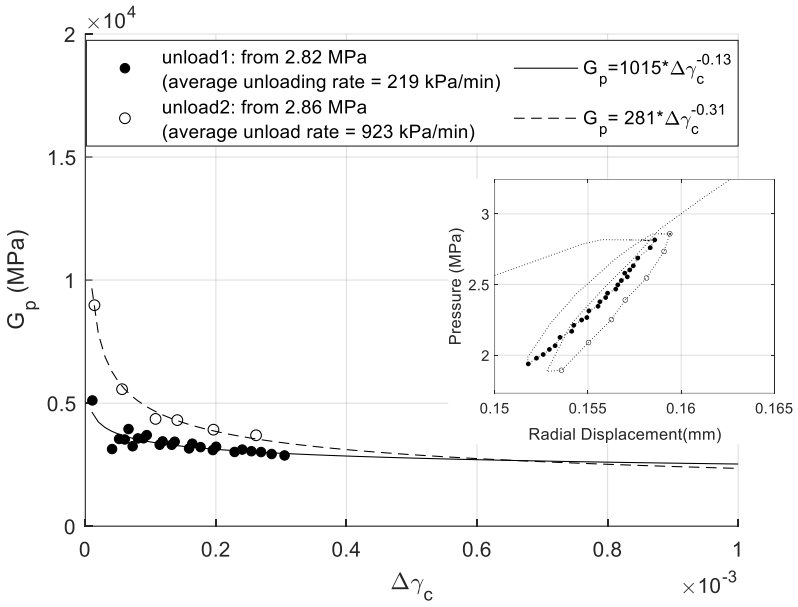

Figure 2-29. Comparison of G_p variations derived from data (BGC-A4 #6, 4.9m) at different unloading rates

2.4.3 Comparison with Reported Triaxial Test Results

The elastic properties of Opalinus Clay were investigated using core samples recovered from borehole BGC-2 in a parallel study (Minardi et al. 2021). It is important to consider the structural anisotropy in the comparison of laboratory and field test results because Opalinus Clay is known to be transversely isotropic with Young's modulus parallel to the bedding plane approximately two to three times greater than the modulus normal to bedding (Favero et al. 2018; Minardi et al. 2021). The pressuremeter loading in boreholes BGC-2 and BGC-A4 was parallel to bedding. Therefore the triaxial tests with the axial loading parallel to the bedding (or "P-tests") were chosen for comparison. For a transversely isotropic specimen, Amadei (1983) showed that the shear modulus parallel to the bedding plane (or "transverse shear modulus") could be derived from a P-test with the measurements of the axial (ε_A) and radial ($\varepsilon_{R//}$) strains in the same plane,

$$G = \frac{E}{2(1-\nu_{hh})} \tag{2-7}$$

where Young's modulus E is determined using the axial stress and strain in unloading and Poisson's ratio ν_{hh} refers to the resultant deformation parallel to bedding by axial compression, i.e., $\nu_{hh} = \varepsilon_{R//} / \varepsilon_A$. An example of the axial and lateral stress-strain response for P-tests reported by Minardi et al. (2021) is shown in Figure 2-30. The test sample was 25mm in diameter and 50mm in length. Sampling disturbance was strictly controlled, and the axial and radial displacements were resolved at small strains by internal

displacement measurement. A single modulus value, E, can be determined using linear regression on unload data (Figure 2-30). Alternatively, an incremental analysis can be performed over the unload data, which yields the secant value of Young's modulus, E_s varying with strain increment (Figure 2-30). A nearly constant v_{hh} (0.21 and 0.18 for the first and the second cycles, respectively) is found for each unloading step in this test. The strain-dependent secant shear modulus, G_s, can therefore be determined using Eqn. (2-7) with E replaced by E_s.

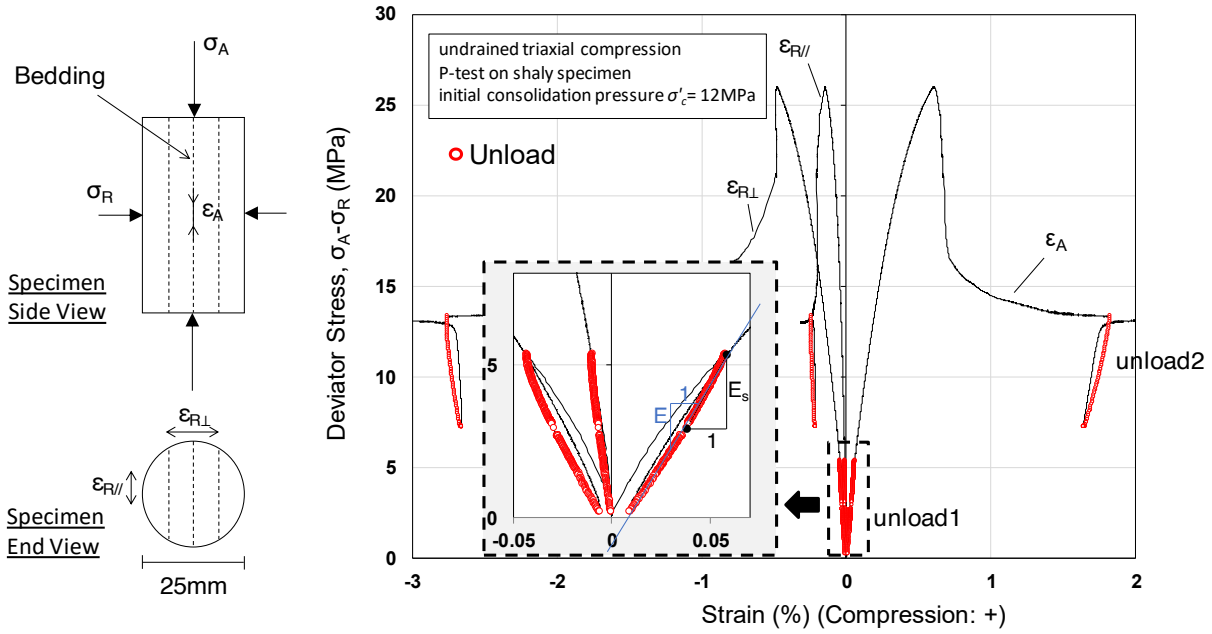

Figure 2-30. Undrained triaxial test on shaly Opalinus Clay sample recovered at 30.75m in borehole BGC-2 with bedding plane aligned with axial loading (P-test).

The variations of the secant shear modulus determined using the incremental analysis are shown in Figure 2-31. It is compared with those derived from a pressuremeter test in borehole BGC-2 both discretely (Eqn. (2-3)) and using the power-law fit (Eqn. (2-5)). The laboratory specimen was taken from 30.75m, and the pressuremeter test was conducted at about 34m, both in the lower shaly facies in borehole BGC-2. As shown in Figure 2-5, the Opalinus Clay is relatively homogeneous and not evidently affected by natural fractures at these locations. To account for different shear modes in the two types of tests, the comparison was made based on a common strain measure, invariant shear strain $\Delta\gamma_s$, which is equal to $\frac{2}{\sqrt{3}}\Delta\varepsilon_c$ or $\frac{\Delta\gamma_c}{\sqrt{3}}$ for the pressuremeter test and equal to $\frac{\sqrt{2}}{3}\sqrt{\left[\left(\Delta\varepsilon_A-\Delta\varepsilon_{R\perp}\right)^2+\left(\Delta\varepsilon_A-\Delta\varepsilon_{R//}\right)^2+\left(\Delta\varepsilon_{R\perp}-\Delta\varepsilon_{R//}\right)^2\right]}$ for the triaxial test (Jardine 1992).

The shear moduli obtained from the triaxial and pressuremeter tests are comparable at different states in Figure 2-31. G_s determined at $\Delta\gamma_s < 0.01\%$ (grey zone in Figure 2-31) from pressuremeter and triaxial tests are susceptible to the scatters of the data and are not appropriately explained by power-law fits. For $\Delta\gamma_s > 0.01\%$, G_s scales inversely with $\Delta\gamma_s$. The dynamic shear modulus parallel to bedding was also determined using ultrasonic shear wave velocity for the intact Opalinus Clay specimens in this field campaign (Lozovyi and Bauer 2018, and Chapter 3) . It varies in a range of 6.8 ~ 8.2 GPa (Figure 2-31) and represents a much smaller strain magnitude at about 10^{-6}.

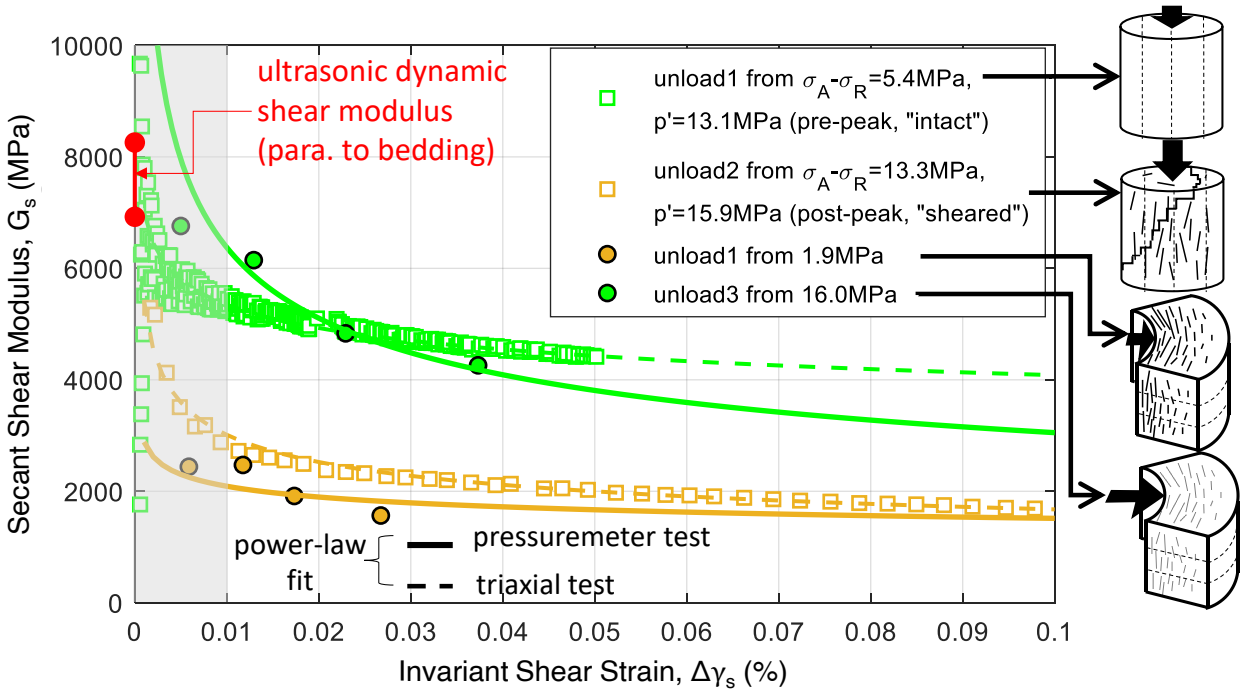

Figure 2-31. Comparison of strain-dependent shear modulus derived for an element from pressuremeter test and triaxial test data. The insert at the right illustrates the damage states of Opalinus Clay at varying loading stages.

For the triaxial test, at $\Delta\gamma_s = 0.1\%$, unload2 at the post-peak phase yields a modulus of about 50% of that determined from the unload1 at the pre-peak phase. The degradation of the elastic moduli after shear failure has been observed in all the triaxial tests reported by Minardi et al. (2021). The evolution of Young's modulus was also quantified by Zhang and Laurich (2020) using unload-reload cycles during axial compression in triaxial tests on the Opalinus Clay. Young's modulus firstly increased with axial stress in the early pre-peak stage then reduced as damage developed upon further loading before peak stress. Damage was found to be fully activated shortly after failure, according to acoustic emission monitoring by Amann et al. (2011), as micro-cracks have fully developed in the specimen and eventually coalesced into a rupture plane. At the residual stress, the inelastic deformation of the specimen is

dominated by the sliding of the rupture plane. Upon unloading, the sliding does not reverse until a critical condition is satisfied when the axial stress is sufficiently reduced. Hence, the stiffness measured using unload2 likely only represents the elastic rebounding of the sheared specimen and is considered as the lower bound of the elastic modulus for the damaged Opalinus Clay solid.

For the pressuremeter measurement at the lowest pressure (p_c = 1.9 MPa), G_s primarily represents the stiffness of damaged Opalinus Clay in the borehole nearfield. This value appears to be constrained by the lower bound obtained from a fully damaged Opalinus Clay specimen under triaxial shearing. For the pressuremeter measurement at the highest pressure (16.0 MPa), G_s represents the stiffness of both re-compacted Opalinus Clay in the damage zone surrounding borehole as well as the intact Opalinus Clay beyond this zone. The fact that the G_s obtained from pressuremeter tests is overall lower than that obtained from the triaxial measurement on an intact specimen could suggest 1) that the stiffness of Opalinus Clay in the borehole damage zone is not fully restored even under the maximum pressuremeter loading, and/or 2) that the laboratory Opalinus Clay specimen is tested at a higher effective stress level than that for the in-situ test. The potential borehole yielding induced by high expansion pressure may further degrade the elastic properties of Opalinus Clay in the borehole nearfield. Despite this constraint, G_s measured after the threshold of 5 MPa is regarded as an "intact" value since more intact rock beyond the borehole damage zone was loaded.

A comparison of "intact" shear moduli from pressuremeter tests in boreholes BGC-2 and BGC-A4 is made with those measured in undrained triaxial P-tests reported by Lozovyi and Bauer (2018) and Minardi et al. (2021) (Figure 2-32). The laboratory measurements use the unload-reload cycles performed far before the peak stress and are summarized in Table 2-5. The shear modulus G derived using linear regression on unload data has a clear discrepancy between in-situ and laboratory results (Figure 2-32(a)). The discrepancy is mainly attributed to the different strain increments at the end of unloading, with an average value of $\Delta\gamma_s$ equal to about 0.02% for the pressuremeter tests and about 0.04% for the triaxial tests. The influence of the strain increment can also be seen when comparing G for different triaxial tests – the shear modulus (G = 3378 MPa) obtained at a higher consolidation pressure (σ'_c = 9 MPa) using the unloading with $\Delta\gamma_s$ = 0.08% is comparable with those (G = 3037 ~ 3824 MPa) determined when σ'_c = 4 MPa but with $\Delta\gamma_s$ < 0.05%. Alternatively, secant shear modulus G_s can be determined at a specified $\Delta\gamma_s$ using the derived nonlinear relationship as shown in Figure 2-31, thereby "normalizing" the results with respect to the strain increment. A comparison is made after G_s is evaluated at $\Delta\gamma_s$ = 0.1% for both types of the tests, and an overall agreement on the modulus values is observed (Figure 2-32(b)). In this case, triaxial tests also demonstrate a more plausible trend of modulus increase with σ'_c, whereas the effective stress state can not be reliably estimated for the pressuremeter tests.

Table 2-5. Summary of triaxial P-tests with unload-reload cycles at the beginning of the tests. Core specimens were recovered from boreholes BGC-1 and BGC-2. Unload data is used for the determination of elastic properties.

Facies	Effective Consolidation Stress, σ'_c	Deviator Stress, σ_A - σ_R at the First Unload	Deviator Stress, σ_A - σ_R at the Peak	Poisson's Ratio		Strain Increment $\Delta\gamma_s$ at the End of Unload	Transverse Shear Modulus		
				ν_{hh}	ν_{hv}		Linear Regression G	Power-law Fit ($G_s=a\Delta\gamma_s^b$)	
	(MPa)	(MPa)	(MPa)	-	-	(%)	(MPa)	a	b
BGC-1 (samples were not taken to failure)									
Sandy	4	3.94	-	0.241	0.757	0.0436	3824	521	-0.258
Sandy	4	0.99	-	0.166	0.678	0.0129	3233	420	-0.231
Shaly	4	1.00	-	0.144	0.794	0.0123	3658	1092	-0.136
Shaly	4	0.99	-	0.148	0.871	0.0155	3328	1358	-0.082
BGC-2									
Shaly	12	5.36	25.86	0.210	0.788	0.0499	4408	1825	-0.117
Shaly	4	4.01	16.30	0.223	0.658	0.0493	3037	826	-0.177
Shaly	9	6.68	21.58	0.201	0.802	0.0797	3378	1655	-0.103

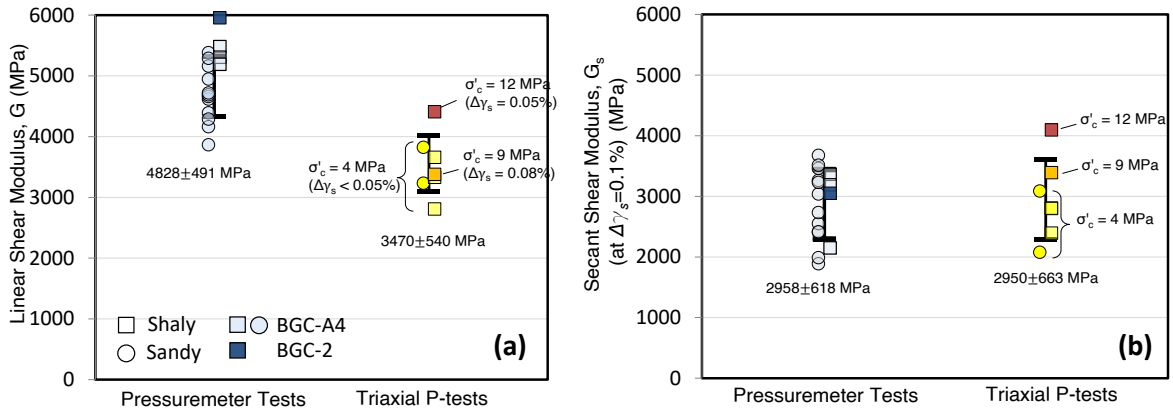

Figure 2-32."Intact" shear modulus measured parallel to the bedding of Opalinus Clay by both triaxial P-tests and pressuremeter tests (p_c > 5 MPa). The error bar in the plot indicates a 68% confidence zone from the mean value.

2.4.4 Explain PMT Anisotropic Moduli using Transversely Isotropic Elastic Parameters

Transversely isotropic (TI) elasticity can be expressed using the generalized form of Hooke's law,

$$[\Delta\boldsymbol{\varepsilon}]_{6\times1} = [\mathbf{C}]^{-1}_{6\times6}[\Delta\boldsymbol{\sigma}]_{6\times1} = \begin{pmatrix} 1/E_h & -\nu_{hh}/E_h & -\nu_{vh}/E_v & 0 & 0 & 0 \\ -\nu_{hh}/E_h & 1/E_h & -\nu_{vh}/E_v & 0 & 0 & 0 \\ -\nu_{hv}/E_h & -\nu_{hv}/E_h & 1/E_v & 0 & 0 & 0 \\ 0 & 0 & 0 & 1/G_{vh} & 0 & 0 \\ 0 & 0 & 0 & 0 & 1/G_{vh} & 0 \\ 0 & 0 & 0 & 0 & 0 & 1/G_{hh} \end{pmatrix} [\Delta\boldsymbol{\sigma}]_{6\times1} \tag{2-8}$$

where $[\Delta\boldsymbol{\sigma}]_{6\times1}$ and $[\Delta\boldsymbol{\varepsilon}]_{6\times1}$ are vectorized stress and strain tensors in a coordinate system orthogonal to the material's symmetry; $[\mathbf{C}]_{6\times6}$ is the elastic stiffness matrix. The subscripts of the elastic parameters refer to their orientations with respect to the bedding plane, namely, *h* (or *hh*) denotes the properties parallel to bedding, *v* denotes the properties normal to bedding, and *vh* (or *hv*) denotes the properties in the plane perpendicular to bedding (Figure 2-33). The seven parameters in the elastic stiffness matrix are further constrained by the following two equations:

$$G_{hh} = \frac{E_h}{2(1+\nu_{hh})} \tag{2-9}$$

$$\frac{E_v}{\nu_{vh}} = \frac{E_h}{\nu_{hv}} \tag{2-10}$$

Hence, five independent parameters are needed to define a TI material.

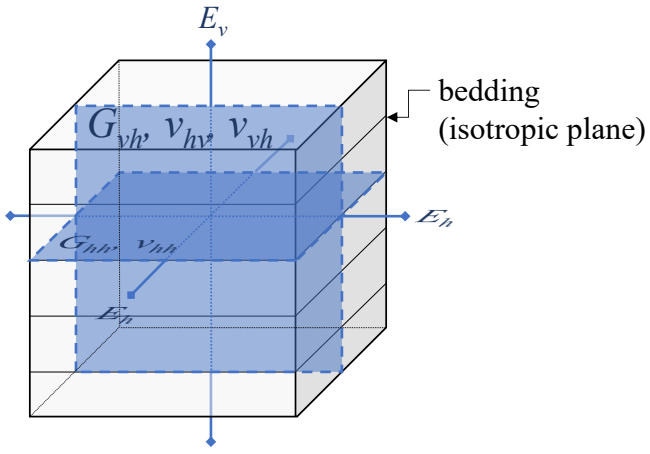

Figure 2-33. Representative axes and planes for TI elastic parameters

All the elastic parameters could be constrained by the triaxial tests on the specimens with different orientations (Amadei 1996). Particularly, E_v and ν_{vh} can be determined using the standard triaxial test on a

specimen with its bedding oriented normal to axial loading (S-test); E_h, ν_{hh}, and ν_{hv} can be determined using the triaxial test on a specimen with its bedding oriented parallel to axial loading (P-test). A triaxial test on a specimen with its bedding oriented in an inclined angle (Z-test) from the axial loading can be useful to derive G_{hv}. However, there are much fewer Z-tests reported than P- and S-tests and are therefore not considered in this study. To estimate G_{hv}, an empirical relationship first introduced by Saint-Venant (1893) can be used,

$$\frac{1}{G_{hv}} = \frac{1}{E_h} + \frac{1}{E_v} + 2\frac{\nu_{vh}}{E_v} \tag{2-11}$$

Amadei and Savage(1991) derived the elastic solution for the borehole expansion in an anisotropic medium under the plane strain condition. The directional modulus at a borehole azimuth under uniform loading can be defined using a nominal parameter G^*,

$$G^* = \frac{\Delta p_c}{2\Delta\varepsilon_c^*} \tag{2-12}$$

where $\Delta\varepsilon_c^*$ is the nominal cavity strain increment responding to a pressure increment Δp_c, defined as $\Delta\varepsilon_c^* = \Delta u_r / r_0$. Δu_r is the measured radial displacement increment at the borehole wall, and r_0 is the initial borehole radius. For the pressuremeter test in a borehole with its axis perpendicular to bedding (Figure 2-34(a)), presumably $\Delta\varepsilon_c^*$ is invariant with azimuth. The derived G^* is equal to the shear modulus in the transverse bedding plane, G_{hh}, as already applied to the pressuremeter test data from borehole BGC-2 and BGC-A4 in Section 2.4.3. For the pressuremeter test in a borehole with its axis parallel to bedding (Figure 2-34(b)), G^* varies with the angle θ measured from the bedding plane,

$$G^* = \frac{1}{2}\frac{1}{\left(A + B\cos 2\theta\right)} \tag{2-13}$$

where A and B are coefficients expressed by transversely isotropic elasticity parameters in the following forms,

$$\begin{aligned} A &= \frac{1}{2}\left[-2C_2 + \left(C_1 + \sqrt{C_1 C_3}\right) \times \sqrt{\frac{2C_2 + C_4}{C_1} + 2\sqrt{\frac{C_3}{C_1}} - 2\sqrt{C_1 C_3}}\right] \\ B &= \frac{1}{2}\left[\left(C_1 - \sqrt{C_1 C_3}\right) \times \sqrt{\frac{2C_2 + C_4}{C_1} + 2\sqrt{\frac{C_3}{C_1}}}\right] \end{aligned} \tag{2-14}$$

Where $C_1 = \frac{1}{E_h}\left(1-\upsilon_{hh}{}^2\right), C_2 = \frac{-\upsilon_{vh}}{E_v}\left(1+\upsilon_{hh}\right), C_3 = \frac{1}{E_v}\left(1-\frac{E_h\upsilon_{vh}^2}{E_v}\right)$ and $C_4 = \frac{1}{G_{vh}}$.

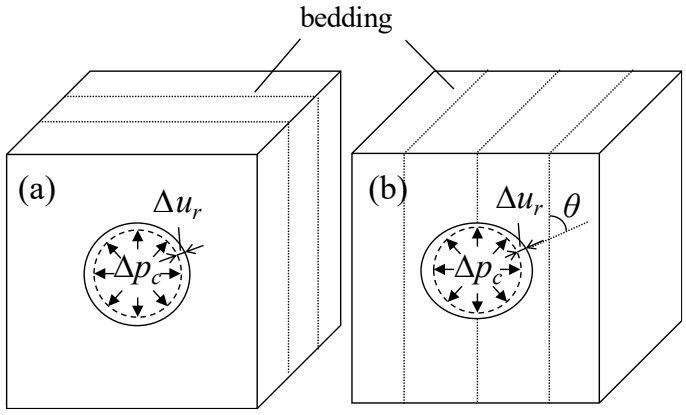

Figure 2-34. Schematic diagrams of the borehole deformation under pressuremeter loading in boreholes oriented (a) perpendicular to bedding and (b) parallel to bedding

For tests in borehole BGC-A6, G^* demonstrates a clear anisotropy with the axis of its maximum magnitude preferentially aligned with the dip of bedding (Figure 2-23). The maximum and minimum magnitudes of G^*, i.e., G^*_{max} and G^*_{min}, and their ratio can be determined from the profile of G^*. These characteristics of anisotropic moduli G^* determined using the unload-reload cycles at p_c > 5 MPa are summarized in Table 2-6. It should be noted that only three tests are considered, because the other two tests, #1 and #5, were impacted by a local natural fracture and excavation-induced disturbance, respectively. For a single test, the variations of G^*_{max} or G^*_{min} and their azimuths are evident from different unloading steps and may be attributed to (1) the impact of expansion pressure and/or (2) the uncertainty associated with the G^* derivation using a limited number of radial displacement measurements. The uncertainty may be reduced by stacking the profiles of G^* from multiple unloading steps and obtaining an averaged profile. The averaged profiles for the three tests are shown in Figure 2-35.

Table 2-6. Characteristics of the anisotropic modulus G^* determined for unloading steps at $p_c > 5$ MPa. The values obtained for the averaged profile of G^* are also summarized for each test.

Test		p_c (MPa)	Unloading Strain Magnitude $\Delta\boldsymbol{\varepsilon}_c^*$ (%)	Azimuth of $\boldsymbol{G}_{max}^*$	$\boldsymbol{G}_{max}^*$ (MPa)	$\boldsymbol{G}_{min}^*$ (MPa)	$\boldsymbol{G}_{max}^*/\boldsymbol{G}_{min}^*$
#2	unload1	6.17	0.029~0.034	70°	2406	1712	1.41
	unload2	9.88	0.032~0.040	172°	2755	2240	1.23
	unload3	14.91	0.038~0.057	24°	2885	1920	1.50
	averaged	> 5		28°	2492	2090	1.18
#3	unload1	5.89	0.037~0.048	34°	1997	1532	1.30
	unload2	10.03	0.035~0.043	28	2542	2046	1.24
	unload3	13.60	0.040~0.054	26	2426	1813	1.34
	averaged	> 5		28°	2319	1798	1.29
#4	unload1	8.04	0.035~0.042	46°	2296	1884	1.22
	unload2	15.31	0.033~0.040	38°	2604	2174	1.20
	averaged	> 5		42°	2447	2031	1.21

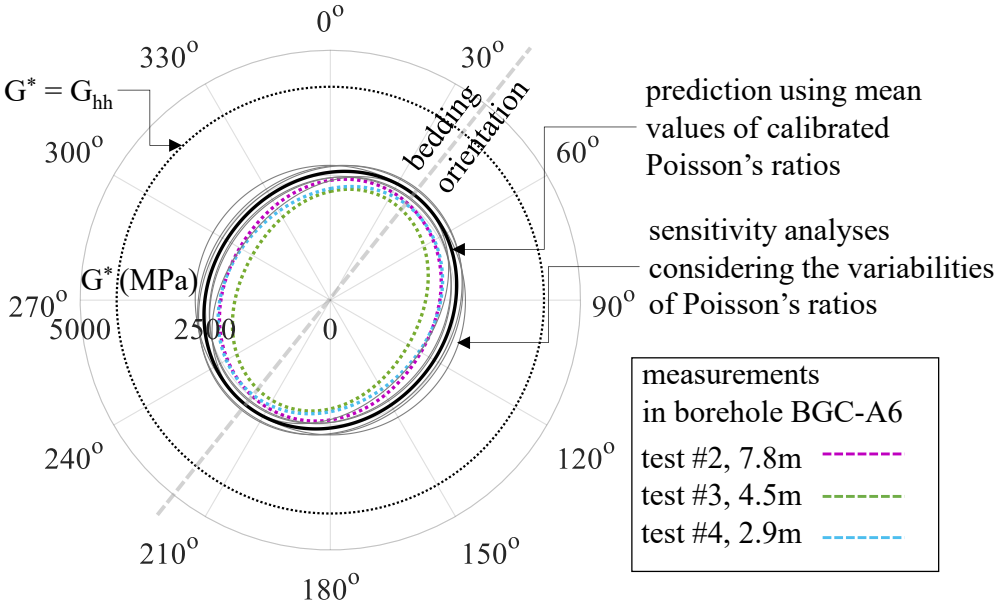

Figure 2-35. Comparison between predicted and measured modulus G^* from pressuremeter tests. The measurement is the averaged G^* profile obtained from multiple unloading steps at $p_c > 5$ MPa in each test. The prediction assumes that the bedding plane is oriented at the azimuth of 40°.

Anisotropic elastic parameters of Opalinus Clay calibrated from the triaxial tests may be used for Eqn. (2-13) to predict the azimuthal variation of G^*. Liu et al., (Under Review) has shown that Poisson's ratios are insensitive to stress and strain and are relatively consistent for different lithofacies. In contrast, the laboratory estimates of Young's moduli are dependent on both stress and strain and have significant scatter especially for the sandy facies. Instead, E_v and E_h can be derived from the transverse shear modulus G_{hh} with the given Poisson's ratio values. G_{hh} was independently determined using pressuremeter tests in borehole BGC-A4 oriented normal to bedding. The borehole was drilled only a few meters away from borehole BGC-A6 mostly in the same sandy facies, and it is also reasonable to assume that the measured moduli are controlled by similar in-situ stresses. However, G_{hh} should be reconciled for different strain magnitudes used in the unloading steps from the tests in these two boreholes. The mean value of cavity strain magnitude (denoted as $\Delta\varepsilon_c$) for unload-reload cycles from borehole BGC-A6 presented in Table 2-6 is 0.040%, while $\Delta\varepsilon_c$ for unload-reload cycles from borehole BGC-A4 is 0.017%. To determine G_{hh} at a given strain magnitude, the power-law relationship can be employed,

$$G_{hh} = \frac{\alpha}{\beta}\left(2\Delta\varepsilon_c\right)^{\beta-1} \tag{2-15}$$

where the two power-law parameters α and β have average values of 855 MPa and 0.805, respectively (Appendix III). This gives G_{hh} = 4270 MPa at $\Delta\varepsilon_c$ = 0.040%. For transversely isotropic elasticity,

E_h is then determined using the relationship with G_{hh} and v_{hh} in Eqn. (2-9), yielding a value of 10,163 MPa. The estimate of E_v is constrained by Eqn. (2-10), yielding a value of 5928 MPa. Another independent elastic parameter G_{hv} is estimated using the empirical relationship (Eqn. (2-11)) and is equal to 2446 MPa.

The azimuthal variation of G^* is predicted for borehole oriented parallel to bedding based on Eqns. (2-13) and (2-14) using the calibrated anisotropic elastic parameters (Figure 2-35). As a comparison, the isotropic G^* equal to G_{hh} as would be predicted for tests with pressuremeter loading parallel to bedding is also included. The difference in the magnitudes of G^* for these two borehole orientations is significant, agreeing with the field measurements (Figure 2-23). The prediction of G^* exhibits a higher magnitude than the measurements in borehole BGC-A6, while the anisotropic ratio G^*_{max}/G^*_{min} from the prediction is 1.13, lower than the measurements (1.18~1.29).

To assess the uncertainty of the prediction, sensitivity analyses are respectively performed on three Poisson's ratios v_{vh}, $v_{hv,}$ and v_{hh}, each varying by one standard deviation (0.07, 0.05, and 0.06, respectively). The predicted azimuthal variation of G^* is shown in (Figure 2-35). The anisotropic ratio G^*_{max}/G^*_{min} is also calculated from the predictions (Figure 2-36), showing its highest sensitivity to the

variation of ν_{vh}. Reducing ν_{vh} from 0.42 to 0.35 can increase the anisotropic ratio from 1.13 to 1.31, while increasing ν_{vh} decreases the anisotropic ratio and can even cause G^*_{max} to be oriented to the axis normal to bedding when $\nu_{vh} = 0.49$.

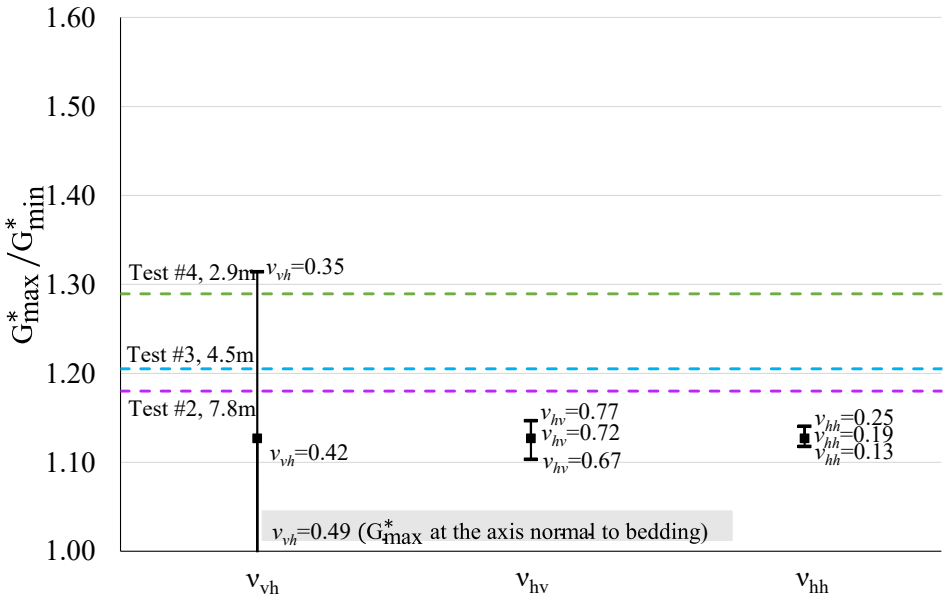

Figure 2-36. Anisotropic modulus ratio determined from three pressuremeter tests in borehole BGC-A6 versus analytical predictions using calibrated anisotropic elastic properties with each Poisson's ratio varying by one standard deviation.

A more probable reason for the large ratio of G^*_{max}/G^*_{min} is that the low stiffness of Opalinus Clay normal to the bedding has been further reduced by the localized borehole damage oriented near the same axis after borehole unloading (Figure 2-2). The effect of damage should remain even when the disturbed rock surrounding the borehole was recompacted at high expansion pressure.

2.5 Summary and Conclusions

To characterize the in-situ stiffness of Opalinus Clay, pressuremeter tests were performed in three boreholes at the Mont Terri Rock Laboratory. High-quality test data were obtained using two different pressuremeter probes. The test intervals were at the length scale of dm where borehole ultrasonic survey revealed substantial local heterogeneity in sandy and carbonate-rich sandy facies in the direction perpendicular to the bedding. Pressure holds and unload-reload cycles were carried out at multiple expansion pressures p_c ranging from 1 to 18 MPa. Shear modulus of Opalinus Clay was evaluated from test data both linearly and by considering the small-strain nonlinearity. The shear modulus was strongly dependent on p_c when $p_c < 5$ MPa and reached a constant value when $p_c > 5$ MPa.

The strain-dependent shear moduli determined from pressuremeter tests were compared with those obtained from triaxial tests on Opalinus Clay specimens, both under compression parallel to bedding. The comparison showed that the transverse shear modulus determined from pressuremeter tests was reasonably constrained by two end members obtained from triaxial tests. At the upper bound, it is constrained by the modulus obtained from an intact specimen. At the lower bound, it is constrained by the fully degraded modulus obtained on the specimen after shear failure. An agreement between the pressuremeter measurement at $p_c > 5$ MPa and triaxial measurement on intact specimens was established on the transverse shear modulus with a mean value of approximately 3 GPa at the shear strain increment of 0.1%. Neglecting the strain dependency in the modulus determination might cause systematic deviation in the comparison.

For the tests in the borehole parallel to the bedding, the shear modulus determined using averaged caliper measurement is approximately half of that determined for the tests in the boreholes perpendicular to the bedding. The azimuthal variation of borehole modulus G^* was determined using the displacement measurement at varying diametric axes. The observed anisotropy of G^* higher expansion pressures can be explained by the structural anisotropy of Opalinus Clay. The latter was further predicted using Amadei and Savage's (1991) solution for cavity expansion in a transversely isotropic medium. The prediction using the anisotropic elasticity parameters determined from laboratory tests generally agrees with the borehole modulus measured at $p_c > 5$ MPa but may be improved by considering the uncertainty of the parameters used and the impact of the localized borehole damage.

Chapter 3

Laboratory Investigation of Stress-dependent Elastic Properties under Varying Stress Paths[3]

3.1 Introduction

Understanding the evolution of the mechanical properties allows for the development of a constitutive model to predict macroscopic behaviors (e.g., yielding and damage) under different loading conditions. In this work, triaxial tests are attempted with the focus on the determinations of both static and dynamic moduli.

For borehole unloading, both stresses in the tangential and radial directions at the borehole wall are modified from the initial condition. For an axisymmetric borehole deformation in an isotropic medium, the element adjacent to the cylindrical cavity is subject to plane strain shearing. In this case, based on the Kirsch's solution (Kirsch 1898), the change of three principal stresses σ_r, σ_θ and σ_z from the far-field at the radius r is,

$$\begin{aligned} \Delta\sigma_r &= \left(p_c - \sigma_0\right)\left(\frac{a_0}{r}\right)^2 \\ \Delta\sigma_\theta &= -\left(p_c - \sigma_0\right)\left(\frac{a_0}{r}\right)^2 \\ \Delta\sigma_z &= 0 \end{aligned} \tag{3-1}$$

where p_c is the internal pressure at the borehole wall and a_0 is the initial borehole radius. Eqn. (3-1) suggests that the mean stress maintains constant at σ_0 after stress redistribution and the plane-strain shear stress becomes $\tau_{ps} = \frac{1}{2}\left(\Delta\sigma_r - \Delta\sigma_\theta\right) = \left(p_c - \sigma_0\right)\left(\frac{a_0}{r}\right)^2$. At the borehole wall,

$$\tau_{ps} = p_c - \sigma_0 = \Delta p_c \tag{3-2}$$

Because of the changes in tangential and radial stresses at the same time, the use of the traditional triaxial stress path with constant lateral stress is deemed inaccurate in the laboratory investigation of the constitutive behavior in the near-borehole field (Aristorenas 1992; Barla 1999; Wild and Amann 2018a; Liu et al. 2019). Boundary stress change for plane strain shearing can be reproduced using a true triaxial testing system. The undrained cavity expansion was simulated by Muir Wood and Wroth (1977) on a cubic specimen using a true triaxial cell that allowed the strains at two independent axes to be changed

[3] A version of this chapter has been accepted for presentation in 56th U.S. Rock Mechanics/Geomechanics Symposium.

simultaneously. Alternatively, Seah and Shrestha (2007) simulated the cavity expansion stress path with the control of the multi-axial stresses and enforced a mean effective stress condition.

The stress paths for unloading from an initially anisotropic stresses condition are more complex and challenging to reproduce by laboratory tests (Wild and Amann 2018a). Local stress concentrations around the cavity should be evaluated separately by triaxial tests with different loading schemes. Although it is impossible to reproduce the exact stress path of Eqn. (3-1) in a conventional triaxial testing apparatus, the important condition of the constant mean stress can be satisfied by simultaneously adjusting axial stress σ_A and radial stress σ_R using the following loading scheme,

$$\Delta\sigma_A = -2\Delta\sigma_R \tag{3-3}$$

Two different shear modes, plane-strain and triaxial shearing, are shown in Figure 3-1,

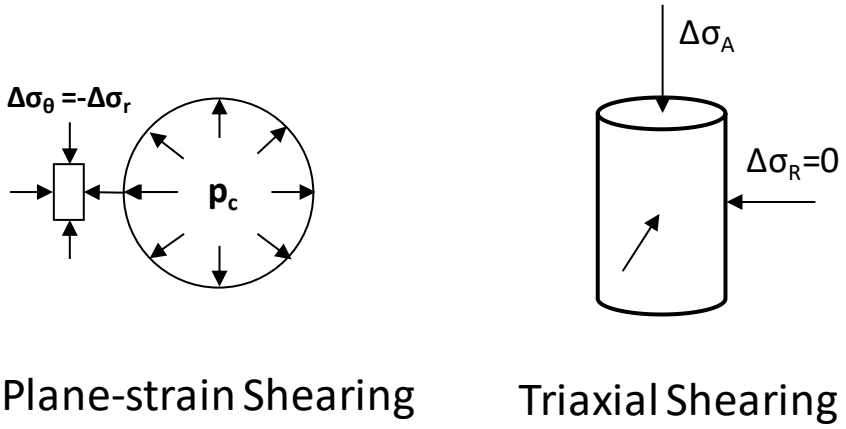

Figure 3-1. Stress paths for plane-strain and triaxial compression shearing

To compare the deviatoric loading condition in two different shear modes, the Von-Mises deviator stress should be used,

$$q = \sqrt{\frac{(\sigma_1 - \sigma_2)^2 + (\sigma_2 - \sigma_3)^2 + (\sigma_3 - \sigma_1)^2}{2}} \tag{3-4}$$

Therefore, in plane-strain shearing,

$$q = \sqrt{3}\Delta p_c \tag{3-5}$$

and in triaxial shearing,

$$q = \frac{3}{2}\Delta\sigma_A \tag{3-6}$$

3.2 Methodology

3.2.1 Testing Specimens

The Opalinus Clay specimens used in this study were obtained from cores taken from borehole BGC-A4. Because the borehole was drilled perpendicular to the bedding, cores were heavily disked with artificial fractures along with bedding (Figure 3-2). The intact core segments were selected for subcoring small testing specimens with a diameter of 1.5 inches. It was found that subcoring along the core axis had a minimum success rate because the weak bonding between bedding layers tended to be broken when subject to the cutting force. Subcoring along the bedding preserved the specimen better when the end faces of the core were confined (Figure 3-3). Therefore, only P-specimens (cut parallel to bedding) were prepared for the tests. Direct contact with the water should be avoided in specimen preparation. To release the heat generated by subcoring, the cutting speed was carefully controlled, with air being circulated at the same time. The end faces of the subcored specimens were later polished using sandpapers so that they were sufficiently flat and parallel.

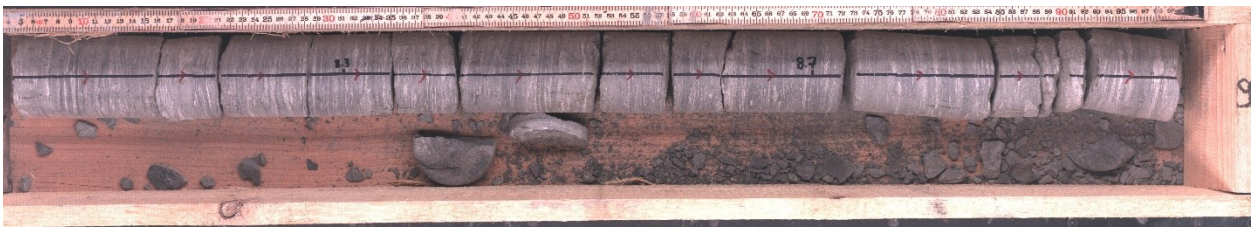

Figure 3-2. Core photos (BGC-A4, depth 8 – 9 m)

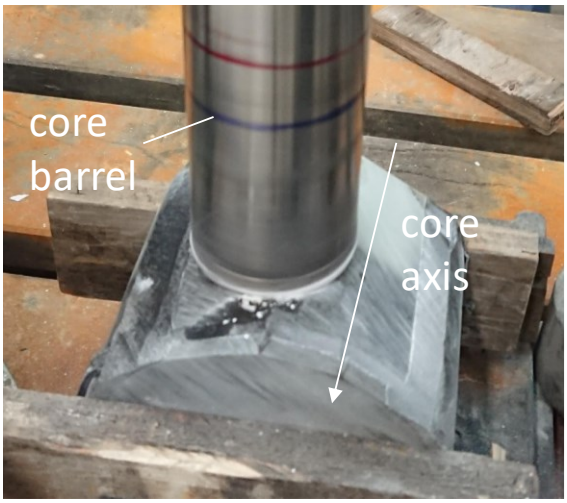

Figure 3-3. Subcoring Opalinus Clay specimen with the end face of the core being confined

A total of eight specimens were prepared for triaxial tests, and six of them were accepted for tests. The information of these six specimens is given in Table 3-1.

Table 3-1. Information of the Opalinus Clay specimens used in triaxial tests

Sample #	Core Depth (m)	Lithofacies	Original Specimen Height, h_0 (mm)	Original Specimen Diameter (mm)	Relative Humidity (%)		Constant Mean (Radial) Stress[b] (MPa)
					Expected	Measured	
E1	2.11~2.33	Sandy	64.43	37.62	33%	41%	5 (2)
E2	2.11~2.33	Sandy	65.44	37.38	95%	99%	5 (0.5)
E3	2.11~2.33	Sandy	61.76	37.61	95%	99%	5
E4	2.11~2.33	Sandy	63.92	37.22	33%	41%	5
F1	12.16~12.44	Shaly	63.28	37.43	95%	99%	7[a]
F2	12.16~12.44	Shaly	63.15	37.57	33%	41%	7

[a.] Mean stress dropped to 5.3 MPa after failure at triaxial compression.

[b.] Specimens E1 and E2 were tested under the CLS path after the CMS test.

The physical properties of the Opalinus Clay specimens from borehole BGC-A4 were also determined. The grain density was measured using He-pycnometry, yielding an average value of 2.64 g/cm^3. This is lower than the values reported from the literature, for example, 2.69 g/cm^3 (Zhang and Laurich 2020; Minardi et al. 2021). The underestimation by He-pycnometry measurement might be associated with two questions – 1) whether the measured volume was the true grain volume because the unconnected pores in the large sample were not infiltrated by helium and 2) whether the samples used for measurement were dry because they might adsorb moisture again from the atmosphere after being dried in the oven. The water-loss porosity was determined using the specimen and grain volumes, the latter of which was calculated using the weight of the oven-dried specimen and the measured grain density of 2.64 g/cm^3. It yielded a mean value of 11.5% with a standard deviation of 2.0% for all eight samples.

The mineralogy of the specimens was analyzed using SEM (Scanning Electron Microscopy)-based methods. The analysis was conducted by Vidence, Inc., and two methods were applied to different batches of specimens – Quantitative Evaluation of Minerals by SEM (QEMSCAN) and Advanced Mineral Identification and Characterization System (AMICS) (Pirrie et al. 2004). The scan can be performed both on the surface of an intact plug sample or the grain particles of a crushed sample. The latter is referred to as pseudo-cutting, and it allows for a mineralogical analysis least biased to the selected scan area of the sample. To prepare the pseudo-cutting samples, the intact specimens were intentionally crushed into particles with a size less than 2mm. The particles were mixed, and a portion of them was randomly selected as analysis samples. For analysis, the samples must be impregnated with resin and

formed into a polished epoxy resin block. Both QEMSCAN and AMICS use backscatter electron (BSE) brightness to distinguish the sample from the background epoxy resin as the first step. The sample is then discretized into multiple analysis points at the resolution as small as 2.3 μm in a 12.5 x 12.5 mm^2 field. At each analysis point, the energy dispersive X-ray spectrometers (EDS) are applied to identify the mineral using the acquired EDS spectra. In this way, the bulk mineralogy of the sample in the whole scanning field can be mapped, and the mineral compositions can be quantified. Mineralogy maps of 8 Opalinus Clay samples identified using this method are provided in Appendix V.

Despite the similar lithological and ultrasonic features of the rock core recovered from upper sandy and upper shaly facies in borehole BGC-A4, an attempt was still made to distinguish the mineralogical difference between these two facies. Figure 3-4 shows the proportions of three major mineral components – quartz, calcite, and smectite clay, according to the mineralogical analysis on four upper sandy and two upper shaly pseudo-cutting samples. As expected, only a subtle difference was observed – both facies are rich in quartz and smectite clays, and the smectite clay content in upper shaly facies is only slightly higher than that in upper sandy facies on average.

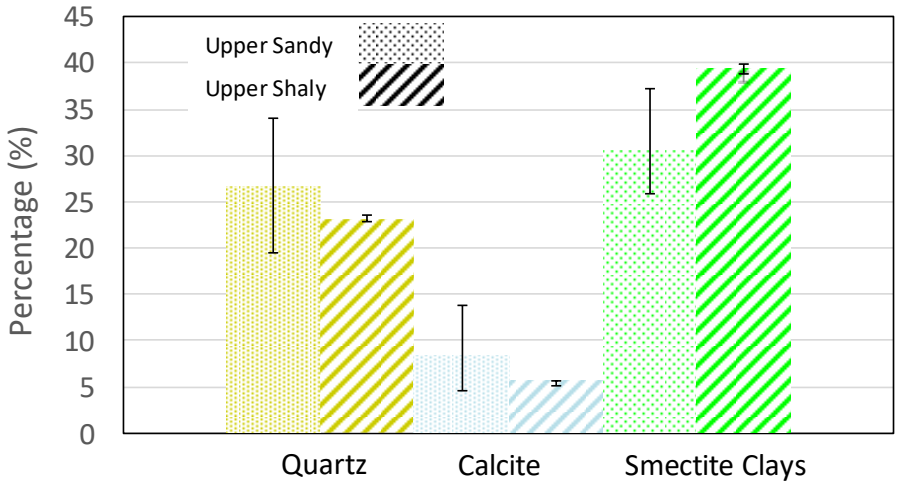

Figure 3-4. Proportions of three minerals in the Opalinus Clay specimens obtained at different facies in borehole BGC-A4. The error bar covers the range of measured values for each group

To achieve different levels of saturation, the vapor equilibrium technique has been considered a preferred method (Leung et al. 1991; Ferrari et al. 2018; Giger et al. 2018a), as it minimizes the swelling-induced microstructural damage as expected from the direct contact with the liquid phase. The technique allows Opalinus Clay specimens to be exposed to water vapor under controlled total suctions. The water vapor was provided by a saturated saline solution seated inside the vacuum chamber (Figure 3-5). Depending on the activity of the solution, the water in the vapor phase will be in equilibrium with the water in the liquid

phase, and a certain degree of relative humidity (RH) was maintained. The corresponding total suction ψ of the vapor can be calculated using psychrometric law,

$$\psi = -\frac{RT\rho_w}{M_w}\log(RH) \tag{3-7}$$

where R is the gas constant, T the absolute temperature, ρ_w the pure water density, M_w the molecular mass of the water. Two saturated saline solutions ($MgCl_2$ and KNO_3) were used in this study and expected to provide RH values of 33% and 95%, respectively, at room temperature around 20°. The actual values measured by the hygrometer are 41% and 99%, corresponding to the total suction of about 120.7 MPa and 1.4 MPa, respectively.

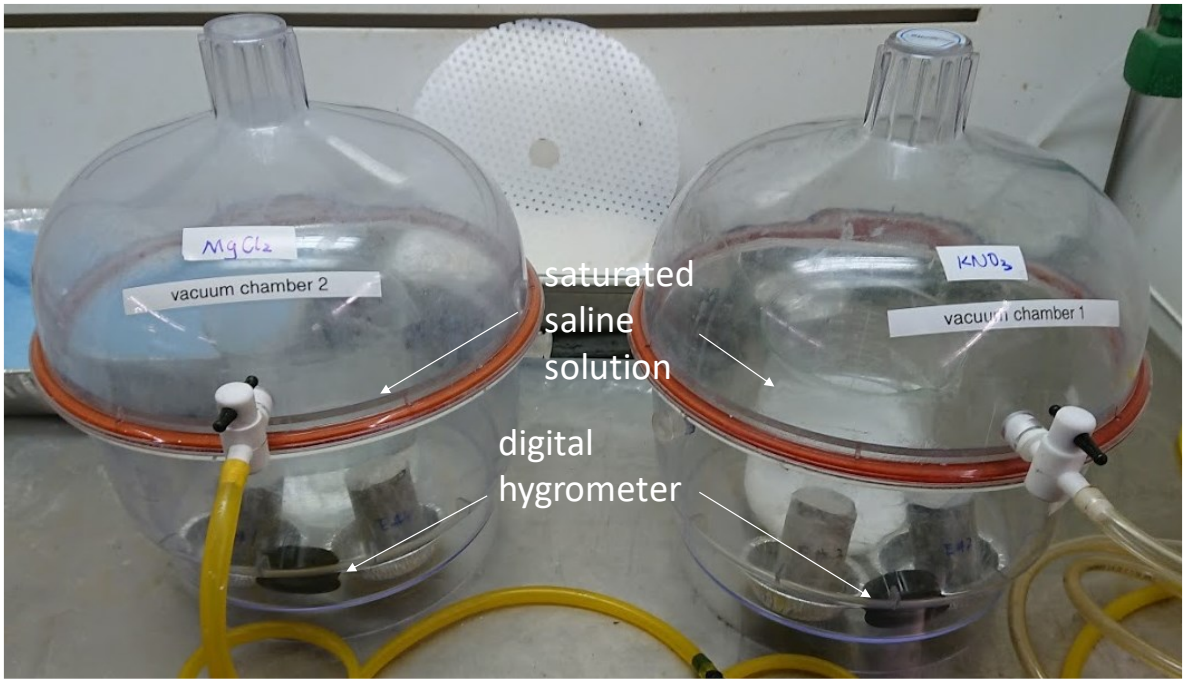

Figure 3-5. Preconditioning of the Opalinus Clay specimens under controlled total suction provided by two different saline solutions ($MgCl_2$ and KNO_3)

The weights of the Opalinus Clay specimens were recorded before and during preconditioning. The weight changes are plotted in Figure 3-6. Wetting to a constant weight only takes a few days while drying is slightly longer, which is consistent with the observations by Mitaritonna et al. (2009)

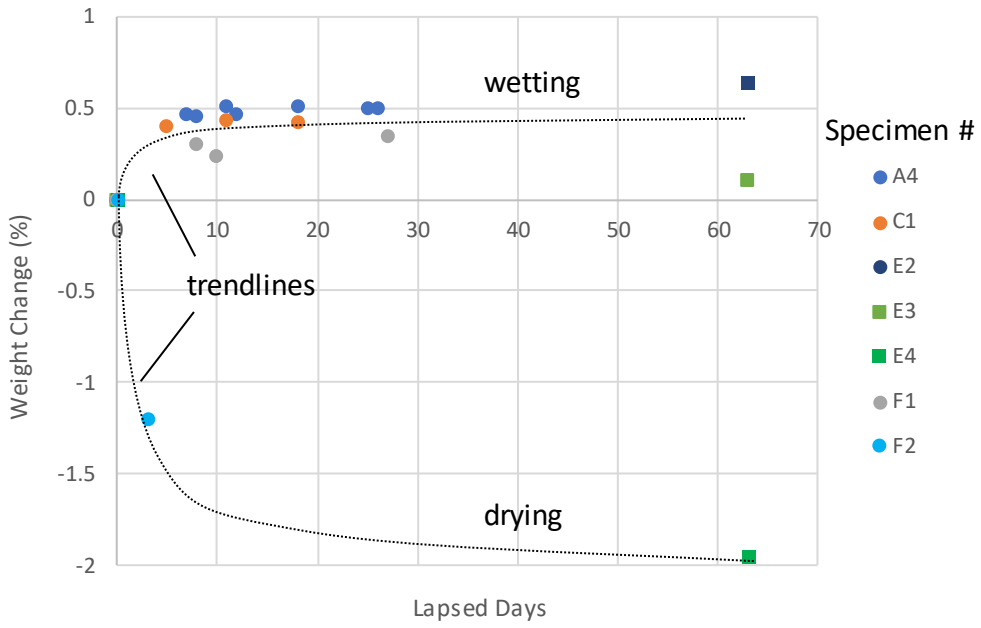

Figure 3-6. Change of the specimen weight during preconditioning.

3.2.2 Testing system

The triaxial testing system used in this study has the independent control of the axial loading and radial pressure (Figure 3-7). Two axial LVDTs and one circumferential LVDT were employed for internal displacement measurement. To enable the wave velocity measurement during triaxial test, the upper and lower end platens were used as the ultrasonic transducer with piezoelectric crystals installed inside. The dimensions of crystal housing in end platens are shown in Figure 3-8. The P- and S-wave crystals were stacked so the entire surface of the 1-inch-diameter S-wave crystal could be bonded to the inner bottom of end platens. Therefore, in the stacked configuration, the interface between two crystals served as the negative pole for the P-wave crystal and the positive pole for the S-wave crystal. A switchbox was designed for each crystal stacking to select P- or S-wave crystal as transmitter or receiver in an ultrasonic survey. However, it was later realized that this was unnecessary because measurement using only S-wave crystals provided an acceptable resolution of both P- and S-wave signals.

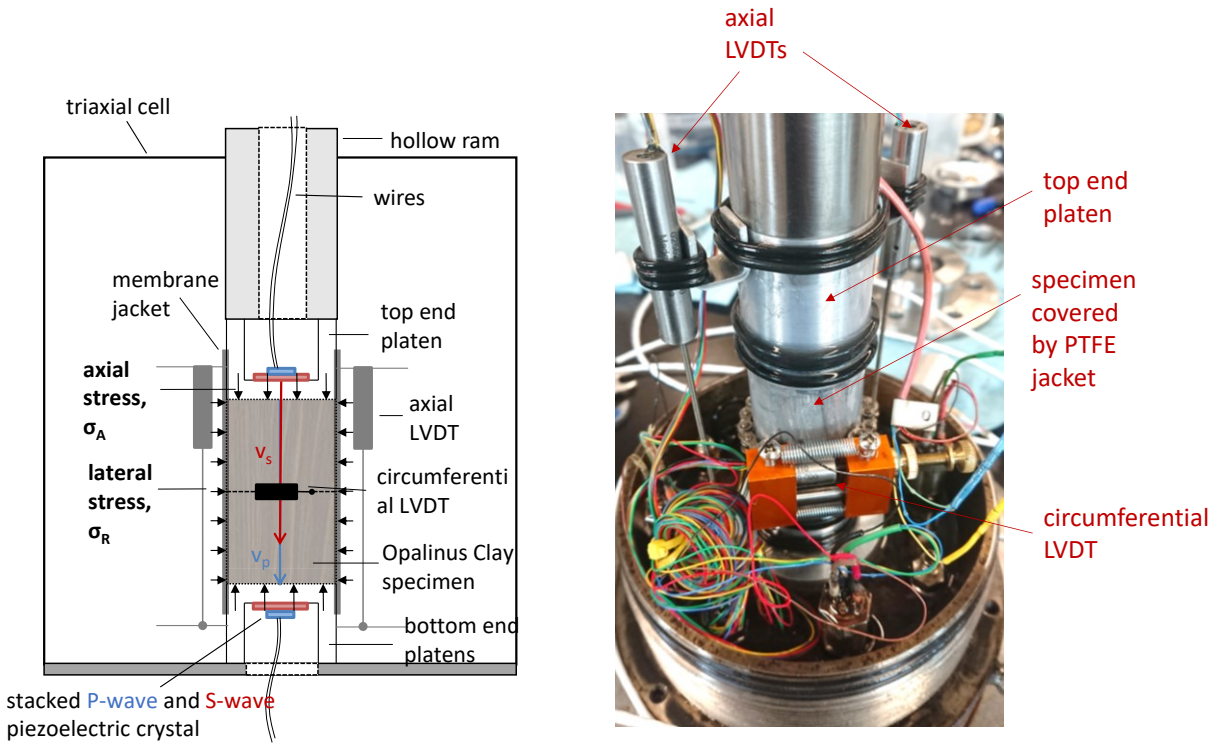

Figure 3-7. Schematic diagram (left) and internal instrumentation (right) of the triaxial testing system with displacement and ultrasonic measurements

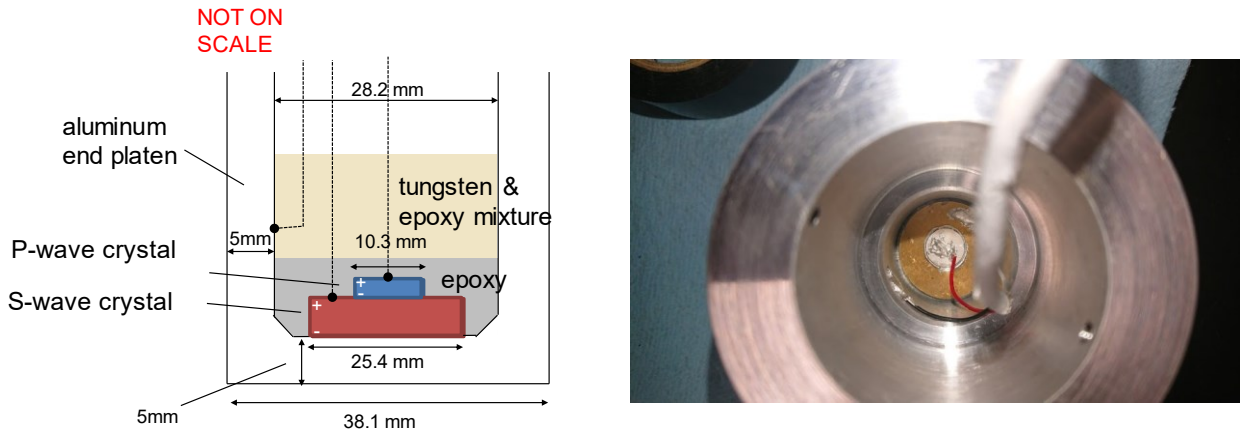

Figure 3-8. Configuration and dimension of the ultrasonic transducer (left). End platen with installed crystal assembly before epoxy back filling (right).

The quality of the data is defined by the signal-to-noise ratio (SNR), or the strength of the received signal given the same excitation energy at the transmitter. To provide the best signal quality, additional design suggestions of ultrasonic transducer were considered according to Wolf (2010) and Yam (2011). They are specified in Table 3-2. The signal quality also depends on the loading that compresses the end platen towards the specimen. The higher stress, the better coupling at the interface is achieved. In the triaxial

tests on the Opalinus Clay, to further reduce the attenuation of the S-wave (and increase the signal amplitude) through the specimen, S-wave crystals were oriented with their polarization direction parallel to the bedding of the specimen.

Table 3-2. Design consideration of the ultrasonic transducer used in this study

Parts	Desired Properties	Considerations	Choices
End Platens	Matching material with an acoustic impedance close to the test sample	The material and dimension of the end platen also depends on its mechanical integrity under the maximum expected axial loading (25MPa or 28.5kN)	Aluminum
	Thickness equal to a quarter of the estimated wavelength		1/4 wavelength of 200kHz PZT-5 crystal ≈ 5mm
Bonding epoxy	Conductive and has low viscosity at the working condition	A thin layer should be attempted, and compression can be applied during curing to strengthen the bonding	Silver conductive epoxy adhesive (8331 MG-Chemicals)
Backing materials	With a similar acoustic impedance of the piezoelectric crystal	An appropriate backing should allow the energy radiated from the back of the crystal to reflect towards the sample without interfering with any signals initially transmitted	The mixture of epoxy adhesive and tungsten with a weight proportion of about 50%/50%
Couplant between specimen and end platen	Has high viscosity	The couplant should be evenly applied to the whole contact surface of the end platens in a thin layer	Shear wave couplant (ECHO Ultrasonics)

The ultrasonic survey system consists of a pair of transducers, pulser, oscilloscope, and a data logging PC (Figure 3-9). The model of pulser used in this study is DPR300 by JSR Ultrasonics. The full width at half maximum (FWHM) of the pulse signal is 10 ~ 70ns, and the pulser has two exciting voltage ranges – 100 to 475V and 100 to 900V. High voltage pulsing is generally avoided since the crystal may be re-poled and damaged after long-term use. Therefore, the lower range (100 to 475V) was chosen to excite crystals.

3.2.3 Wave Signal Acquisition and Processing

The typical signals acquired at the oscilloscope are shown in Figure 3-10. The wave received after transmission through the testing specimen is synchronized with the triggering signal. It should be noted that unusual noise was observed at the initial portion of the received signal. The noise likely stems from the strong voltage triggering from the pulser. It induces electromagnetic interference to the signal receiving lines that are not fully shielded. This is not regarded as an issue because the noise quickly

decays before the first arrival can be identified. It can also be eliminated through the windowing approach, as will be shown later.

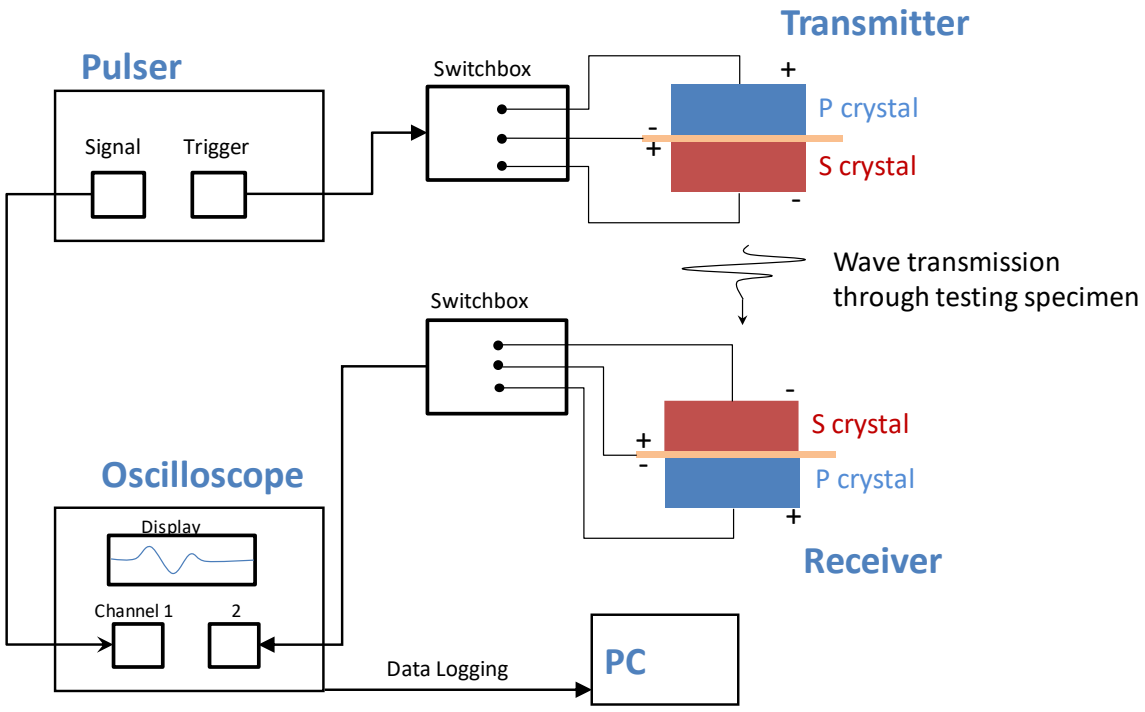

Figure 3-9. Schematic diagram of the device connection for ultrasonic survey

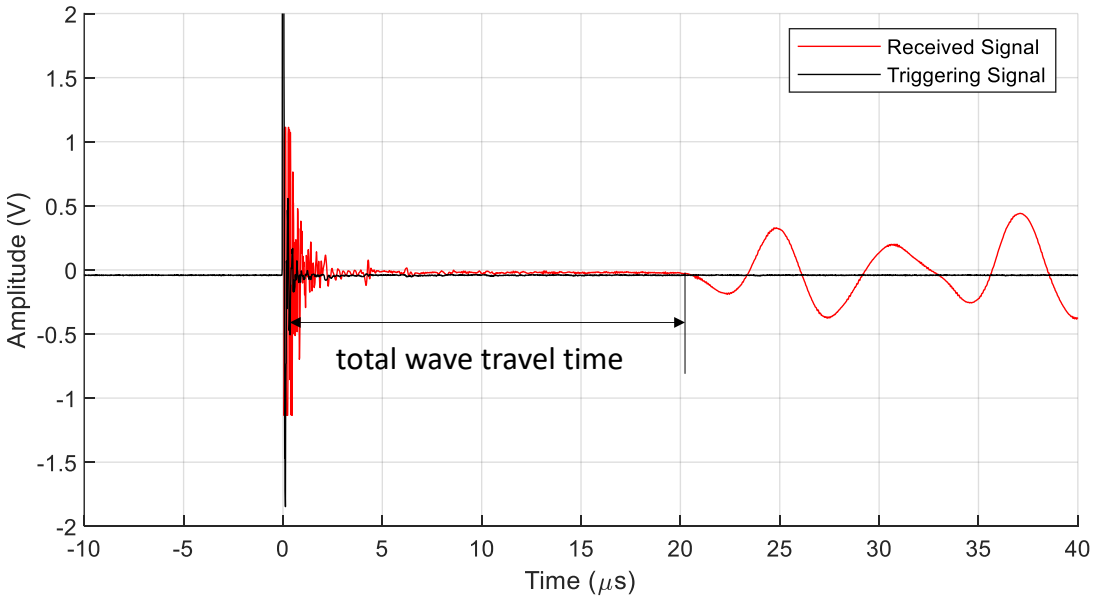

Figure 3-10. Raw waveforms displayed at the oscilloscope

The trial survey was performed through the acrylic specimen. Figure 3-11 shows the signals obtained from P-to-P (transmitting/receiving using P-wave crystal) and S-to-S (transmitting/receiving using S-wave crystal) modes. Both P- and S-wave crystals have natural frequencies equal to 200kHz as specified by manufacturers. However, the received wave signal after Fast Fourie Transform (FFT) shows several peaks over the frequency spectrum for the P-to-P mode (Figure 3-12). For the S-to-S mode, the peaks are localized in the lower range of the frequency spectrum (100~400 kHz).

It was found that the first wave phase in S-to-S mode arrived at the receiver about 1 μs earlier than that in P-to-P mode. Given that P-wave travels about twice as fast as S-wave in acrylic, the first wave phase observed in the S-wave transmission mode is likely a P-wave. The 1 μs difference in travel time between two first arrivals results from different traveling distances in the two modes – in P-to-P mode, P-wave also transmits through the thickness (4.6mm) of S-wave crystals. For the S-to-S mode, a second spike can be picked up at about 50 μs, likely indicating the arrival of the true S-wave. The precursor P-wave signal mixed in the S-to-S mode has also been observed in other similar experiment setups (e.g., Yam (2011)). There are two possible reasons for the generation of the additional wave – 1) the vibration of crystal disk may not be dominated by one specified mode, and other modes may coexist depending on the input triggering signal and the dimension of the crystals with respect to the buffering medium (Kunkel et al. 1990); 2) the wave conversion at the outer free surfaces of the end platen/specimen as well as the interfaces between specimen beddings. According to Stephenson (1978), the wave conversion is pronounced when the wavelength (at the magnitude of 1cm in this study) is close to the diameter of the crystal disk (2.54 cm).

Because the S-to-S mode has both P- and S-wave transmissions, the data from this mode is deemed sufficient for the determination of the two wave velocities if both wave arrivals can be identified. Another advantage of using S-to-S is that the signal has a higher signal-to-noise ratio than P-to-P mode when propagating waves through Opalinus Clay specimens. The wave with the lower concentrated resonant frequencies in S-to S mode tends to have less attenuation through porous geomaterials.

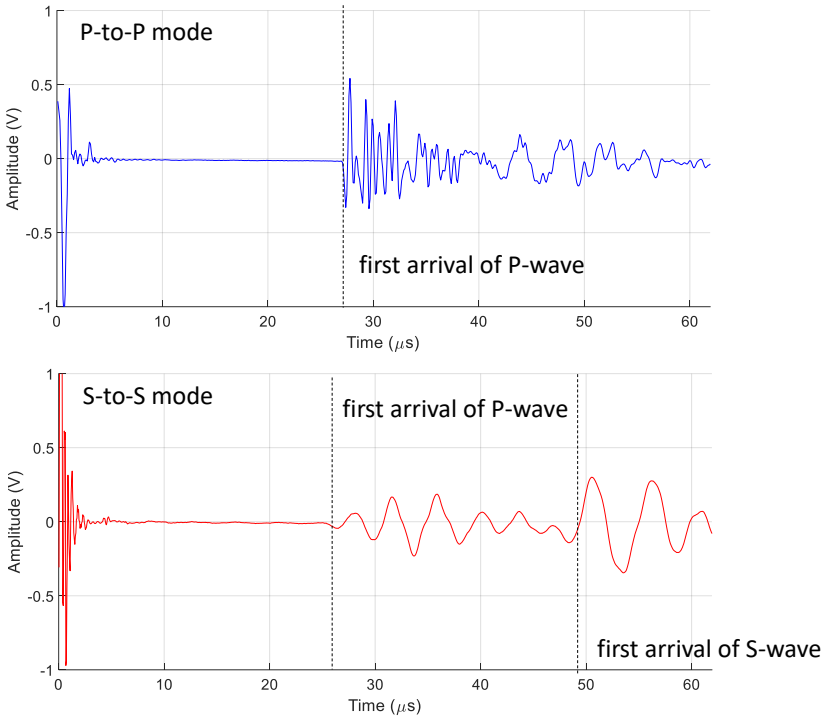

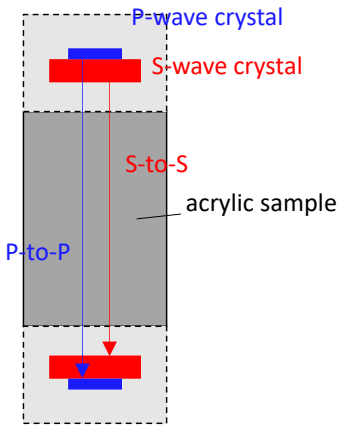

Figure 3-11. Received signals for P-to-P and S-to-S modes

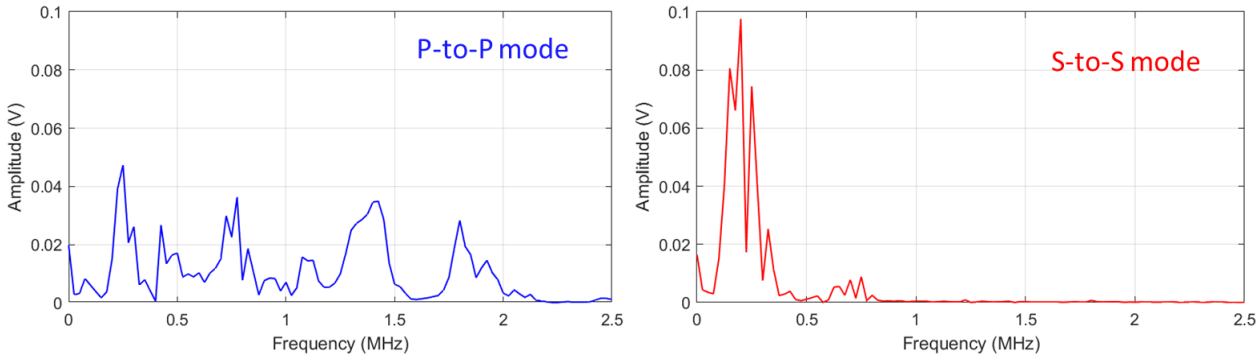

Figure 3-12. Frequency spectrum analysis using FFT for the received signal in the time interval of 20~60 μs

The time offset between time zero and the first wave arrival is the measured total travel time t_{total} between transmitting crystal and receiving crystal. To obtain the travel time t through the specimen only, the time delay t_{delay} caused by signal triggering and wave transmission through the end platens should be subtracted, i.e., $t = t_{total} - t_{delay}$. Typically, t_{delay} can be calibrated by propagating the wave through a face-to-face configuration, where the specimen is excluded. However, because the estimated arrival time for P- and S-wave in such the configuration (<5μs) stays within the zone of initial noise, it would be hard to identify the true arrival time.

Alternatively, a calibration procedure is suggested by Meléndez-Martínez (2006), and samples with the same velocity v but in different lengths can be used to determine t_{delay}. The total travel time, t_{total}, for the wave transmitting through a sample with height h is,

$$t_{total} = t_{delay} + \frac{h}{v} \tag{3-8}$$

and can be written as,

$$h = -vt_{delay} + vt_{total} \tag{3-9}$$

Therefore, t_{delay} and v can be derived from a linear fit of h versus t_{total} from multiple measurements. Two sets of cylinder samples made of aluminum and acrylic, respectively, are used in the calibration (Figure 3-13). As mentioned earlier, only t_{delay} for the S-to-S mode needs to be calibrated. It appears that the first arrival can be confidently identified for P-waves through acrylic samples and S-waves through aluminum samples. Figure 3-13 shows the results from these calibrations, and the linear regression yields t_{delay} equal to 3.40 μs and 5.17 μs for P- and S-wave transmissions[4], respectively.

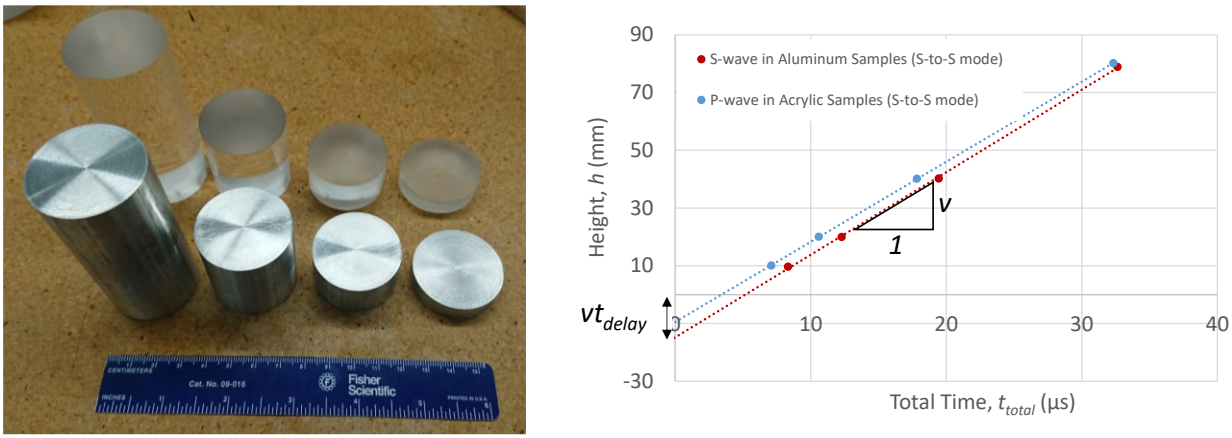

Figure 3-13. Calibration of t_{delay} using dummy samples with multiple lengths (left) and results (right)

Three post-processing approaches were suggested by Leong et al. (2004) to improve the signal quality further. They are stacking, windowing, and filtering. The data logged from the oscilloscope was already averaged from a stack of 16 signals. Applying windowing eliminated the initial noise (Figure 3-14). The lowpass filtering aimed to remove the high-frequency oscillations (> 400kHz in this case). This technique has no effect on the data with a high signal-to-noise ratio, while the data with a low signal-to-noise ratio were smoothed so that the first arrival could be reliably picked.

[4] t_{delay} is calibrated to the first trough of P-wave arrival and the first peak of S-wave arrival, respectively (Figure 3-11, S-to-S mode).

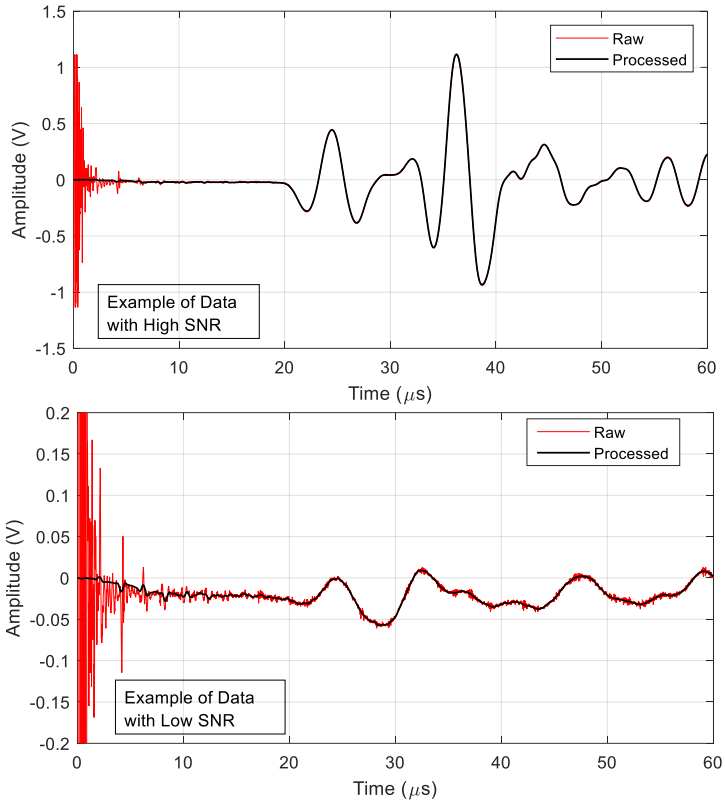

Figure 3-14. Comparisons between the raw data and the processed data after windowing and lowpass filtering for the cases with high and low signal-to-noise ratios (SNR). Note that the scales for the y-axis are different.

3.2.4 Triaxial Tests under Constant Mean Stress Path

Triaxial tests were performed on six Opalinus Clay specimens preconditioned under different moisture conditions (Table 3-1). The triaxial loading includes three segments - 1) isotropic loading (and unloading) to initial stress state, 2) triaxial compression at the constant mean stress, and 3) triaxial extension at the constant mean stress (Figure 3-15). For tests on samples E1, E3, and E4, isotropic stress to 5 MPa was directly imposed in the first loading segment, whereas for tests on samples E2, F1, and F2, higher isotropic stress (e.g.,10 MPa) was imposed first and then reduced to the desired stress level. The latter approach was intended to enhance the coupling between end platens and specimens with higher initial stress. The 2nd and 3rd loading segments aimed to approximate the stress paths of borehole unloading and reloading for an element near the borehole wall. Different mean stress of 7 MPa was attempted in tests on samples F1 and F2, so that the effect of mean stress could be assessed. In the absence of feedback control of axial and confining stresses, the loading was adjusted manually. For every 1.5 MPa deviatoric stress change, a 1 MPa increase (decrease) of the axial stress σ_A followed by a 0.5 MPa decrease (increase) of the confining stress σ_R was applied. Ultrasonic survey was performed after each loading increment to measure wave velocity evolution along the loading paths. Unload-reload cycles were also attempted to

measure static modulus at multiple stress levels. However, the measurement was strongly affected by the hysteresis observed in the cycle over a 4 MPa axial stress change. The hysteresis was caused by the seating effects of end-platens and the tilting of the axial LVDTs (Perbawa et al. 2019). The issue was acknowledged but not resolved, given the available experiment condition. Therefore, the determination of static modulus was deemed unsuccessful.

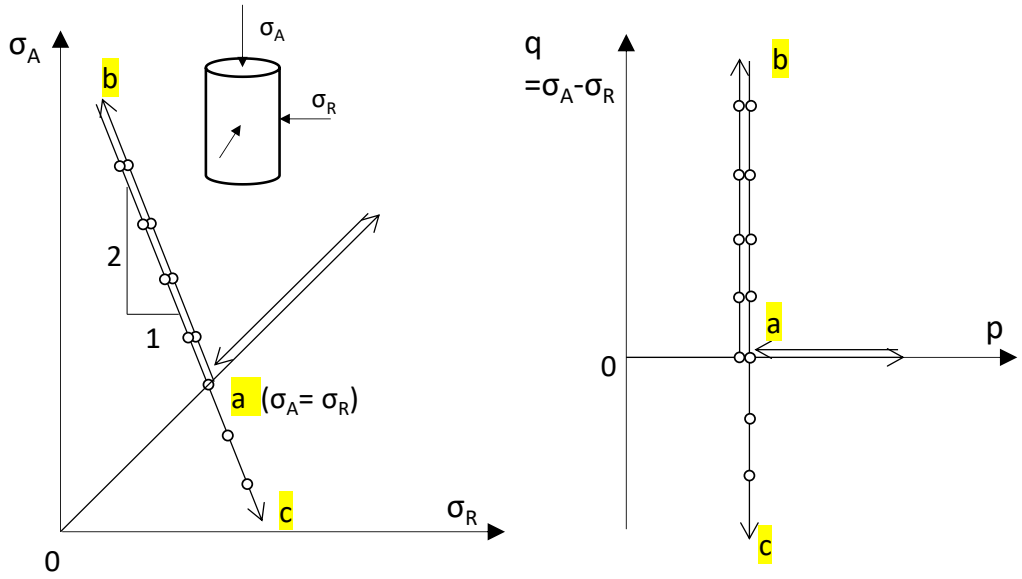

Figure 3-15. Loading path of triaxial tests with ultrasonic surveys performed at multiple stress levels denoted by markers: 1) 0→a: isotropic loading and unloading; 2) a→b: triaxial compression at constant mean stress; 3) b→c: triaxial extension at constant mean stress.

3.3 Test Results

3.3.1 Stress-strain Curves

The stress-strain curves measured in the triaxial test on Opalinus Clay specimen F2 are shown in Figure 3-16. Strength weakening was observed after peak stress at q = 19.5 MPa, and the confining stress was adjusted so that the mean stress could be kept constant at 7 MPa during the rest of the triaxial compression stage.

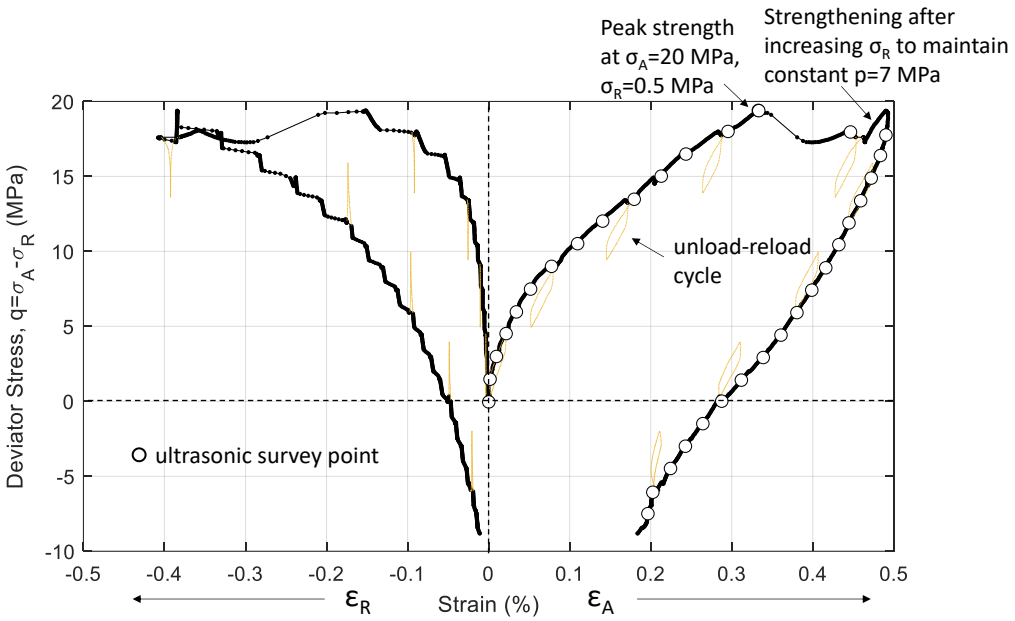

Figure 3-16. Stress-strain curve from triaxial tests on Opalinus Clay specimen F2. Note that unload-reload cycles are not used in the analysis for their poor quality

The effect of specimen saturation on the stress-strain curve during triaxial compression can be seen in Figure 3-17 – higher moisture (i.e., higher water saturation) softens and weakens the specimen response under stress. The same saturation-dependent behavior has been observed by Wild et al. (2014) and Zhang and Laurich (2020). The cohesive and frictional resistance between clay particles is reduced because of the increased thickness of bound water-films after moisture intake.

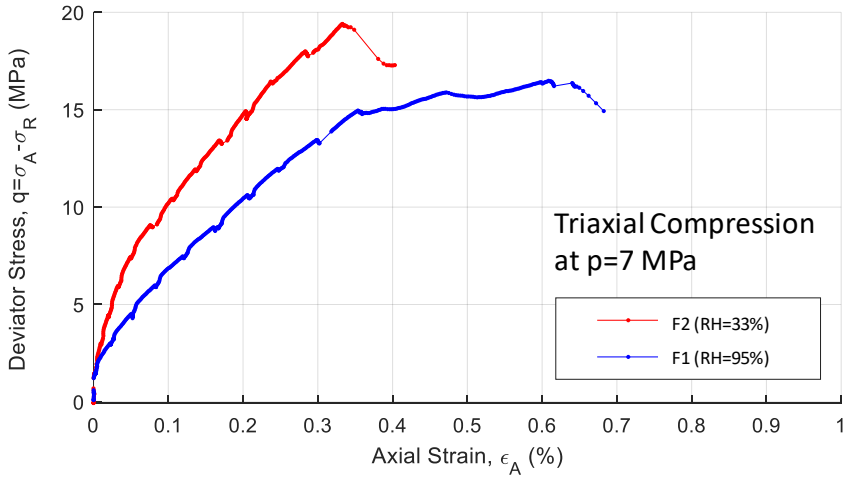

Figure 3-17. Stress-strain curves from triaxial compression on Opalinus Clay specimens preconditioned under different relative humidity

3.3.2 Ultrasonic Wave Velocities

The wave velocity after each stress increment in a triaxial test is determined using,

$$v = \frac{h}{t} \tag{3-10}$$

where h is updated according to the current specimen deformation, i.e., $h = h_0 (1 - \varepsilon_A)$, and P- or S-wave arrival time is identified from the received waveforms as the trough and peak of their first phases, respectively (e.g., Figure 3-18). To accurately pick the points, the function *findpeaks* was employed in MATLAB, and the peak or trough point was determined in the selected phase intervals. The accuracy is also subject to the quality (i.e., the signal-to-noise ratio) of the signal and the resolution of the data. The highest resolution of the oscilloscope used is 80 MHz (i.e., data is acquired every 12.5 ns). Therefore, the worst deviation of the displayed point away from the true local peak/rough is 6.25 ns (consider two symmetrical points surrounding local peak/rough). This is equivalent to about 0.03% error in the wave velocity calculation for a wave traveling through a 60 mm solid in a time period of 20 μs.

The signal quality and the calculated wave velocity at the initial stress state for all six tests are summarized in Table 3-3. Picking a local peak of either P- or S-wave using a consistent wave phase was challenging in the cases with low signal quality (e.g., test E4 in Figure 3-18(a)), and the determination of velocity is considered unreliable. In contrast, for the tests with medium or high signal qualities, the first arrivals of the P-wave and S-wave phases can be clearly identified (Figure 3-18(b)&(c)).

Table 3-3. Summary of the ultrasonic survey for all triaxial tests

Sample #	Quality of the Signal[a]	At the Initial Isotropic Stress State ($q = 0$)			Deviator Stress $\lvert q \rvert$ (MPa) at Damage Initiation[b]	
		$v_{p,0}$ (m/s)	$v_{s,0}$ (m/s)	$E_{dyn,0}$ *(GPa)*	TC	TE
E1	High	2920	1774	19.2	-	4.5
E2	Medium	2995	1646	17.5	12	-
E3	High	2859	1535	14.2	12	3
E4	Low	-	-	-	-	-
F1	Medium	2969	1764	19.3	15	0.5
F2	High	3030	1799	20.0	19.5	7.5

[a.] the criterion is based on the peak amplitude of signal: high: > 0.5V; medium: 0.1 ~ 0.5V; low: < 0.1V.

[b.] TC: triaxial compression; TE: triaxial extension.

For the triaxial test on specimen F2, the variations of calculated P- and S-wave velocities, v_p and v_s, with stress are shown in Figure 3-19, In triaxial compression, v_p exhibits a gradual reduction to the peak deviator stress at about 19.5 MPa, where abrupt reductions are observed for both v_p and v_s. In triaxial extension, the reversal of stress path tends to recover the reduced v_p but only to a limited extent once the stress returns to the initial isotropic state (q = 0). Further velocity reductions were also observed near the end of the triaxial extension stage.

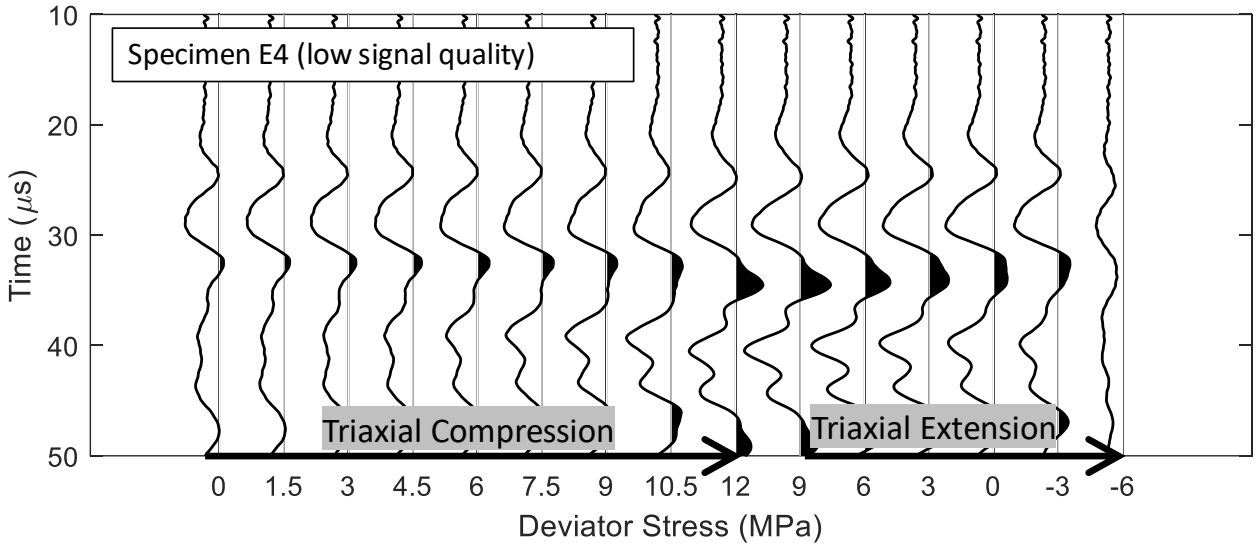

(a)

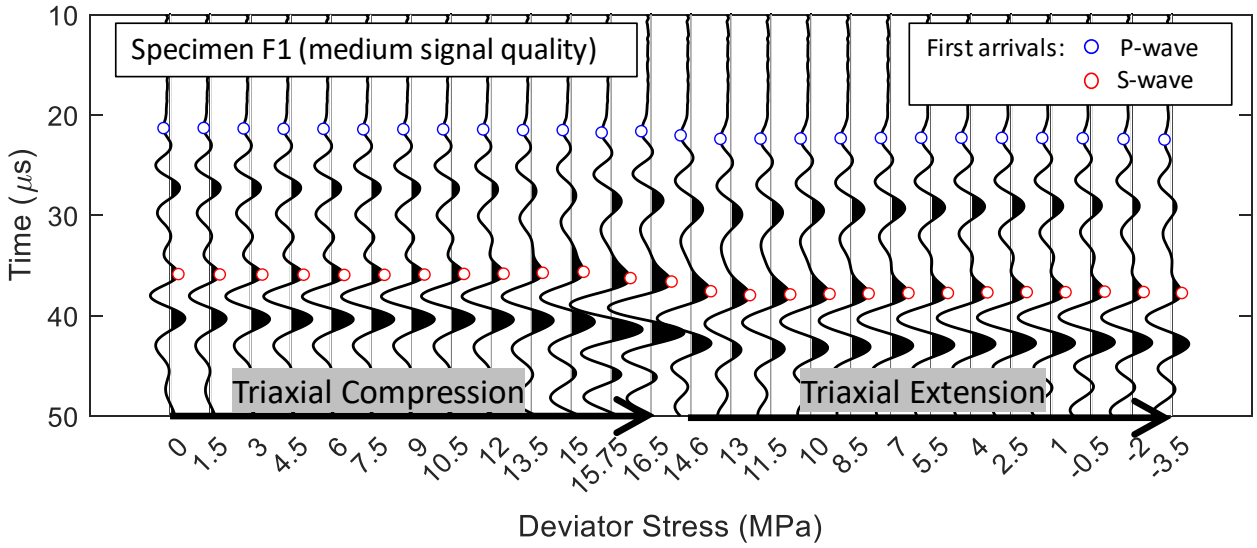

(b)

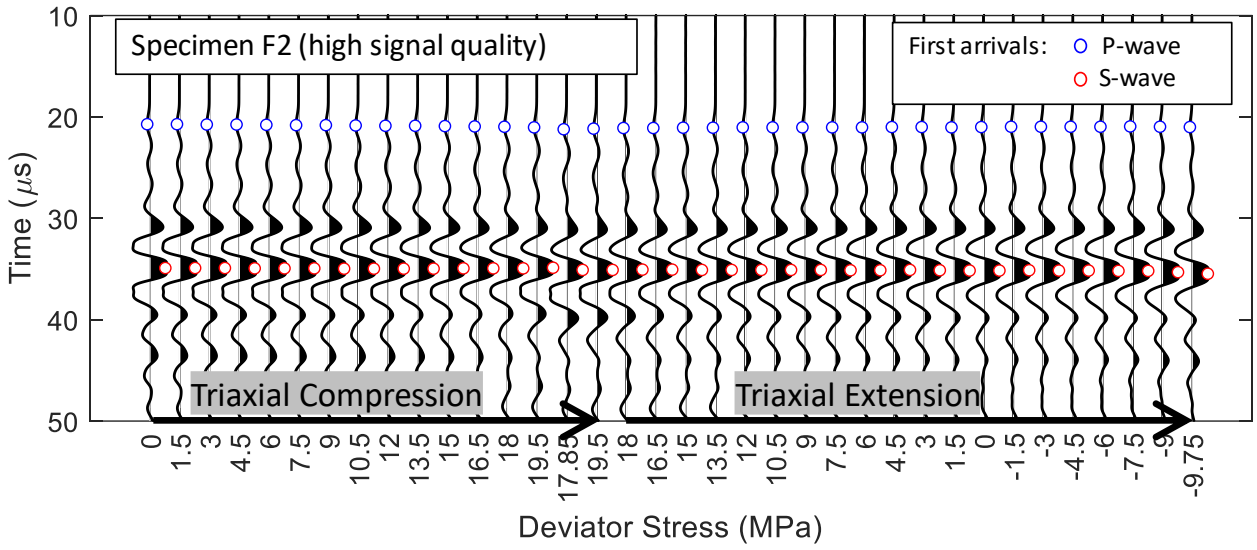

(c)

Figure 3-18. Received waveforms in S-to-S transmission mode for triaxial tests on three Opalinus Clay specimens - (a) E3, (b) F1, and (c) F2. Blue and red circles are the identified P- and S-wave arrivals, respectively. Note that the amplitude of the waveforms in each test is adjusted by a constant factor for better illustration.

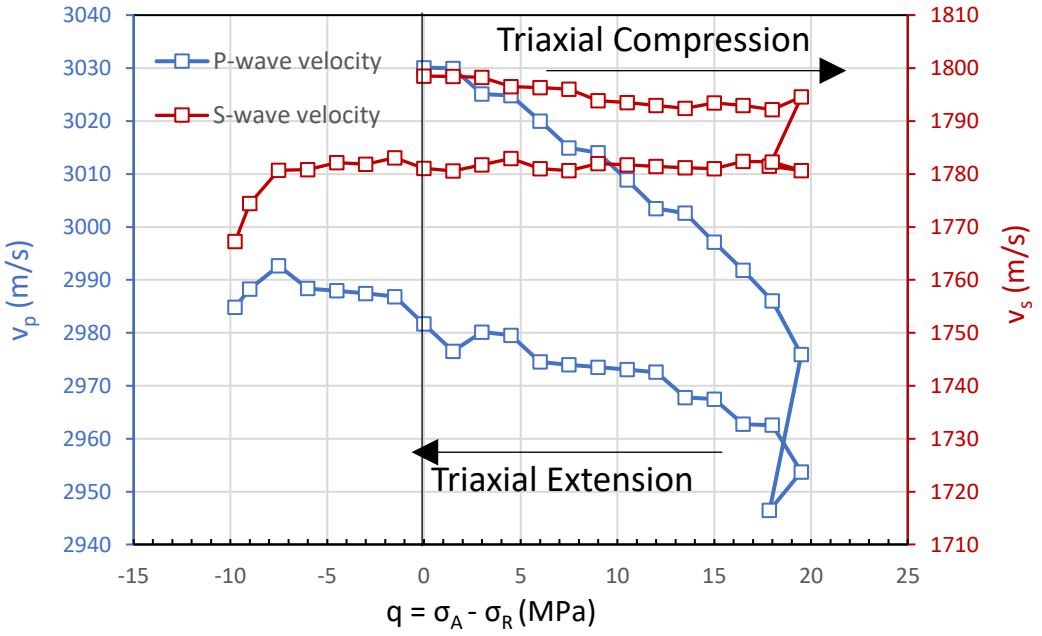

Figure 3-19. Velocity evolutions during the triaxial test on Opalinus Clay specimen F2

3.4 Discussion

3.4.1 Observed Damage on the Opalinus Clay Specimens

The Opalinus Clay specimens are examined before and after tests. Some are selected for micro-CT scanning at the resolution of 8.5μm/voxel using the Skyscan 1172 Scanner from the Earth and Atmospheric Sciences department at the University of Alberta. Despite careful core handling, partially opened interbedded fissures are observed in most Opalinus Clay specimens before tests (e.g., Figure 3-20 (a)). In some specimens, these fissures can be visually identified. The CT-scan image obtained from a part of the specimen closely reveals all the existing fissures (Figure 3-20 (a)). The weak interbedded bondings of Opalinus Clay were suggested in many other laboratory and field investigations (e.g., Corkum and Martin 2007). The intactness of the specimens could hardly be preserved unless a unique protocol (including the use of the oil-based subcoring system, Giger, pers. comm.) was employed. Nevertheless, the prepared specimens in this study still maintained a reasonable degree of integrity and were considered suitable for testing.

Different types of stress-induced fracturing are observed on the Opalinus Clay specimens after triaxial tests (Figure 3-20 (b)). Near one of the existing vertical fissures, the Micro-CT image shows a branch of newly-developed cracks (Figure 3-20 (iii)), and more dominantly, a sub-horizontal fracture (Figure 3-20 (iv)) that cuts through from the specimen surface is observed. These two types of fracturing may be attributed to damage initiated at the two triaxial loading stages, respectively.

For triaxial compression on P-specimen with lower confining pressure (in this case, σ_R = 0.5 MPa at the onset of damage), axial splitting and buckling of bedding are the dominant mechanisms of the failure, and local tensile cracks are developed preferentially parallel to bedding (Lisjak et al. 2014b). As the damaging process during triaxial compression is controlled in this study (with increased confining stress applied to the specimen before a substantial strength softening occurred (e.g., Figure 3-16)), a progressive extensile fracturing response was not triggered. However, the branch of local cracks shows evidence of the initiated damage.

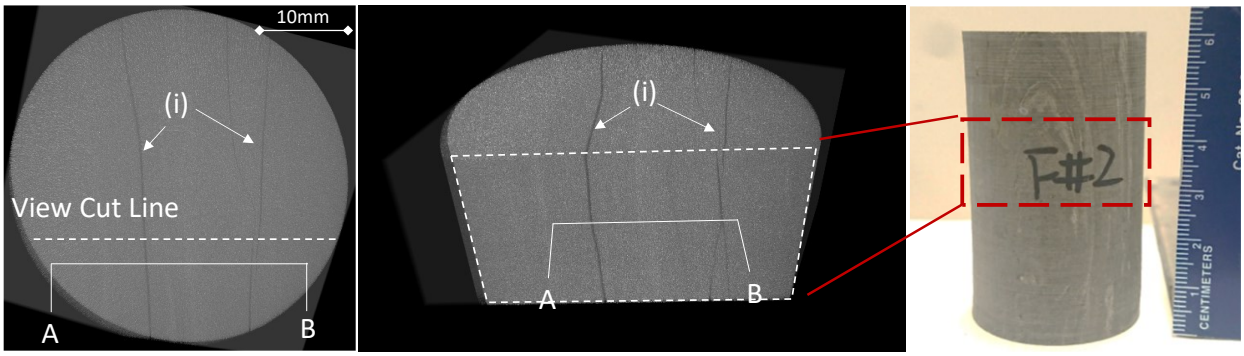

(a) before test

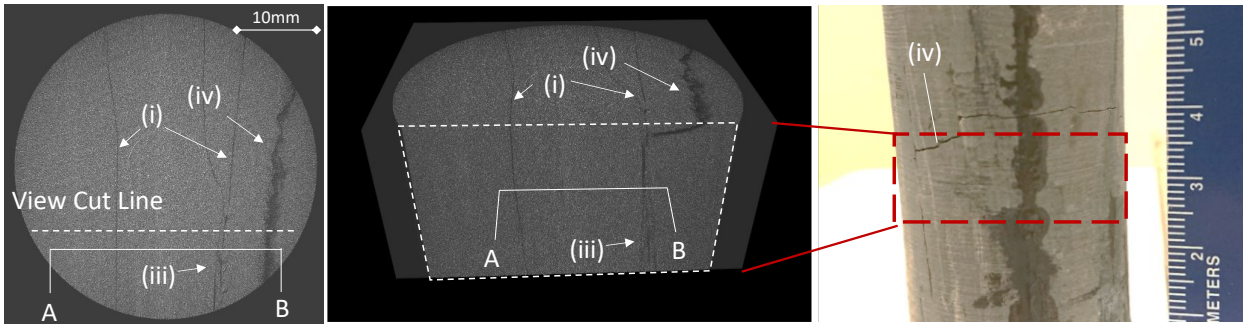

(b) after test

Figure 3-20. Examination of Opalinus Clay specimen F#2 before and after triaxial tests. Some notable features are (i) two major existing vertical fissures (parallel to bedding), (iii) a branch of local cracks near one of the existing vertical fissures (iv) the sub-horizontal fracture terminated at another vertical fissure.

The sub-horizontal fracture was likely induced under the triaxial extension stage when the maximum principal stress was lateral stress. The low fracture angle (with the inclination of fracture from horizontal plane less than 30°) is because of the low axial stress (σ_A = 2 MPa) at the onset of the damage, which agrees with the observations by Zhang and Laurich (2020) from their triaxial extension tests.

3.4.2 Evolutions of the Wave Velocities

In order to assess the velocity evolution along the stress path in different triaxial tests, the changes of v_p and v_s are normalized by the initial velocity values, $v_{p,0}$ and $v_{s,0}$, respectively (Figure 3-21). The stress where the velocity starts to decrease dramatically can be identified for all the tests in Figure 3-21, except E1, where the damage is not likely initiated. The progressive reduction of ultrasonic wave velocity is accompanied by the micro-fracturing process and is considered a useful measure for identifying the onset of damage in Opalinus Clay (Popp and Salzer (2007).

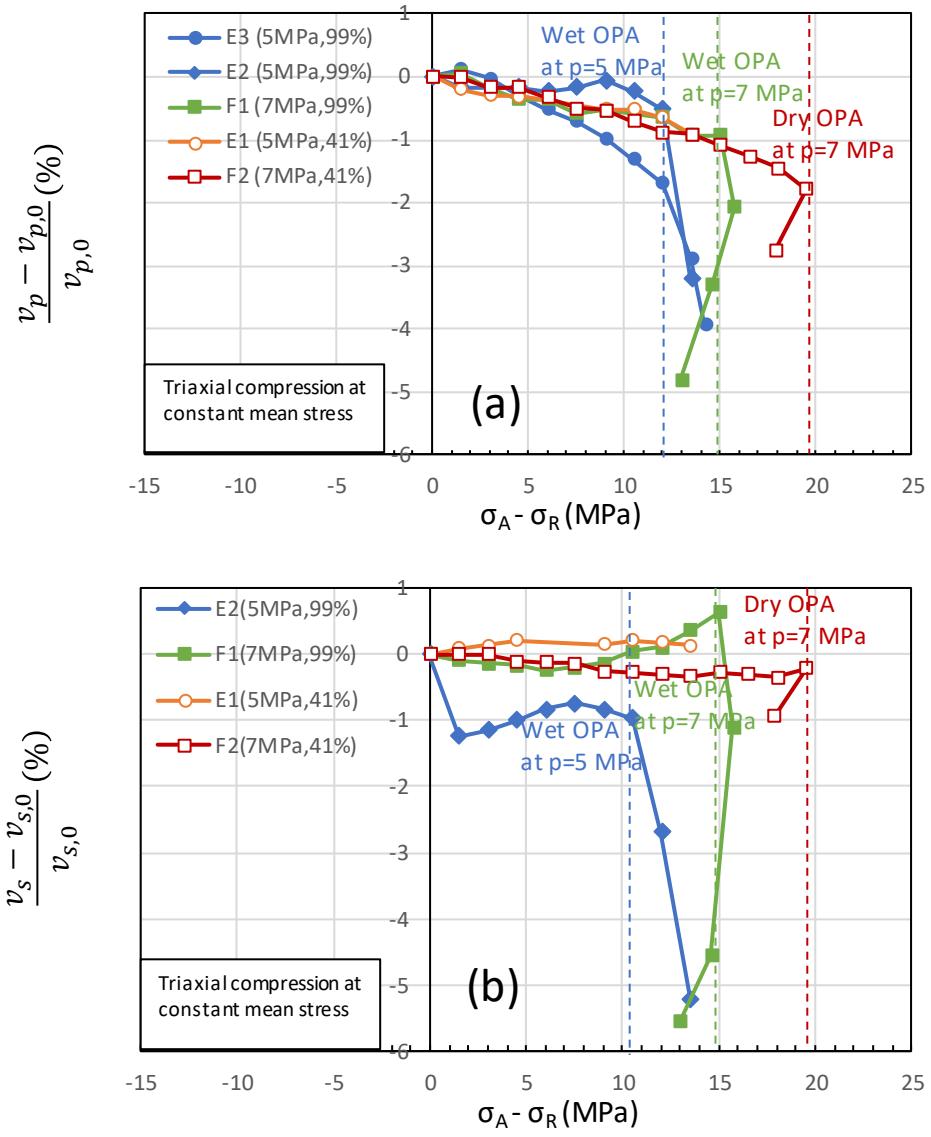

Figure 3-21. Evolutions of the (a) P- and (b) S-wave velocities during triaxial compression for specimens with different mean stresses p and preconditioned moistures. Vertical dash lines mark the stresses where damage by triaxial compression occurred.

During triaxial extension after stress reversal, the measured wave velocity, especially v_p, was gradually recovered (Figure 3-22). However, the recovery at the return of the initial stress state ($\sigma_A = \sigma_R$) was limited for the specimens that were initially damaged, indicating the permanent effect of mechanical damage. Velocity reduction was observed after a further increase of reverse deviator stress (σ_R - σ_A) during triaxial extension (Figure 3-22). The stress where the velocity reduction becomes remarkable is defined as the damage initiation stress σ_D under extension.

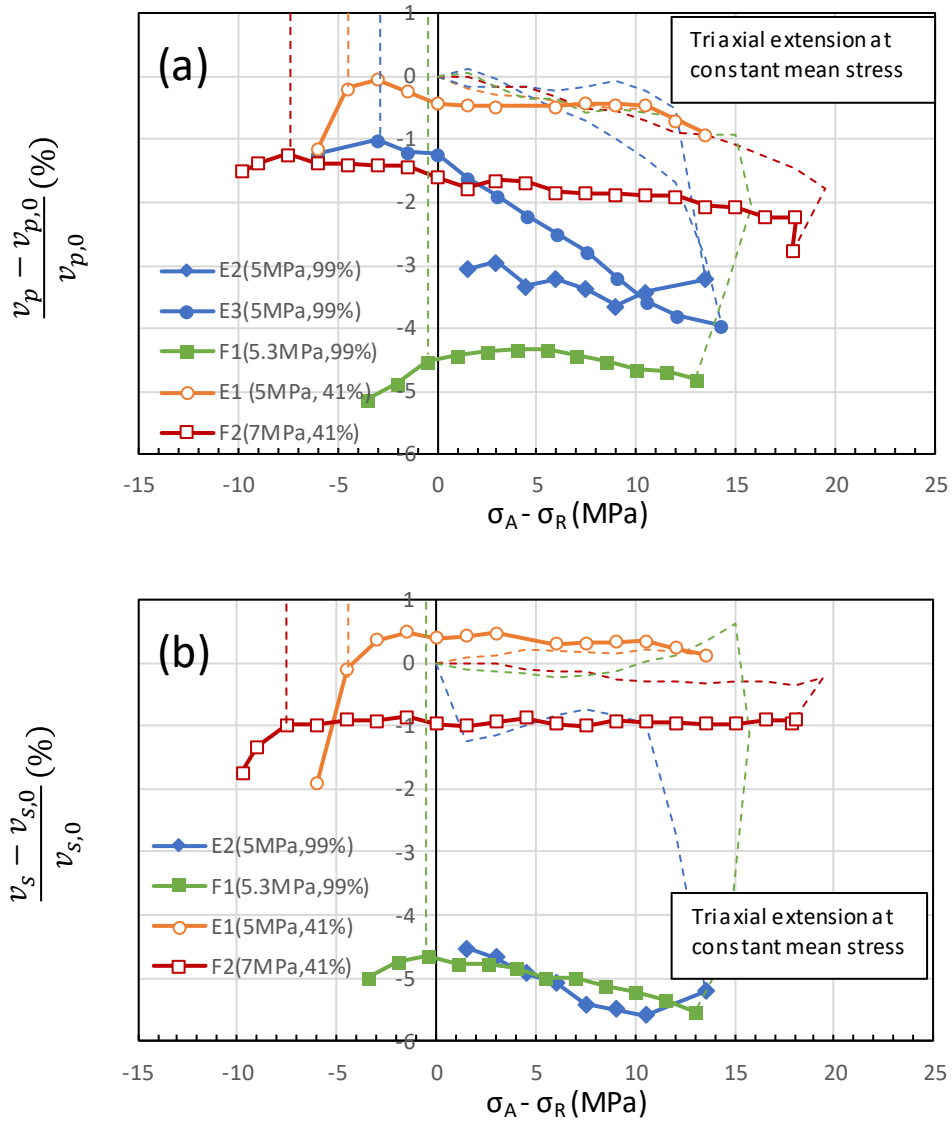

Figure 3-22. Evolutions of the (a) P- and (b) S-wave velocities during triaxial extension for specimens with different mean stresses p and preconditioning relative humidity. Vertical dash lines mark the stresses where damage by triaxial extension occurred. Note that the mean stress reduces to 5.3 MPa (from 7 MPa) in triaxial extension for test F1.

3.4.3 Dynamic Moduli and The Effect of Stress Path

The velocities determined at the initial isotropic stress states are listed in Table 3-3. The dynamic moduli of the Opalinus Clay specimen can be calculated using the following equations,

$$E_{dyn} = \rho \frac{v_s^2 \left(3v_p^2 - 4v_s^2\right)}{v_p^2 - v_s^2} \qquad (3\text{-}11)$$

$$G_{dyn} = \rho v_s^2$$

where a reported value equal to 2.52g/cm^3 (Bossart et al. 2017) is used for the bulk density of ρ. Note that the calculation of Young's modulus E_{dyn} in Eqn. (3-11) is only valid for isotropic rock but provides a good approximation of the E_{dyn} in the loading direction for the rock with transversely isotropic elasticity (Sone and Zoback 2013). The calculation of G_{dyn} in Eqn. (3-11) determines the shear modulus value in the plane of the shear wave polarization. The comparisons between dynamic moduli obtained for specimens preconditioned in different moistures are shown in Figure 3-23. Similar to wave velocities, the modulus values appear to be higher in the group of "dry" specimens than "wet" specimens. Increase of the mean stress also increases the modulus values for the specimens in the same group.

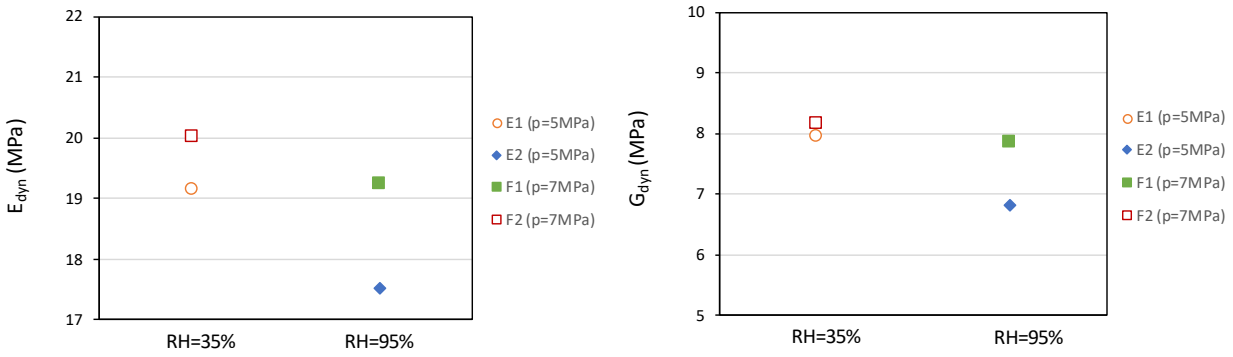

Figure 3-23. Calculated dynamic Young's modulus E and shear modulus G at the initial stress state and bulk density equal to 2.52 g/cm^3.

One aspect of this study is to evaluate the dependence of the elastic moduli on stress. Similar to velocity evolutions presented in Section 3.4.2, the change of the dynamic modulus E_{dyn} with deviator stress is normalized by the initial value $E_{dyn,0}$ (Figure 3-24). With inevitable fluctuations caused by the uncertainty in travel time picking, E_{dyn} is found to be constant or slightly reduced in general with the increase of the deviator stress before the damage. Additional investigations were conducted on the specimens E1 and E2 but under a traditional triaxial compression path (i.e., lateral stress is kept constant). Figure 3-26 shows that E_{dyn} increases with the increase of deviator stress under such stress path before damage initiation. The trend of the increase matches that observed from the triaxial undrained tests on fluid saturated specimens reported in NAB 19-18, regardless of the lithofacies, specimen orientations, and confining stress. In comparison, the dynamic modulus is reduced after peak stress, and the reduction is more abrupt for the tests on dry specimens under low lateral stress, i.e., E1 and E2 from this study.

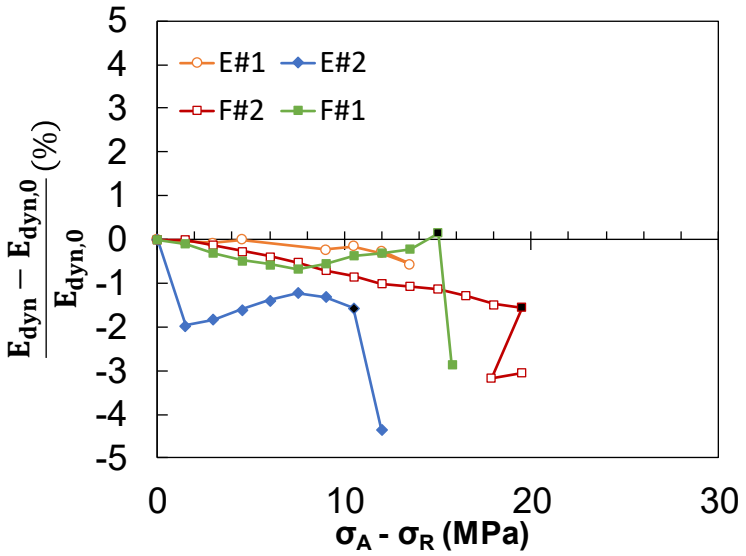

Figure 3-24. Evolution of the dynamic Young's modulus E_{dyn} during triaxial compression under constant mean stress ($\Delta p = 0$). Black dots remark damage initiation.

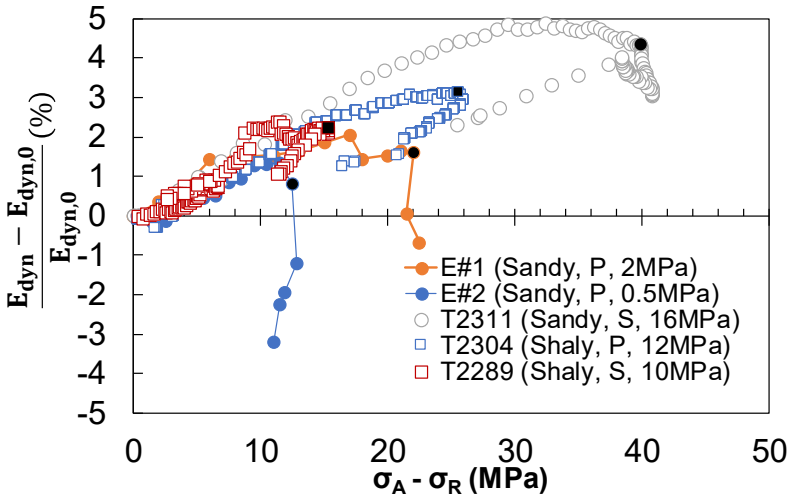

Figure 3-25. Evolution of the dynamic Young's modulus E_{dyn} during triaxial compression under constant lateral stress ($\Delta\sigma_R = 0$). The legend notates – test number (facies, test orientation, and lateral stress (or effective consolidation stress for undrained tests)). Note that tests on dry specimens E1 & E2 were conducted after triaxial tests under constant mean stress. Three tests reported in NAB 19-18 are performed under consolidated undrained conditions. Black dots remark damage initiation.

3.4.4 Comparison with the Evolution of Static Moduli

The evolution of the static moduli of the Opalinus Clay has been investigated by Zhang and Laurich (2020) using unload-reload cycles over small strain along the triaxial compression stress path. The

modulus value obtained at each unload-reload cycle for their tests are normalized to a reference modulus value obtained at σ_A - σ_R = 5 MPa (Figure 3-26). Similar to the trend of the dynamic modulus, the static modulus also exhibits an increase during triaxial compression and drops after damage initiation. However, the magnitude of increase (in percentage) is more substantial in the static modulus than the dynamic modulus, which indicates that the influences of the strain amplitude and/or dispersion might not be consistent at different stress levels. Static modulus evaluation was also attempted in this study with a constant mean stress path, but the unload-reload cycles did not provide reliable results due to the limitation of the testing system, as mentioned earlier. However, the tests with unload-reload measurements under a constant mean stress path were reported by Liu et al.(2019) on another argillaceous claystone, Callovo-Oxfordian claystone. Similar to the dynamic modulus evolution in Figure 3-24, the static modulus shown in their tests also exhibited a slight degradation with deviator stress before the damage (dilation) of the specimen. From a constitutive perspective, the comparison of modulus evolution between the two stress paths indicates that the elastic modulus of the argillaceous claystone may be strongly dependent on the mean stress but can not be described by it alone.

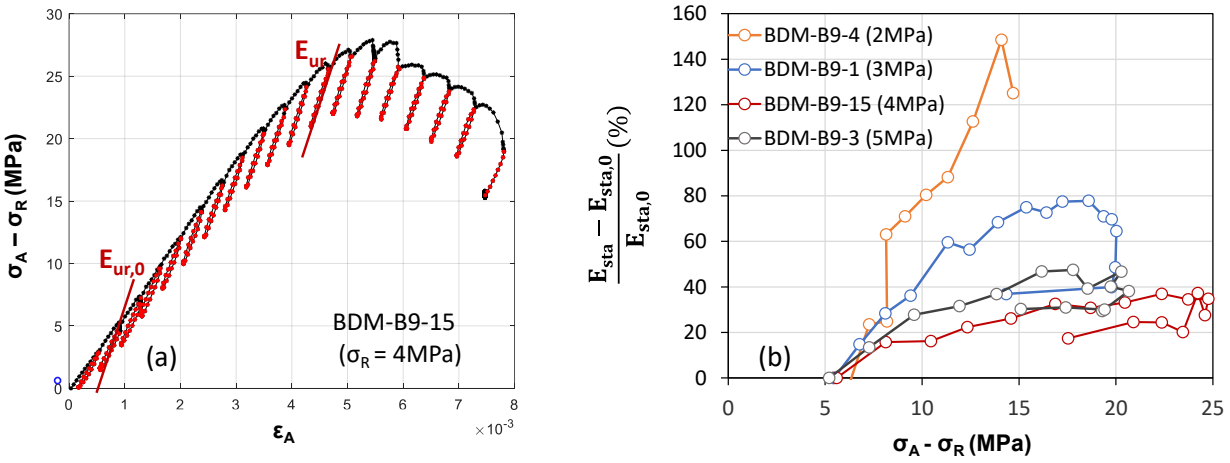

Figure 3-26. (a) Example triaxial test with multiple unload-reload cycles on Opalinus Clay specimens reported by Zhang and Laurich (2020). (b) Evolution of the static Young's modulus evaluated using unload-reload cycles at different deviator stress σ_A - σ_R levels. The reference modulus value $E_{sta,0}$ is obtained at the deviator stress equal to 5 MPa. The legend shows the test number (confining stress).

3.4.5 Damage Initiation Stress

Despite a small number of tests conducted in this study, the assessment of the damage initiation stresses obtained from different tests demonstrates its dependence on both the preconditioning RH and the imposed mean stress. By either increasing mean stress or desaturating the specimen, the damage initiation stress was increased. This is consistent with the observations by Zhang and Laurich (2020), who

performed a large number of tests on sandy Opalinus Clay specimens and associated the damage initiation stress q_D with the specimen's volumetric dilation at varying confining stresses and specimen saturations (Figure 3-27). The damage initiation was also identified in the undrained triaxial tests on Opalinus Clay specimens using the measured pore pressure response (e.g., Minardi et al. 2021). Since the damage-induced specimen dilation tends to reduce the excess pore pressure after initial compression, the stress threshold where the excess pore pressure becomes the maximum can be considered as damage initiation. Figure 3-27 also shows q_D identified using the dynamic modulus evolution (Figure 3-25) from another series of undrained tests reported in NAB 19-18. The damage stress thresholds obtained on unsaturated specimens are above those obtained from undrained tests on saturated specimens. The difference might be caused by the use of the total stress for tests on unsaturated specimens, as the pore pressure is not measured.

For the triaxial extension, the dependence of this damage initiation stress on the mean stress and preconditioning RH is shown in Figure 3-28. q_D has a lower boundary in triaxial extension than triaxial compression, which also agrees with Zhang and Laurich (2020)'s observation. q_D was also identified from two undrained tests under triaxial extension on shaly Opalinus Clay specimens (NAB 19-18) using the measured pore pressure response. Unlike in triaxial compression, the same damage envelope can be used for both unsaturated and saturated Opalinus Clay specimens.

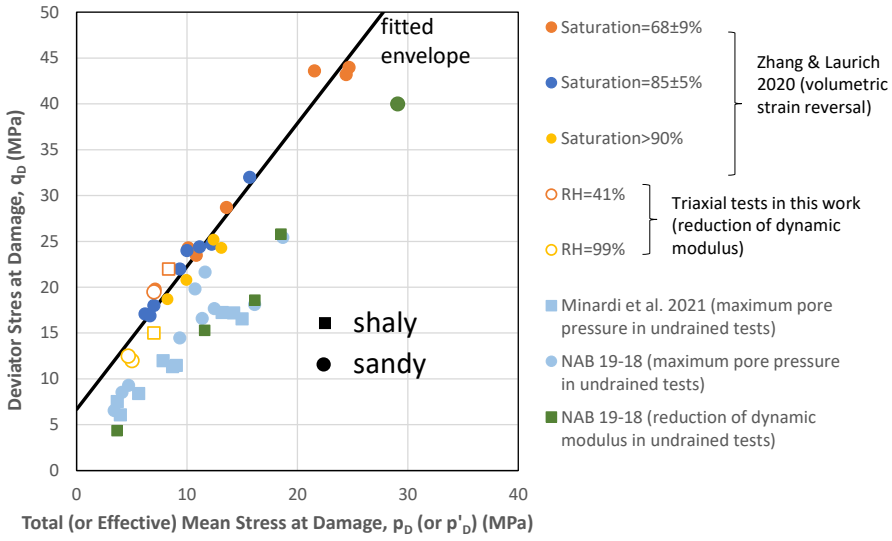

Figure 3-27. Damage initiation stresses identified from different tests on Opalinus Clay specimens under triaxial compression

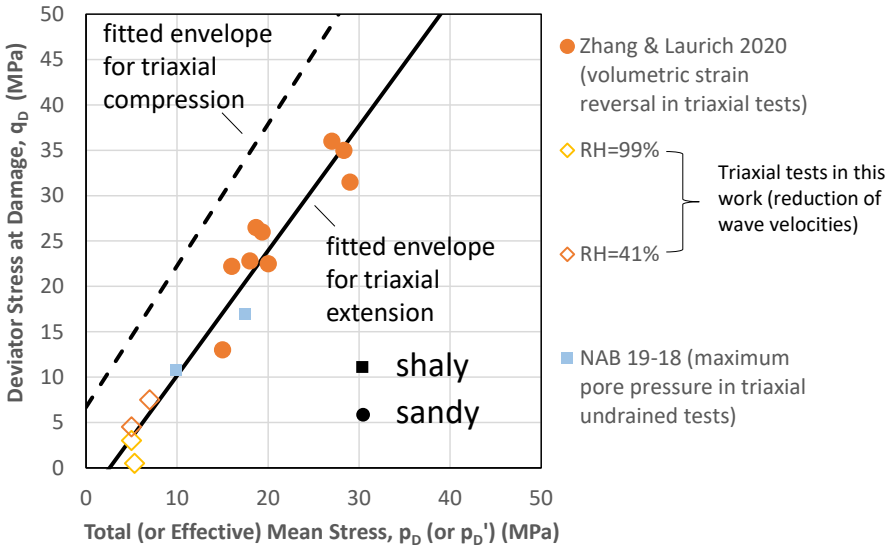

Figure 3-28. Damage initiation stresses identified from different tests on Opalinus Clay specimens under triaxial extension

3.4.6 Interpretation using Stress-dependent Fracture Properties

Due to the weak bonding and fissures preferentially oriented parallel to bedding, the Opalinus Clay specimen can be treated like a rock mass with a set of parallel fractures (Figure 3-29). The total compliance for the general case of an arbitrarily fractured rock mass was given by Schoenberg and Sayers (1995),

$$S_{ijkl} = S_{ijkl,b} + \sum_m S^m_{ijkl,f} \tag{3-12}$$

where two additive components are background compliance tensor $S_{ijkl,b}$ and excess compliance tensor $S^m_{ijkl,f}$ induced by the m^{th} set of fractures. For the rock mass with a single rotationally symmetric fracture set,

$$S_{ijkl,f} = \frac{Z_T}{4}\left(\delta_{ik}n_l n_j + \delta_{jk}n_l n_i + \delta_{il}n_k n_j + \delta_{jl}n_k n_i\right) + \left(Z_N - Z_T\right)n_i n_j n_k n_l \tag{3-13}$$

where Z_T and Z_N are the tangential and normal compliances of fractures, respectively, and they are functions of the stress. Note that the application of Eqns. (3-13) and (3-14) require the rock to be treated as the effective medium, i.e., the wavelength should be long compared to the spacings of the fractures.

For the fracture set whose normal is aligned with axis 1, i.e., **n**=(1,0,0), $s^m_{ijkl,f}$ can be written in the Voigt form,

$$\left[\mathbf{S}_f\right] = \begin{bmatrix} Z_N & & & & & \\ & 0 & & & & \\ & & 0 & & & \\ & & & 0 & & \\ & & & & Z_T & \\ & & & & & Z_T \end{bmatrix} \tag{3-14}$$

If $\mathbf{S}_b$ can be characterized by two isotropic elastic parameters λ_b and μ_b, elastic stiffness tensor **C** can be derived in Voigt form,

$$\begin{aligned} \left[\mathbf{C}\right] &= \left[\mathbf{S}_b + \mathbf{S}_f\right]^{-1} \\ &= \begin{bmatrix} C_{11} & C_{12} & C_{13} & & & \\ C_{21} & C_{22} & C_{23} & & & \\ C_{31} & C_{32} & C_{33} & & & \\ & & & C_{44} & & \\ & & & & C_{55} & \\ & & & & & C_{66} \end{bmatrix} \\ &= \begin{bmatrix} M_b(1-\delta_N) & \lambda_b(1-\delta_N) & \lambda_b(1-\delta_N) & & & \\ \lambda_b(1-\delta_N) & M_b(1-r_b^2\delta_N) & \lambda_b(1-r_b\delta_N) & & & \\ \lambda_b(1-\delta_N) & \lambda_b(1-r_b\delta_N) & M_b(1-r_b^2\delta_N) & & & \\ & & & \mu_b & & \\ & & & & \mu_b(1-\delta_T) & \\ & & & & & \mu_b(1-\delta_T) \end{bmatrix} \end{aligned} \tag{3-15}$$

where $M_b = \lambda_b + 2\mu_b$, $r_b = \lambda_b / M_b$, $\delta_T = \dfrac{Z_T\mu_b}{1+Z_T\mu_b} \in [0,1)$ and $\delta_N = \dfrac{Z_N M_b}{1+Z_N M_b} \in [0,1)$. It can be seen from Eqn. (3-15) that when the shear modulus parallel to the fracture plane (perpendicular to axis 1), i.e., C_{44} is independent of the fracture compliance and equal to the background shear modulus μ_b. Therefore, the velocity of the shear wave polarizing in the same plane (e.g., Figure 3-29) is not affected by the variation of the fracture compliance with the change of the imposed stress. The modulus corresponding to

the P-wave transmission in our case, i.e., C_{33}, is controlled by δ_N. It is equal to M_b when the normal fracture compliance Z_N is zero and approaches zero if Z_N increases to a substantially high magnitude.

A reasonably constant v_s observed during both triaxial compression and extension stages before damage initiation (e.g., Figure 3-19) agrees with the prediction by Eqn. (3-15). The decrease of v_p in triaxial compression can be explained by the opening of the fissures and hence the increase of Z_N when the confining stress σ_R is reduced. In contrast, v_p increases in triaxial extension as fissures close in the increase of σ_R.

By assuming that the rock properties at the initial condition are the background properties, the evolution of Z_N can be quantified, and its relationship with confining stress is derived for both triaxial compression and extension stages using the data from the test on F2 (Figure 3-30). The higher Z_N at the same stress state in triaxial extension than the triaxial compression indicates the increase of the fracture intensity after damage.

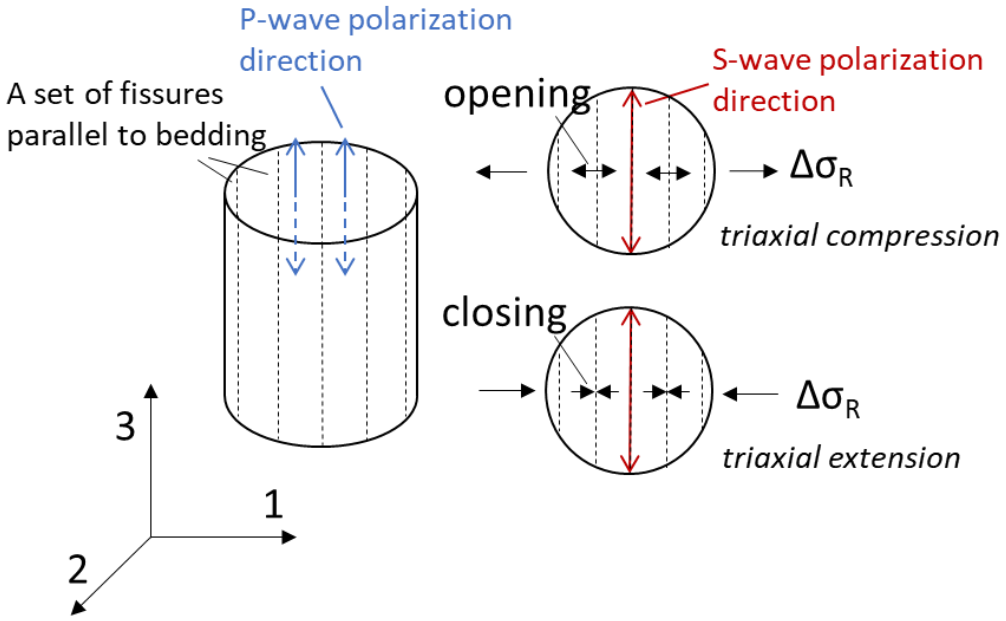

Figure 3-29. Fracture set and structural alterations of Opalinus Clay specimen during triaxial compression and extension before damage initiation

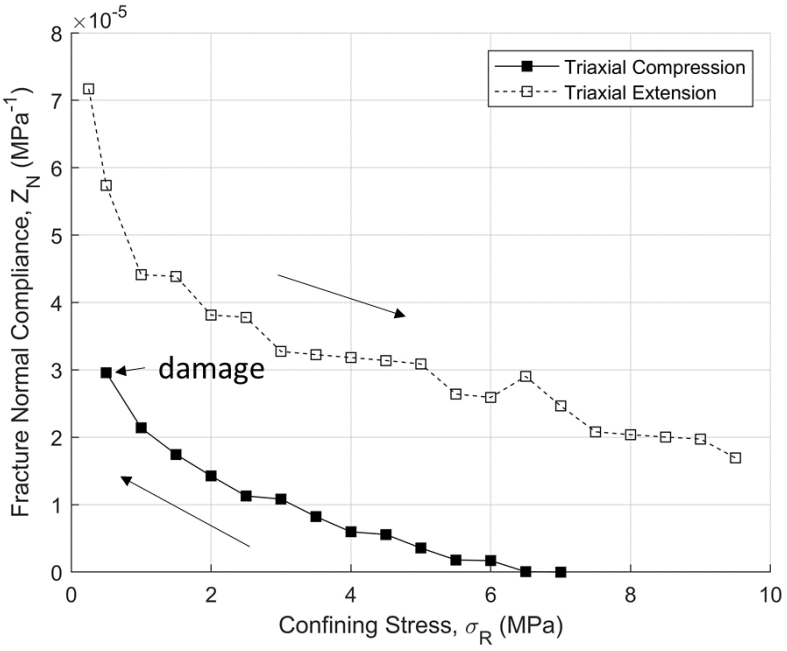

Figure 3-30. Stress-dependent fracture compliance Z_N derived from the evolution of v_p in triaxial tests on specimen F2.

3.5 Summary and Conclusions

To investigate the evolution of the elastic properties along the stress path during borehole unloading and pressuremeter expansion, triaxial tests were conducted on the Opalinus Clay specimens with onboard ultrasonic surveys. The axial loading and ultrasonic wave propagation were both parallel to the bedding of the specimens. A cycle of triaxial compression and extension was applied to each test specimen under constant mean stress conditions.

The wave velocities and dynamic moduli determined at the initial isotropic stress condition are shown to be dependent on the stress magnitude and the preconditioning relative humidity (RH). P-wave velocity v_p generally reduced under triaxial compression and increased under triaxial extension, whereas S-wave velocity v_s stayed nearly constant before damage initiated. Compared to the reported evolution of static modulus during a triaxial loading, the sensitivity of dynamic modulus to stress is not significant for the given stress range. The damage initiation stress was identified at the level where the velocity had a dramatic change and was dependent on both the mean stress and saturation. Two types of damage were identified, respectively, under triaxial compression and triaxial extension, corresponding to different fracturing characteristics observed in the specimen after the test.

The evolution of dynamic modulus under the two different stress paths before damage can be clearly distinguished and can not be simply described as a function of a single stress measure. The dependence of

the P-wave velocity on the lateral stress was shown to be dominated by the macro-structure of the specimen in this study, such as the pre-existing fissures/weak bonding subparallel to bedding. The influence of the fissure compliance under stress can be quantified for both triaxial compression and extension stages using the velocity data based on the effective medium theory. The specimen damage under triaxial compression was demonstrated by the abrupt increase of the normal compliance of the fissures.

Chapter 4

Modeling Static Moduli Evolution Based on Laboratory Measurements with Implications for In-situ Testing[5]

4.1 Introduction

Argillaceous rocks have been given growing interest in recent years because of their potential to be the host geological media for radioactive waste repositories. They exhibit low permeability, minor economic value, and swelling upon moisture intake, which are considered favorable for radioactive waste isolation (Gens 2013). These rocks were often subject to cycles of geological processes, such as sedimentation, consolidation, uplifting, and erosion/weathering, which create complex microstructures. An accurate characterization of the constitutive behavior under different mechanical and environmental conditions, therefore, becomes challenging.

An essential aspect of these constitutive properties is elastic stiffness, and it governs the prediction of ground movements during repository construction and operation. Due to the presence of compliant phases, including pores, microfractures, and organic contents, the elastic stiffness of argillaceous rocks was shown to be nonlinear and stress-dependent (Corkum and Martin 2007; Giger et al. 2018a; Minardi et al. 2021), even though some have processed very low porosity (e.g., Tournemire shale (Niandou et al. 1997)). Therefore the elastic parameters determined from testing must be associated and applied at the stress state or strain amplitude where these parameters were measured (Fjær 2019).

The increase of Young's modulus with confining pressure has been observed from triaxial tests on argillaceous rocks (Niandou et al. 1997; Gautam and Wong 2006; Corkum and Martin 2007; Favero et al. 2018; Giger et al. 2018a). Under an increase of deviatoric stress, the evolution of the elastic stiffness tends to be anisotropic according to the ultrasonic wave velocity measurements on the rock specimens at varying axes (Sayers et al. 1990; Johnson and Rasolofosaon 1996; Dewhurst and Siggins 2006; Siegesmund et al. 2014). The preferential increase of the velocity or elastic modulus in the direction of compression has been recognized as the closure of the pre-existing micro-discontinuities. However, the increase of deviatoric stress towards peak strength initiates additional micro-fractures inside the rock specimens, which were observed from post-loading micrographic images (Hallbauer et al. 1973; Chiarelli et al. 2000) and inferred from recorded acoustic emission events (Scholz 1968; Zang et al. 1996; Amann et al. 2011). These micro-fracturing processes under stress cause the reductions of both modulus (Niandou

[5] A version of this chapter has been published in Rock Mechanics and Rock Engineering; the MATLAB element testing code and Fortran subroutine for finite element implementation developed for this chapter are available at https://github.com/sd104400/OPA_Modeling

et al. 1997; Chiarelli et al. 2003; Heap and Faulkner 2008; Zhang and Laurich 2020) and wave velocity (Sayers 1990; Dewhurst and Siggins 2006; Fjaer 2006; Popp and Salzer 2007). Li and Fjaer (2012) identified the onset of micro-fracturing and explained the evolutions of static and dynamic moduli by modeling uniaxial compression tests.

The stress-induced material degradation is macroscopically depicted as mechanical damage in the framework of continuum mechanics (Chaboche 2003; Lemaitre and Desmorat 2005). To model the constitutive behaviors of argillaceous rocks, the damage has been coupled with other mechanisms in formulations, such as plasticity (Bertrand and Collin 2017; Parisio and Laloui 2017), thermal expansion (Gens et al. 2007), and capillary effect by desaturation (Shao et al. 2006). The decision for which models to use in numerical simulations does not only rely on whether they can explain the physical mechanisms but more often whether the parameters used in the models can be calibrated with available experimental observations. With this consideration, it is attempted to start with a phenomenological model.

In this work, the constitutive behavior of an argillaceous claystone, Opalinus Clay, is studied based on laboratory and field measurements. The evolution of the elastic modulus measured at varying stress levels in multi-staged triaxial tests is examined using three stress-dependent stiffness functions. The stress-induced elastic anisotropy is emphasized in the constitutive modeling. Formulations of damage and plasticity are incorporated to predict stress-strain relations at the pre-peak and post-peak stages. The finite element implementation of the model is used to predict the measured modulus variation from the pressuremeter test at the Mont Terri Rock Laboratory in Switzerland. The effect of the unloading-induced borehole damage on the measured modulus is discussed.

4.2 Material and Laboratory Tests

The Opalinus Clay has a porosity measured by mercury intrusion porosimetry of 5 % to 12 %, with 12-28 % of the visible porosity from microcracks (Houben et al. 2014). Depending on the difference in mineral compositions, Opalinus Clay can be subdivided into three lithofacies – shaly, sandy, and carbonate-rich sandy facies. The mechanical behaviors of the Opalinus Clay specimens were observed to vary from facies to facies (Siegesmund et al. 2014). The difference in mechanical properties was also recognized when loading was applied in different directions with respect to the bedding and on the Opalinus Clay specimens with different saturations (or moisture conditions) (Wild et al. 2014).

A series of triaxial tests by Grasle and Plischke (2011) is used to investigate the mechanical behavior of the Opalinus Clay in both pre- and post-failure stages. The specimens used in their tests were obtained from core samples in the sandy facies of Opalinus Clay from borehole BLT-A2 at the Mont Terri Rock Laboratory. The specimens from this borehole have mineral contents of calcite, quartz, and clay in the

ranges of 12~36%, 34~44%, and 18~23%, respectively. The presence of the coarse cemented carbonates is visible (e.g., Figure 4-1) in the specimens and implies a considerable degree of heterogeneity in its mechanical properties.

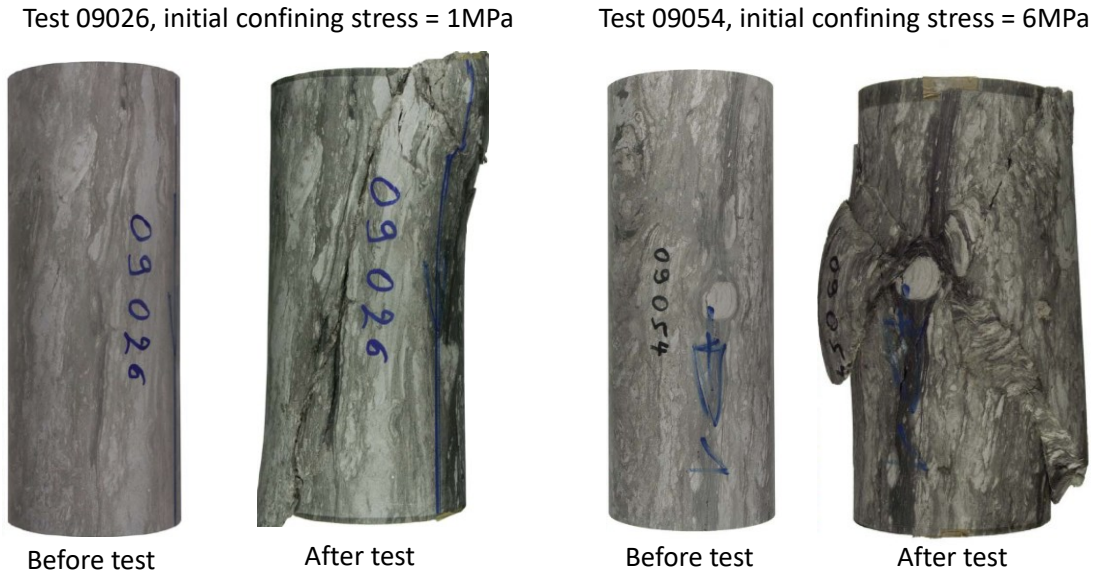

Figure 4-1. Photos of Opalinus Clay specimens before and after multi-staged triaxial tests

After core recovery, the core samples were protected from drying and oxidation by being stored in nitrogen-filled plastic liners. The sample was carefully trimmed into cylindrical specimens with 100mm diameter and 220mm length for triaxial testing. To avoid undesirable friction effects at the contact surfaces of the specimen with end platens and rubber jacket, the specimen was covered with a thin layer of Teflon foil.

Triaxial compression was performed on these specimens with an axial strain rate of 10^{-5}/s under an undrained boundary condition. To be consistent with the loading direction in the pressuremeter tests in boreholes drilled perpendicular to the bedding (Section 4.6), only the specimens with bedding aligned with the axial loading are chosen in this study. Different confining pressure was applied initially on different test specimens to determine the peak shear strength profiles. This has led to the development of the failure planes oriented at different angles with respect to the loading axis, e.g., as shown in Figure 4-1. To evaluate the evolution of the elastic modulus during loading, unload-reload cycles were conducted at multiple axial stress levels before failure. After failure, axial compression continued under adjusted confining pressures at multiple stages, each followed by unloading at the end. As will be seen later, the unloading at the residual strength allows the modulus of a fully damaged specimen to be assessed. In these tests, only the axial deformation was measured, by a set of 3 linear variable displacement

transducers (LVDTs) installed around the specimen at the azimuths of 0°, 120°, and 240°. The averaged axial displacement is used in the calculation of the axial strain. An example test result is shown in Figure 4-2.

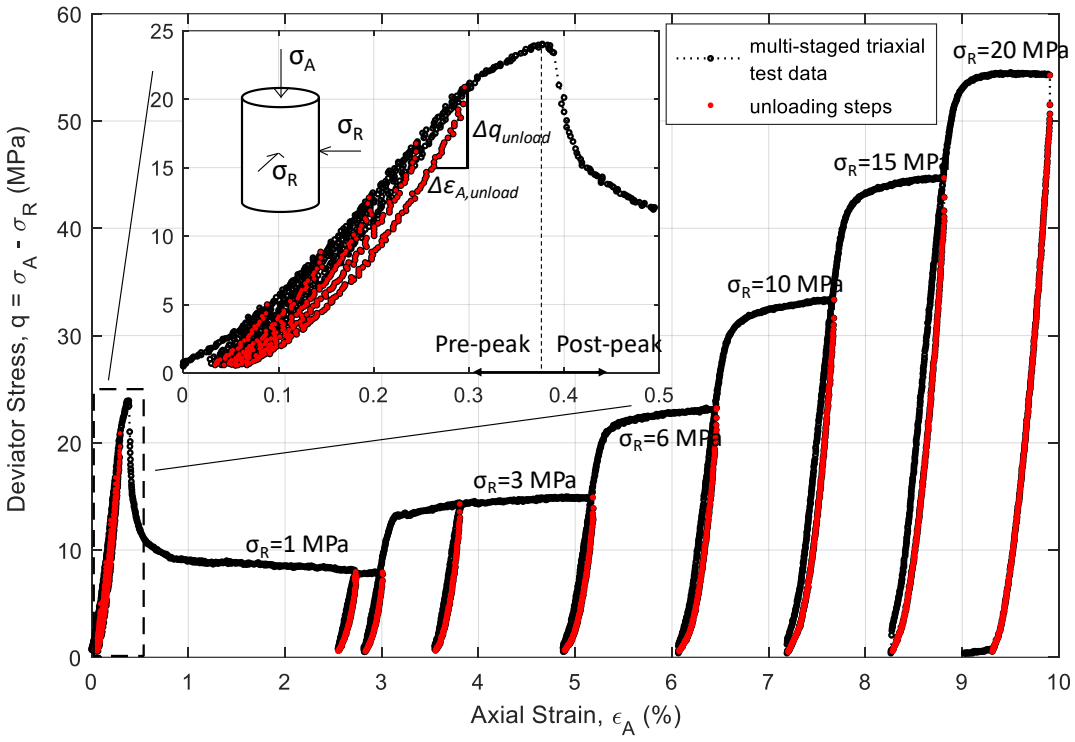

Figure 4-2. Multi-staged triaxial test (Test 09026) on sandy Opalinus Clay with unload-reload cycles in both pre-peak and post-peak stages (Graesle and Plischke 2011)

4.3 Stress-dependent Elastic Modulus

Elastic modulus has been commonly evaluated using secant or tangent lines on the stress-strain curves. However, for weak rocks like Opalinus Clay with unconfined compressive strength (*UCS*) < 25MPa, the stress-strain response of initial loading is strongly dependent on frictional behaviors such as microcrack closure and sliding (Corkum and Martin 2007). Therefore, the true elastic properties of Opalinus Clay can not be properly derived from a monotonic loading curve. By modeling the compression of rock with internal sliding cracks, David et al. (2012) showed that modulus evaluated from the initial part of unloading is less likely affected by these frictional behaviors. The modulus measurement using unload-reload cycles along the triaxial compression loading path showed a significant improvement over the use of stress-strain curve (Plona and Cook 1995) and adopted in many laboratory tests on argillaceous rocks (e.g., Niandou et al. 1997; Chiarelli et al. 2003; Minardi et al. 2018; Zhang and Laurich 2020). Therefore,

the modulus determined from unload-reload cycles, particularly the unloading portion, will be used to assess the relationship of elastic stiffness with stress levels in this study.

The secant Young's modulus is evaluated from the unload data using

$$E_{unload} = \frac{\Delta q_{unload}}{\Delta \varepsilon_{A,unload}} \tag{4-1}$$

where Δq_{unload} and $\Delta \varepsilon_{A,unload}$ are the changes of deviator stress q ($:=\sigma_A-\sigma_R$) and axial strain ε_A in the unload.

Due to the nonlinear response of Opalinus Clay, even at the small strain, E_{unload} reduces with the axial strain amplitude during unloading. The tangent of the unload data taken immediately after stress reversal is suggested in evaluating elastic modulus if the strain measurement (e.g., by strain gauges (Minardi et al. 2018)) is sensitive enough to capture the initial material response. For a measurement system with less sensitivity, for instance, by LVDTs in this case, E_{unload} may be evaluated at a constant strain amplitude so that the effect of stress can be assessed. E_{unload} is evaluated at different strain amplitudes using the unload data, and the dependence of E_{unload} on stress appears to be stable in trend for both pre-peak and post-peak stages when $\Delta\varepsilon_A = 0.1\%$ (Figure 4-3). Therefore, $\Delta\varepsilon_A = 0.1\%$ is chosen in this study, and E_{unload} measured at this strain amplitude is also given in Table 4-1.

Table 4-1. Elastic modulus evaluated at $\Delta\varepsilon_{A,unload} = 0.1\%$ from all unload segments in Test 09026 shown in Figure 4-2

σ_R	*stress measured at the start of unloading*		*Measured* E_{unload}	E_{unload} *predicted by three stress-dependent formulations*		
	p	σ_A		(GPa)		
(MPa)	(MPa)	(MPa)	(GPa)	$E = E^{(1)}\sigma_R^b$ *(Sig3DM)*	$E = E^{(1)} p^{b}$ ** *(PDM)*	$E = E^{(1)}\sigma_A^b$ *(AniDM)*
Pre-peak				$E^{(1)} = 9.8GPa$ * $b = 0.40$	$E^{(1)} = 4.5GPa$ $b = 0.50$	$E^{(1)} = 2.7GPa$ $b = 0.52$
1	2.7	6.0	6.6	9.8	7.4	7.4
1	3.9	9.8	8.3	9.8	8.9	9.2
1	5.3	13.8	10.1	9.8	10.4	10.8
1	6.6	17.8	11.4	9.8	11.6	12.1
1	8.0	21.9	12.8	9.8	12.7	13.4
Post-peak				$E_d = E\left(1-d_{\max}\right)^{1-b}$		
				d_{max}=0.62	d_{max}=0.56	d_{max}=0.50
1	3.7	9.0	5.6	5.5	5.8	6.6
1	3.6	8.9	5.8	5.5	5.7	6.6
3	7.8	17.3	8.9	8.5	8.4	9.0
3	8.0	17.9	9.0	8.5	8.5	9.1
6	13.7	29.2	11.4	11.3	11.1	11.5
10	21.1	43.3	13.9	13.8	13.8	14.0
15	29.9	59.7	17.0	16.2	16.4	16.4
20	38.1	74.3	17.6	18.2	18.5	18.2

*. an average unloading modulus value (E = 9.8 GPa) at the pre-peak stage is used.
**. p is mean stress.

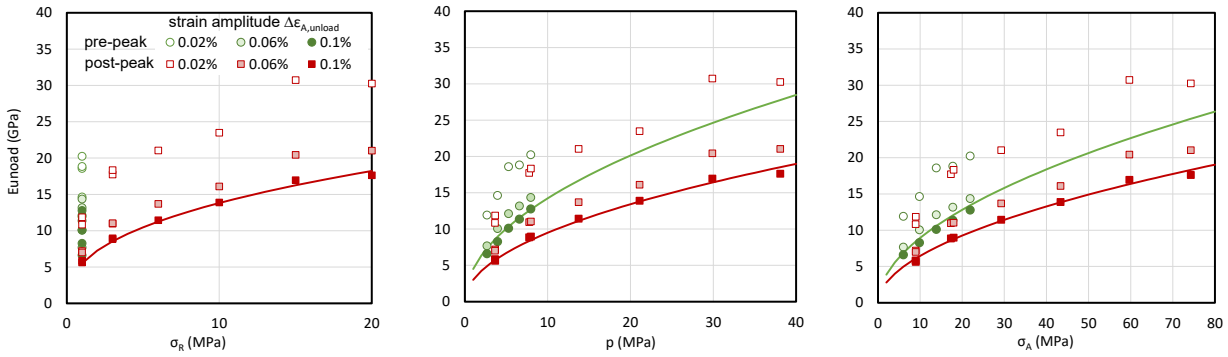

Figure 4-3. Stress dependency of the elastic modulus determined at varying unloading strain amplitudes from Test 09026. Variations of elastic modulus for $\Delta\varepsilon_{A,unload} = 0.1\%$ are fitted using three different stress-dependent functions. Fitting parameters are listed in Table 4-1.

Based on an extensive dataset, Kulhawy (1975) proposed a relationship where Young's modulus is dependent on minimum principal stress σ_3 and referred to as *Sig3DM*

$$E_{unload} = \frac{\Delta q_{unload}}{\Delta \varepsilon_{A,unload}} \tag{4-2}$$

where $E^{(ref)}$ at a reference compressive stress $\sigma_3^{(ref)}$ and σ_3 is equal to the confining pressure σ_R in a triaxial compression test. Eqn. (4-2) was adopted by Favero et al. (2018) to characterize the stress-dependency of Young's modulus of Opalinus Clay. Let $\sigma_3^{(ref)}$ = 1 MPa and $E^{(ref)} = E^{(1)}$, so Eqn. (4-2) becomes

$$E = E^{(1)} \sigma_3^b \tag{4-3}$$

For an isotropic solid with a constant Poisson's ratio, Eqn. (4-3) can be generalized for tensorial representation,

$$\mathbf{C} = \mathbf{C}^{(1)} \sigma_3^b \tag{4-4}$$

where $\mathbf{C}^{(1)}$ is the elastic stiffness of the material when σ_3 = 1 MPa.

It should be noted that *Sig3DM* does not explain the increase E_{unload} at a constant σ_3 (=σ_R) observed at the pre-peak stage (Table 4-1 and Figure 4-3). It was found that the increase of elastic modulus was the result of the preferential micro-fracture closure caused by a uniaxial stress increase (Corkum and Martin 2007; Zhang and Laurich 2020). For this reason, the dependence of the stiffness on mean stress p seems to be more appropriate and referred to as *PDM,*

$$E = E^{(1)} p^b \tag{4-5}$$

or its corresponding tensorial representation:

$$\mathbf{C} = \mathbf{C}^{(1)} p^b \tag{4-6}$$

where $E^{(1)}$ and $\mathbf{C}^{(1)}$ respectively define Young's modulus and stiffness tensor when p is equal to 1 MPa. As will be shown later, the formulation with the mean stress dependency does not predict the nonlinear expansion observed from pressuremeter tests in Opalinus Clay.

The stress-induced elastic stiffness change is shown to be anisotropic under a deviatoric stress increment (Wu and Hudson 1991; Niandou et al. 1997). Micromechanical models were proposed to predict the anisotropic evolution of the stiffness under non-hydrostatic stress (e.g., Mavko et al. 1995; Sayers 1999). The calibration of these models usually requires elastic stiffness/compliance tensor to be adequately characterized along a path of hydrostatic compression from zero to very high pressure on an intact rock specimen. This type of measurement is not usually available in a conventional geotechnical testing

laboratory. In this work, to capture the stress-induced anisotropy as informed from triaxial tests, a phenomenon-based formulation is proposed and referred to as *AniDM,*

$$\mathbf{C} = \mathbf{P} : \mathbf{C}^{(1)} : \mathbf{P} \tag{4-7}$$

where $\mathbf{C}^{(1)}$ is the elastic stiffness of the material under hydrostatic stress equal to 1 MPa, and $\mathbf{P}$ is a 4th-order projection tensor inspired by Ju's (1989) formulation to allow the components of the elastic stiffness tensor to be accounted by the principal stresses. The components of $\mathbf{P}$ are computed,

$$P_{ijkl} = Q^*_{ia} Q^*_{jb} Q_{ka} Q_{lb} \tag{4-8}$$

where $\mathbf{Q}$ and $\mathbf{Q}^*$ are 2nd-order regular and stress-dependent spectral projection tensors, respectively. Both $\mathbf{Q}$ and $\mathbf{Q}^*$ depend on the principal directions $\mathbf{v}_i$ of the stress tensor $\boldsymbol{\sigma}$,

$$\mathbf{Q} = \sum_{i=1}^{3} \mathbf{v}_i \otimes \mathbf{v}_i ; \mathbf{Q}^* = \sum_{i=1}^{3} \alpha_i^{1/4} \mathbf{v}_i \otimes \mathbf{v}_i \tag{4-9}$$

where $\otimes$ is dyadic operator and $\mathbf{Q}^*$ has a term α_i as a function of the associated principal stress σ_i. Eqns. (4-7), (4-8), and (4-9) lead to the stress-dependent stiffness tensor with its components,

$$C_{ijkl} = \left(\alpha_i \alpha_j \alpha_k \alpha_l\right)^{\frac{1}{4}} C^{(1)}_{ijkl} \tag{4-10}$$

In particular, for the case where three principal stresses are coaxial with the material coordinate, $\mathbf{C}$ can be written using Voigt notation:

$$\mathbf{C} = \begin{bmatrix} C^{(1)}_{11}\alpha_1 & C^{(1)}_{12}\sqrt{\alpha_1\alpha_2} & C^{(1)}_{13}\sqrt{\alpha_1\alpha_3} & & & \\ C^{(1)}_{21}\sqrt{\alpha_1\alpha_2} & C^{(1)}_{22}\alpha_2 & C^{(1)}_{23}\sqrt{\alpha_2\alpha_3} & & & \\ C^{(1)}_{31}\sqrt{\alpha_1\alpha_3} & C^{(1)}_{32}\sqrt{\alpha_2\alpha_3} & C^{(1)}_{33}\alpha_3 & & & \\ & & & C^{(1)}_{44}\sqrt{\alpha_2\alpha_3} & & \\ & & & & C^{(1)}_{55}\sqrt{\alpha_1\alpha_3} & \\ & & & & & C^{(1)}_{66}\sqrt{\alpha_1\alpha_2} \end{bmatrix} \tag{4-11}$$

By adopting the power-law function for α_i, i.e., $\alpha_i = \sigma_i^b$, Eqn. (4-10) predicts the same stress-dependent elastic modulus as by Eqns. (4-3) and) under a hydrostatic loading ($\alpha_1 = \alpha_2 = \alpha_3 = p$). The diagonal terms of $\mathbf{C}$ coincide with the formulation of the stress-compliance matrix proposed by Hardin and Blandford (1989) for stress-induced elastic anisotropy in soils. α_i is restricted to be positive, and a lower bound can be set when the stress becomes tensile, for instance, $\alpha_i = 0.01^b$ when $\sigma_i \leq 0$. It should be noted that inherent

anisotropy has been commonly considered to model the elasticity of the Opalinus Clay (Nguyen and Le 2015; Bertrand and Collin 2017; Parisio et al. 2018; Ismael et al. 2019). The current formulation allows the reference stiffness tensor $\mathbf{C}^{(1)}$ to be defined with arbitrary anisotropy. However, as the dependence of the stiffness on the stress path is the primary focus of this work, an isotropic elasticity is assumed for the Opalinus Clay at the reference pressure.

By Eqn. (4-11), an initially isotropic solid becomes transversely isotropic under triaxial stresses. The Young's modulus E_1 in the direction of the axial loading σ_1 (Figure 4-4) is,

$$E_1 = C_{11} - \frac{2C_{13}^2}{C_{33} + C_{23}} = \left(C_{11}^{(1)} - \frac{2C_{13}^{(1)2}}{C_{33}^{(1)} + C_{23}^{(1)}} \right) \alpha_1 = E^{(1)} \sigma_A^b \tag{4-12}$$

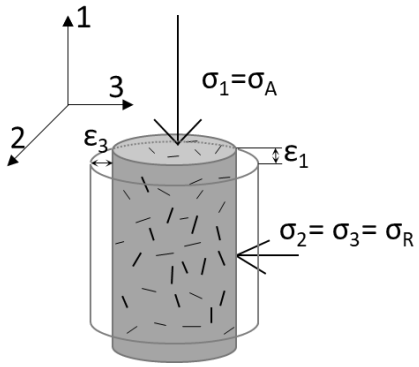

Figure 4-4 Coordinate framework for triaxial test

Eqn. (4-12) allows the stress-dependent parameters $E^{(1)}$ and b to be conveniently calibrated using triaxial test data as only a single stress quantity σ_A is required.

The Poisson's ratio v_{13} defining the strain in the radial direction, ε_3, induced by strain in the axial direction ε_1,

$$v_{13} = \frac{C_{13}}{C_{33} + C_{23}} = \frac{C_{13}^{(1)}}{C_{33}^{(1)} + C_{23}^{(1)}} \sqrt{\frac{\alpha_1}{\alpha_3}} = v^{(1)} \left(\frac{\sigma_A}{\sigma_R} \right)^{\frac{b}{2}} \tag{4-13}$$

where $v^{(1)}$ is the Poisson's ratio when hydrostatic loading is equal to 1 MPa.

4.4 Elastoplastic Damage Model Formulations

4.4.1 Modulus Degradation

E_{unload} obtained at the post-peak stage has a degraded value at a given stress magnitude, compared to that obtained at the pre-peak stage (Table 4-1 and Figure 4-3). In the continuum damage mechanics

framework, stiffness degradation manifests the creation and development of microfractures in a representative elementary volume under homogeneous stress conditions (Chaboche 2003). This leads to an increase in equivalent area for the external stress to act on, which can be represented by a scalar variable d for a uniform micro-fracture growth (Lemaitre and Desmorat 2005). The external stress $\boldsymbol{\sigma}_d$ (or nominal stress tensor) on the damaged solid is then written,

$$\boldsymbol{\sigma}_d = \boldsymbol{\sigma}\left(1-d\right) \tag{4-14}$$

where $\boldsymbol{\sigma}$ denotes the stress acting on the area of undamaged material, or damage effective stress as usually defined in the literature. Under the assumption of strain equivalence, the elastic stiffness is then reduced by the same ratio from the undegraded stiffness $\mathbf{C}$,

$$\mathbf{C}_d = \mathbf{C}\left(1-d\right) \tag{4-15}$$

4.4.2 Damage Criteria

To formulate damage criteria, the energy release rate was often used to characterize the evolution of the damage from the free energy principle (Ju 1989; Halm and Dragon 1996; Shao et al. 2006). Total strain measures were also used to propose the damage criteria so that the model could be directly calibrated with experiment observations (Mazars and Pijaudier-Cabot 1989; Chiarelli et al. 2003). Alternatively, a stress-based criterion could be formulated but would not adequately predict the growth of damage in the presence of significant plastic flows after failure (Ju 1989).

Damage activation was generally associated with the dilation of the argillaceous specimens. The relationship between the microfracture development and the measured dilation (either lateral or volumetric) was confirmed through triaxial tests with AE monitoring (Amann et al. 2011), staged micrographic studies (Hallbauer et al. 1973), or ultrasonic velocity or elastic modulus measurements (Popp and Salzer 2007; Zhang and Laurich 2020). Therefore, in this work, it is assumed that tensile strain (analogous to "mode I" crack opening mechanism) is responsible for the dilation and thus damage evolution. The following damage loading function is considered:

$$f_d = h\left(\boldsymbol{\varepsilon}^-\right) - d \tag{4-16}$$

where $h(\boldsymbol{\varepsilon}^-)$ is a damage hardening function in tensile strain $\boldsymbol{\varepsilon}^-$, which is obtained through a 4$^{\text{th}}$-order projection tensor $\mathbf{P}^-$,

$$\boldsymbol{\varepsilon}^- = \mathbf{P}^- : \boldsymbol{\varepsilon} \tag{4-17}$$

The formulation of $\mathbf{P}^-$ is similar to the projection tensor $\mathbf{P}$ in Eqn. (4-8) but with $\mathbf{Q}^*$ replaced by tensile spectral tensor $\mathbf{Q}^-$,

$$P^-_{ijkl} = Q^-_{ia} Q^-_{jb} Q_{ka} Q_{lb} \tag{4-18}$$

where $\mathbf{Q}^- = \sum_K^3 H\left(\varepsilon_K\right)\left(\mathbf{v}_K \otimes \mathbf{v}_K\right)$, ε_K and $\mathbf{v}_K$ are the K^{th} eigenvalue and eigenvector of strain tensor, respectively, and $H(\,)$ is a Heaviside function. The following function for $h(\boldsymbol{\varepsilon}^-)$ is proposed,

$$h\left(\boldsymbol{\varepsilon}^-\right) = d_{\max}\left(1 - \exp\left(\frac{c_0 - \left\|\boldsymbol{\varepsilon}^-\right\|}{c_1}\right)\right) \tag{4-19}$$

where c_0 and c_1 are two function parameters, respectively defining the strain threshold and the rate of damage growth, and $\left\|\boldsymbol{\varepsilon}^-\right\|$ is the L2-norm of tensile strain. Eqn. (4-19) allows the evolution of damage to be defined with two important characteristics – the initial high micro-fracture growth rate and the convergence to a limit at the large extension. The second characteristic was inferred from the acoustic emission (AE) events recorded by Amann et al (2011) during unconfined compression testing. It showed that damage was fully activated shortly after the peak stress when the micro-fractures coalesced into macro rupture planes. The limit of damage d_{max}, was adopted in the damage formulation proposed by Parisio and Laloui (2017).

To ensure a monotonic evolution of damage, the following conditions of damage rate $\dot{d}$ needs to be satisfied,

$$\begin{cases} \dot{d} = 0 & \text{if } f_d < 0 \text{ or } f_d = 0, \dot{f}_d < 0 \\ \dot{d} > 0 & \text{if } f_d = 0 \text{ and } \dot{f}_d = 0 \end{cases} \tag{4-20}$$

For damaged solids, the recovery of the elastic stiffness under compression is considered a unilateral effect (Mazars et al. 1990; Chaboche 1993; Carol and Willam 1996; Halm and Dragon 1996; Cormery and Welemane 2002; Zhu and Shao 2017). The unilateral effect defines the impact of micro-crack closure along certain axes on the elastic properties at the macro-scale. The formulation of a unilateral condition is commonly established to take into account the deformation of brittle materials that are under cyclic loading and can be defined as a function of either stress or strain. From an earlier version of this work, the stiffness recovery under unilateral compression is explicitly modeled (more details can be found in Appendix VII). A unilateral condition based on the minimum principal stress is favored. However, since the stress-dependent stiffness functions proposed in Section 4.3 essentially depict the same phenomenon,

regardless of the damage state of the solids, the unilateral condition appears to be redundant and is not considered in the current version of the formulation.

4.4.3 Plasticity

Plasticity is formulated in the damage effective stress space $\boldsymbol{\sigma}$, such that plastic flow occurs only in the undamaged material domain. The formulation assumes that the solid part of rock still behaves as a continuous medium after failure, and the possible discontinuous and heterogeneous behaviors of the rupture plane at the macroscale are not represented. As will be seen later, the formulation reduces the nominal strength of a damaged solid. It is also computationally effective because the nominal stress $\boldsymbol{\sigma}_d$ is updated after the computation for plasticity is completed. To demonstrate the formulation, the Drucker-Prager type of failure criterion is considered,

$$f_p = q - Bp - (1-d)\kappa \tag{4-21}$$

where B and κ are two strength parameters associated with the material friction and cohesion. In Eqn. (4-21), the cohesion term is explicitly expressed as a function of the damage variable d. It accounts for the post-peak strain softening mechanism where the shear strength gradually reduces to its residual value as the damage continues to develop (Figure 4-5).

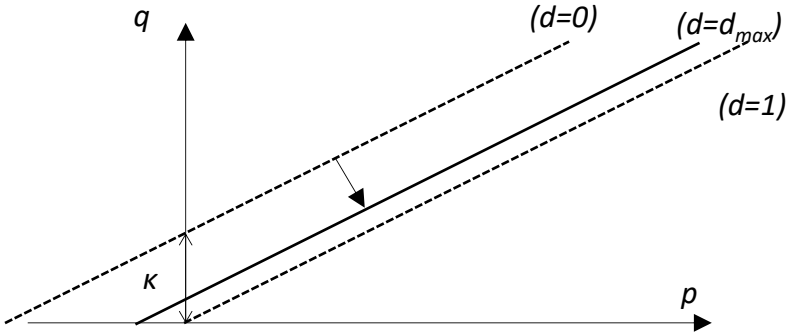

Figure 4-5. Yield function at varying damage state

When shear failure occurs, the total strain rate $\dot{\boldsymbol{\varepsilon}}$ is then decomposed into elastic $\dot{\boldsymbol{\varepsilon}}^e$ and plastic $\dot{\boldsymbol{\varepsilon}}^p$ components,

$$\dot{\boldsymbol{\varepsilon}} = \dot{\boldsymbol{\varepsilon}}^e + \dot{\boldsymbol{\varepsilon}}^p \tag{4-22}$$

Plastic strain rate $\dot{\boldsymbol{\varepsilon}}^p$ is predicted by flow rule associated with the yield function f_p,

$$\dot{\boldsymbol{\varepsilon}}^{p} = \dot{\lambda}\frac{\partial f_p}{\partial \boldsymbol{\sigma}} \tag{4-23}$$

A simplification is made to Eqn. (4-23) so that the plastic flow is independent of damage, i.e., $\frac{\partial f_p}{\partial d}\frac{\partial d}{\partial \boldsymbol{\sigma}} = 0$.

The plasticity multiplier $\dot{\lambda}$ is determined through the consistency condition,

$$\dot{f}_p = \frac{\partial f_p}{\partial \boldsymbol{\sigma}}\dot{\boldsymbol{\sigma}} + \frac{\partial f_p}{\partial d}\dot{d} = 0 \tag{4-24}$$

To distinguish elastic unloading from plastic loading at the yield surface, the Kuhn-Tucker condition is applied,

$$\begin{cases} \dot{\lambda} = 0 & \text{if } f_p < 0 \text{ or } f_p = 0 \text{ and } \dot{f}_p < 0 \\ \dot{\lambda} \geq 0 & \text{if } f_p = 0 \text{ and } \dot{f}_p = 0 \end{cases} \tag{4-25}$$

4.5 Model Integration and Calibration

With the proposed stress-dependent stiffness and plastic-damage formulations, the stress-strain relation can be written,

$$\boldsymbol{\sigma}_d = (1-d)\mathbf{C} : \boldsymbol{\varepsilon}^{e} \tag{4-26}$$

or in its rate form,

$$\dot{\boldsymbol{\sigma}}_d = (1-d)\left(\dot{\mathbf{C}} : \boldsymbol{\varepsilon}^{e} + \mathbf{C} : \dot{\boldsymbol{\varepsilon}}^{e}\right) - \dot{d}\mathbf{C} : \boldsymbol{\varepsilon}^{e} \tag{4-27}$$

The use of the total strain in damage formulation allows the damage and plasticity to be updated sequentially with strain increment. This simplifies the integration procedure while the nature of the coupling between damage and plasticity still holds in an implicit process to solve for prescribed boundary stresses. Since the stiffness tensor **C** depends on the stress tensor **σ**, two treatments can be considered in each increment (e.g., $n+1^{th}$): 1) update $\mathbf{C}_{n+1}$ using $\boldsymbol{\sigma}_n$ from the n^{th} increment, or 2) update $\mathbf{C}_{n+1}$ with $\boldsymbol{\sigma}_{n+1}$ in an iterative procedure in the current increment. The first treatment reduces computational effort significantly but suffers from accumulated numerical errors. Both treatments require small computational steps given the predicted nonlinear material behavior. The algorithm for the incremental integration of the model with the second treatment is specified in Appendix I. To solve for the boundary conditions with prescribed stress (e.g., triaxial test), the Newton-Raphson method is employed.

With Eqns. (4-14) and (4-15), the degraded modulus measured in triaxial tests can explicitly be determined,

$$E_d = E^{(1)}\sigma^b\left(1-d\right) = E^{(1)}\sigma_d^b\left(1-d\right)^{1-b} \tag{4-28}$$

where generic term σ refers to $\sigma_R, p,$ and σ_A when one of the three stress-dependent modulus functions (*Sig3DM*, *PDM,* and *AniDM,* respectively) is used to calibrate the variations of Young's modulus. An example of the calibration was already given for Test 09026 in Table 4-1 and Figure 4-3. For the post-peak stage, all the unloading modulus was obtained on a specimen at residual strength, so the limit of damage d_{max} is used in Eqn. (4-28). Figure 4-6 shows the variations of elastic modulus fit by Eqn. (4-28) using *AniDM* (Eqn. (4-13)) for all three tests considered in this work. The calibrated values for $E^{(1)}$ and b vary from test to test, but the variations (2.1 ~ 2.7 GPa and 0.50 ~ 0.58 respectively) are not significant and may be due to the local lithological heterogeneity of the test specimens.

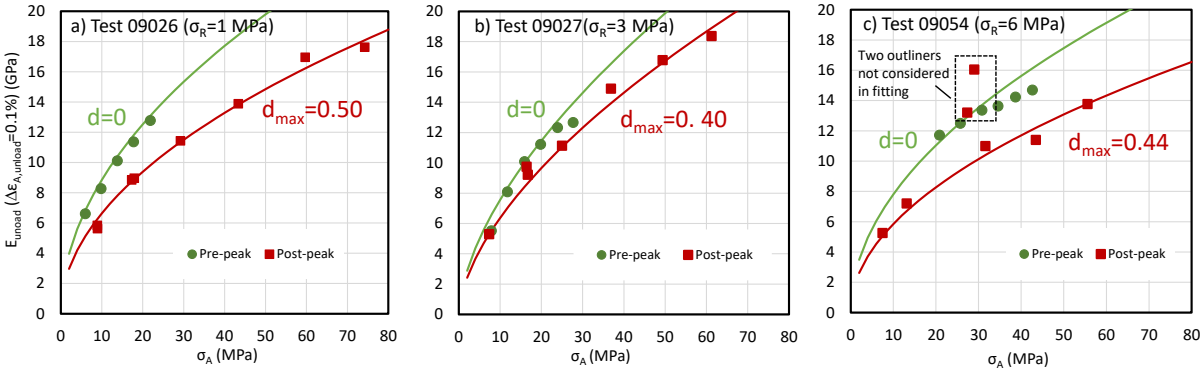

Figure 4-6. Measured stress dependency of elastic modulus (markers) versus the predictions (dash lines) using Eqn. (4-28) with parameters assigned for three multi-stage triaxial tests – a) $E^{(1)}$=2.7 GPa, b=0.52, b) $E^{(1)}$=2.1 GPa, b=0.58 and c) $E^{(1)}$=2.5 GPa, b=0.50.

The constitutive relations predicted by the proposed elastoplastic damage model for a triaxial compression test are demonstrated in Figure 4-7. The onset of the damage may be recognized by the predicted deflection from the elastic phase of deformation. The corresponding axial strain ε_{di} is derived using the condition $c_0 - \left\|\boldsymbol{\varepsilon}^-\right\| = 0$ (Eqn. (4-19)). As shown in Figure 4-7, the net tensile strain $\left\|\boldsymbol{\varepsilon}^-\right\|$ is the difference of the compressive strain induced in isotropic compression from the lateral tensile strain occurring during subsequent triaxial shearing. Thus, ε_{di} can be written,

$$\varepsilon_{di} = \frac{1}{\nu}\left[\frac{\sqrt{2}}{2}c_0 + \left(1-2\nu^{(1)}\right)\frac{\sigma_R^{1-b}}{E^{(1)}}\right] \tag{4-29}$$

where v is equal to v_{13} in Eqn. (4-13) for the transverse isotropy induced by stress according to *AniDM*. c_0 is then determined by Eqn. (29) once the damage initiation strain ε_{di} is identified from the data. Determining c_1 in Eqn. (4-19) is not straightforward as it relates to the transition from the damage initiation to a complete damage state after specimen failure. Without independent characterization of damage growth, such as AE monitoring, a trial-and-error procedure may be required, along with the calibration of strength parameters. The nominal peak stress q_d is predicted from Eqns. (4-14) and (4-21),

$$q_d = Bp_d - \left(1-d\right)^2 \kappa \tag{4-30}$$

To calibrate parameters B and κ from test data, d at the peak stress is also required according to Eqn. (4-30). This d value is dependent on the confining stress σ_R in two ways in this formulation – 1) the damage is initiated later and therefore less developed at the peak stress under higher σ_R according to Eqn. (4-29), and 2) higher σ_R also tends to extend the pre-peak growth of damage because of the higher peak stress p_d. Due to this ambiguity, different d values at the peak stress were tried in the calibration of B and κ. It shows in Figure 4-8 that the failure envelopes with three sets of B and d can all reasonably match the measured peak strengths. The failure envelopes are compared with those calibrated for other reported triaxial tests on Opalinus Clay specimens in Figure 4-8. The test conditions for these tests are summarized in Table 4-2. It should be noted that only the tests with reported total stress conditions are considered here, and tests on specimens with different orientations are not distinguished because it only introduces minor discrepancy (Favero et al. 2018; Wild and Amann 2018b; Minardi et al. 2021). The comparison reveals the significant impacts of the specimen saturation, the confining stress magnitude, and the shear modes on the calibrated peak strength profiles.

The residual strength can be predicted using the same sets of strength parameters and the damage limit d_{max}, which is approximately equal to 0.5 as estimated by comparing the elastic moduli between intact and sheared specimens (Figure 4-6). Measured residual strengths from three tests can be well fitted using different values for parameter B (Figure 4-9). B represents the frictional component of the shear strength, and its variation from test to test may be explained by different orientations of the failure planes (Figure 4-1).

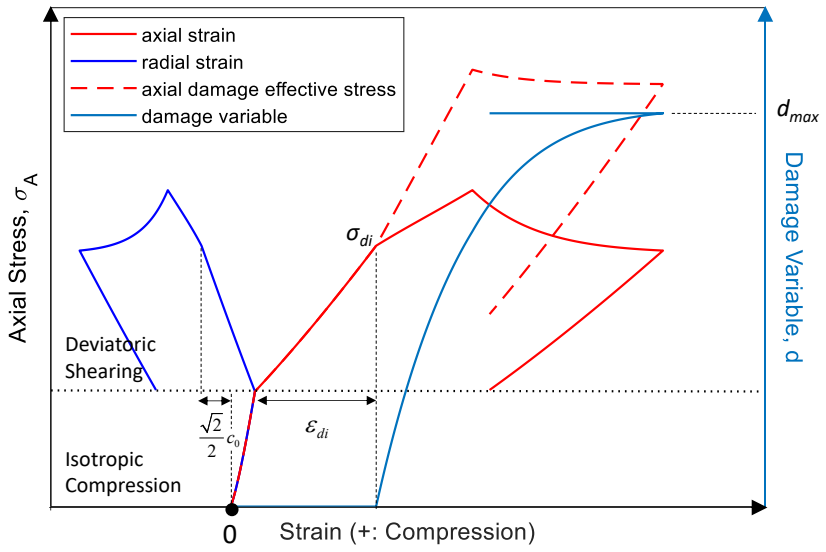

Figure 4-7. Triaxial stress-strain curve predicted using the proposed elastoplastic damage formulation

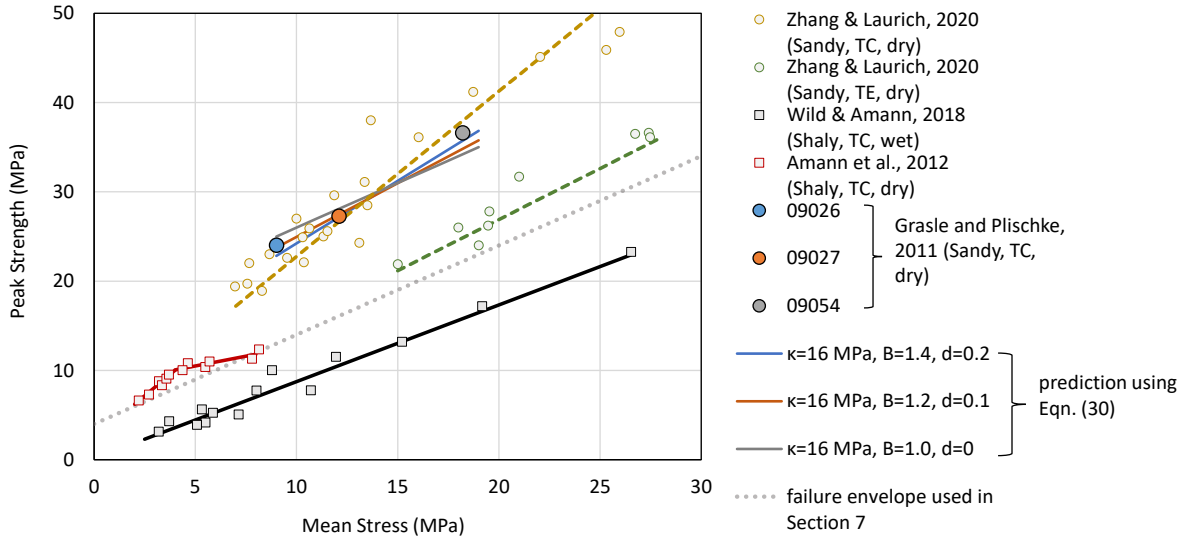

Figure 4-8. Failure envelopes fitted on the measured peak shear strengths, compared with those obtained for Opalinus Clay specimens in different facies (shaly/sandy) and tested under different shear modes (triaxial compression (TC)/ triaxial extension (TE)).

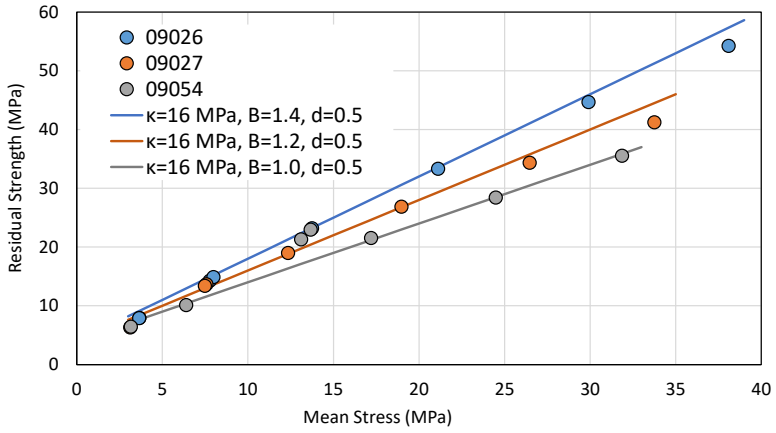

Figure 4-9. Failure envelopes fitted on the measured residual shear strengths

Table 4-2. Summary of the strength parameters calibrated from the reported triaxial tests on Opalinus Clay specimens under varying conditions

References	Facies	Specimen Condition	σ_R	Shear Mode*	κ	B
Zhang and Laurich (2020)	Sandy	Water-vapor wetted to varying saturations	0.5 ~ 10 MPa	TC	4.3	1.9
			1 ~ 3.4 MPa	TE	2.6	1.1
Amann et al. (2012)	Shaly	Not pretreated	0 ~ 0.5 MPa	TC	2.4	1.9
			0.5 ~ 4 MPa	TC	8.3	0.4
Wild and Amann (2018)	Shaly	Pore fluid saturated under undrained condition	1.6 ~ 18 MPa	TC	0.1	0.9
*. TC: triaxial compression ($\Delta\sigma_R = 0$, $\Delta\sigma_A > 0$); TC: triaxial extension ($\Delta\sigma_R > 0$, $\Delta\sigma_A = 0$).						

With eight calibrated (Table 4-3), the multi-staged triaxial test can be predicted with satisfying agreement (Figure 4-10). The current model can not predict the dependence of modulus with strain amplitude as shown in Figure 4-3. Therefore, as opposed to 2.1 ~ 2.7 GPa calibrated for $\Delta\varepsilon_A = 0.1\%$ from three tests, $E^{(1)}$ is adapted to a smaller value (0.8 ~ 1.2 GPa) to predict the larger deformation ($\Delta\varepsilon_A > 0.2\%$) in both loading and unloading.

Table 4-3. Calibrated model parameter values for Opalinus Clay specimen

$E^{(1)}$	$v^{(1)}$	b	B	κ	d_{max}	c_0	c_1
(GPa)				(MPa)			
0.8 ~ 1.2	0.2	0.5	1.0 ~ 1.4	16	0.5	0.001	0.0015

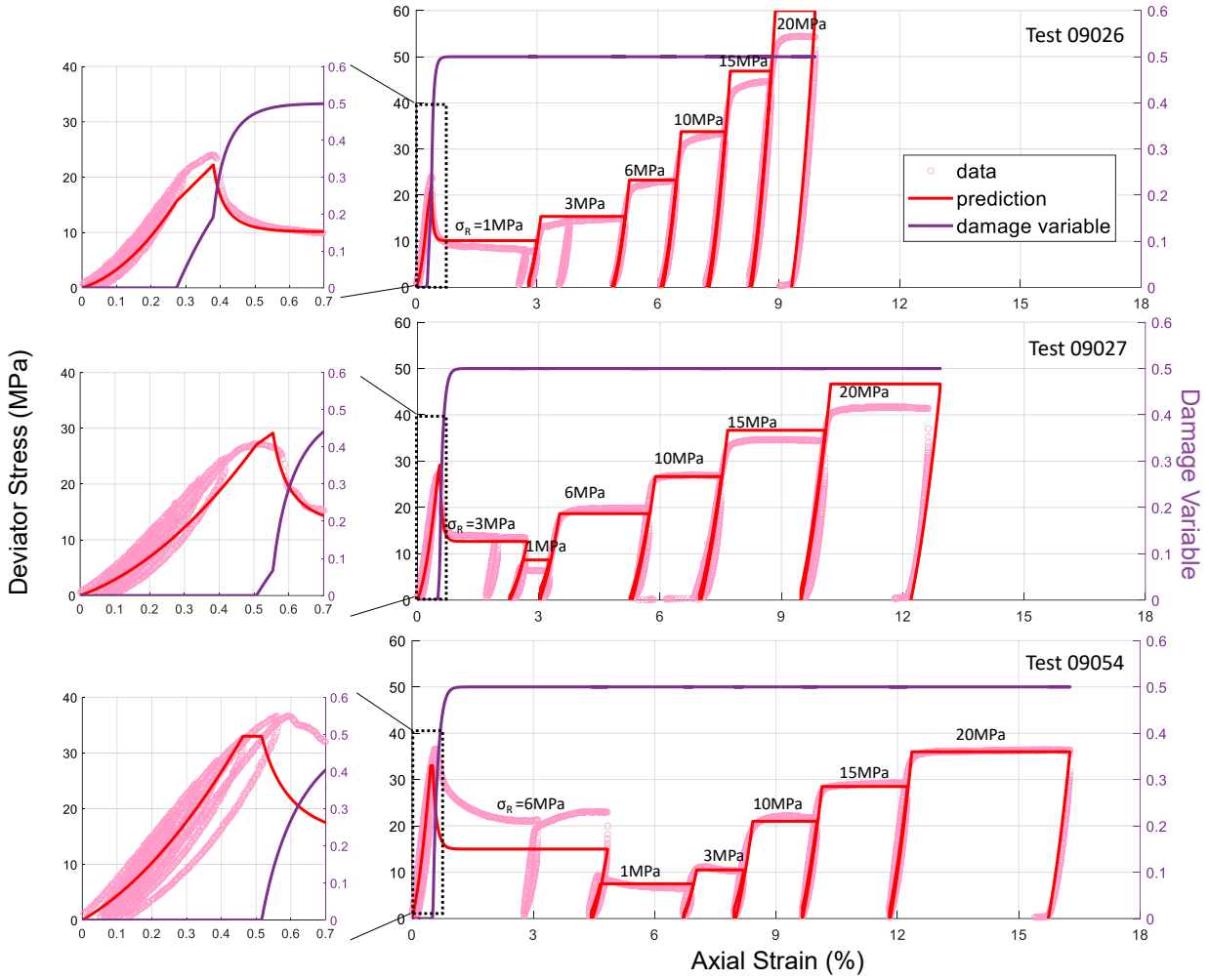

Figure 4-10. Prediction of the stress-strain curve for multi-staged triaxial test using elastoplastic damage model with *AniDM*. Model parameters are given in Table 4-3 with different $E^{(1)}$ and B used for three tests: $E^{(1)}$ =1.2 GPa, 0.8 GPa and 0.9 GPa, and B=1.4, 1.2 and 1.0 for Tests 09026, 09027 and 09054, respectively.

The damage initiation has been commonly associated with the dilatancy of the Opalinus Clay specimens (Popp and Salzer 2007; Amann et al. 2011, 2012; Wild and Amann 2018b; Zhang and Laurich 2020). Due to the absence of the radial strain measurement in the tests from this study, the specimen dilation could not be directly identified. Zhang and Laurich (2020) reported the stresses at the dilatancy threshold from their triaxial tests on the sandy Opalinus Clay specimens under similar testing conditions (Figure 4-11). The damage initiation stress predicted using the proposed strain-based damage criterion with the calibrated model parameters reasonably agrees with Zhang and Laurich (2020)'s measurements. Furthermore, the difference in the damage initiation stresses between triaxial compression (TC) and extension (TE) modes has also been well captured by the prediction.

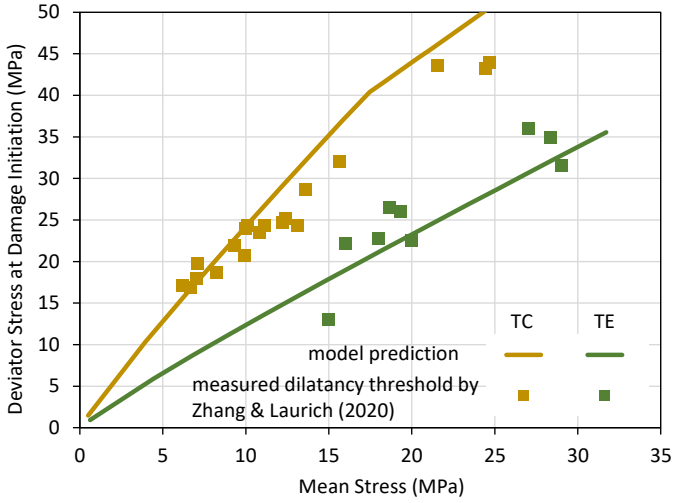

Figure 4-11. Comparison of the measured dilatancy thresholds reported by Zhang and Laurich (2020) and the predicted damage initiation stress using the proposed formulation with parameters given in Table 4-3. TC: triaxial compression; TE: triaxial shearing.

The evolutions of elastic parameters along the predicted stress-strain curve can be evaluated based on Eqns. (4-12) and (4-13). They are compared with measurements from triaxial tests reported by Zhang and Laurich (2020) in Figure 4-12. These measurements were conducted using unload-reload cycles from the start of uniaxial compression to an extended strain after failure, each with limited axial stress change (≤6 MPa). The radial strain measurement in their tests allowed the evolution of Poisson's ratio to be determined. The prediction based on the proposed constitutive model has well captured the observed evolution of these elastic parameters at different test stages (Figure 4-12).

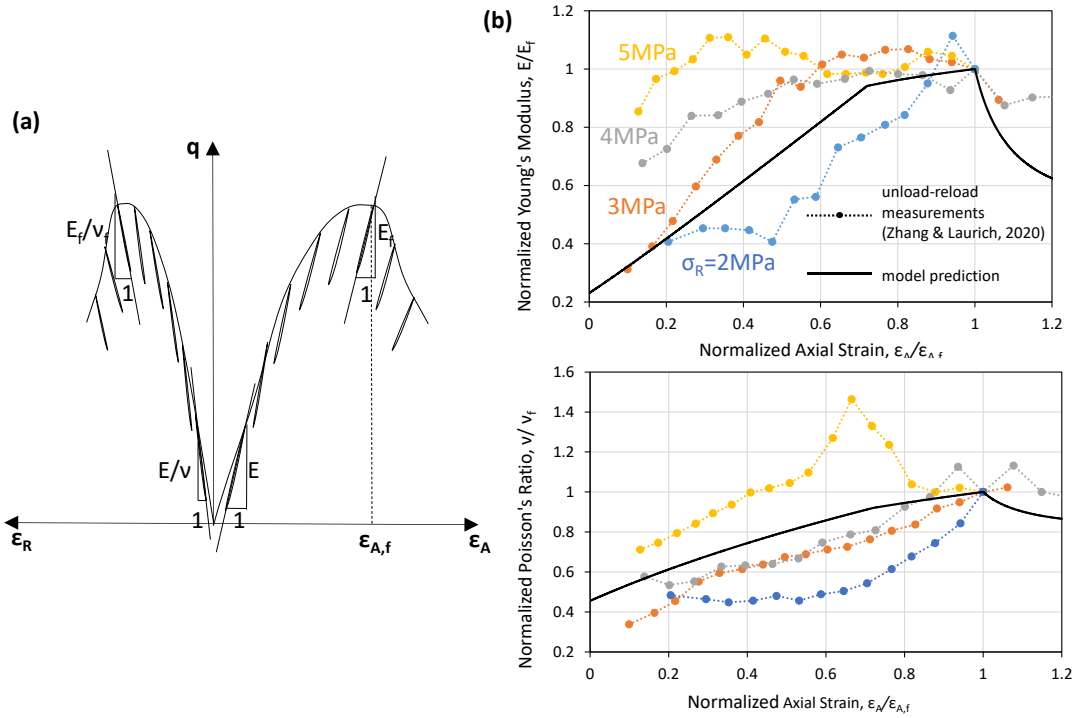

Figure 4-12. (a) Schematic diagram of the stress-strain curve with multiple unload-reload cycles in the triaxial compression test on Opalinus Clay reported by Zhang and Laurich (2020) (b) Variations of E and v from prediction using *AniDM* for test 09026 versus measurement. Quantities are normalized to the values at failure, i.e., E_f, v_f, and $\varepsilon_{A,f}$, for better representation of all four tests.

4.6 Finite Element Modelling of Borehole Response

Pressuremeter tests were used to characterize the in-situ stiffness of Opalinus Clay at the Mont Terri Rock Laboratory. An example of test data obtained from pressuremeter tests in borehole BGC-A4 is shown in Figure 4-13. The displacement readings are values averaged from six independent caliper measurements at the testing plane. Two pressuremeters were used, respectively, with the calipers in direct contact with the borehole wall and the calipers sitting behind the inflatable membrane. In the later case, the membrane stiffness and compression were calibrated carefully (Appendix II). A significant portion of tests in borehole BGC-A4 was performed in sandy Opalinus Clay. Given the borehole orientation, the pressuremeter loading was approximately parallel to the beddings of Opalinus Clay. The initial expansion tended to close the micro-discontinuities in the rock surrounding the borehole (Clarke and Smith 1992; Huang et al. 1999). These micro-discontinuities might be naturally present or drilling-induced. To determine the shear modulus and its stress dependency, unload-reload cycles at multiple pressure levels were performed in these tests. The unloading did not follow the loading path, indicating the accumulated frictional deformation as the micro-discontinuities closed upon loading. The shear modulus evaluated

from the unload data in these pressuremeter tests also exhibited a certain amount of nonlinearity. Therefore, a small-strain analysis similar to that applied to the triaxial tests was performed to evaluate the shear modulus at a constant strain amplitude (Chapter 2). A strong dependence of the shear modulus G_p on expansion pressure p_c was observed in the initial loading range (< 5MPa). The study assumes that the borehole deforms cylindrically under an isotropic in-situ stress condition. The radial displacement u_r normalized by the initial borehole radius r_0, defined as cavity strain ε_c, is used for the test data interpretation.

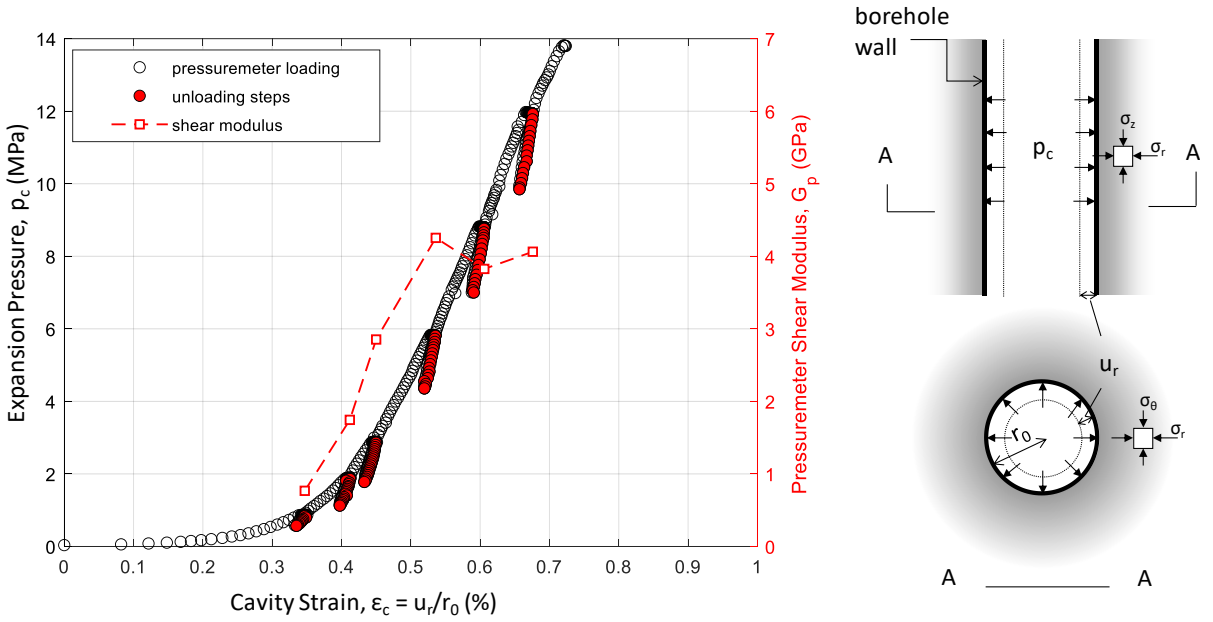

Figure 4-13. Example data from pressuremeter tests in borehole BGC-A4 with unload-reload cycles for the evaluation shear modulus G_p of in-situ Opalinus Clay

To predict the borehole expansion in pressuremeter testing, the proposed constitutive model was implemented in a finite element code Abaqus™ as a user-defined material (UMAT) subroutine. An axisymmetric model is established with the displacement constrained in the axis of the borehole (Figure 4-14). The mesh is gradually densified towards the borehole wall such that the size of the smallest element is only 1/6 of the element size at the far-field boundary.

An initial isotropic boundary stress σ_0 of 5 MPa was applied, which was close to the reported mean in-situ stress at the Mont Terri Rock Laboratory (Martin and Lanyon 2003). Two modeling stages were simulated sequentially: initial borehole unloading and pressuremeter loading. In the simulation, the borehole pressure p_c is decreased initially to zero and then increased to in-situ stress σ_0. At both stages, sufficiently small steps ($\leq$ 0.025 MPa) are applied, and the radial displacement at the borehole surface responding to the change of p_c is predicted.

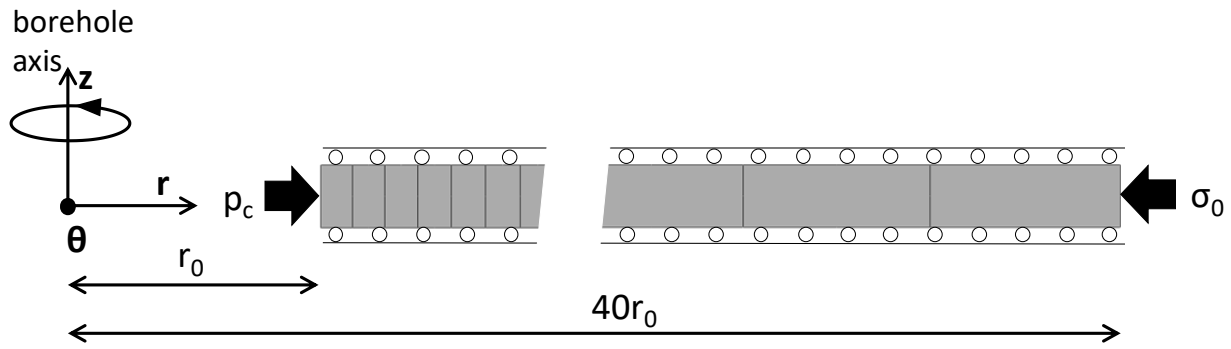

Figure 4-14. FE configuration for modeling axisymmetric borehole deformation.

A comparison is made among predictions using the three proposed stress-dependent stiffness functions. The parameter values $E^{(1)}$ and b from Table 4-1 are used in the simulation. The use of the strength parameters given in Table 4-3 does not predict damage or failure in the medium for the given boundary loading conditions, so only the elastic borehole deformation is predicted (Figure 4-15). The predicted deformation is reversible in the cycle of unloading and loading. To compare with the shear modulus determined using unloads from pressuremeter test data, an apparent shear modulus value G_a is evaluated discretely as the tangent of the predicted relationship between pressure and cavity strain, i.e., $dp_c/2d\varepsilon_c$. Its variation with p_c is shown in Figure 4-15.

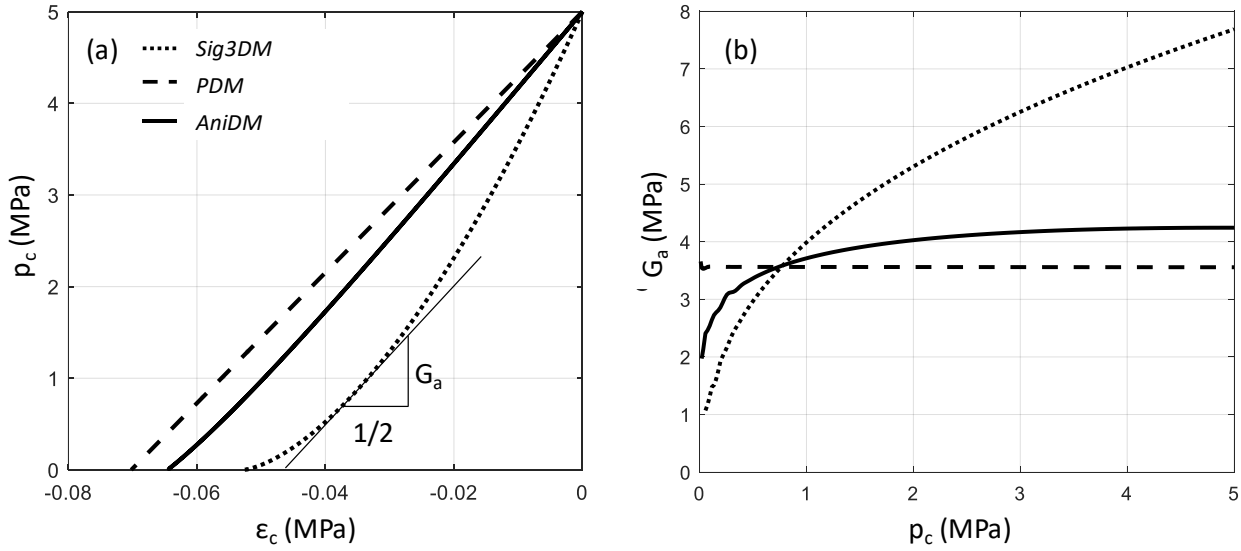

Figure 4-15. Predicted variations of elastic borehole deformation and apparent shear modulus with radial stress at the borehole wall using three stress-dependent stiffness functions with calibrated $E^{(1)}$ and b (Table 4-1)

The borehole deformation predicted using *PDM* is linear and matches that obtained using a linear elastic model with a constant shear modulus determined by $E^{(1)}$ and $\nu^{(1)}$. This is the consequence of the pure

shear mode ($\Delta\sigma_r = -\Delta\sigma_\theta$ and $\Delta\sigma_z = 0$) for the cavity expansion/contraction in an isotropic medium where mean stress stays constant. Therefore, *PDM* fails to predict the variation of the shear modulus measured in the increase of expansion pressure in the current model configuration. The prediction using *Sig3DM* is identical with the closed-form solution derived by Santarelli and Brown (1987) and shows a strong nonlinear deformation at the low radial stress. The predicted borehole response using *AniDM* is also nonlinear, but the nonlinearity is less pronounced than that using *Sig3DM*. Predicted G_a using *AniDM* tends to gradually reach a limit when the p_c approaches the initial stress at 5MPa, which agrees with the field observations.

The elastic borehole deformation predicted using *PDM* is linear and matches that obtained using a linear elastic model with a constant shear modulus determined by $E^{(1)}$ and $\nu^{(1)}$. This is the consequence of the plane strain shear mode for the cavity expansion/contraction in an isotropic medium where mean stress stays constant. The prediction using *Sig3DM* is identical with the closed-form solution derived by Santarelli and Brown (1987) and shows a strong nonlinear deformation at the low radial stress. The predicted borehole response using *AniDM* is also nonlinear, but nonlinearity is less pronounced than that using *Sig3DM*. Predicted G_a using *AniDM* tends to gradually reach a limit when p_c approaches the initial stress at 5MPa, which agrees with the observations.

Figure 4-16 shows the predicted radial variation of stress in three cases. Again, the prediction using *PDM* matches the linear elastic model. The predicted tangential stress σ_θ using *Sig3DM* does not reach its maximum at the borehole surface, as also addressed by Santarelli and Brown (1987) and Ewy and Cook (1990). Other models using a radius-dependent modulus (Wu and Hudson 1991; Nawrocki and Dusseault 1995) predict the same trend - low tangential stress at the borehole surface but high deviator stress inside the medium. By contrast, the model accounting for stress-induced anisotropy (*AniDM*) predicts higher deviator stress than the linear elastic model at the borehole surface, however still not high enough to initiate shear failure.

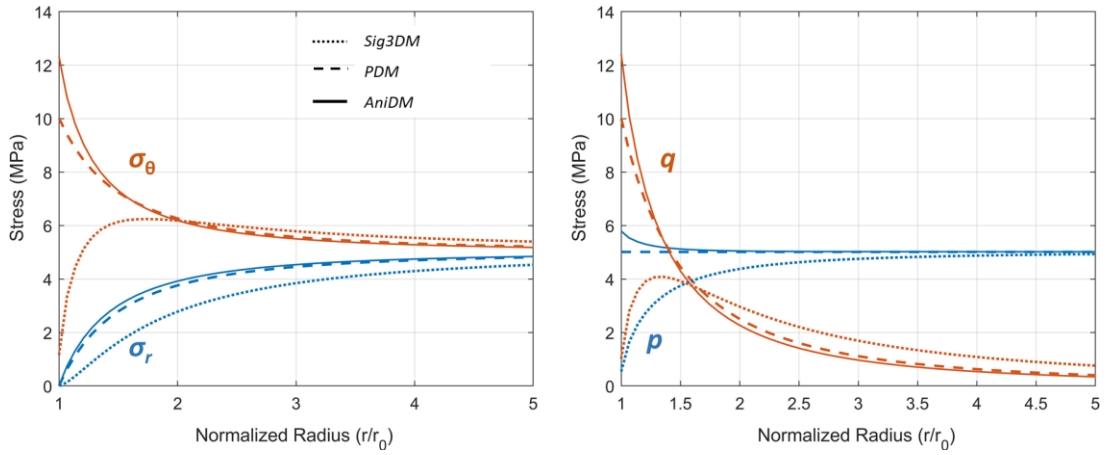

Figure 4-16. Predicted radial variation of stress after stress relief ($p_c = 0$) using three stress-dependent stiffness functions with calibrated $E^{(1)}$ and b (Table 4-1)

4.7 Discussion on the Borehole Damage

The disturbance in the formation surrounding the borehole caused by drilling can be characterized using borehole acoustic surveys (Hornby 1992; Balland and Renaud 2009; Schuster 2019). For a borehole drilled in a highly stressed ground, the stress concentration in the borehole vicinity tends to reach the damage threshold with the substantial reduction of the wave velocity (Winkler 1997). The velocity reduction under high deviatoric stress was measured on the Opalinus Clay (Chapter 3). The radial extent of damage into the borehole wall is defined as the borehole damage zone (BDZ). BDZ has been identified in the field by Balland and Renaud (2009) and Schuster (2009) using refraction tomography analysis on the high-resolution borehole ultrasonic data obtained at different underground laboratories. This study employed interval velocity measurements (IVM) before the pressuremeter tests at 5cm step along the borehole BGC-A4. The Opalinus Clay in the near-borehole field was covered by the rays traveling over different distances (Figure 4-17 (a)). The variation of P-wave velocity v_p in both longitudinal and radial directions of the borehole is resolved after a tomography inversion on the P-wave phases of the entire IVM datasets (e.g., (Figure 4-17 (b)). The overall increase of v_p from the borehole wall to far-field over a radial extent of > 2cm (~ $0.5r_0$) implies the near-borehole damage after drilling unloading.

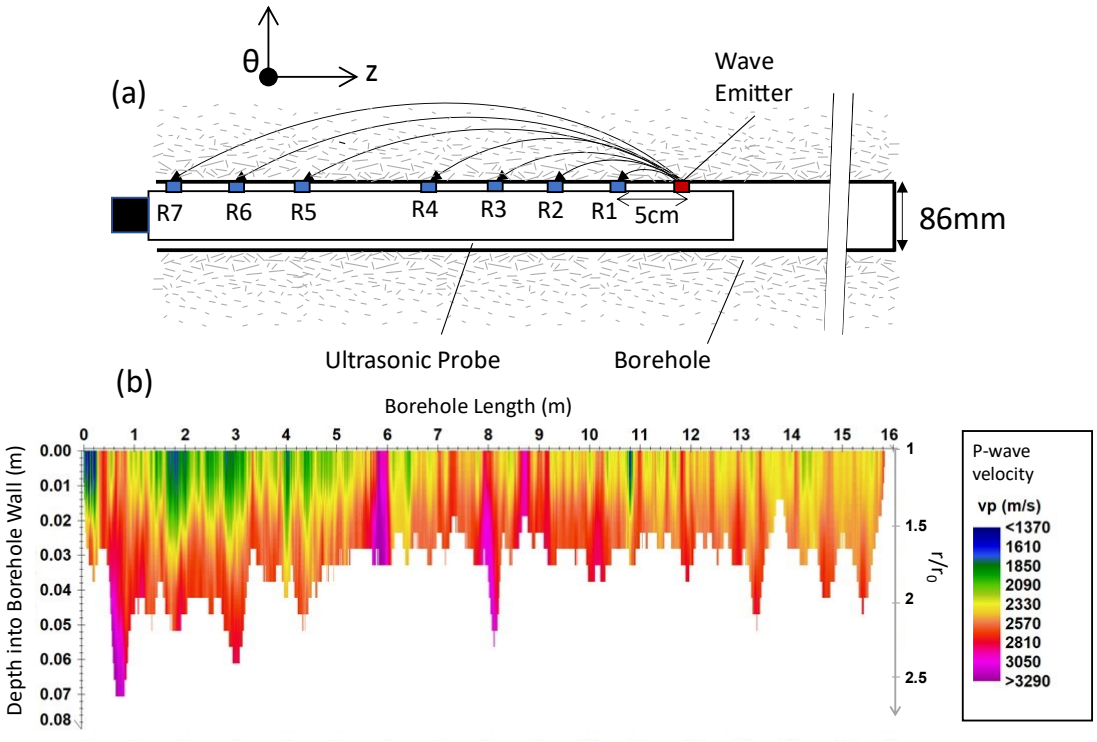

Figure 4-17. (a) Interval velocity measurement (IVM) in borehole BGC-A4 and the example of velocity data obtained from receivers spaced at varying distances from the wave emitter. (b) Tomography inversion results of P-wave velocity distribution in the near-borehole region along borehole BGC-A4 (Schuster, In preparation).

The absence of near-borehole damage/failure from the prediction using the calibrated model parameters in Table 4-2 might be due to the following reasons: (1) the assumption of isotropic far-field stress underestimated the stress concentration. The BDZ is likely to be localized if the actual anisotropic far-field stresses are considered; (2) the specimen condition in the laboratory investigation may not be representative of the in-situ Opalinus Clay. Drying was allowed during specimen preparation before triaxial testing. It was shown by Wild et al. (2014) and Zhang and Laurich (2020) that the strength of the desaturated specimens increased remarkably. A systematic reduction of the cohesion was also observed by Zhang and Laurich (2020) after specimens were re-saturated with water vapor. The unloading of the borehole by drilling was likely rapid and occurring under an undrained condition without loss of moisture. Therefore, a failure envelope predicting lower peak strength for saturated Opalinus Clay may be more appropriate; (3) the confining pressure ($\geq$ 1 MPa) used in the triaxial tests is higher than what is expected for a fully unloaded borehole. It was shown by Amann et al. (2012) that under confining stress $\leq$ 0.5 MPa, the failure mode of Opalinus Clay was dominated by axial splitting, and a failure envelope with lower cohesion (Table 4-2) was concluded for such the stress range; (4) the test data from triaxial compression

tends to overestimate the shear strength using Drucker-Prager criterion (Figure 4-8). As a more probable shear mode in the case of borehole unloading, pure shear is likely to yield a failure envelope between triaxial compression and triaxial extension due to the dependence on the intermediate principal stress.

Given the considerations above, a failure envelope with a reduced κ equal to 4 MPa will be used to predict the response of in-situ Opalinus Clay under drilling unloading (Figure 4-8). The damage strain threshold c_0 and rate-controlling parameter c_1 are also reduced respectively to 2.5e-4 and 5e-4 so that damage would occur before the peak stress and grow rapidly to the limit. Admittedly, these adjustments of the model parameters are subjective and remain unverified in the absence of laboratory data from undrained tests on sandy Opalinus Clay at low confining pressure. Nevertheless, rather than reproducing the in-situ borehole response, the primary goal of this study is to investigate how the stiffness degradation in the BDZ would affect the pressuremeter measurements using the proposed modeling approach. For this reason, three scenarios with different damage limits d_{max}, respectively equal to 0.5, 0.6, and 0.7, are considered in the following demonstration.

Figure 4-18(a) shows the predicted borehole deformation during a cycle of unloading and loading for cases with damage and without damage. The evolution of the damage at the borehole wall is plotted with the borehole convergence (denoted by negative cavity strain) during unloading. Little inelastic borehole deformation is predicted upon the onset of the damage until the shear failure occurs. The induced tensile plastic strain after failure in the radial direction accelerates the damaging process. Higher d_{max} leads to faster degradation associated with more significant borehole convergence and a larger predicted extent of BDZ into the borehole wall (Figure 4-18(b)).

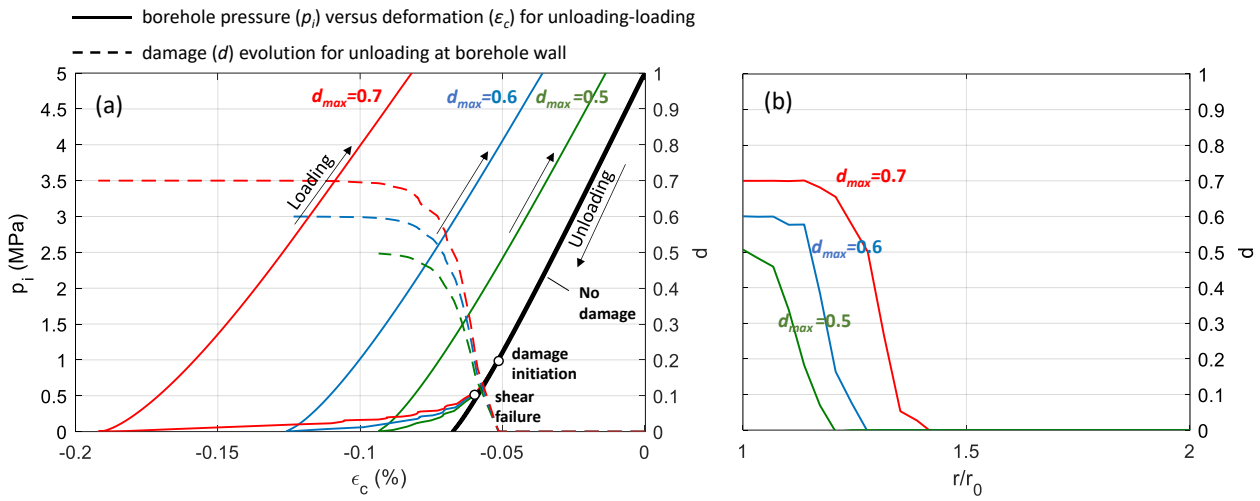

Figure 4-18. (a) Borehole deformation and damage evolution in two sequential stages of unloading and loading predicted using the proposed elastoplastic damage model with *AniDM*. (b) Predicted radial variations of damage at the end of unloading. Three cases with different damage limits d_{max} are presented.

The apparent shear modulus G_a is determined using the predicted borehole expansion for each case with a different extent of unloading-induced BDZ (Figure 4-19). Similar to the case without BDZ, G_a becomes less pressure-dependent in the increase of p_c and finally reaches a limit when the initial stress is restored. In the presence of the BDZ, the limit reached is lower than that when damage is absent. The more severe the borehole damage is, for instance, when $d_{max} = 0.7$, the faster this limit will be reached. By considering the unloading-induced damage, the prediction appears to better approximate the pressuremeter measurements in the lower pressure range. However, the strong dependence of G_a on p_c at p_c <3 MPa is still not well represented with the current model.

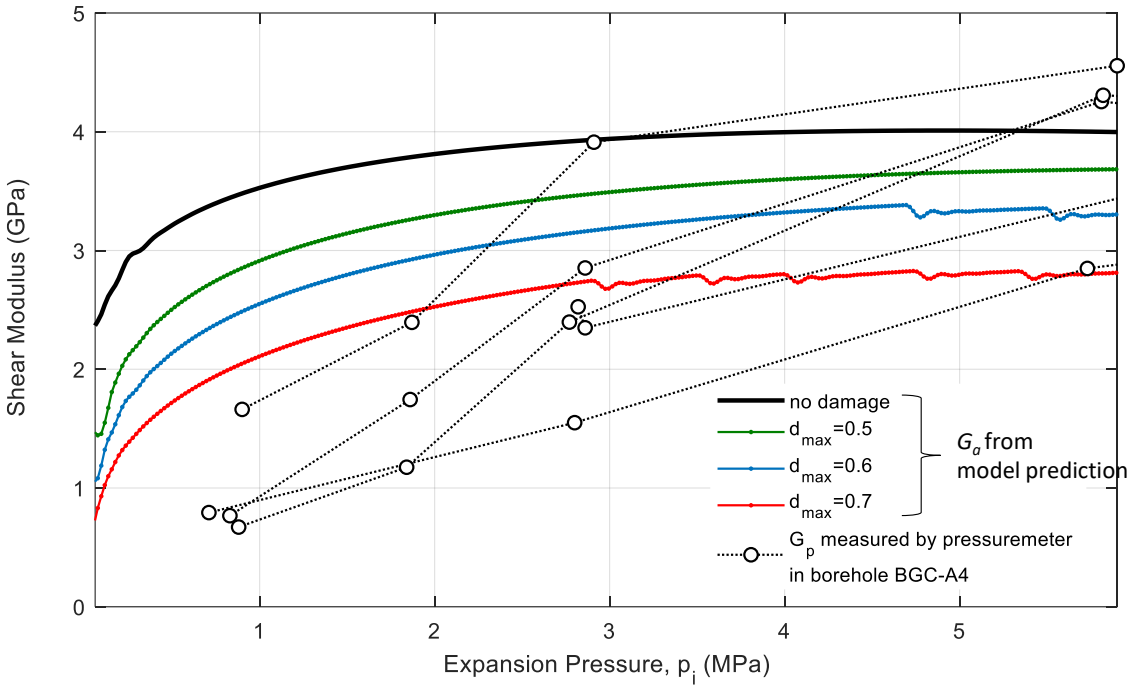

Figure 4-19. Variation of shear modulus derived from the computed expansion curves versus the measured shear modulus determined using unloads from pressuremeter tests in borehole BGC-A4.

As mentioned earlier, the axisymmetric model used in this study may be oversimplified in the investigation of the localized borehole damage given the anisotropic in-situ stress condition. The 2D plane-strain or 3D full borehole model should be applied, and a comparison with the anisotropic borehole response using the independent caliper measurements at multiple azimuths in the expansion plane, as suggested by Liu et al. (2021a), may be more meaningful. It should also be noted that using laboratory specimens under symmetrical loading may not correctly characterize the damage and failure behaviors of the in-situ Opalinus Clay under a more complicated boundary condition, for example, during borehole unloading. The unloading stress path has been approximated using conventional triaxial tests by Aristorenas (1992) for the case with initial isotropic stress as well as by Wild and Amann (2018b) for the case with anisotropic initial stress. The latter also addressed the critical influence of the orientation of the bedding plane with respect to the applied stress in these investigations. However, the failure modes that were observed around boreholes, such as the localized shear fracture network and progressive bedding plane buckling (Kupferschmied et al. 2015), are still not readily reproduced on cylindrical laboratory specimens. Furthermore, the difference in micro/macro-fracture development during the increase of deviatoric loading under low and high confinement is challenging to capture by adopting a continuum approach, despite the recent advances in the multiscale modeling approach (e.g., Zhu and Shao 2017). All these limitations, besides the uncertainty in model parameters, have led to the inaccurate prediction of the

borehole damage as well as the subsequent expansion against the damaged rock in this study. Alternatively, the continuum-discontinuum approach has shown its advantages and provided promising prospects of simulating the damage and failure processes at varying scales and boundary conditions, particularly when the geological structures (e.g., beddings and fractures) primarily impacts the mechanical response of the rock (Lisjak et al. 2014a, 2015). Nevertheless, this work has demonstrated an effective numerical routine to quantify laboratory and in-situ measurements in Opalinus Clay under a simple constitutive framework.

4.8 Summary and Conclusions

This work presents an example to quantify the laboratory and field measurements under a simple constitutive framework. A set of multi-staged triaxial test data on Opalinus Clay was analyzed. The evolution of elastic modulus was addressed and assessed using three stiffness functions which are dependent on minimum principal stress (*Sig3DM*), mean stress (*PDM*), and full stress tensor (*AniDM)*, respectively. Due to the nature of stress-induced anisotropy in weak rocks, *Sig3DM* was not able to explain the increase of the modulus under uniaxial compression. *AniDM* was incorporated in a formulation in which damage and plasticity were coupled. It showed that the model has successfully predicted the elastic modulus variation and the stress-strain behavior with a small number of constitutive parameters.

Implementing the model into a finite element code allows the borehole response in a cycle of unloading and reloading to be predicted. Under the assumption of the axisymmetric expansion, the elastic predictions for borehole deformation and local stress distribution using three stiffness functions were discussed. The observed increase of apparent shear modulus G_a in the increase of expansion pressure can be explained when *Sig3DM or AniDM* was used, whereas *PDM* predicted a constant modulus value during expansion as would be predicted using a linear elastic model.

As indicated by the ultrasonic survey, borehole damage is absent if the calibrated model parameters are used to predict borehole unloading. The possible reasons might be related to the simplified isotropic stress field used in the prediction and the conditions of the specimens used in the laboratory tests that are not representative of the undrained borehole unloading. A criterion with reduced strength and damage initiation stress was used to demonstrate the borehole damage and its effect on the pressuremeter measurement. It was found that with more intense borehole damage, a lower limit of G_a will be reached after the radial stress recovered to in-situ stress at the borehole wall.

The limitation of the current model has been addressed given the difficulties of using the tests on laboratory specimens to reproduce the unloading-induced damage under a more complex stress path in

borehole drilling. The continuum-discontinuum modeling approach may more accurately capture the impact of the geological structures and induced discontinuities at varying scales and boundary conditions. Nevertheless, this work has demonstrated an effective numerical routine to quantify laboratory and in-situ measurements in Opalinus Clay.

Chapter 5

Investigations on Localized Borehole Damage and Its Relation to In-situ Stresses

5.1 Introduction

Localized damage zones around underground openings have been observed at different scales at the Mont Terri Rock Laboratory (Amann et al. 2017). Underground excavation relieves the stress in the rock mass and induces stress redistribution around the excavation. Mechanical disturbance to the ground is likely when the redistributed stress exceeds the stress threshold of yielding or damage. Near the excavation surface, this disturbance can be as severe as the development of fracture networks. By drilling boreholes into the tunnel wall and overcoring them after they were injected with resin, Bossart et al. (2002) identified different unloading-induced fracture groups in Opalinus Clay. The area into the tunnel wall where unloading fractures are present was defined as an excavation disturbance (or damage) zone (EDZ). They found the unloading fractures can be either parallel or oblique to beddings depending on the trajectory of the tunnel and the location of the fractures. They further refined the EDZ into an inner zone and an outer zone, according to the frequency and interconnectedness of the unloading fractures. The characterization of EDZ and its spatial and temporal evolutions at the Mont Terri site have also been conducted by Schuster et al. (2001), Thöny (2014), and Yong et al. (2017) using drillcore mapping, televiewer images, ultrasonic velocity logging, and seismic refraction tomography. These investigations suggested that the EDZ at the Mont Terri Rock Laboratory is dominated by extensional fracturing at the sidewalls and bedding-parallel slip at the excavation roofs and inverts. The radial extent of the EDZ with a length of approximately one excavation radius was usually observed.

To investigate the EDZ and its hydromechanical properties around a cylindrical opening in Opalinus Clay, a micro-tunnel with a diameter of about 1m was drilled horizontally at the Mont Terri site (Marschall et al. 2006). The damage observed at the tunnel wall immediately after drilling was primarily controlled by the far-field stresses in the cross-section plane, the weak geological structures (e.g., faults and weakly cemented layers), and the structural anisotropy of mechanical properties (e.g., uniaxial compressive strength). Labiouse and Vietor (2014) and Kupferschmied et al. (2015) investigated the development of the unloading-induced damage at borehole scale using hollow cylinder tests and in-situ experiments by overcoring boreholes with diameters ranging from 86mm to 101mm. For boreholes drilled parallel to the bedding plane, it was found that the borehole damage zone (BDZ) was localized at the azimuth perpendicular to bedding, and BDZ transitioned from shear fractures propagating parallel to bedding shortly after drilling (12 hours) to progressive bedding slice buckling that extends radially into

the borehole wall over a long period. Such the time-dependent damage was also recognized by Marschall et al. (2006), who suggests two factors should be responsible – 1) excess pore pressure dissipation from the overstressed zone towards the tunnel/borehole wall and the far-field, and 2) weathering effects by cycles of de- and re-saturation due to relative humidity change at the site.

In this study, the visual evidence (e.g., borehole image) of the borehole wall damage in borehole BGC-A4 after drilling is unavailable. A major amount of previous studies were conducted in boreholes parallel or oblique to bedding and have shown that borehole damage in Opalinus Clay was dominated by structurally related failures, e.g., bedding-parallel breakouts, rather than overstressing. Within my knowledge, the effect of overstressing was only exclusively investigated by Labiouse and Vietor (2014) in hollow cylinder tests on the core specimens cut perpendicular to bedding. In these tests, borehole wall damage was not evident on the inner wall of the specimens after borehole unloading from an initial stress of 4.5 MPa. However, the isotropic initial stress and the small diameter of the borehole (14mm) adopted in these tests might compromise the representativeness of their findings for in-situ conditions.

The localized excavation (or borehole) damage zone can be predicted, given the stress redistribution around the borehole and the damage criteria specified for the material. The analytical solutions, for example, derived by Kirsch (1898) and Amadei (1983) for a homogeneous medium with a circular opening under biaxial boundary stresses, can be used in near-borehole stress prediction. The stress solution for a circular opening in the medium that has deformed plastically after yielding was also derived with some restrictive assumptions (e.g., Detournay and Fairhurst 1987). To take into account more sophisticated physical processes in the problem, numerical approaches have been growingly employed as the computational capability is improved. The hydro-mechanically coupled behavior of the Opalinus Clay during and after excavation was modeled using the finite element method (FEM) at the in-situ condition by Le and Nguyen (2015), Parisio et al. (2018), Ismael et al. (2019). The constitutive models they used incorporated a few important constitutive characteristics of Opalinus Clay, including elastic and plastic anisotropy, mobilization of shear strength, and/or creep. The agreement between the numerical prediction and the field observation was encouraging. As a more recently developed approach, the finite-discrete element method (FDEM) was utilized by Lisjak et al. (2014a) to investigate the deformation and damaging process of the Opalinus Clay in the near field after steps of excavation. The approach allowed a more realistic representation of the damage in the stratified rocks with the different types of fracture creation and propagation depending on the local stress concentration and has successfully captured the interaction of those fractures with geological structures such as faults.

As indicated by Eqn. (1-11), in a homogeneous and isotropic elastic medium, the response of the borehole to the change of internal pressure p_c would be uniform and independent of the far-field stresses. However,

as addressed in Section 1.4, borehole unloading is likely to induce local modifications of the mechanical properties because of the stress redistribution. These local property changes would lead to an anisotropic borehole response under subsequent loading. Besides, in this study, the assumption of the isotropy is challenged by the strong structural anisotropy of the Opalinus Clay. For loading that is not parallel to bedding, the deformation of the borehole varies with azimuth, for example, as shown for the pressuremeter tests in borehole BGC-A6. Furthermore, because of the non-uniformly redistributed stress in the near-borehole field, borehole yielding under pressuremeter loading at high pressure would also become anisotropic, as demonstrated by Liu et al. (2021a). Therefore, an anisotropic borehole response should be expected given the factors listed above.

In this chapter, the localized borehole damage after mechanical unloading will be predicted using both analytical and numerical approaches under the in-situ condition. Some evidence of the near-borehole disturbance at GC experiments will also be provided. Their validities to inform the anisotropic far-field stresses will be discussed at the end.

5.2 Prediction of Localized Borehole Damage Zone (BDZ)

5.2.1 Plane-strain Analysis

The elastic stress field around the borehole is calculated using Kirsch's solution (1-10). The in-plane principal stresses, σ_{max} and σ_{min}, directly determined using the in-situ stress tensor (Table 2-1), are considered in this analysis. The analysis shows that high deviator stress, σ_θ - σ_r, in the borehole vicinity at the orientation of σ_{min} (Figure 5-1), whereas low deviator stress (≤ 6 MPa) is predicted near the borehole wall at the orientation of σ_{max}. Damage near the unconfined borehole wall can be estimated by comparing the deviator stress with peak strength q_f predicted using the generalized Hoek-Brown failure criterion calibrated by Amann et al. (2012) for the Opalinus Clay in triaxial tests at low confining stress (0 to 4 MPa), i.e., $q_f = 6.6\ MPa\left(91.5\frac{\sigma_3}{6.6}+1\right)^{0.15}$, where the minimum principal stress σ_3 is equal to the radial stress σ_r. The results suggest a localized failure zone extends to $r/r_0 >$ ~1.15 from the borehole wall. The circumferential boundary of the failure zone can be estimated using the condition of $\sigma_\theta - \sigma_r = q_f$ at the borehole wall, where q_f is equal to *UCS* as $\sigma_r = 0$. Popp and Salzer (2007) and Amann et al. (2011) have shown that volumetric dilation of the Opalinus Clay was initiated when the deviator stress exceeds approximately 50% of the peak strength. Using this dilatational criterion as an upper bound, the damage zone may extend well beyond the predicted failure zone.

Assuming that unloading occurred under the undrained condition, the excess pore pressure Δu in the borehole vicinity can be predicted based on the premise that it is equal to the change of the total mean stress Δp. Figure 5-1 shows the radial variations of predicted Δu and radial effective stress σ'_r calculated

using $\sigma'_r = \sigma_r - (\Delta u + u_0)$. The high negative σ'_r near the borehole wall suggests that the Opalinus Clay might yield under tension, making an extended failure/damage zone more likely.

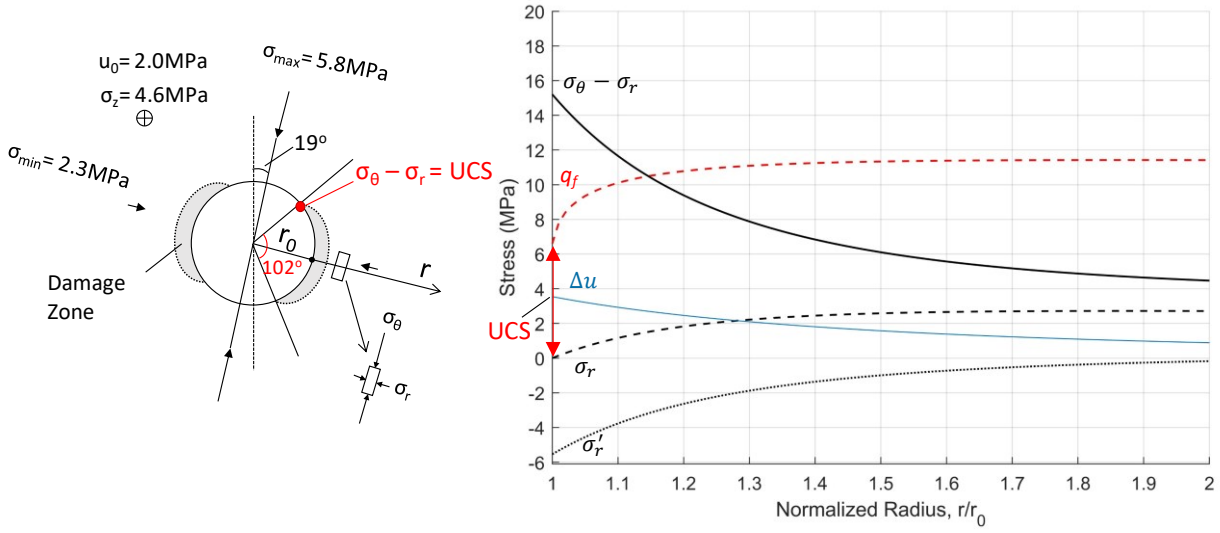

(a) Borehole BGC-A4

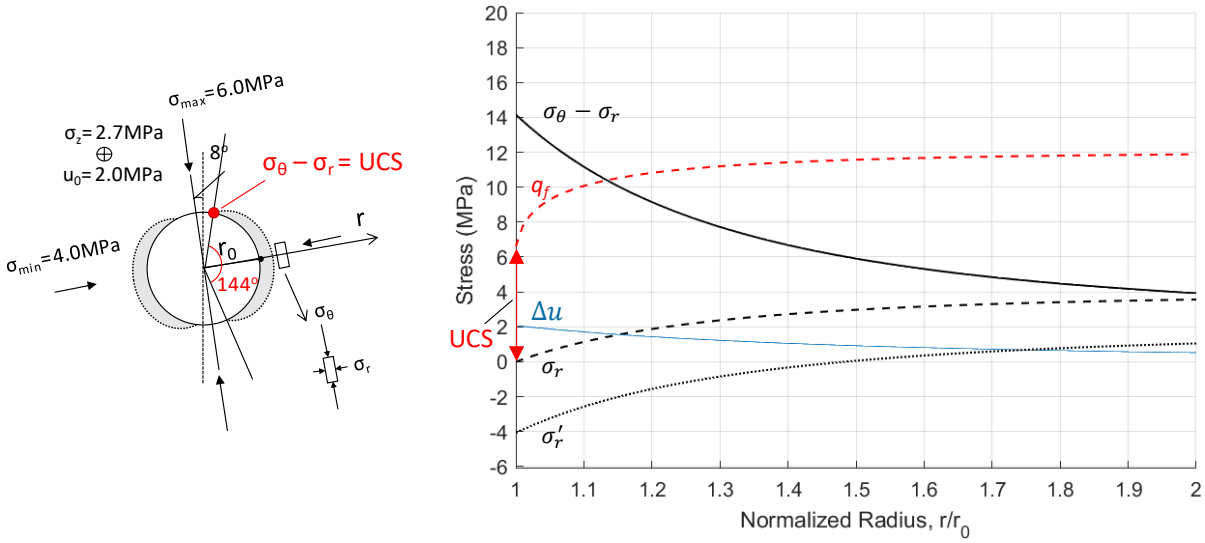

(b) Borehole BGC-A6

Figure 5-1. Schematic damage zone around two test boreholes after drilling unloading predicted using in-situ stress estimate in Table 2-1 (left). Predicted radial distribution of stresses using Kirsch's solution (right) under undrained condition along the axis of σ_{min} in comparison with the failure strength predicted using the criterion proposed by Amann et al. (2012).

5.2.2 Numerical Prediction with Elasto-plastic Damage Model

To explore the initiation of the localized borehole damage and the response of the damaged Opalinus Clay under pressuremeter loading, plane strain models with different boundary conditions are used (Figure

5-2). In these models, a ratio of 1:13.3 is adopted for the model size (width or height) versus the diameter of the borehole. The mesh in the borehole nearfield is densified. The anisotropic boundary stresses are defined in Table 5-1 using the far-field stresses projected on the planes perpendicular to boreholes BGC-A4 and BGC-A6, respectively.

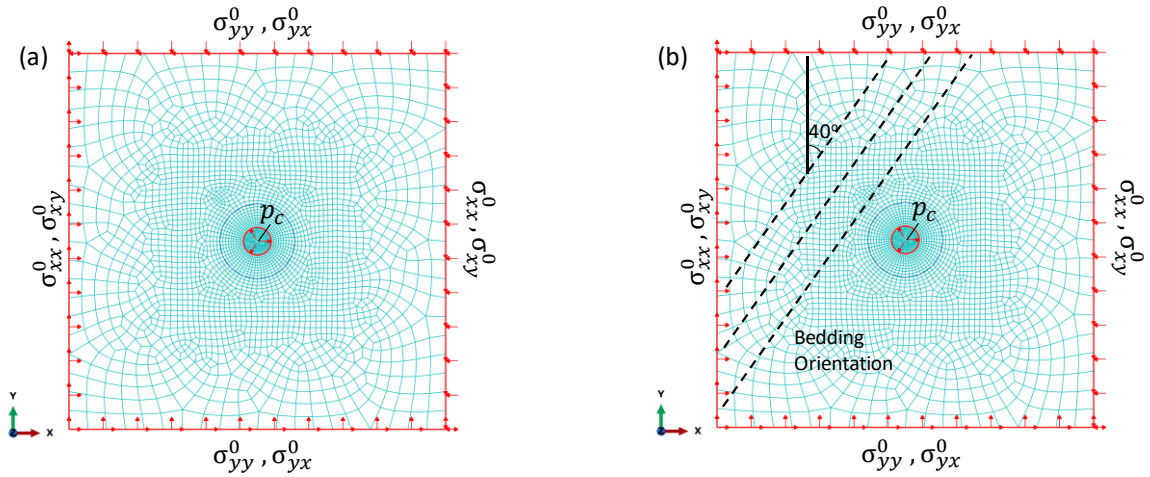

Figure 5-2. Plane strain models for simulation of borehole unloading and pressuremeter loading: (a) borehole drilled perpendicular to the bedding plane, and (b) borehole drilled parallel to the bedding plane.

Table 5-1. Boundary stresses applied in the plane strain models

Model for Borehole	σ^0_{xx}	σ^0_{yy}	σ^0_{xy} or σ^0_{yx}
	(MPa)		
BGC-A4	2.7	5.4	1.1
BGC-A6	4.0	6.0	-0.3
Sign convention: compressive normal stress is + and shear stress on the positive (negative) face heading towards the negative (positive) direction of an axis is +;			

The constitutive model used in this study employs the elastoplastic damage formulation in Chapter 4 with strength and damage parameters adapted for the undrained unloading given in Table 5-2. The stress-dependent elastic stiffness provided in the original formulation is replaced by the constant anisotropic elastic properties given in Table 5-3. In the modeling, an initial equilibrium is established in a geostatic step under the assigned boundary stress condition, followed by two additional steps – borehole unloading and loading, where the stress at the borehole boundary is modified. To predict the development of damage, a net strain tensor, i.e., the strain subtracted by the initial strain induced in the geostatic step, is used.

Table 5-2. Strength and damage parameters used in numerical modeling

B	κ	d_{max}	c_0	c_1
	(MPa)			
1	4	0.5	2.5e-4	5e-4

Table 5-3. Elastic properties of the Opalinus Clay used in finite element modeling

E_v	E_h	ν_{hh}	ν_{hv}	G_{hv}
3.7 GPa	7.0 GPa	0.19	0.76	3.0 GPa

Predictions for borehole unloading ($p_c = 0$) show that damage develops in the entire borehole annulus (Figure 5-3). It should be noted that the extent of BDZ predicted in Figure 5-3 is dependent on the total tensile strain induced by borehole unloading. Therefore, a larger extent of BDZ is predicted for Case (a) in the axis of σ_{max} as a result of more elastic strain being released than in the axis of σ_{min}. On the other hand, intense damage is predicted near the borehole wall at the azimuth of σ_{min} due to the increase of the plastic strain after shear failure is locally initiated (Figure 5-4).

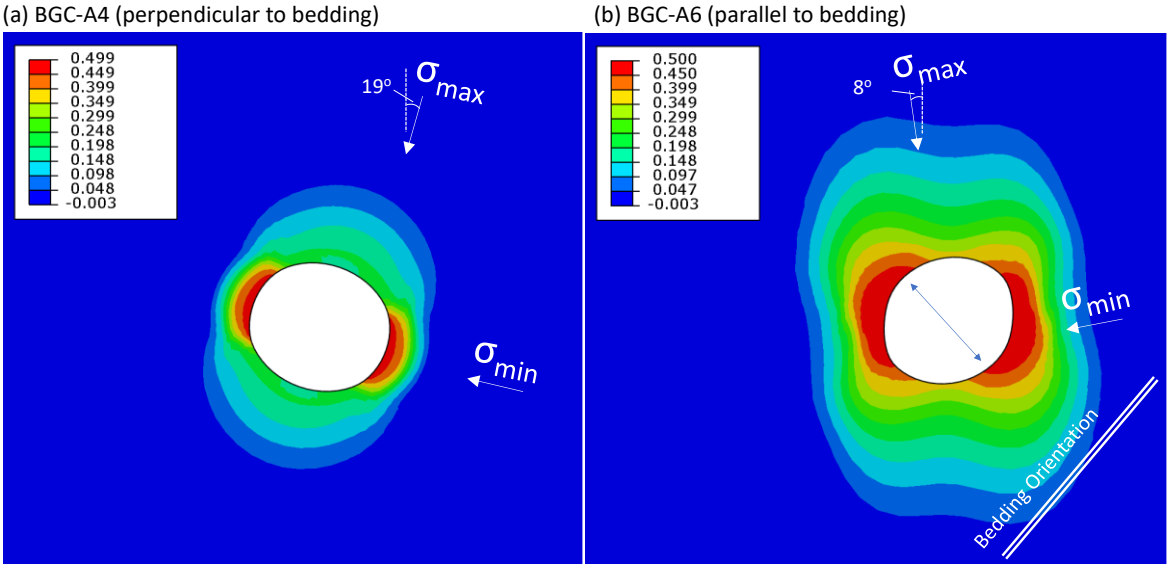

Figure 5-3. Prediction of damage distribution around borehole using proposed elastoplastic damage formulation under plane strain condition. Note that the borehole deformation is exaggerated by 100 times.

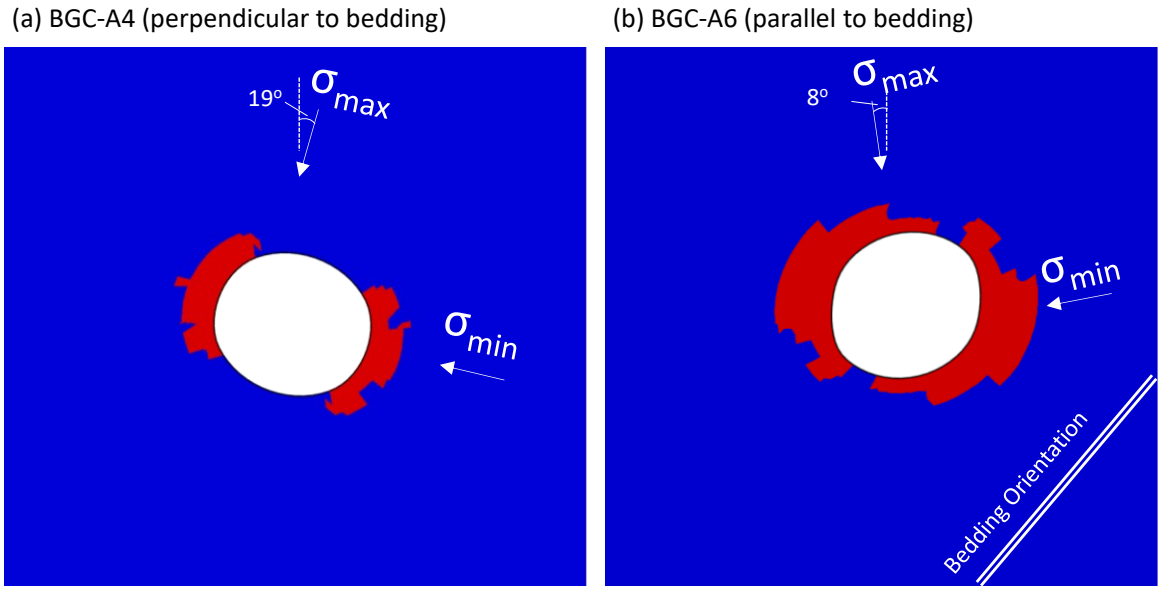

Figure 5-4. Localized shear failure zone after borehole unloading. Note that the borehole deformation is exaggerated by 100 times.

The extended BDZ in the axis of σ_{max} shown in Figure 5-3 may not be realistic. The damaged zone was shown to be more extensive in the axis of σ_{min} than that of $\sigma_{max,}$ according to the borehole ultrasonic measurements in similar argillaceous claystone and under the similar in-situ stress condition (Balland and Renaud, 2009). The prediction may be improved by (a) increasing the strain threshold c_0 so that damage initiation would be delayed till a more significant elastic tensile strain occurs, or (b) defining the damage initiation as a function of deviator stress rather than strain. The latter replaces Eqn. (4-16) with a Drucker-Prager type function, similar to the failure criterion considered in Chapter 4,

$$f_d = q - B_D p - \kappa_D \tag{5-1}$$

where two parameters B_D and κ_D need to be specified. In this case, 0.8 and 2 MPa are assigned to B_D and $\kappa_{D,}$ respectively, so the damage initiation criterion sits properly below the failure criterion (Figure 5-5). In addition to Eqn. (5-1), The growth of damage needs to be formulated after activation. To allow damage growth even when deviator stress drops below the threshold, which is generally observed for strength weakening materials, the strain-based growth function similar to Eqn. (4-19) is used,

$$d = d_{\max}\left(1 - \exp\left(\frac{-\left\|\boldsymbol{\varepsilon}_d^-\right\|}{c_1}\right)\right) \tag{5-2}$$

where the tensile strain $\boldsymbol{\varepsilon}_d^-$ is defined as the difference between the current strain tensor $\boldsymbol{\varepsilon}$ and the strain tensor $\boldsymbol{\varepsilon}_{di}$ recorded when damage is initiated, i.e., $\boldsymbol{\varepsilon}_d = \boldsymbol{\varepsilon} - \boldsymbol{\varepsilon}_{di}$. These modifications can be conveniently incorporated into the original formulation proposed in Chapter 4.

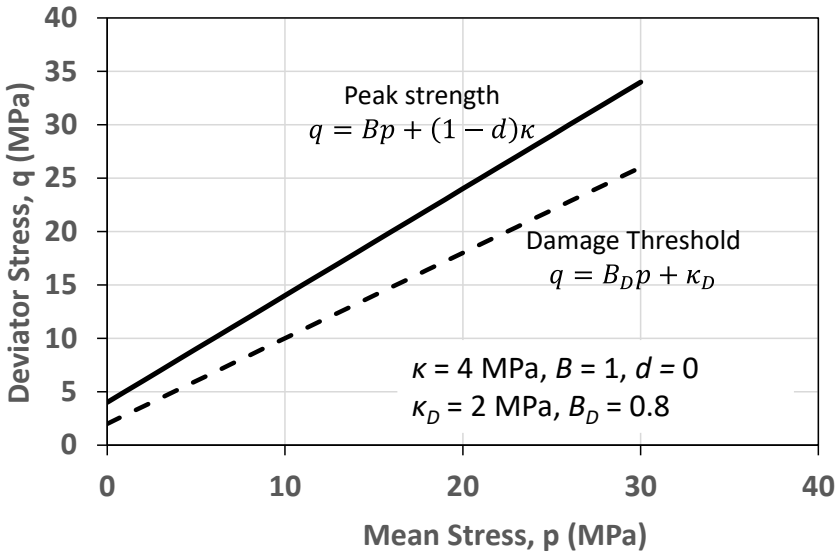

Figure 5-5. Stress-based failure and damage initiation criteria

Figure 5-6 shows the BDZs predicted using the modified models, respectively, with an increased strain threshold c_0 = 5e-4 and a stress-based damage initiation criterion. The predicted damage is still present in the axis of σ_{min} but is absent in the axis of σ_{max}.

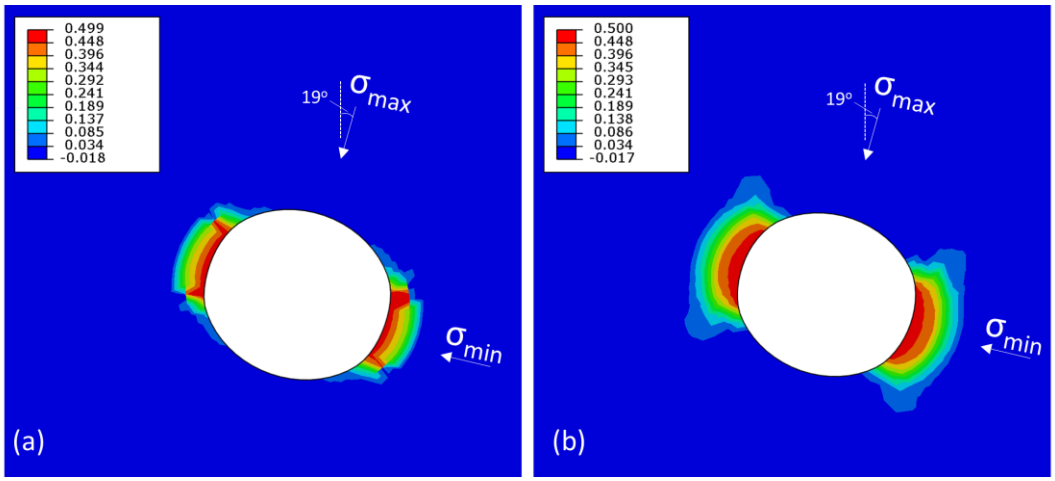

Figure 5-6. Predicted borehole damage zone around borehole BGC-A4 (perpendicular to bedding) with (a) increased damage initiation strain threshold c_0 = 5e-4 and (b) stress-based damage initiation criterion (κ_D = 2 MPa and B_D = 0.8). Note that the borehole deformation is exaggerated by 100 times.

For Case (b) in Figure 5-3, the axis of the borehole is parallel to the bedding. The prediction shows that the BDZ is preferentially developed in a wide azimuthal range approximately aligned with the axis of σ_{min}. Images obtained by the borehole camera (e.g., Figure 5-7) show extended borehole breakouts perpendicular to the bedding plane, indicating that the damage, in this case, is dominated by structural instability rather than stress concentration. The strain-based damage criterion (Eqn. (4-19)) adopted in this study also has difficulty reproducing such the damage mechanism. Instead of seeking a different numerical scheme, different internal variables were tried for the damage criterion. Among them, volumetric dilation induced by borehole unloading is found to be preferentially developed in the axis perpendicular to bedding. Therefore, in this case, the tensile strain volumetric strain ε_v is used rather than the normalized tensile strain $\left\|\boldsymbol{\varepsilon}^{-}\right\|$ in the original formulation. The same model parameters given in Table 4-2 are applied except that c_0 is replaced by a smaller value, 1e-5, to define the volumetric strain at the damage initiation. The predicted damage zone is localized in the axis approximately perpendicular to bedding and is more consistent with the observation (Figure 5-7). However, as mentioned in Chapter 4, a continuum mechanics model suffers from the difficulty of reproducing rock breakage and fragmentation shown in this case. Also, for modeling the material with the post-peak softening behavior, the finite element solutions can encounter serious strain localization issues, which are strongly dependent on the model meshes (de Borst et al. 1993). This may also lead to the failure to find a solution for a boundary value problem, for example, where the material is specified with a high damage limit and fast degradation rate to simulate the breakage. Although some numerical treatments on the element formulation have been proposed to overcome the undesired strain localization in damage modeling (Jin and Arson 2017; Parisio

et al. 2018; Sarkar et al. 2019), reproducing the discrete behaviors that are present in the observed rock damage behavior is challenging. A discontinuum or continuum-discontinuum model may be sought in the future to account for severe rock damage, such as borehole breakout.

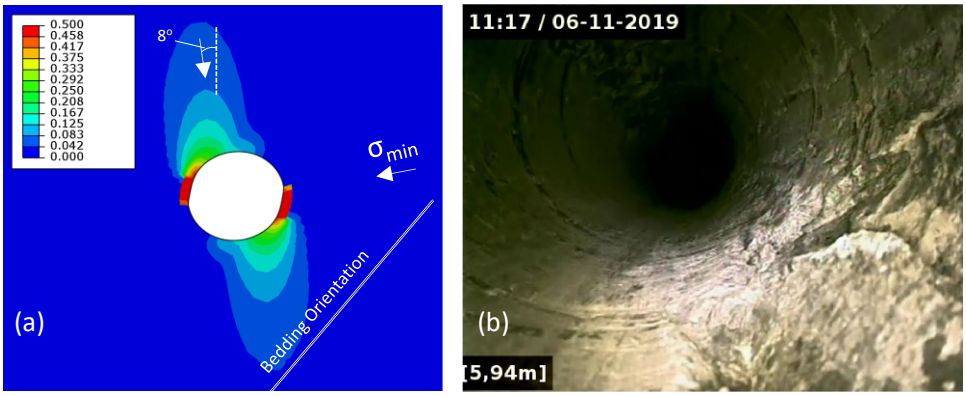

Figure 5-7. (a) damage distribution around borehole predicted based on the volumetric dilation, (b) an example of observed borehole wall damage in borehole BGC-A6 (parallel to bedding)

5.3 Field Evidence of Localized Near-borehole Disturbance

5.3.1 Rotational Interval Velocity Measurement (ROT-IVM)

Rotational interval velocity measurement (ROT-IVM) is a technique to propagate the waves at varying azimuths along the borehole wall (Schuster 2019). The measurement usually starts with the array of an emitter and multiple receivers on the ultrasonic probe positioned at 0° (facing towards the borehole top). It rotates in steps of 15° for the next survey until a full 360° is covered (Figure 5-8). By conducting ROT-IVM, the heterogeneity of the acoustic properties in the borehole circumferential direction can be characterized. When the borehole is drilled perpendicular to beddings, such heterogeneity is likely associated with the local stress field around the borehole.

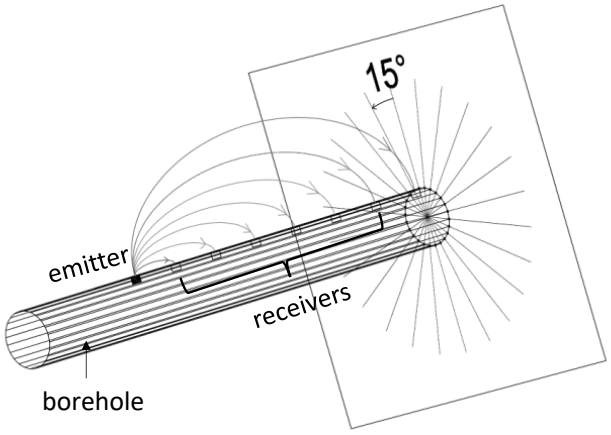

Figure 5-8. Schematic diagram of ROT-IVM at one depth interval

In this field campaign, two series of ROT-IVM were conducted three days apart at multiple depths in borehole BGC-A4. The 1st series was before pressuremeter tests (PMT), followed by the repeat series after the tests. The depth intervals covered by ROT-IVM approximately overlap PMT locations (Figure 5-9). Besides, to characterize the variation of the acoustic properties over the entire borehole length, the interval velocity measurement (IVM) is also available in this borehole, as described in Chapter 2.

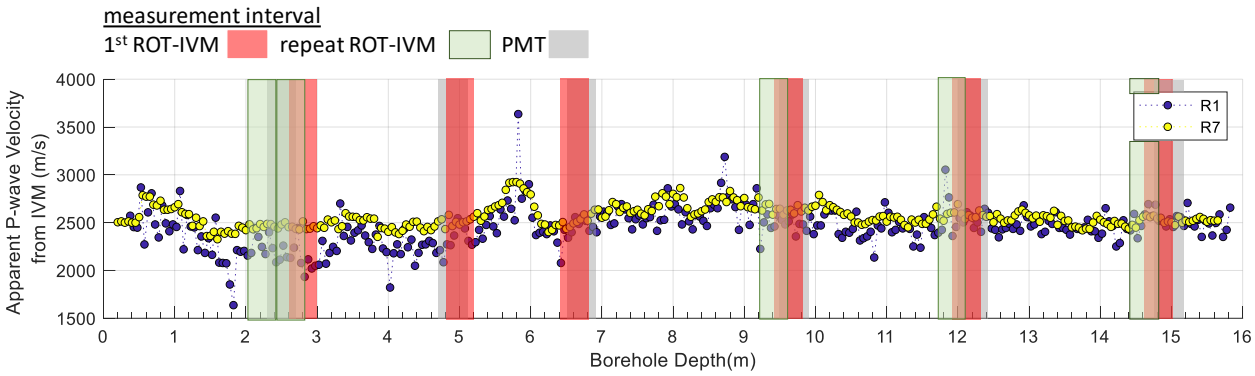

Figure 5-9. Locations of ROT-IVM and PMT in borehole BGC-A4. The background velocity logs are the apparent P-wave velocity determined from IVM over the whole borehole length using the shortest (R1, 5cm) and longest (R7, 40cm) emitter-receiver offsets, respectively.

Same as IVM, at a given azimuth, the travel time t identified from the wave obtained over a given emitter-receiver offset x can be used to calculate the apparent wave velocity for the corresponding ray path. The azimuthal variation of apparent P-wave velocity $v_{p,\,app}$ determined from ROT-IVM is shown in Figure 5-10. For the measurement at 3m, a strong anisotropy of $v_{p,\,app}$ is revealed using the short-wave traveling offsets (R1 ~ R4). In contrast, $v_{p,\,app}$ determined using the measurements from R5 ~ R7 are more or less isotropic. This might indicate that the anisotropy is present in the near-borehole region and that the elastic stiffness is generally higher at the azimuths within ranges of 90°~120° and 270°~300°. However, the same trend of $v_{p,\,app}$ is not present in the measurements at other depths, where less discrepancy between $v_{p,\,app}$ obtained at different receivers are observed.

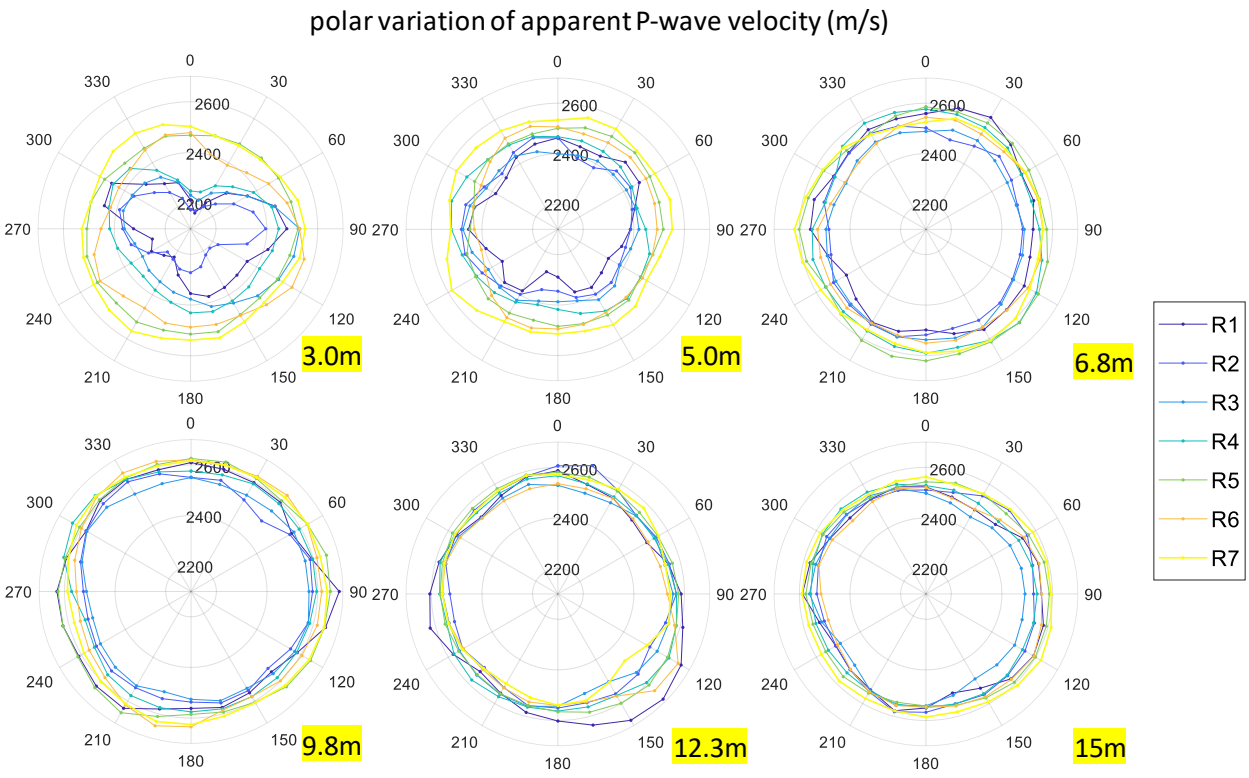

Figure 5-10. Apparent P-wave velocity $v_{p,\,app}$ determined from the 1st ROT-IVM in borehole BGC-A4. Note that the velocity at each azimuth is averaged over three measurements, including two neighboring azimuths

Data obtained from ROT-IVM can be further interpreted using tomographic inversion so that the entire velocity field around the borehole can be estimated. The inversion analysis was performed by Balland and Renaud (2009) on the same type of borehole logging data. In this study, a scheme is adopted to invert the velocity field from azimuth to azimuth sequentially. For each inversion, the ray inversion code *rayinvr* developed by Zelt and Smith (1992) for ray tracing and inversion in 2D velocity structure is used. Refraction is considered the only wave propagation mode, and the velocity structure is restrained from varying in the axial direction of the borehole. The inverted velocity structure is satisfying when the rays traveling through this structure arrive at the given receiver locations (R1 ~ R7) at approximately the same time as measured. More details of the inversion scheme can be found in Appendix VII, with an example given as a demonstration.

To automate the inversion for the entire ROT-IVM dataset, *rayinvr* is called and read through a MATLAB script. A 2D velocity field at the borehole cross-section (e.g., Figure 5-11) is constructed by interpolating the inverted velocity structures at all azimuths. The maximum resolved radius is limited by the penetration depth of the wave propagating over the largest emitter-receiver offset. The comparison with $v_{p,\,app}$ in Figure 5-10 shows that the inverted v_p has a higher spatial variation - it increases rapidly

from the borehole wall at a lower-bound value of about 2 km/s to the far-field of about 2.8 km/s as indicated at the maximum resolved radius. However, the inversion tends to attenuate the anisotropy of the inverted v_p compared to that of $v_{p,\,app}$. This was also observed by Balland and Renaud (2009) from their tomography analysis on a similar type of data. The region in the borehole annulus with a velocity close to the lower-bound value is identified and possibly indicates the extent of intense damage. For the measurement at 3m, the intense damage zone has a maximum radial extent of 1~2 cm, preferably covering the top and bottom parts of the borehole wall. The extent of the borehole damage is smaller and less anisotropic in the measurements at deeper intervals (e.g., 9.8m, 12.3m, and 15m). The convergence of velocity measured over shorter offset (e.g., by R1) and larger offset (e.g., by R7) from ROT-IVM at deeper depth agrees with the IVM logging shown in Figure 5-9.

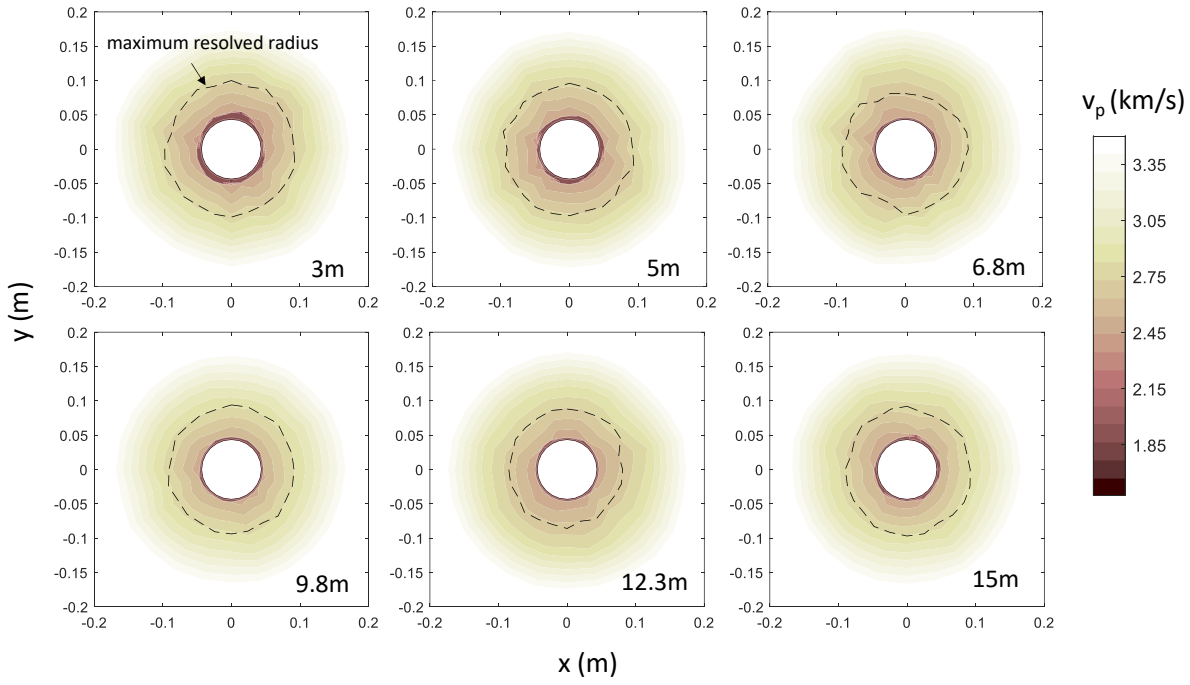

Figure 5-11. Variation of the inverted velocity in the borehole cross-section from 1st ROT-IVM at different depths (the depth is the location of the emitter) in borehole BGC-A4

5.3.2 Pressuremeter Test (PMT)

In pressuremeter tests, the difference in borehole deformation captured by individual caliper arms in different axes may reveal the anisotropy of the ground. It was attempted by Rocha (1970) and Zalesky et al. (2007) to measure the anisotropic deformability of the rock mass using the displacement readings from diametric transducers for cycles of loading and unloading. For PMT in GC experiments at the Mont Terri Rock Laboratory, the anisotropy of borehole modulus G^*, defined as $G^* = p_c \big/ \left(2\varepsilon_c^*\right)$, can be identified

using the measurements from different pairs of the caliper arms. ε_c^* is the radial displacement normalized by the initial borehole radius, i.e., $\varepsilon_c^* = u_r / r_0$. In Figure 5-12, G^* is determined for the test in the borehole drilled perpendicular to beddings. Hence, the influence of the structural anisotropy on the pressuremeter measurement is not dominant in this case. Even so, a strong anisotropy of G^* can be seen at lower unloading pressures (< 5 MPa), with the maximum G^* aligned with the axis at approximately 90° and 270°. The anisotropy decreases as the expansion pressure increases, and the variation of G^* becomes stable at the higher expansion pressure levels (> 5 MPa).

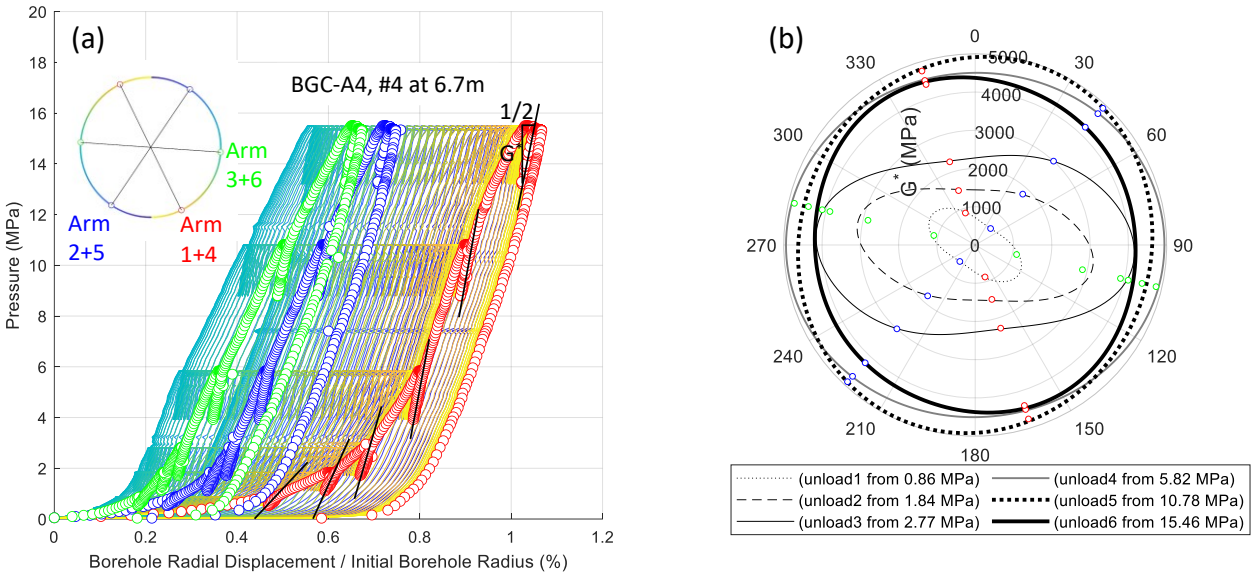

Figure 5-12. (a) Determination of the borehole modulus G^* using the pairs of the caliper measurements (solid dots) or the borehole deformation curves (lines) corrected for varying azimuths; (b) the azimuthal variations of G^* obtained at different unloading pressure levels. The test data is obtained in test #4 in borehole BGC-A4 (perpendicular to the beddings).

The interpretation of G^* is applied to all the test data obtained from borehole BGC-A4 except test #1, where unload-reload cycles were not attempted. Pronounced anisotropy of borehole modulus is observed at the lower pressure levels (Figure 5-13(a)) nearly for all the tests. In contrast, the borehole modulus obtained at the higher-pressure levels tends to be isotropic. The observed evolutions of G^* and its anisotropy with pressure may be explained by the heterogeneous response of the Opalinus Clay at the borehole wall during pressuremeter loading. It was indicated in earlier chapters that the mechanical properties of the medium might be perturbed by local stress concentration around a borehole unloaded from anisotropic in-situ stresses. As a demonstration, the conceptual state of Opalinus Clay in the borehole nearfield is hypothesized in Figure 5-14. For the scenario where the stress concentration exceeds the damage threshold of the rock, the borehole damage zone (BDZ) infused with the extensile micro-

fractures is preferentially developed in the direction of the minimum in-plane stress σ_{min}. The subsequent pressuremeter loading tends to close these micro-fractures in the BDZ and recover the elastic modulus surrounding the borehole to different extents. This hypothesis, however, needs to be further examined with additional physical evidence.

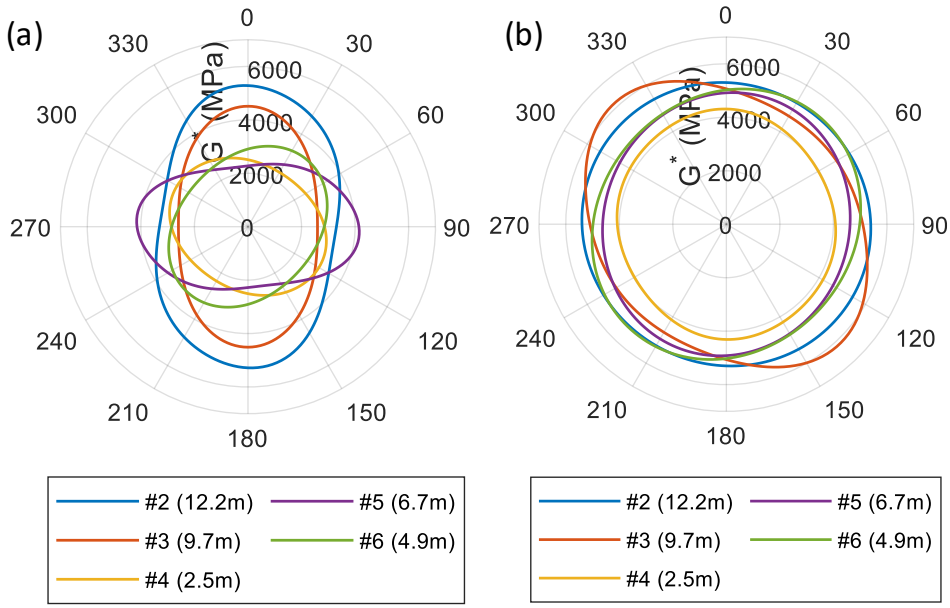

Figure 5-13. azimuthal variations of G^* determined using unload-reload cycles at the (a) lower presure levels (p_c = 2.77 ~ 2.91 MPa) and (b) higher pressure levels (p_c = 8.40 ~ 10.78 MPa). Note that test #1 does not have unload-reload cycles.

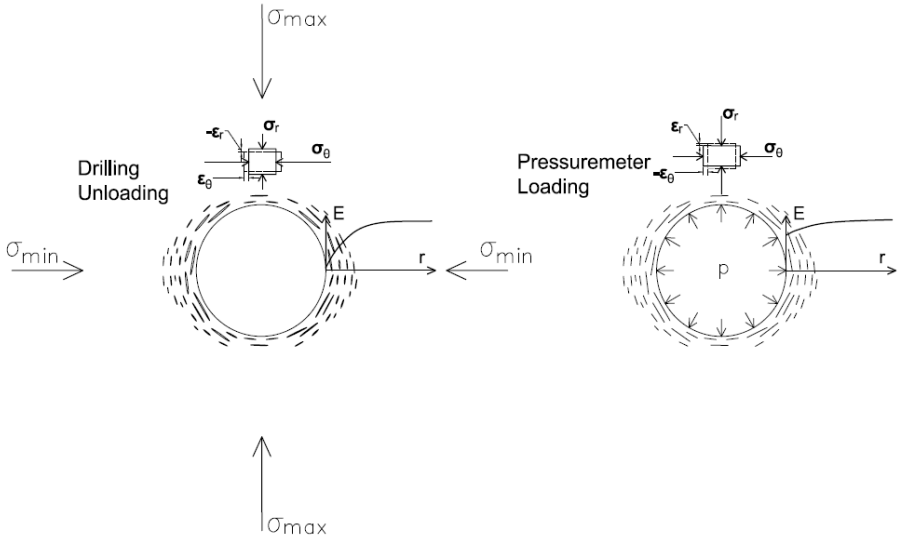

Figure 5-14. Conceptual state of near-borehole micro-crack opening/initiation and closure during unloading and reloading, respectively. The evolution of the modulus E in radius at two stages is illustrated.

5.4 Discussion on the Discrepancy between BDZ Indications

The P-wave velocity contour in Figure 5-11 indicates that the BDZ is preferentially localized at the upper (0°) and lower parts (90°) of borehole annulus according to ROT-IVMs at 3m and 5m in borehole BGC-A4. Suppose the azimuth of the minimum G^* determined from PMT at lower pressure levels also reflects the location of the BDZ. In that case, G^* obtained from PMTs at 2.5m, 4.9m, and 6.7m shown in Figure 5-13 have a rough agreement with ROT-IVM indication, while G^* obtained at 9.7m and 12.2m indicates that the BDZ is oriented at the azimuths near 90° and 270°. The latter is closer to the prediction based on stress analysis, as shown in Figure 5-1 (a) or Figure 5-6.

Maybe a question that needs to answer first is why ROT-IVMs at deeper depths (> 5m) exhibit minimum or no evidence of borehole damage. Based on the findings from laboratory investigation (Chapter 3), the change of wave velocity (or dynamic modulus) is not significant after an Opalinus Clay specimen is damaged under high deviatoric stress, only with a maximum of 5% reduction from its original value. This 5% difference might not be well resolved by the velocity model with a limited number of layers. More likely, the averaging effect of wave transmission over a larger offset (e.g., 20cm for R4 in Figure 2-8) will mask a local reduction of the velocity when damage at the borehole wall appears to be non-uniform in the borehole longitudinal direction because of pronounced heterogeneity in lithofacies at the centimeter scale.

One may also ask for ROT-IVM at 3m why the inverted v_p does show a noticeable velocity drop by about 30% from the far-field to the borehole wall. To answer this question, it is important to keep in mind that other factors might influence the wave velocity value at the same time. One of them is moisture. The impact of moisture on the wave velocity was demonstrated in Chapter 3 from measurement on samples preconditioned under different relative humidities. A more relevant study can be found in Mitaritonna et al. (2009), who subjected the Opalinus Clay specimens to a cycle of wetting and drying and measured the evolution of the wave velocity using a low-frequency pulse (≤ 54 kHz). They found the change of the velocity value could be as significant as up to 30% after the specimen was desaturated in an environment with relative humidity dropping from 99% to 50%. The effect of the moisture-related de- or re-saturation in the test borehole BGC-A4 was also implied in Figure 2-11, showing the temporal variation of the apparent P-wave velocity over three days. After the first measurements, ROT-IVM was also repeated in borehole BGC-A4 at multiple depths covering a few PMT intervals. A comparison was made between the 1st and repeat measurements showing the significant changes in the magnitude and anisotropy of $v_{p,\,app}$ almost at every receiver (R1 ~ R7). The change was most pronounced for the waves received at R1, suggesting its high sensitivity to the residual effect of pressuremeter loading and/or the atmospheric moisture variation over time. It should also be noted that compared to the deeper depths (e.g., 9.8m in Figure 5-15), the shallower section of the borehole (e.g., at 3.0m) could be more affected by the air

ventilation from the tunnel and undergo a longer exposure to the atmosphere. The moisture (and saturation) variation is therefore not consistent throughout the borehole, and its impact on the ROT-IVM is difficult to quantify. For this reason, the use of the velocity data alone to characterize the mechanical disturbance of the borehole wall becomes challenging.

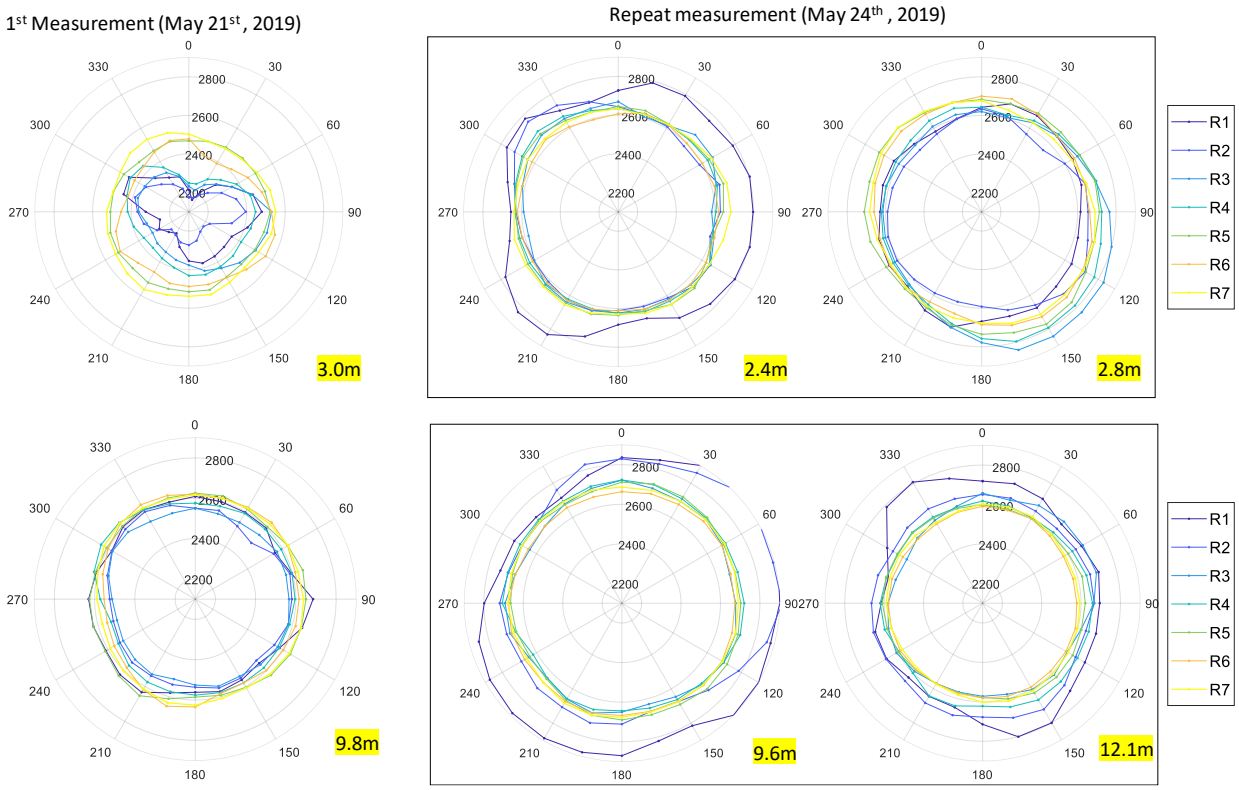

Figure 5-15. Comparison of apparent P-wave velocities $v_{p,\,app}$ (m/s) obtained from the 1st ROT-IVM and repeat ROT-IVM at the similar depths

5.4.1 Stress Field along Test Boreholes

G^* has shown different anisotropies between tests at shallower (2.5m, 4.9m, and 6.7m) and deeper (9.7m and 12.2m) depths. According to the stress analysis, for example, in Figure 5-18, the location and extent of BDZ are determined by the magnitude and orientation of far-field stresses at the borehole cross-section plane. Therefore, the rotation of G^* may be a consequence of the change of the local stress field from depth to depth. The excavation may perturb the local stress field at the shallower test intervals near the borehole collar.

To investigate how and to which borehole depth the local stress varies after excavation, a 3D stress analysis was performed for the two test boreholes, BGC-A4 and BGC-A6, using the finite element models shown in Figure 5-16. It should be noted that the excavation of the drift ahead of Niche2 was after the tests in borehole BGC-A4, so it is not considered in stress modeling for Case 1. In both modeling

cases, the medium is assumed to be transversely isotropic. The isotropic plane is parallel to the beddings of the Opalinus Clay that have a dipping angle of approximately 50° (Figure 5-16). The elastic properties used in the modeling are calibrated from the laboratory investigation (Section 2.4.3) and listed in Table 5-3.

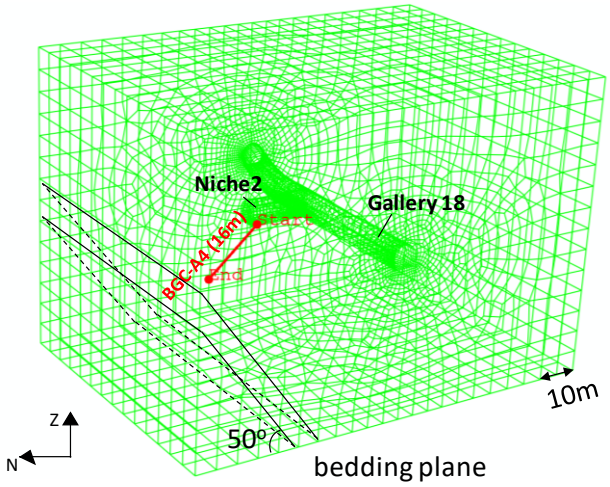

Case 1

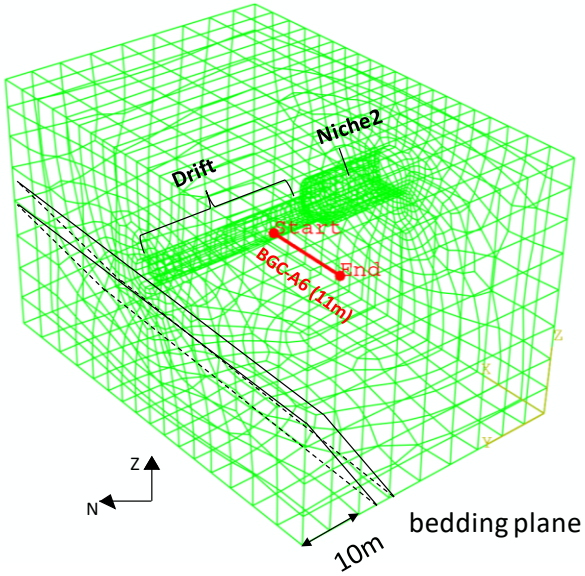

Case 2

Figure 5-16. Finite element models (only surface meshes are included in the illustration) for stress analysis along boreholes (a) BGC-A4 and (b) BGC-A6

The computed distribution of the deviator stress ($\sigma_1 - \sigma_3$) around the excavation is shown in Figure 5-17. An intense stress concentration is predicted at the corners where the niche is connected with the drift/gallery. The excavation only gently perturbs the stresses along the borehole trajectories. The computed stress can be further projected on the plane perpendicular to the borehole (Figure 5-18), and in this way, the far-field stresses at the pressuremeter testing planes can be estimated. It is found that the influence of the excavation on the stress field extends to a depth of about 4m along the borehole axis in both boreholes. The rotation of the far-field stresses in the testing plane is observed, with the maximum changes of about 50° and 15° at the borehole collar for boreholes BGC-A4 and BGC-A6, respectively. However, at the PMT depth nearest to the borehole collar, this stress rotation is quickly reduced to less than 10° in each case. Therefore, the rotation of G^* from shallower to deeper depths shown in Figure 5-13 is not likely caused by the rotation of the local stress field.

It should be kept in mind that the actual disturbance induced by excavation may also depend on other factors not considered in this study, such as the excavation methods (Bossart et al. 2002) and the unloading stress path (Corkum 2006) - the temporal variations of both total stress and pore pressure would impact the stress state at the end of the excavation.

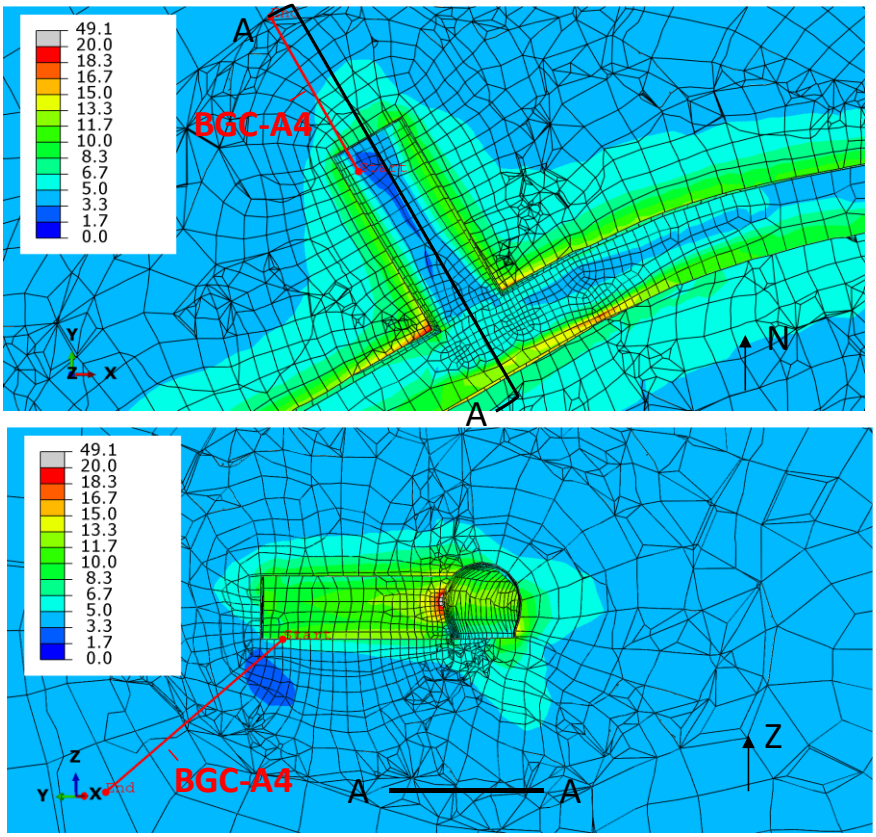

(a) Case 1

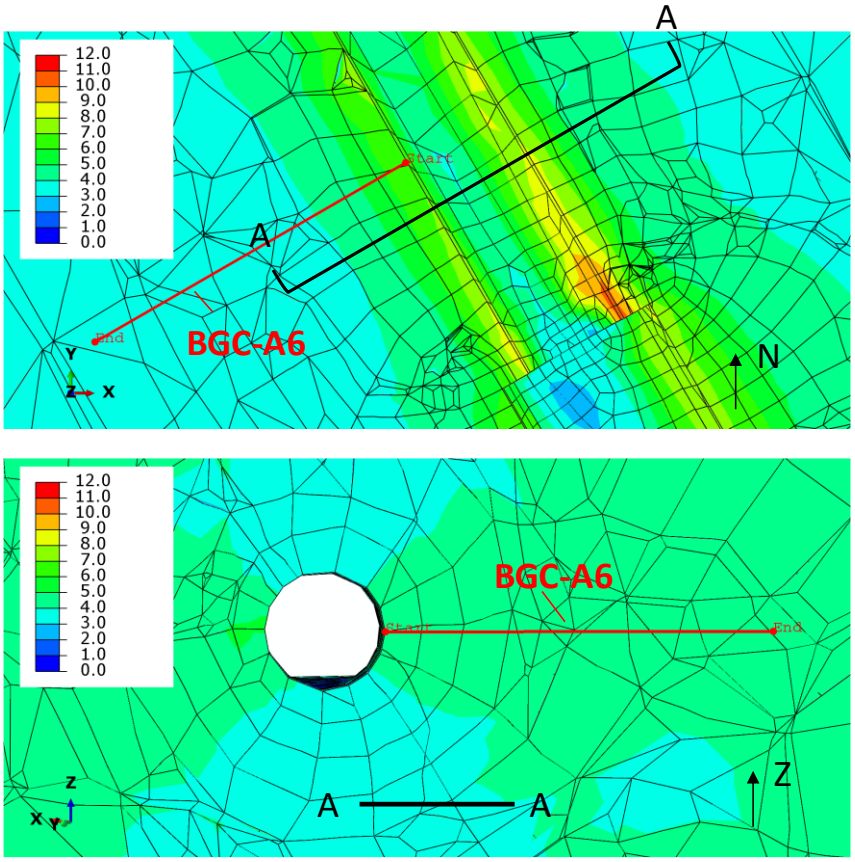

(b) Case 2

Figure 5-17. Distribution of the deviator stress ($\sigma_1 - \sigma_3$) around the excavation from stress modeling for two cases

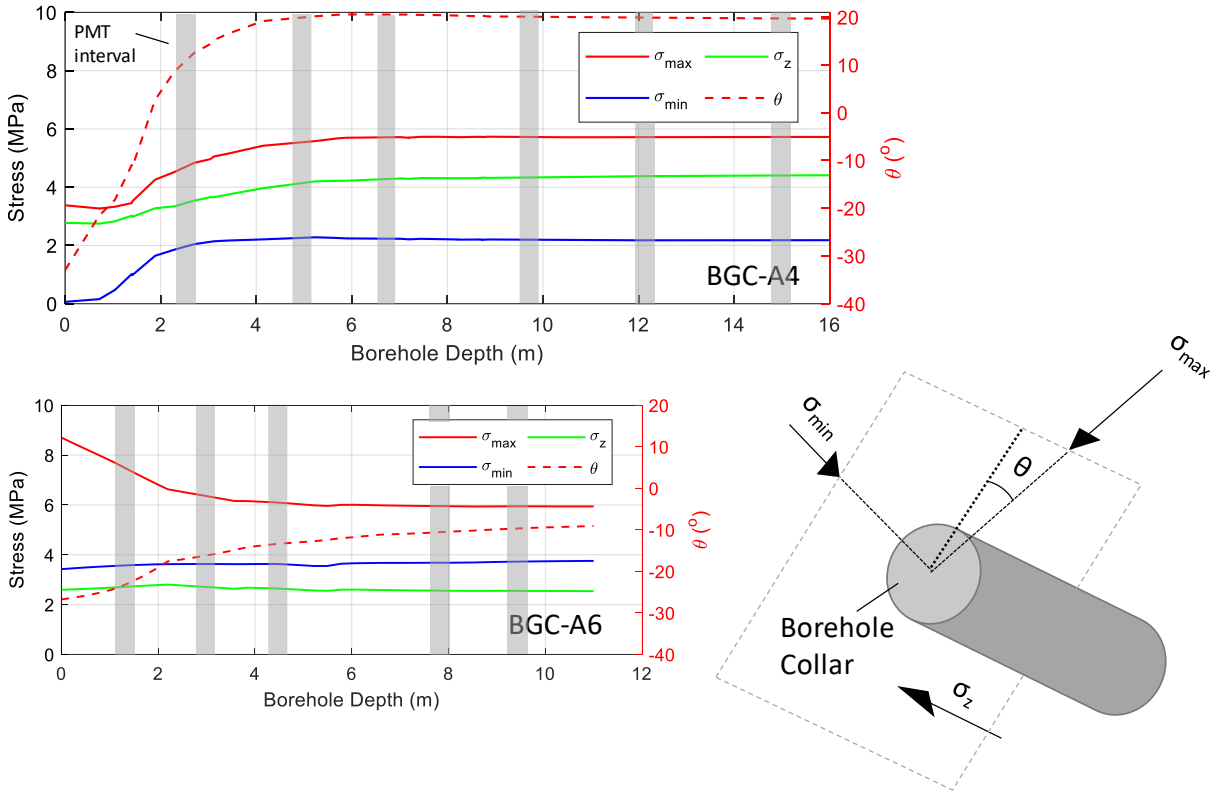

Figure 5-18. Predicted variation of stresses in the plane perpendicular to boreholes BGC-A4 and BGC-A6. σ_{max} and σ_{min} are the maximum and minimum principal stresses respectively in the plane of the borehole cross-section, and σ_z is the far-field stress perpendicular to the plane.

5.4.2 Impact of Stress-dependent Elastic Stiffness

It was discussed in both Chapters 3 and 4 that the elastic stiffness is also explicitly dependent on the stress, so the local stress redistribution around an unloaded borehole would change the elastic properties from the virgin state, even when borehole damage is absent. In this section, to demonstrate the effect of stress-dependent stiffness on G^* under an anisotropic in-situ stress condition, numerical examples will be given using the proposed constitutive model in Chapter 4.

The finite element model used in this study consists of a quadrant of the borehole cross-section, where the stresses σ_{max} and σ_{min} in the XY plane are initially applied parallel to the Y- and X-axes, respectively (Figure 5-19). The model has a minimum thickness in the Z direction. The longitudinal stress σ_z is applied initially in the geostatic step, followed by two successive steps - 1) an unloading step with the reduction of normal and shear stress at the borehole wall and 2) a reloading step with the increase of normal stress p. The stress boundary in the Z direction is replaced by a fixed normal displacement boundary in the last two steps so that the plane-strain condition can be provoked. The far-field stresses estimated for borehole BGC-A4 are considered in this example – σ_{max} = 5.8 MPa, σ_{min} = 2.3 MPa and σ_z = 4.6 MPa.

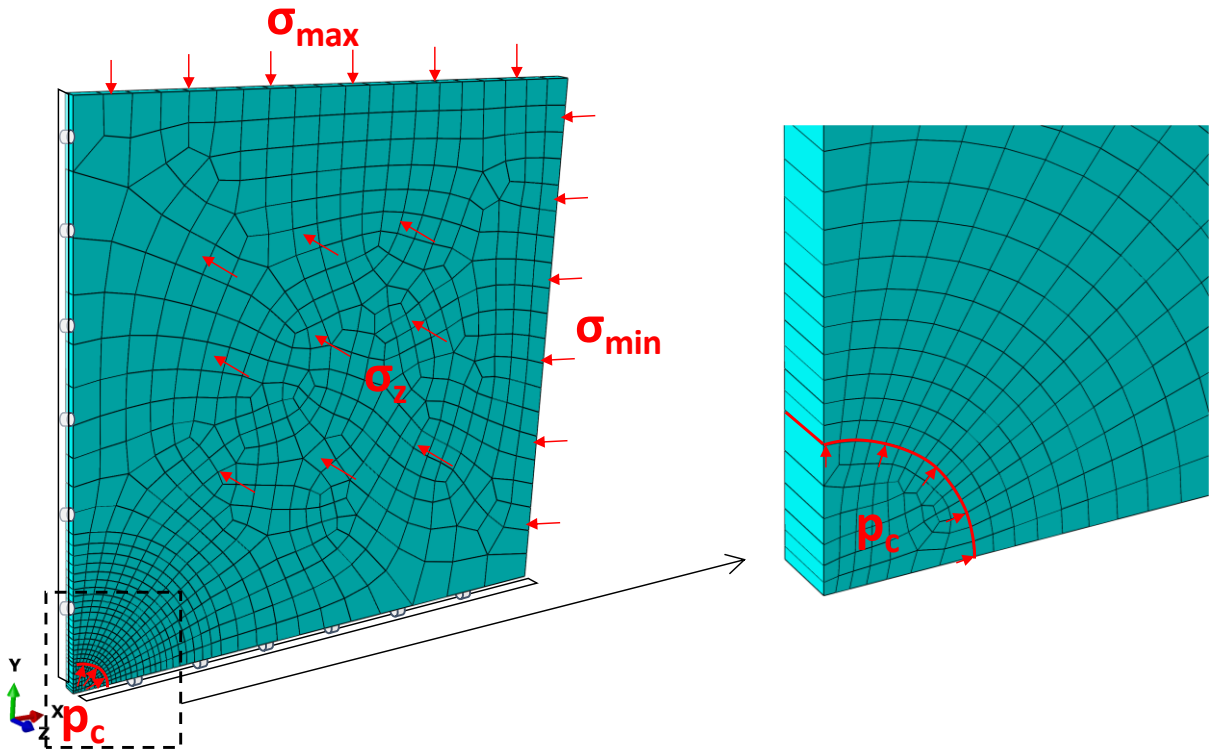

Figure 5-19. Geometry and boundary conditions for borehole unloading and loading modeling under anisotropic boundary stresses.

To model the pressuremeter tests in borehole BGC-A4, the medium is assumed to be isotropic elastic initially. Three stress-dependent stiffness formulations were proposed and discussed in Chapter 4. The function that considered the stress-induced anisotropy (*AniDM*) was favored due to its capability of capturing the nonlinearities of stress-strain response in both triaxial and pressuremeter tests. However, *AniDM* also has drawbacks. For example, in Chapter 3, Young's modulus E remains almost constant with an increase of the axial stress σ_A under a constant mean stress path in triaxial tests, whereas *AniDM* would predict an increase of E with σ_A. In comparison, the stiffness function based on the mean stress p (*PDM*) is more appropriate to account for the change of E regardless of the stress path. It should also be noted that unlike the case of the axisymmetric borehole boundary considered in Chapter 4, the mean stress is expected to vary both radially and circumferentially around a borehole when anisotropic boundary stresses are imposed. Therefore, *PDM* would not suffer from the drawback of predicting constant elastic stiffness, as shown in Chapter 4. For this reason, *PDM* is adopted in this study.

Two model parameters $E^{(1)}$ and $\nu^{(1)}$ required for *PDM* were calibrated in Chapter 4 from triaxial test data reported by Graesle and Plischke (2011) (Table 5-4). In addition, to investigate the borehole response with different stress-dependent stiffness nonlinearities, $b = 0$ (i.e., constant elastic modulus) and $b = 0.25$

are also considered. $E^{(1)}$ is adjusted accordingly for the latter two cases so that the elastic stiffness is consistent at the initial condition with the mean stress p equal to 4.23 MPa for all cases.

Table 5-4. Nonlinear elastic properties considered in the modeling

Case	$E^{(1)}$	$v^{(1)}$	b	$E^{(initial)}$	$p^{(initial)}$
	(GPa)			(GPa)	(MPa)
1	9.26	0.2	0	9.26	4.23
2	6.45	0.2	0.25		
3	4.50	0.2	0.5		

Three cases were first predicted without the consideration of damage, i.e., $d = 0$. An example of the predicted variation of the elastic modulus E after borehole stress relief is shown in Figure 5-20 using the normalized parameter, i.e., $E / E^{(initial)}$. As expected, the mean stress increase near the azimuth of σ_{min} stiffens rock in the near field, while stiffness decreases near the azimuth of σ_{max}. The predicted expansion with a uniform borehole pressure increase from 0 to 2 MPa for this case is shown in Figure 5-21. Borehole modulus G^* at varying axes is evaluated, for example, at $p_c = 1$ MPa, so that the impact of the local stress concentration on the pressuremeter measurement can be assessed. The azimuthal variations of G^* predicted for three cases in Table 5-4 are shown in Figure 5-22.

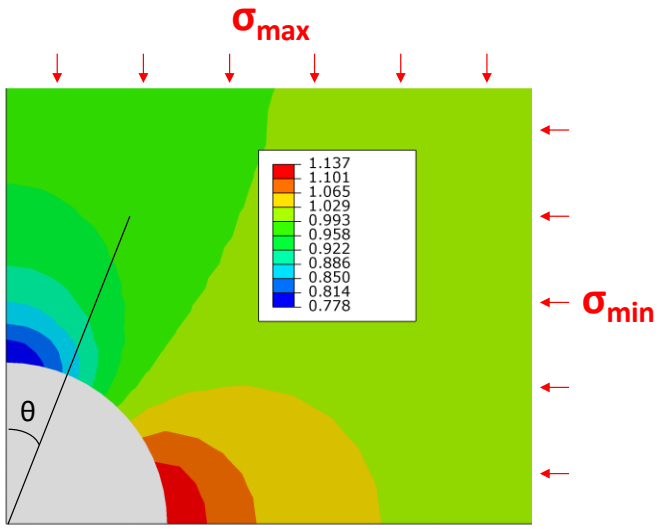

Figure 5-20. Spatial variation of elastic modulus after borehole unloading normalized by the initial elastic modulus, $E/E^{(initial)}$, based on the prediction using *PDM* with $b = 0.25$ in an elastic case.

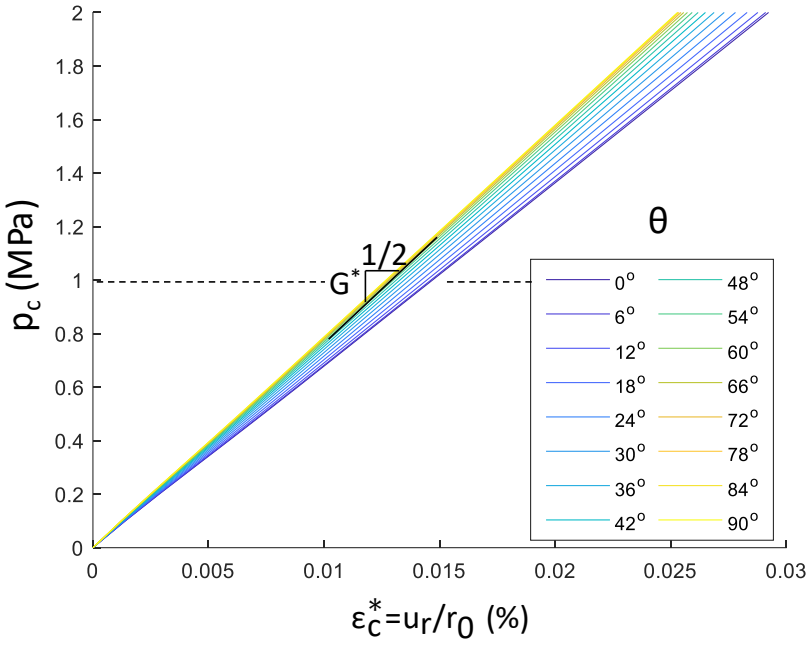

Figure 5-21. Evaluation of borehole modulus G^* using predicted pressure versus expansion curve at varying axes.

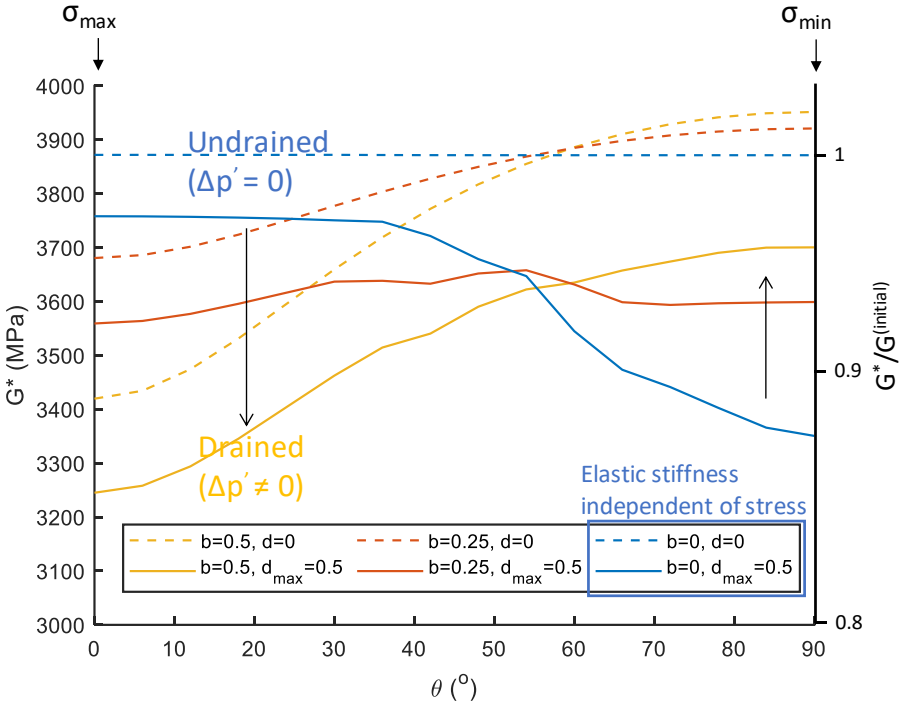

Figure 5-22. Azimuthal variations of G^* for different cases with and without BDZ. The transition from undrained to drained borehole unloading assumes that the stiffness is dependent on effective mean stress p'.

Borehole damage is further considered in all three cases using the stress-based damage and failure criteria shown in Figure 5-5. The predicted borehole damage zone is preferentially localized at the azimuth of σ_{min}, for example, in Figure 5-23 (a). The damage effect is coupled with the stress dependency in the prediction, and an example of the predicted modulus variation around an unloaded borehole is shown in Figure 5-23 (b). It can be seen that in the axis of σ_{min}, the elastic stiffness is significantly degraded near the borehole wall due to damage, whereas beyond this damage zone, the modulus is increased because of the stress concentration effect. Therefore, for the three cases with localized BDZ, the predicted modulus at $\theta = 90^{o}$ may be affected by both borehole damage and stress concentration. When the stiffness is independent of stress, i.e., $b = 0$, G^{*} variation is dictated by the borehole damage, and a lower modulus is predicted at $\theta = 90^{o}$ than $\theta = 0^{o}$. As b increases, the impact of stress concentration eventually surpasses the impact of damage, and a higher G^{*} is predicted at $\theta = 90^{o}$ than $\theta = 0^{o}$. It is worth noting from these examples that when the borehole damage is present, G^{*} is reduced at every azimuth. This demonstrates that the localized BDZ has a global effect on the pressuremeter measurement.

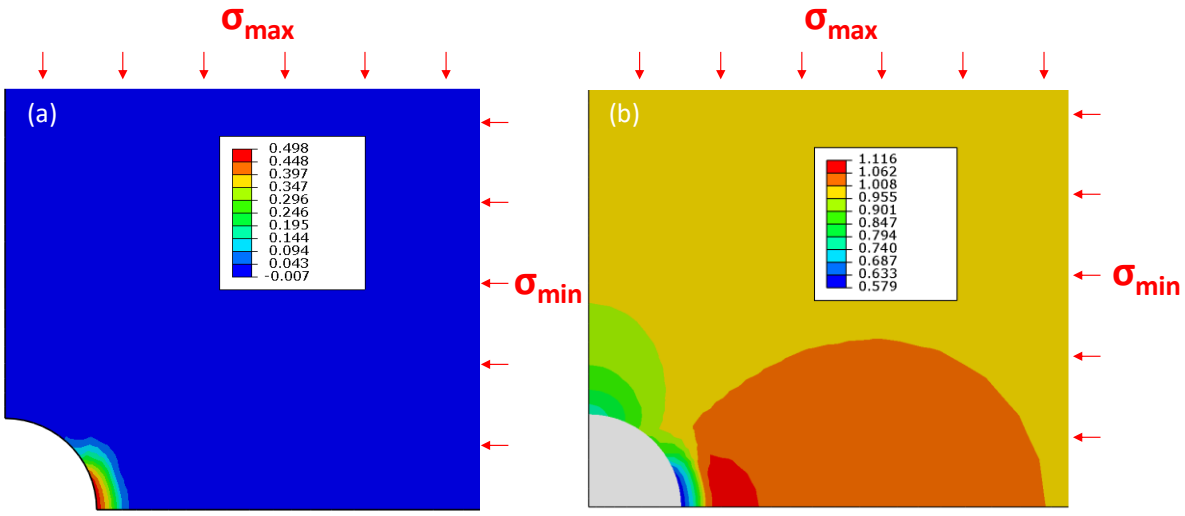

Figure 5-23. (a) predicted localized damage zone and (b) elastic modulus E normalized by $E^{(initial)}$ for b = 0.25.

For the in-situ Opalinus Clay saturated by pore fluid, it is more reasonable to define the stiffness as a function of the effective stress rather than the total stress, i.e., $E = E^{(1)}p'^{b}$. As mentioned earlier, the unloading of a borehole at the time of drilling is likely undrained. The stress redistribution around the borehole in an initially anisotropic stress field would lead to the local generation of excess pore water pressure Δu_w. If assuming that the Δu_w is only dependent on the mean stress change Δp and considering that the Biot coefficient is equal to 1, i.e., $\Delta u_w = \Delta p$, the effective mean stress should remain constant

upon undrained unloading. Liu (2015) has shown the stress path for two locations near the borehole wall, respectively, in the axes of σ_{max} and σ_{min} under this simplified condition (Figure 5-24). With $\Delta p' = 0$ immediately after drilling, E remains equal to $E^{(initial)}$, and the model prediction is equivalent to the case when $b = 0$. In the period of relaxation after drilling, excess pore pressure tends to dissipate either towards the borehole wall or the far-field, and eventually $\Delta u_w = 0$. At this stage, the change of the effective stress is equal to the change of total stress after borehole unloading, and the model prediction based on the total stress becomes adequate. This transition from undrained to drained conditions is remarked in Figure 5-22 for the case of $b = 0.5$ with the presence of BDZ. It suggests that the drainage condition can change the azimuth of the maximum (or minimum) G^* measured in pressuremeter tests. For borehole BGC-A4, drilling has spanned four days. Opalinus Clay at the deeper depths should have shorter excess pore pressure dissipation than at the shallower borehole depths that were drilled earlier. Furthermore, in the following three days of pressuremeter tests, deeper intervals were tested earlier than the shallower intervals, so the difference in the time allowed for drainage became even greater between them. Therefore, the former case was likely to be undrained, and the borehole modulus variation should be dominated by the localized damage. In contrast, the Opalinus Clay in the latter case was likely to be drained, and the effect of local stress concentration should play a significant role in borehole modulus variation. This provides a plausible reason for the observed rotation of G^* from shallow to deep depths. In fact, the azimuths of the maximum G^* for the two tests at deeper depths of 9.7m and 12.2m are approximately aligned with the azimuth of estimated σ_{max}, which agrees with the presumed undrained condition.

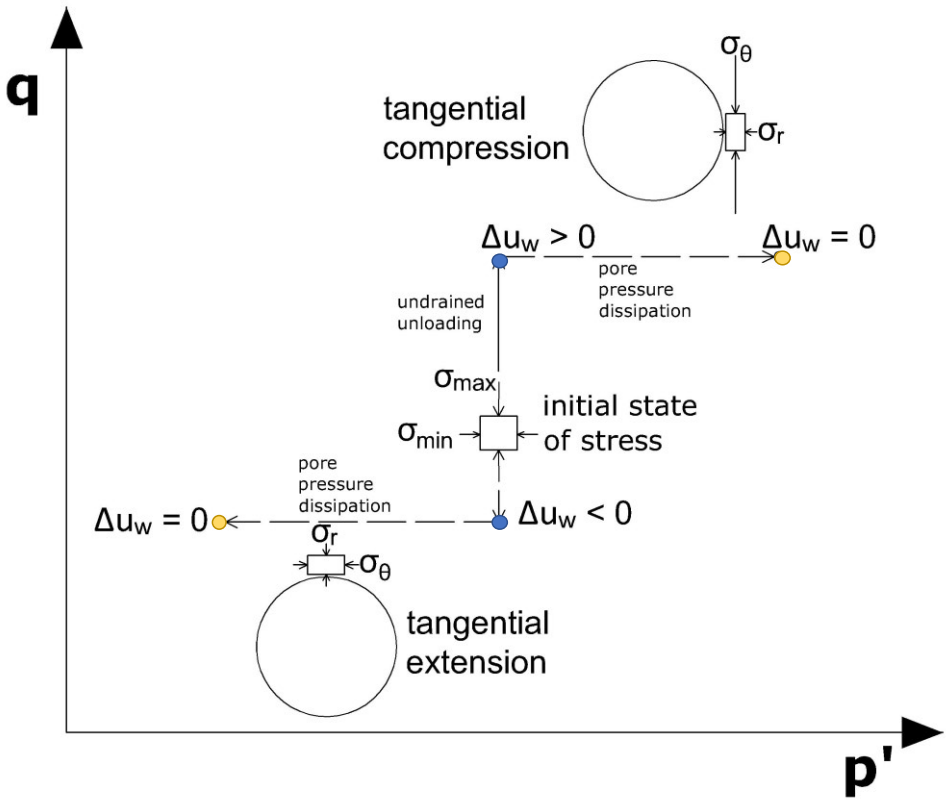

Figure 5-24. Effective stress path of rock elements at different locations near borehole wall (after Liu (2015))

5.5 Other Indications of In-situ Stress Orientation

In a recent experimental study by Liu et al. (2018), the non-uniform expansion of the borehole under pressuremeter loading in the soft cement block with polyaxial boundary stresses was investigated. Pressuremeter expanded horizontally in their tests. The results from three series of tests using different horizontal stress ratios (σ_H/σ_h) are shown in Figure 5-25(a). They observed that borehole had the maximum expansion in the direction of σ_H after yielding.

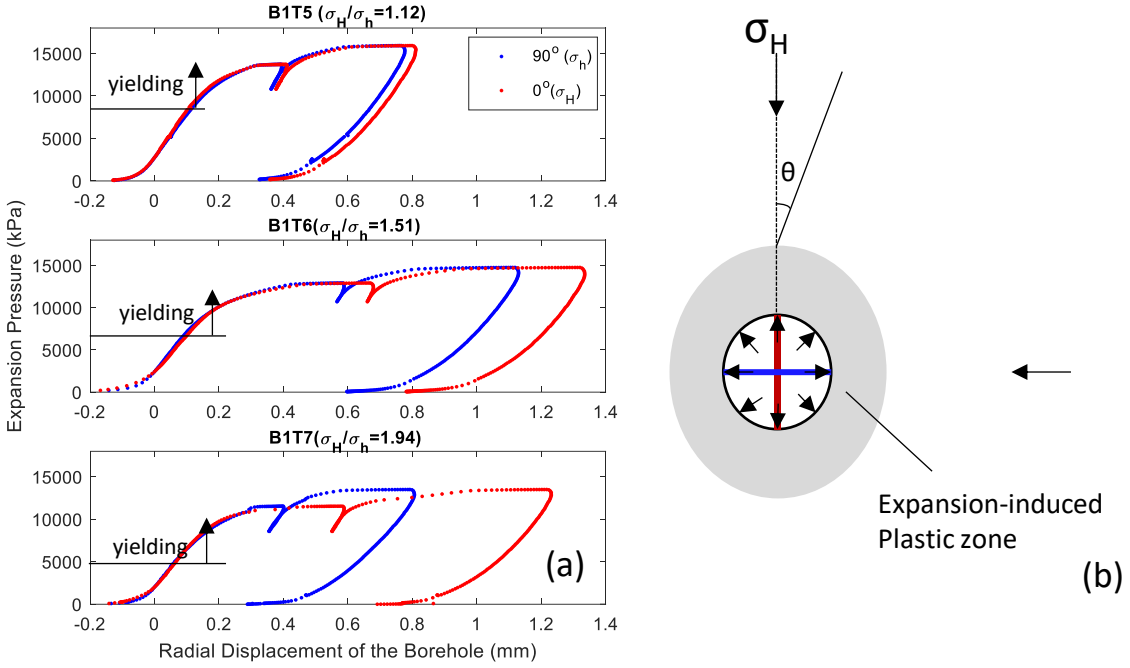

Figure 5-25. Non-uniform plastic borehole expansion in the medium under anisotropic in-plane boundary stresses: (a) data from large-scale experiment under varying boundary stress ratio σ_H/σ_h (Liu et al. 2018) and (b) schematic of expansion-induced plastic zone

According to Kirsch's equation, the shear stress at the borehole wall under an expansion pressure p_c is,

$$\tau = \frac{1}{2}\left(\sigma_r - \sigma_\theta\right) = p_c - \frac{\left(\sigma_H + \sigma_h\right)}{2} + \left(\sigma_H - \sigma_h\right)\cos(2\theta) \tag{5-3}$$

Therefore, the medium with a uniform shear strength τ_f would yield first at $\theta = 0^o$ and last at $\theta = 90^o$, when $\tau = \tau_f$. This suggests that the development of borehole plastic zone is not azimuthally uniform, as demonstrated by Zhou et al. (2016), Zhuang and Yu (2019), and Gong et al. (2021) with their solutions for cavity expansion in the medium confined by biaxial boundary stresses. The plastic zone grows faster at $\theta = 0^o$ (Figure 5-25(b)). Based on analytical and numerical results, Liu (2015), Zhou et al. (2016), Liu et al. (2021a) have shown that the plastic cavity expansion following the onset of yielding was non-uniform with the maximum magnitude at $\theta = 0^o$, agreeing with the experimental observation. The determination of the plastic expansion at varying azimuths from the pressuremeter test curves has therefore been considered by Liu et al. (2021a) in identifying the orientations of σ_H or σ_h. For materials with relatively high shear strength such as Opalinus Clay, the challenge associated with this approach remains in 1) the difficulty of yielding the ground of the high shear strength under the allowable expansion pressure limit (~ 20MPa for high-pressure dilatometer by Cambridge In-situ, Ltd) and 2) the

difficulty of identifying the yielding points as well as the plastic deformation from the test curves even if the material has yielded. Liu et al. (2021a) also discussed the effect of the anisotropic stiffness on the sequence of borehole yielding. The high borehole modulus at the azimuth of σ_h would draw the location of the initial yielding at the borehole wall from the azimuth of σ_H. However, this effect becomes negligible when a high far-field stress anisotropy or a low stiffness anisotropy is present in the expansion plane, which is the case of borehole BGC-A4.

Yielding also induces microstructural damage to the clay shales. An accelerated creep rate was recognized by Zhang and Laurich (2020) from their creep tests on Opalinus Clay specimens after yielding occurred at the deviator stress equal to 15 MPa. Using the estimated mean in-situ stress σ_0 equal to 4.23 MPa, the expansion pressure that reaches this deviator stress (σ_r - σ_θ) threshold at the borehole is 11.73 MPa according to Eqn. (5-3). Figure 5-26 shows time-dependent expansions measured at different pressure levels from PMTs in borehole BGC-A4. Accelerated creep behavior is observed in all the cases when p_c > 11.73 MPa. It suggests that the borehole had already yielded before the last pressure hold was performed.

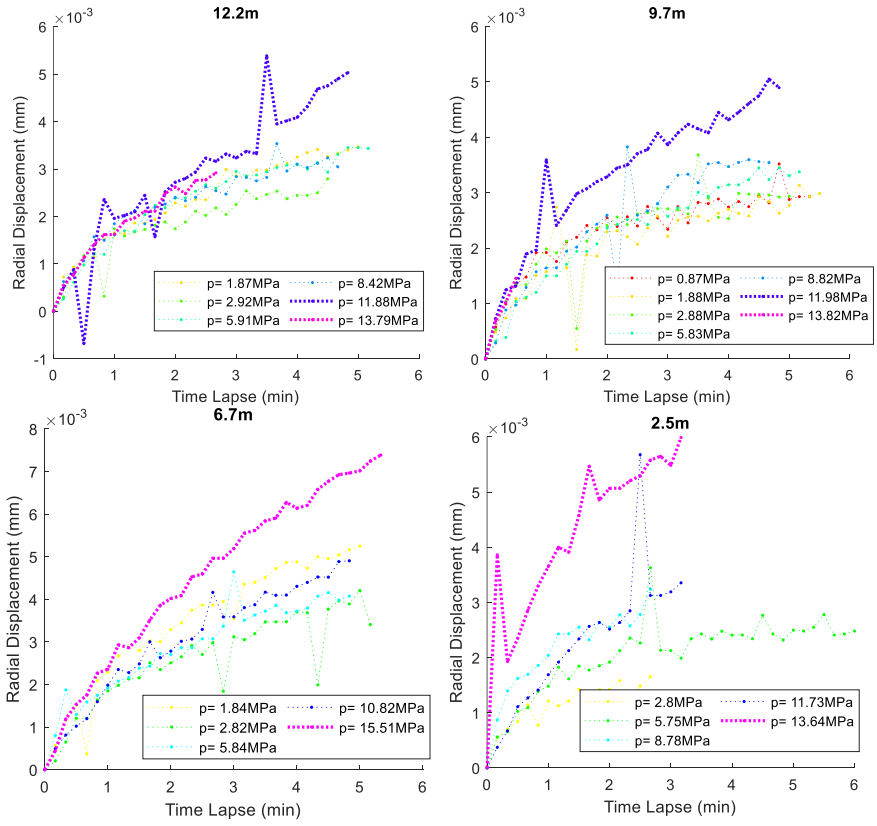

Figure 5-26. Time-dependent borehole expansion during pressure holds in PMT in borehole BGC-A4 at different pressure levels p_c. Data at the pressure holds with p_c > 11.73 MPa is highlighted. Note that two other tests do not have proper pressure hold data.

Azimuthal variation of borehole expansion during pressure holds in the testing plane can be calculated using the borehole expansion curves obtained for varying azimuths in Figure 2-22. Figure 5-27 shows the increase of the borehole expansions at the end of pressure holds from the test at 9.7m. The orientation for the maximum (or minimum) creep changes from low pressure to high pressure. This implies an evolution of the local damage/yielding zone around the borehole under expansion. At the low-pressure levels (e.g., 0.87 MPa), the maximum expansion along the direction subparallel to the minimum in-plane stress σ_{min} suggests the location of the unloading-induced damage zone, whereas at the high-pressure levels (e.g., 11.98 MPa), the maximum expansion that occurred in the direction subparallel to the maximum in-plane stress σ_{max} suggests the growth of the expansion-induced damage in the same direction.

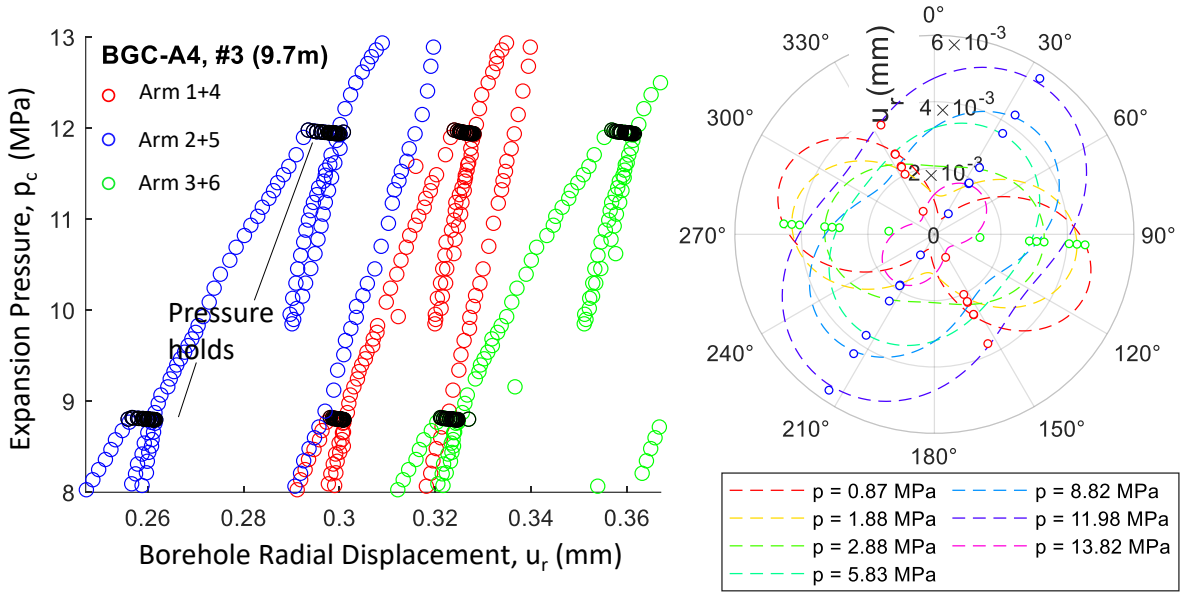

Figure 5-27. (a) Time-dependent borehole expansion monitored at different caliper axes during pressure holds and (b) borehole expansion accumulated at the end of pressure holds at multiple pressure levels p_c in PMT at 9.7m in borehole BGC-A4. Data from pressure hold at p_c = 13.82 MPa is not included due to insufficient hold time.

The measured anisotropic borehole creeps after borehole yielding under high expansion pressure are plotted in Figure 5-28. The trend of the maximum creep can be identified with a distinct orientation ranging from 0° to 35°, which implies the direction of σ_{max}. This encouragingly agrees with the orientation of the σ_{max} projected from the reported in-situ stress tensor (Table 2-1) on the borehole cross-section plane.

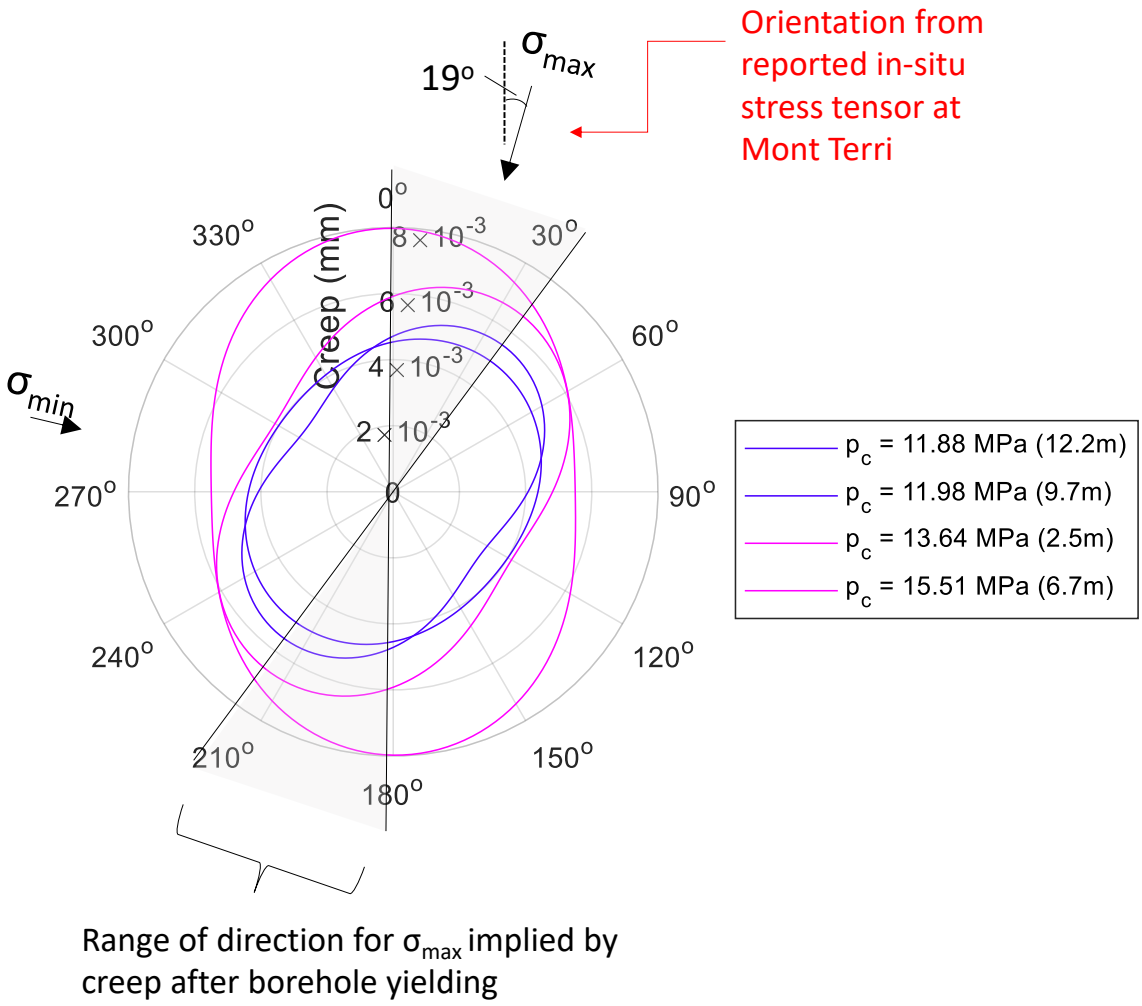

Figure 5-28. Time-dependent borehole expansion during pressure holds after borehole yielding and the implication of the in-plane stress orientation in borehole BGC-A4. Note that the in-plane far-field stresses are projected from the in-situ stress tensor given in Table 2-1.

5.6 Summary and Conclusions

In this chapter, the development of localized borehole damage zone (BDZ) due to drilling unloading has been investigated using plane-strain analysis. The elastic analysis using Kirsch's solution with reported in-situ stress suggested that BDZ covers more than half of the borehole annulus with a radial extent of >5 mm for both boreholes BGC-A4 and BGC-A6. BDZ was also predicted using a finite element analysis with the elastoplastic damage model proposed in Chapter 4. The dependence of BDZ development on the far-field stresses and the bedding orientation can be reasonably predicted when appropriate damage criteria were considered, as shown for the two boreholes respectively drilled perpendicular and parallel to bedding.

Local disturbance around the borehole was measured using rotational interval velocity measurement (ROT-IVM) in borehole BGC-A4. The spatial variation of the P-wave velocity v_p in the plane perpendicular to the borehole axis was interpreted using tomography inversion analysis on ROT-IVM data. The extent of the near-borehole disturbance zone with low v_p was identified. However, caution should be taken when using this disturbance zone to represent BDZ because v_p can be very sensitive to the atmospheric moisture variation, as demonstrated by the repeat measurement three days later.

The azimuthal variations of borehole modulus determined using pressuremeter test (PMT) data at lower pressure levels were also used to indicate the orientation of BDZ. The measured borehole modulus had a significant rotation from shallower ($\leq$ 6.7m) to deeper ($\geq$ 9.7m) test depths in borehole BGC-A4. The rotation could not be explained by the rotation of the local stress field from the bottom of the borehole to the borehole collar because the 3D stress analysis only revealed a limited stress disturbance zone (< 4m) near the excavation. To seek other explanations, the dependence of the elastic stiffness on mean stress was considered in the plane-strain modeling. The stiffening effect of local stress concentration was shown to compete with damage in the direction of σ_{min}, and the predicted anisotropy of borehole modulus could be different from the case when only the BDZ was considered. For undrained unloading, pore pressure response needs to be included in the analysis, and the elastic stiffness is dependent on the effective mean stress p' rather than the total mean stress p. This leads to a possible scenario where the borehole modulus can vary temporally from undrained ($\Delta p' = 0$) to drained ($\Delta p' > 0$) condition and potentially explains the difference in borehole moduli measured at shallower and deeper depths of the borehole BGC-A4.

The determination of BDZ has been challenged by the uncertainties addressed above, and it is unreliable to inform the far-field stress orientation based on the interpreted BDZ alone. Alternatively, measuring anisotropic borehole response after yielding under high expansion pressure has been shown as a promising technique to characterize the orientation of in-plane major (or minor) far-field stresses. For borehole BGC-A4, the far-field stress orientation suggested from the creep measurement during pressure holds after yielding has an encouraging agreement with the reported in-situ stress orientation.

Chapter 6

Summary and Conclusions

Opalinus Clay is a designated host rock for future radioactive waste disposal in Switzerland. Characterizing the elastic stiffness of Opalinus Clay and its evolution is important in the ground deformation prediction and active seismic monitoring during the construction and operation of disposal repositories. In this thesis, an in-situ method, pressuremeter testing, was employed in three boreholes at the Mont Terri Rock Laboratory to determine the in-situ elastic stiffness of the Opalinus Clay. Elastic stiffness was also evaluated using the historical triaxial test data and the data from supplementary laboratory investigation in this thesis. The assessment of the results obtained from both pressuremeter tests and laboratory triaxial tests allowed for developing a unified constitutive framework to predict the evolution of the elastic stiffness under varying stress paths. An elastoplastic damage model incorporating the stress dependency of the elastic stiffness was formulated for this purpose. The implementation of the model in finite element analysis enabled the prediction of borehole response during drilling unloading and pressuremeter loading, which lent some insights into the interpretation of field data.

Chapter 1 laid out the background of this research and introduced the critical factors to be considered in evaluating the elastic stiffness of rocks. It emphasized the in-situ methods of the elastic stiffness measurement and the challenges one should be aware of in obtaining representative elastic stiffness values.

In Chapter 2, geological settings and in-situ testing techniques employed in the field campaign at Mont Terri Rock Laboratory were introduced. Shear modulus was measured by pressuremeter testing in Oplainus Clay using the unload-reload cycles. It revealed small-strain nonlinearity and a strong stress dependency at expansion pressure $p_c < 5$ MPa. The interpreted shear modulus showed an agreement with those measured from triaxial tests on laboratory specimens when small-strain nonlinearity, elastic anisotropy, shear mode, and loading path were considered. The local discontinuities in the rock mass, such as the fault plane, are also shown to affect the measured modulus, but the influence is constrained by their location and orientation in the test interval. A reduced modulus resulting from mechanical damage was recognized at the initial pressuremeter loading and the post-peak stage of triaxial loading. A representative modulus value of approximately 3 GPa was established for intact Opalinus Clay at the Mont Terri site for the shear strain amplitude at 1e-3. The comparison between laboratory and in-situ measurement has been further extended to the anisotropic elastic stiffness determination. The prediction using the anisotropic elasticity parameters obtained from laboratory tests agreed with the anisotropic

borehole modulus measured at $p_c > 5$ MPa in a borehole drilled parallel to bedding planes. However, the agreement can be improved by considering the localized borehole damage induced by drilling unloading.

In Chapter 3, the evolution of the elastic stiffness under a borehole unloading and loading cycle was investigated using triaxial tests on Opalinus Clay specimens with continuous ultrasonic wave measurement. Under axial compression, the measured dynamic elastic properties exhibited different variations between triaxial tests with constant lateral and constant mean stresses. The results suggested a dominant dependence of the elastic stiffness on the mean stress. However, the dependency is complicated by the orientations of wave propagation/polarization and applied stresses with respect to the bedding structures. Damage initiation was identified at the stress where the wave velocity rapidly reduced. This stress threshold was shown to be lower for tests conducted under the fluid-saturated specimens than those conducted on unsaturated specimens. The stress threshold also differs between triaxial compression and triaxial extension.

In Chapter 4, the evolution of elastic stiffness was modeled for the full range from the initial loading to the post-peak shear failure using multi-stage triaxial tests data on dry Opalinus Clay specimens reported by Graesle and Plischke (2011). The evolution of elastic modulus was assessed using three stiffness functions dependent on the minimum principal stress (*Sig3DM*), mean stress (*PDM*), and full stress tensor (*AniDM*), respectively. Damage initiation and plastic yielding were also considered using strain- and stress-based formulations, respectively. The model successfully captured the elastic modulus variation and stress-strain behavior in the entire multi-staged triaxial tests. The axisymmetric borehole response in a cycle of unloading and reloading was predicted by implementing the proposed constitutive model into a finite element (FE) code. The use of *Sig3DM* or *AniDM* reproduced the nonlinear borehole deformation during the initial expansion at low pressure ($p_c < 5$ MPa). The absence of borehole damage in the prediction may indicate the inadequacy of using the strength and damage parameters calibrated from tests on dry specimens for the undrained unloading expected during borehole drilling. The modeling with reduced strength and damage threshold allowed for investigation of borehole damage development and its effect on the pressuremeter measurement. It predicted a lower pressuremeter shear modulus value in the case of borehole damage, even when the radial stress was recovered to in-situ stress at the borehole wall.

In Chapter 5, the development of localized borehole damage zone due to drilling unloading has been investigated using plane-strain analysis under in-situ conditions. The dependences of borehole damage development on the far-field stresses and the bedding orientation were investigated using different damage criteria. As one promising technique for local borehole damage detection, rotational interval velocity measurement (ROT-IVM) might be, however, governed by the sensitivity of the P-wave velocity to the saturation variation near the borehole wall. The azimuthal variation of borehole modulus measured

in pressuremeter tests at low-pressure levels could also indicate the orientation of the local borehole damage zone. However, the indication might be complicated by the competition between the damage and stress dependency of stiffness in the borehole nearfield.

Both experimental and modeling studies in this work have shown that drilling-induced borehole damage in this type of weak shale can influence the pressuremeter measurement and lead to the underestimation of the intact elastic properties.

The following research work can be considered in the future:

- The low sensitivity of the dynamic elastic properties of the Opalinus Clay to applied deviatoric stresses can be investigated at a frequency range lower than that used in this study (~200 kHz). It may provide insights to explain the discrepancy with the static elastic properties that exhibit high sensitivity to the applied stress.
- Because the geological structures and their evolution under triaxial stress have a significant on the elastic and acoustic properties of Opalinus Clay, further experiments can be conducted on the specimens with varying orientations and under multi-axial loading (or true triaxial stress) conditions.
- In this study, the image evidence of the borehole damage in borehole BGC-A4 was not available at the time of drilling. This evidence, for example, by televiewer, is critical in identifying the locations and orientations of discontinuities, whether natural or induced, at the borehole wall. Other in-situ measurements, such as continuous ultrasonic velocity and resistivity loggings, are also necessary to quantify the temporal evolutions of the saturation and petrophysical properties at the borehole wall. These measurements will allow for accurate characterization of the initial borehole condition before PMT.
- The discontinuum or continuum-discontinuum numerical approaches can be employed in modeling the discrete damage behaviors, such as bedding breakage, as observed in borehole BGC-A6. This will allow for a more realistic prediction of borehole response in a cycle of unloading and reloading. This may also capture the frictional behavior of Opalinus Clay, even at a small strain. However, the calibration of the model parameters at the grain scale can be challenging.

References

Amadei B (1983) Rock Anisotropy and the Theory of Stress Measurement. Springer-Verlag Berlin Heidelberg

Amadei B (1996) Importance of anisotropy when estimating and measuring in situ stresses in rock. Int J Rock Mech Min Sci Geomech Abstr 33:293–325. https://doi.org/10.1016/0148-9062(95)00062-3

Amadei B, Savage WZ (1991) Analysis of borehole expansion and gallery tests in anisotropic rock masses. Int J Rock Mech Min Sci 28:383–396. https://doi.org/10.1016/0148-9062(91)90077-Y

Amann F, Alan E, Frederick K, Valentin E, Gischig S, Blu M (2011) Experimental Study of the Brittle Behavior of Clay shale in Rapid Unconfined Compression. Rock Mech Rock Eng 44:415–430. https://doi.org/10.1007/s00603-011-0156-3

Amann F, Kaiser P, Button EA (2012) Experimental study of brittle behavior of clay shale in rapid triaxial compression. Rock Mech Rock Eng 45:21–33. https://doi.org/10.1007/s00603-011-0195-9

Amann F, Wild KM, Loew S, Yong S, Thoeny R, Frank E (2017) Geomechanical behaviour of Opalinus Clay at multiple scales: results from Mont Terri rock laboratory (Switzerland). Swiss J Geosci 110:151–171. https://doi.org/10.1007/s00015-016-0245-0

Aristorenas G V. (1992) Time-Dependent Behavior of Tunnels Excavated in Shale. Massachusetts Institute of Technology

Balland C, Renaud V (2009) High-resolution velocity field imaging around a borehole: Excavation-damaged zone characterization. Geophysics 74:XE223-E232. https://doi.org/10.1190/1.3237115

Barla M (1999) Tunnels in swelling ground: simulation of 3D stress paths by triaxial laboratory testing. Politecnico di Torino

Batzle ML, Han DH, Hofmann R (2006) Fluid mobility and frequency-dependent seismic velocity - Direct measurements. Geophysics 71:1–9. https://doi.org/10.1190/1.2159053

Bertrand F, Collin F (2017) Anisotropic modelling of Opalinus Clay behaviour: From triaxial tests to gallery excavation application. J Rock Mech Geotech Eng 9:435–448. https://doi.org/10.1016/j.jrmge.2016.12.005

Bieniawski ZT (1967) Mechanism of brittle fracture of rock. Part I-theory of the fracture process. Int J Rock Mech Min Sci 4:. https://doi.org/10.1016/0148-9062(67)90030-7

Biot M a. (1956) Theory of Propagation of Elastic Waves in a Fluid-Saturated Porous Solid. I. Low-Frequency Range. J Acoust Soc Am 28:168–178. https://doi.org/10.1121/1.1908239

Blechschmidt I, Vomvoris S (2011) Underground research facilities and rock laboratories for the development of geological disposal concepts and repository systems. Geol Repos Syst safe Dispos spent Nucl fuels Radioact waste 82–118. https://doi.org/10.1533/9781845695422.1.82

Bolton MDM, Whittle RWR (1999) A non-linear elastic/perfectly plastic analysis for plane strain undrained expansion tests. Géotechnique 49:133–141. https://doi.org/10.1680/geot.1999.49.1.133

Bossart P, Bernier F, Birkholzer J, Bruggeman C, Connolly P, Dewonck S, Fukaya M, Herfort M, Jensen M, Matray JM, Mayor JC, Moeri A, Oyama T, Schuster K, Shigeta N, Vietor T, Wieczorek K (2017) Mont Terri rock laboratory, 20 years of research: introduction, site characteristics and overview of experiments. Swiss J Geosci 110:3–22. https://doi.org/10.1007/s00015-016-0236-1

Bossart P, Meier PM, Moeri A, Trick T, Mayor JC (2002) Geological and hydraulic characterisation of the excavation disturbed zone in the Opalinus Clay of the Mont Terri Rock Laboratory. Eng Geol 66:19–38. https://doi.org/10.1016/S0013-7952(01)00140-5

Bossart P, Wermeille S (2003) Mont Terri Project - Geology, Paleohydrology and Stress Field of the Mont Terri Region. Report of the Federal Office for Water and Geology (FOWG)

Bouasse H, Career Z (1903) On the tensile curves of vulcanized rubber. Ann Fac Sci Toulouse Math Ser 2 5:257–283

Carol I, Willam K (1996) Spurious energy dissipation/generation in stiffness recovery models for elastic degradation and damage. Int J Solids Struct 33:2939–2957. https://doi.org/10.1016/0020-7683(95)00254-5

Carter BJ, Lajtai EZ, Petukhov A (1991) Primary and remote fracture around underground cavities. Int J Numer Anal Methods Geomech 15:21–40. https://doi.org/10.1002/nag.1610150103

Chaboche JL (1993) Development of Continuum Damage Mechanics for Elastic Solids Sustaining Anisotropic and Unilateral Damage. Int J Damage Mech 2:311–329. https://doi.org/10.1177/105678959300200401

Chaboche JL (2003) Damage Mechanics. In: Comprehensive Structural Integrity. Pergamon, pp 213–284

Chiarelli A-S, Ledesert B, Sibai M, Karami M, Hoteit N (2000) Influence of mineralogy and moisture content on plasticity and induced anisotropic damage of a claystone; application to nuclear waste

disposals. Bull la Société Géologique Fr 171:621–627. https://doi.org/10.2113/171.6.621

Chiarelli AS, Shao JF, Hoteit N (2003) Modeling of elastoplastic damage behavior of a claystone. Int J Plast 19:23–45. https://doi.org/10.1016/S0749-6419(01)00017-1

Clarke BG (1995) Pressuremeters in geotechnical design. CRC Press

Clarke BG, Smith A (1992) Self-boring pressuremeter tests in weak rocks. Constr Build Mater 6:91–96

Corkum AG (2006) Non-Linear Elastic Behaviour of Opalinus Clay Around Underground Excavations. University of Alberta

Corkum AG, Martin CD (2007) The mechanical behaviour of weak mudstone (Opalinus Clay) at low stresses. Int J Rock Mech Min Sci 44:196–209. https://doi.org/10.1016/j.ijrmms.2006.06.004

Cormery F, Welemane H (2002) A critical review of some damage models with unilateral effect. 29:391–395

Coulson JH (1979) Suggested Methods for Determining In-situ Deformability of Rock. Int J Rock Mech Min Sci Geomech Abstr 16:195–214

David EC, Brantut N, Schubnel A, Zimmerman RW (2012) Sliding crack model for nonlinearity and hysteresis in the uniaxial stress-strain curve of rock. Int J Rock Mech Min Sci 52:9–17. https://doi.org/10.1016/j.ijrmms.2012.02.001

de Borst R, Sluys LJ, Muhlhaus H (1993) Fundamental Issues in Finite Element Analyses of Localization of Deformation. Eng Comput 10:99–121

Desbois G, Höhne N, Urai J, Bésuelle P, Viggiani G (2017) Deformation in cemented mudrock (Callovo-Oxfordian Clay) by microcracking, granular flow and phyllosilicate plasticity: Insights from triaxial deformation, broad ion beam polishing and scanning electron microscopy. Solid Earth 8:291–305. https://doi.org/10.5194/se-8-291-2017

Detournay E, Fairhurst C (1987) Two-dimensional elastoplastic analysis of a long, cylindrical cavity under non-hydrostatic loading. Int J Rock Mech Min Sci 24:197–211. https://doi.org/10.1016/0148-9062(87)90175-6

Dewhurst DN, Siggins AF (2006) Impact of fabric, microcracks and stress field on shale anisotropy. Geophys J Int 165:135–148. https://doi.org/10.1111/j.1365-246X.2006.02834.x

Eaton BA (1969) (1969) Fracture gradient prediction and its application in oilfield operations. J Pet Technol 246:1353–1360

Ewy RT, Cook NGW (1990a) Deformation and fracture around cylindrical openings in rock-II. Initiation, growth and interaction of fractures. Int J Rock Mech Min Sci 27:409–427. https://doi.org/10.1016/0148-9062(90)92714-P

Ewy RT, Cook NGW (1990b) Deformation and fracture around cylindrical openings in rock-I. Observations and analysis of deformations. Int J Rock Mech Min Sci 27:387–407. https://doi.org/10.1016/0148-9062(90)92714-P

Ewy RT, Stankovic RJ (2010) Shale swelling, osmosis, and acoustic changes measured under simulated downhole conditions. SPE Drill Complet 25:177–186. https://doi.org/10.2118/78160-PA

Fang X (2018) A stable explicit workflow for borehole stress calculation in tilted transversely isotropic formations. 52nd US Rock Mech Symp

Fang X, Fehler M, Zhu Z, Chen T, Brown S, Cheng A, Toksöz MN (2013) An approach for predicting stress-induced anisotropy around a borehole. Geophysics 78:D143–D150

Favero V, Ferrari A, Laloui L (2018) Anisotropic behaviour of Opalinus Clay through consolidated and drained triaxial testing in saturated conditions. Rock Mech Rock Eng 51:1305–1319. https://doi.org/10.1007/s00603-017-1398-5

Ferrari A, Minardi A, Ewy R, Laloui L (2018) Gas shales testing in controlled partially saturated conditions. Int J Rock Mech Min Sci 107:110–119. https://doi.org/10.1016/j.ijrmms.2018.05.003

Fjaer E (2006) Modeling the stress dependence of elastic wave velocities in soft rocks. Proc 41st US Rock Mech Symp - ARMA's Golden Rocks 2006 - 50 Years Rock Mech 1–8

Fjær E (2019) Relations between static and dynamic moduli of sedimentary rocks. Geophys Prospect 67:128–139. https://doi.org/10.1111/1365-2478.12711

Fjaer E, Holt RM, Raaen AM, Horsrud P (2008) Petroleum related rock mechanics, 2nd edn. Elsevier Science

Fjær E, Stroisz AM, Holt RM (2013) Elastic dispersion derived from a combination of static and dynamic measurements. Rock Mech Rock Eng 46:611–618. https://doi.org/10.1007/s00603-013-0385-8

Gaede O, Karpfinger F, Jocker J, Prioul R (2012) Comparison between analytical and 3D finite element solutions for borehole stresses in anisotropic elastic rock. Int J Rock Mech Min Sci 51:53–63. https://doi.org/10.1016/j.ijrmms.2011.12.010

Gautam R, Wong RC (2006) Transversely isotropic stiffness parameters and their measurement in

Colorado shale. Can Geotech J 43:1290–1305. https://doi.org/10.1139/t06-083

Gens A (2013) On the hydromechanical behaviour of argillaceous hard soils-weak rocks. In: Anagnostopoulos A, Pachakis M, Tsatsanifos C (eds) Proceedings of the 15th European Conference on Soil Mechanics and Geotechnical Engineering. Athens, Greece, Greece, pp 71–118

Gens A, Vaunat J, Garitte B, Wileveau Y (2007) In situ behaviour of a stiff layered clay subject to thermal loading: Observations and interpretation. Geotechnique 57:207–228. https://doi.org/10.1680/ssc.41080.0011

Giger SB, Ewy RT, Favero V, Stankovic R, Keller LM (2018a) Consolidated-undrained triaxial testing of Opalinus Clay: Results and method validation. Geomech Energy Environ 14:16–28. https://doi.org/10.1016/j.gete.2018.01.003

Giger SB, Lozovyi S, Bauer A, Schuster K, Furche M, Martin D (2018b) Reconciling static and dynamic elastic properties of Opalinus Clay at multiple scales. In: Laloui L, Ferrari A (eds) International Symposium on Energy Geotechnics. Lausanne

Gong W, Yang C, Li J, Xu L (2021) Undrained cylindrical cavity expansion in modified cam-clay soil: A semi-analytical solution considering biaxial in-situ stresses. Comput Geotech 130:103888. https://doi.org/10.1016/j.compgeo.2020.103888

Goodman RE (1989) Introduction to Rock Mechanics, 2nd Editio. John Wiley & Sons, Inc.

Goodman RE, Van TK, Heuz E (1968) Measurement of rock deformability in boreholes. 10th US Symp Rock Mech 523–556

Graesle W, Plischke I (2011) LT-A Experiment: Mechanical behavior of Opalinus Clay, Data report from Phase 15. Mont Terri Technical Note TN 2010-86.

Haimson B (2007) Micromechanisms of borehole instability leading to breakouts in rocks. Int J Rock Mech Min Sci 44:157–173. https://doi.org/10.1016/j.ijrmms.2006.06.002

Hallbauer DK, Wagner H, Cook NGW (1973) Some observations concerning the microscopic and mechanical behaviour of quartzite specimens in stiff, triaxial compression tests. Int J Rock Mech Min Sci 10:713–726. https://doi.org/10.1016/0148-9062(73)90015-6

Halm D, Dragon A (1996) A model of anisotropic damage by mesocrack growth; unilateral effect. Int J Damage Mech 5:384–402

Hansen NR, Schreyer HL (1995) Damage Deactivation. J Appl Mech 62:450.

https://doi.org/10.1115/1.2895951

Hardin BO, Blandford GE (1989) Elasticity of particulate materials. J Geotech Eng 115:788–805. https://doi.org/10.1061/(ASCE)0733-9410(1989)115:6(788)

Hawkins AB, Pinches GM (1992) Engineering description of mudrocks. Q J Eng Geol 25:17–30. https://doi.org/10.1144/gsl.qjeg.1992.025.01.02

Heap MJ, Faulkner DR (2008) Quantifying the evolution of static elastic properties as crystalline rock approaches failure. Int J Rock Mech Min Sci 45:564–573. https://doi.org/10.1016/j.ijrmms.2007.07.018

Hight DW, McMillan F, Powell JJM, Jardine RJ, Allenou CP (2003) Some characteristics of London clay. Characterisation Eng Prop Nat soils 2:851–907

Hoek E, Diederichs MS (2006) Empirical estimation of rock mass modulus. Int J Rock Mech Min Sci 43:203–215. https://doi.org/10.1016/j.ijrmms.2005.06.005

Holt RM, Bauer A, Fjær E, Stenebråten JF, Szewczyk D, Horsrud P (2015) Relating static and dynamic mechanical anisotropics of shale. 49th US Rock Mech / Geomech Symp 2015 2:833–839

Hornby BE (1992) Tomographic reconstruction of near-borehole slowness using refracted borehole sonic arrivals. Geophysics 58:1726–1738. https://doi.org/10.1190/1.1822195

Hostettler B, Reisdorf AG, Jaeggi D, Deplazes G, Bläsi H, Morard A, Feist-Burkhardt S, Waltschew A, Dietze V, Menkveld-Gfeller U (2017) Litho- and biostratigraphy of the Opalinus Clay and bounding formations in the Mont Terri rock laboratory (Switzerland). Swiss J Geosci 110:23–37. https://doi.org/10.1007/s00015-016-0250-3

Houben ME, Desbois G, Urai JL (2014) A comparative study of representative 2D microstructures in Shaly and Sandy facies of Opalinus Clay (Mont Terri, Switzerland) inferred form BIB-SEM and MIP methods. Mar Pet Geol 49:143–161. https://doi.org/10.1016/j.marpetgeo.2013.10.009

Houlsby GTT, Carter JPP (1993) The effects of pressuremeter geometry on the results of tests in clay. Géotechnique 4:567–576. https://doi.org/10.1680/geot.1993.43.4.567

Huang AB, Pan IW, Liao JJ, Wang CH, Hsieh SY (1999) Pressuremeter tests in poorly cemented weak rocks. In: Vail Rocks 1999 - 37th U.S. Symposium on Rock Mechanics (USRMS). Vail, CO, pp 247–252

IAEA (2012) The Safety Case and Safety Assessment for the Disposal of Radioactive Waste. IAEA Saf

Stand Ser Specif Saf Guid No SSG-23 140

Ismael M, Konietzky H, Herbst M (2019) A new continuum-based constitutive model for the simulation of the inherent anisotropy of Opalinus clay. Tunn Undergr Sp Technol 93:103106. https://doi.org/10.1016/j.tust.2019.103106

Jardine RJ (1992) Nonlinear stiffness parameters from undrained pressuremeter tests. Can Geotech J 29:436–447. https://doi.org/10.1139/t92-048

Jardine RJ, Symes NJ, Burland JB (1984) The measurement of soil stiffness in the triaxial apparatus. Géotechnique 34:323–340. https://doi.org/10.1680/geot.1985.35.3.378

Jin W, Arson C (2017) Non-local micromechanical anisotropic damage modeling for quasi-brittle materials : formulation and implementation. In: American Rock Mechanics Association

Johnson PA, Rasolofosaon PNJ (1996) Nonlinear elasticity and stress-induced anisotropy in rock. J Geophys Res Earth 101:3113–3124. https://doi.org/10.1029/95jb02880

Ju JW (1989) On energy-based coupled elastoplastic damage theories: Constitutive modeling and computational aspects. Int J Solids Struct 25:803–833. https://doi.org/10.1016/0020-7683(89)90015-2

Kirsch G (1898) Die theorie der elastizitat und die bedurinisse der festigkeitslehre. V D J 42:797–807

Klinkenberg M, Kaufhold S, Dohrmann R, Siegesmund S (2009) Influence of carbonate microfabrics on the failure strength of claystones. Eng Geol 107:42–54. https://doi.org/10.1016/j.enggeo.2009.04.001

Kulhawy FH (1975) Stress deformation properties of rock and rock discontinuities. Eng Geol 9:327–350

Kunkel HA, Locke S, Pikeroen B (1990) Finite-Element Analysis of Vibrational Modes in Piezoelectric Ceramic Disks. IEEE Trans Ultrason Ferroelectr Freq Control 37:316–328. https://doi.org/10.1109/58.56492

Kupferschmied N, Wild KM, Amann F, Nussbaum C, Jaeggi D, Badertscher N (2015) Time-dependent fracture formation around a borehole in a clay shale. Int J Rock Mech Min Sci 77:105–114. https://doi.org/10.1016/j.ijrmms.2015.03.027

Labiouse V, Vietor T (2014) Laboratory and in situ simulation tests of the excavation damaged zone around galleries in opalinus clay. Rock Mech Rock Eng 47:57–70. https://doi.org/10.1007/s00603-013-0389-4

Lauper B, Jaeggi D, Deplazes G, Foubert A (2018) Multi-proxy facies analysis of the Opalinus Clay and depositional implications (Mont Terri rock laboratory, Switzerland). Swiss J Geosci 111:383–398. https://doi.org/10.1007/s00015-018-0303-x

Le AD, Nguyen TS (2015) Hydromechanical response of a bedded argillaceous rock formation to excavation and water injection. Can Geotech J 52:1–17. https://doi.org/10.1139/cgj-2013-0457

Lemaitre J, Desmorat R (2005) Engineering Damage Mechanics - Ductile, Creep, Fatigue and Brittle Failures, 1st edn. Springer-Verlag Berlin Heidelberg

Leong EC, Yeo SH, Rahardjo H (2004) Measurement of wave velocities and attenuation using an ultrasonic test system. Can Geotech J 41:844–860. https://doi.org/10.1139/T04-041

Leung K, Steiger RP, Leung PK (1991) Consolidated undrained triaxial test procedure for shales. In: The 32nd US Symposium on Rock Mechanics (USRMS). pp 637–646

Li L, Fjaer E (2012) Modeling of stress-dependent static and dynamic moduli of weak sandstones. J Geophys Res Solid Earth 117:1–16. https://doi.org/10.1029/2011JB009019

Lisjak A, Grasselli G, Vietor T (2014a) Continuum-discontinuum analysis of failure mechanisms around unsupported circular excavations in anisotropic clay shales. Int J Rock Mech Min Sci 65:96–115. https://doi.org/10.1016/j.ijrmms.2013.10.006

Lisjak A, Tatone BSA, Mahabadi OK, Grasselli G, Vietor T, Marschall P (2015) Simulating the mechanical re-compaction of the EDZ in an indurated claystone (Opalinus clay). ISRM Reg Symp EUROCK 2015 639–644

Lisjak A, Tatone BSAA, Grasselli G, Vietor T (2014b) Numerical modelling of the anisotropic mechanical behaviour of opalinus clay at the laboratory-scale using FEM/DEM. Rock Mech Rock Eng 47:187–206. https://doi.org/10.1007/s00603-012-0354-7

Liu L Characterization and Modelling of Elastic Stiffness Evolution of Opalinus Clay based on Field and Laboratory Measurements. University of Alberta

Liu L (2015) Numerical Study of Reservoir Geomechanical Pressuremeter Testing under Anisotropic In-situ Stresses. University of Alberta

Liu L, Chalaturnyk R, Deisman N, Zambrano-Narvaez G (2021a) Anisotropic borehole response from pressuremeter testing in deep clay shale formations. Can Geotech J 58:1159–1179. https://doi.org/10.1139/cgj-2019-0801

Liu L, Fu H, Chalaturnyk R, Weng D, Zambrano G, Steve Z (2018) An experimental study of pressuremeter testing under polyaxial boundary stress condition. In: Proceedings of GeoShanghai 2018 International Conference: Multi-physics Processes in Soil Mechanics and Advances in Geotechnical Testing. Springer Singapore, pp 449–457

Liu L, Giger S, Martin D, Chalaturnyk R, Deisman N (2021b) Stress and strain dependencies of shear modulus from pressuremeter tests in Opalinus Clay. In: The 6th international conference on geotechnical and geophysical site characterization. Budapest

Liu L, Martin D, Giger SB, Chalaturnyk R Assessment of anisotropic elastic parameters using laboratory triaxial and in-situ pressuremeter tests in Opalinus Clay

Liu Z, Shao J, Xie S, Conil N, Talandier J (2019) Mechanical Behavior of Claystone in Lateral Decompression Test and Thermal Effect. Rock Mech Rock Eng 52:321–334. https://doi.org/10.1007/s00603-018-1573-3

Lozovyi S, Bauer A (2019) Static and dynamic stiffness measurements with Opalinus Clay. Geophys Prospect 67:997–1019. https://doi.org/10.1111/1365-2478.12720

Marschall P, Distinguin M, Shao H, Bossart P, Enachescu C, Trick T (2006) Creation and evolution of damage zones around a microtunnel in a claystone formation of the Swiss Jura Mountains. Proc - SPE Int Symp Form Damage Control 2006:851–860. https://doi.org/10.2523/98537-ms

Marschall P, Giger S, De La Vassière R, Shao H, Leung H, Nussbaum C, Trick T, Lanyon B, Senger R, Lisjak A, Alcolea A (2017) Hydro-mechanical evolution of the EDZ as transport path for radionuclides and gas: insights from the Mont Terri rock laboratory (Switzerland). Swiss J Geosci 110:173–194. https://doi.org/10.1007/s00015-016-0246-z

Martin CD (1997) The effect of cohesion loss and stress path on brittle rock strength. Can Geotech J 34:698–725. https://doi.org/10.1139/t97-030

Martin CD, Lanyon GW (2003) Measurement of in-situ stress in weak rocks at Mont Terri Rock Laboratory, Switzerland. Int J Rock Mech Min Sci 40:1077–1088. https://doi.org/10.1016/S1365-1609(03)00113-8

Martin CD, Stimpson B (1994) The effect of sample disturbance on laboratory properties of Lac du Bonnet granite. Can Geotech J 31:692–702. https://doi.org/10.1139/t94-081

Mavko G, Jizba D (1991) Estimating grain-scale fluid effects on velocity dispersion in rocks. Geophysics 56:1940–1949. https://doi.org/10.1190/1.1443005

Mavko G, Mukerji T, Dvorkin J (2009) The Rock Physics Handbook - Tools for Seismic Analysis of Porous Medium, 2nd Editio. Cambridge University Press, New York

Mavko G, Mukerji T, Godfrey N (1995) Predicting stress-induced velocity anisotropy in rocks. Geophysics 60:1081–1087. https://doi.org/10.1190/1.1443836

Mazars J, Berthaud Y, Ramtani S (1990) The unilateral behaviour of damaged concrete. Eng Fract Mech 35:629–635. https://doi.org/10.1016/0013-7944(90)90145-7

Mazars J, Pijaudier-Cabot G (1989) Continuum Damage Theory—Application to Concrete. J Eng Mech 115:345–365. https://doi.org/10.1061/(asce)0733-9399(1989)115:2(345)

Meier T, Rybacki E, Reinicke A, Dresen G (2013) Influence of borehole diameter on the formation of borehole breakouts in black shale. Int J Rock Mech Min Sci 62:74–85. https://doi.org/10.1016/j.ijrmms.2013.03.012

Meléndez-Martínez J (2006) Geomechanical Performance Assessment of CO2 – EOR Geological Storage Projects. University of Alberta

Minardi A, Ferrari A, Ewy R, Laloui L (2018) Nonlinear Elastic Response of Partially Saturated Gas Shales in Uniaxial Compression. Rock Mech Rock Eng 51:1–12. https://doi.org/10.1007/s00603-018-1453-x

Minardi A, Giger SB, Ewy RT, Stankovic R, Stenebråten J, Soldal M, Rosone M, Ferrari A, Laloui L (2021) Benchmark study of undrained triaxial testing of Opalinus clay: Results and implications for robust testing. Geomech Energy Environ 25:. https://doi.org/10.3997/2214-4609.201900334

Mitaritonna G, Pineda J, Arroyo M, Romero E (2009) The effect of drying-wetting cycles on the seismic properties of an anisotropic claystone. Poromechanics IV - 4th Biot Conf Poromechanics 286–293

Mukerji T, Mavko G (1994) Pore fluid effects on seismic velocity in anisotropic rocks. Geophysics 59:233–244. https://doi.org/10.1190/1.1443585

NAGRA (2020) NAB 20-09 Arbeitsbericht

Nawrocki PA, Dusseault MB (1995) Modelling of damaged zones around boreholes using a radius-dependent Young's modulus. Rock Mech Rock Eng 28:227–239. https://doi.org/10.2118/96-03-04

Ng C, Bolton M, Dasari G (1995) Small strain stiffness of a carbonate stiff clay. Soils Found 35:109–114. https://doi.org/10.3208/sandf.35.4_109

Nguyen TS, Le AD (2015) Development of a constitutive model for a bedded argillaceous rock from

triaxial and true triaxial tests [1]. Can Geotech J 52:1072–1086. https://doi.org/10.1139/cgj-2013-0323

Niandou H, Shao JF, Henry JP, Fourmaintraux D (1997) Laboratory investigation of the mechanical behaviour of Tournemire shale. Int J Rock Mech Min Sci 34:3–16. https://doi.org/10.1016/S1365-1609(97)80029-9

Nussbaum C, Bossart P, Amann F, Aubourg C (2011) Analysis of tectonic structures and excavation induced fractures in the Opalinus Clay, Mont Terri underground rock laboratory (Switzerland). Swiss J Geosci 104:187–210. https://doi.org/10.1007/s00015-011-0070-4

Ong SHSH (1994) Borehole Stability. University of Oklahoma

Ortiz M (1985) A constitutive theory for the inelastic behavior of concrete. Mech Mater 4:67–93. https://doi.org/10.1016/0167-6636(85)90007-9

Palmer AC (1972) Undrained plane-strain expansion of a cylindrical cavity in clay: a simple interpretation of the pressuremeter test. Géotechnique 22:451–457. https://doi.org/10.1680/geot.1973.23.2.284

Parisio F, Laloui L (2017) Plastic-damage modeling of saturated quasi-brittle shales. Int J Rock Mech Min Sci 93:295–306. https://doi.org/10.1016/j.ijrmms.2017.01.016

Parisio F, Vilarrasa V, Laloui L (2018) Hydro-mechanical Modeling of Tunnel Excavation in Anisotropic Shale with Coupled Damage-Plasticity and Micro-dilatant Regularization. Rock Mech Rock Eng 51:3819–3833. https://doi.org/10.1007/s00603-018-1569-z

Pei J (2003) Effect of Sample Disturbance in Opalinus Clay Shales. Massachusetts Institute Of Technology

Perbawa A, Gramajo E, Finkbeiner T, Santamarina JC (2019) Global vs local strain measurements in triaxial tests – Implications. Rock Mech Rock Eng. https://doi.org/10.1007/s00603-021-02389-z

Pineda JA, Alonso EE, Romero E (2014) Environmental degradation of claystones. Geotechnique 64:64–82. https://doi.org/10.1680/geot.13.P.056

Pirrie D, Butcher AR, Power MR, Gottlieb P, Miller GL (2004) Rapid quantitative mineral and phase analysis using automated scanning electron microscopy (QemSCAN); potential applications in forensic geoscience. Geol Soc Spec Publ 232:123–136. https://doi.org/10.1144/GSL.SP.2004.232.01.12

Plona TJ, Cook JM (1995) Effects of stress cycles on static and dynamic Young's moduli in Castlegate

sandstone. 35th US Symp Rock Mech USRMS 1995 155–160

Poller A, Smith P, Mayer G, Hayek M (2014) Modelling of Radionuclide Transport along the Underground Access Structures of Deep Geological Repositories (TR 14-10)

Popp T, Salzer K (2007) Anisotropy of seismic and mechanical properties of Opalinus clay during triaxial deformation in a multi-anvil apparatus. Phys Chem Earth 32:879–888. https://doi.org/10.1016/j.pce.2006.04.022

Reed MB (1986) Stresses and displacements around a cylindrical cavity in soft rock. IMA J Appl Math (Institute Math Its Appl 36:223–245. https://doi.org/10.1093/imamat/36.3.223

Reinhardt HW, Cornelissen HAW (1984) Post-peak cyclic behaviour of concrete in uniaxial tensile and alternating tensile and compressive loading. Cem Concr Res 14:263–270. https://doi.org/10.1016/0008-8846(84)90113-3

Rocha M (1970) New techniques in deformability testing of in situ rock masses. Am Soc Test Mater STP 477:39–57. https://doi.org/10.1520/STP29139S

Rocscience (2006) Examine2D - 2D Stress Analysis for Underground Excavations

Rybacki E, Reinicke A, Meier T, Makasi M, Dresen G (2015) What controls the mechanical properties of shale rocks? - Part I: Strength and Young's modulus. J Pet Sci Eng 135:702–722. https://doi.org/10.1016/j.petrol.2015.10.028

Saint-Venant B (1893) Sur la distribution des elastici & autour de chaque point d'un sohde ou dun milieu de contexture quelconque. J Math Pures Appl 7–8:353–430

Santarelli FJ, Brown ET (1987) Performance of deep well bores in rock with a confining pressure-dependent elastic modulus. In: 6th ISRM Congress. A.A. Balkema., Montreal, pp 1217–1222

Sarkar S, Singh I V., Mishra BK, Shedbale AS, Poh LH (2019) A comparative study and ABAQUS implementation of conventional and localizing gradient enhanced damage models. Finite Elem Anal Des 160:1–31. https://doi.org/10.1016/j.finel.2019.04.001

Sayers CM (1990) Inversion of ultrasonic wave velocity measurements to obtain the microcrack orientation distribution function in rocks. Eng Fract Mech 35:743–749. https://doi.org/10.1016/0013-7944(90)90157-C

Sayers CM (1999) Stress-dependent seismic anisotropy of shales. Geophysics 64:93–98. https://doi.org/1-4244-1484-9/08/$25.00

Sayers CM, Van Munster JG, King MS (1990) Stress-induced Ultrasonic Anisotropy in Berea Sandstone. Int J Rock Mech Min Sci Geomech Abstr 27:429–436. https://doi.org/DOI: 10.1016/0148-9062(90)92715-Q

Schoenberg M, Sayers CM (1995) Seismic anisotropy of fractured rock. Geophysics 60:204–211. https://doi.org/10.1190/1.1443748

Scholz CH (1968) Microfracturing and the inelastic deformation of rock in compression. J Geophys Res 73:1417–1432. https://doi.org/10.1029/jb073i004p01417

Schuster K (2019) Mini-Seismic Methods for the in-situ characterization of clay rocks—Examples from URL Meuse/Haute-Marne (France) and HADES URF (Belgium). Geomech Energy Environ 17:16–28. https://doi.org/10.1016/j.gete.2018.09.005

Schuster K (2009) Detection of borehole disturbed zones and small scale rock heterogeneities with geophysical methods. In: EC-TIMODAZ-THERESA International Conference, Impact of thermo-hydro-mechanical chemical (THMC). Luxembourg, pp 135–145

Schuster K, Alheid HJ, Böddener D (2001) Seismic investigation of the Excavation damaged zone in Opalinus Clay. Eng Geol 61:189–197. https://doi.org/10.1016/S0013-7952(01)00054-0

Schuster K, Amann F, Yong S, Bossart P, Connolly P (2017) High-resolution mini-seismic methods applied in the Mont Terri rock laboratory (Switzerland). Swiss J Geosci 110:213–231. https://doi.org/10.1007/s00015-016-0241-4

Schwerzmann A, Funk M, Blatter H (2006) Borehole logging with an eight-arm caliper-inclinometer probe. J Glaciol 52:381–388. https://doi.org/10.3189/172756506781828520

Seah TH, Shrestha D (2007) Simulation of pressuremeter shearing mode by true triaxial apparatus. Geotech Test J 30:141–151

Shao JF, Jia Y, Kondo D, Chiarelli AS (2006) A coupled elastoplastic damage model for semi-brittle materials and extension to unsaturated conditions. Mech Mater 38:218–232. https://doi.org/10.1016/j.mechmat.2005.07.002

Siegesmund S, Popp T, Kaufhold A, Dohrmann R, Gräsle W, Hinkes R, Schulte-Kortnack D (2014) Seismic and mechanical properties of Opalinus Clay: Comparison between sandy and shaly facies from Mont Terri (Switzerland). Environ Earth Sci 71:3737–3749. https://doi.org/10.1007/s12665-013-2768-2

Sone H, Zoback MD (2013) Mechanical properties of shale-gas reservoir rocks — Part 1: Static and dynamic elastic properties and anisotropy. Geophysics 78:

Stephenson WR (1978) Ultrasonic Testing for Determining Dynannic Soil Moduli. ASTM STP 654 179–195

Szewczyk D, Bauer A, Holt RM (2016) A new laboratory apparatus for the measurement of seismic dispersion under deviatoric stress conditions. Geophys Prospect 64:789–798. https://doi.org/10.1111/1365-2478.12425

Tapponnier P, Brace WF (1976) Development of Stress-Induced Mlcrocracks m Westerly Granite. Int J Rock Mech Min Sci Geomech Abstr 13:103–112

Thöny R (2014) Geomechanical analysis of excavation-induced rock mass behavior of faulted opalinus clay at the Mont Terri underground rock laboratory (Switzerland). ETH

Thury M, Bossart P (1999) The Mont Terri rock laboratory, a new international research project in a Mesozoic shale formation, in Switzerland. Eng Geol 59:347–359. https://doi.org/10.1016/s0013-7952(99)00015-0

Timoshenko SP, Goodier JN (1934) Theory of Elasticity, 1st edn. McGraw-Hill, New York

Wagner D, Müller B, Tingay M (2004) Correcting for tool decentralization of oriented six-arm caliper logs for determination of contemporary tectonic stress orientation. Petrophysics 45:530–539

Walsh JB (1965) The effect of cracks on the uniaxial elastic compression of rocks. J Geophys Res 70:399–411. https://doi.org/10.1029/jz070i002p00399

Whittle R (1999) Using non-Linear elasticity to obtain the engineering properties of clay-a new solution for the self-boring pressuremeter test. Gr Eng 32:30–34

Wild KM, Amann F (2018a) Experimental study of the hydro-mechanical response of Opalinus Clay – Part 2: Influence of the stress path on the pore pressure response. Eng Geol 237:92–101. https://doi.org/10.1016/j.enggeo.2018.02.011

Wild KM, Amann F (2018b) Experimental study of the hydro-mechanical response of Opalinus Clay – Part 1: Pore pressure response and effective geomechanical properties under consideration of confinement and anisotropy. Eng Geol 237:32–41. https://doi.org/10.1016/j.enggeo.2018.02.012

Wild KM, Wymann LP, Zimmer S, Thoeny R, Amann F (2014) Water Retention Characteristics and State-Dependent Mechanical and Petro-Physical Properties of a Clay Shale. Rock Mech Rock Eng

48:427–439. https://doi.org/10.1007/s00603-014-0565-1

Windle D, Wroth CP (1977) Use of a self-boring pressuremeter to determine the undrained properties of clays. Gr Eng 10:37–46. https://doi.org/10.1016/0148-9062(78)90751-9

Windle D, Wroth CP (1975) Analysis of the pressuremeter test allowing for volume change. Géotechnique 25:598–604. https://doi.org/10.1680/geot.1975.25.3.598

Winkler KW (1996) Azimuthal velocity variations caused by borehole stress concentrations. J Geophys Res 101:8615–8621

Winkler KW (1997) Acoustic evidence of mechanical damage surrounding stressed boreholes. Geophysics 62:16–22

Winkler KW, D'Angelo R (2006) Ultrasonic borehole velocity imaging. Geophysics 71:F25–F30. https://doi.org/10.1190/1.2194532

Wolf K (2010) Laboratory Measurements and Reservoir Monitoring of Bitumen Sand Reservoirs. Stanford University

Wood DM (1990) Strain-dependent moduli and pressuremeter tests. Geotechnique 40:509–512. https://doi.org/10.1680/geot.1991.41.4.621

Wood DM, Wroth CP (1977) Some laboratory experiments related to the results of pressuremeter tests. Géotechnique 27:181–201. https://doi.org/10.1680/geot.1977.27.2.181

Wu B, Hudson JA (1991) Stress-induced anisotropy in rock and its influence on wellbore stability. In: 32nd U.S. Symposium on Rock Mechanics, USRMS 1991. pp 941–950

Yam H (2011) CO2 Rock Physics: A Laboratory Study. University of Alberta

Yong S, Loew S, Schuster K, Nussbaum C, Fidelibus C (2017) Characterisation of Excavation-Induced Damage Around a Short Test Tunnel in the Opalinus Clay. Rock Mech Rock Eng 50:1959–1985. https://doi.org/10.1007/s00603-017-1212-4

Yu H (2000) Cavity Expansion Methods in Geomechanics. Kluwer Academic Publishers

Yuan Y, Xu B, Palmgren C (2013) Design of caprock integrity in thermal stimulation of shallow oil-sands reservoirs. J Can Pet Technol 52:266–278. https://doi.org/10.2118/149371-PA

Zalesky M, Bühler C, Burger U, John M (2007) Dilatometer tests in deep boreholes in investigation for Brenner base tunnel. In: Barták, Hrdina, Romancov, Zlámal (eds) Underground Space – the 4th

Dimension of Metropolises. Taylor & Francis Group, Prague, pp 283–288

Zang A, Wagner CF, Dresen G (1996) Acoustic emission, microstructure, and damage model of dry and wet sandstone stressed to failure. J Geophys Res 101:

Zelt CA, Smith RB (1992) Seismic traveltime inversion for 2-D crustal velocity structure. Geophys J Int 108:16–34. https://doi.org/10.1111/j.1365-246X.1992.tb00836.x

Zhang CL, Laurich B (2020) Mechanical behavior of sandy facies of Opalinus Clay under different load conditions. J Rock Mech Geotech Eng 12:223–241. https://doi.org/10.1016/j.jrmge.2019.09.005

Zhou H, Kong G, Liu H (2016) A semi-analytical solution for cylindrical cavity expansion in elastic–perfectly plastic soil under biaxial in situ stress field. Géotechnique 66:584–595. https://doi.org/10.1680/jgeot.15.P.115

Zhu Q, Shao J (2017) Micromechanics of rock damage: Advances in the quasi-brittle field. J Rock Mech Geotech Eng 9:29–40. https://doi.org/10.1016/j.jrmge.2016.11.003

Zhuang PZ, Yu HS (2019) A unified analytical solution for elastic-plastic stress analysis of a cylindrical cavity in Mohr-Coulomb materials under biaxial in situ stresses. Geotechnique 69:369–376. https://doi.org/10.1680/jgeot.17.P.281

Zoback M (2010) Reservoir Geomechanics. Cambridge University Press, Cambridge, UK

Appendix I. Ultrasonic Velocity Logs with Core Photos for Test Holes

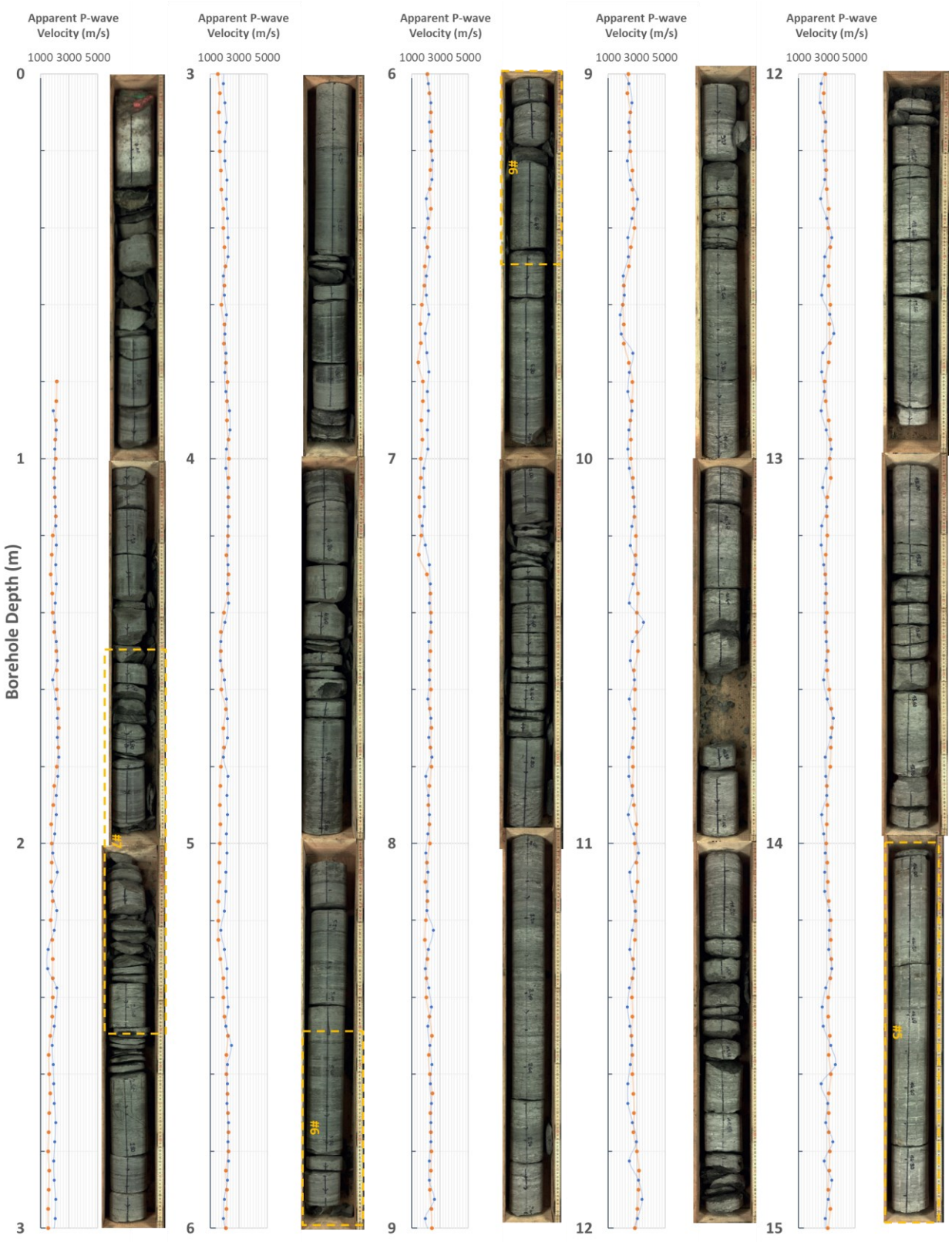

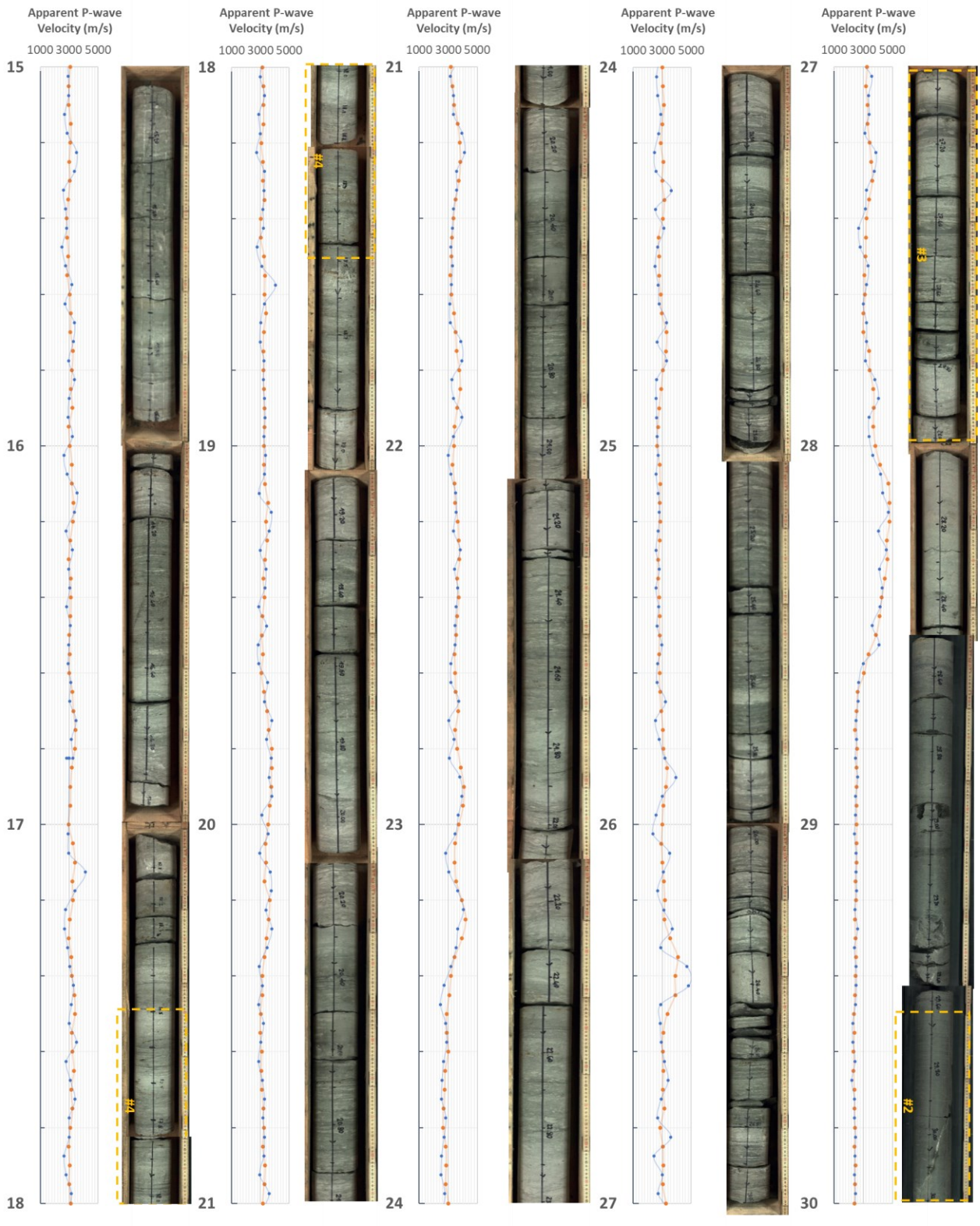
Apparent P-wave Velocity (m/s)
1000 3000 5000
15
16
17
18
#1
Apparent P-wave Velocity (m/s)
1000 3000 5000
18
19
20
21
#4
Apparent P-wave Velocity (m/s)
1000 3000 5000
21
22
23
24
Apparent P-wave Velocity (m/s)
1000 3000 5000
24
25
26
27
Apparent P-wave Velocity (m/s)
1000 3000 5000
27
28
29
30
#3
#2

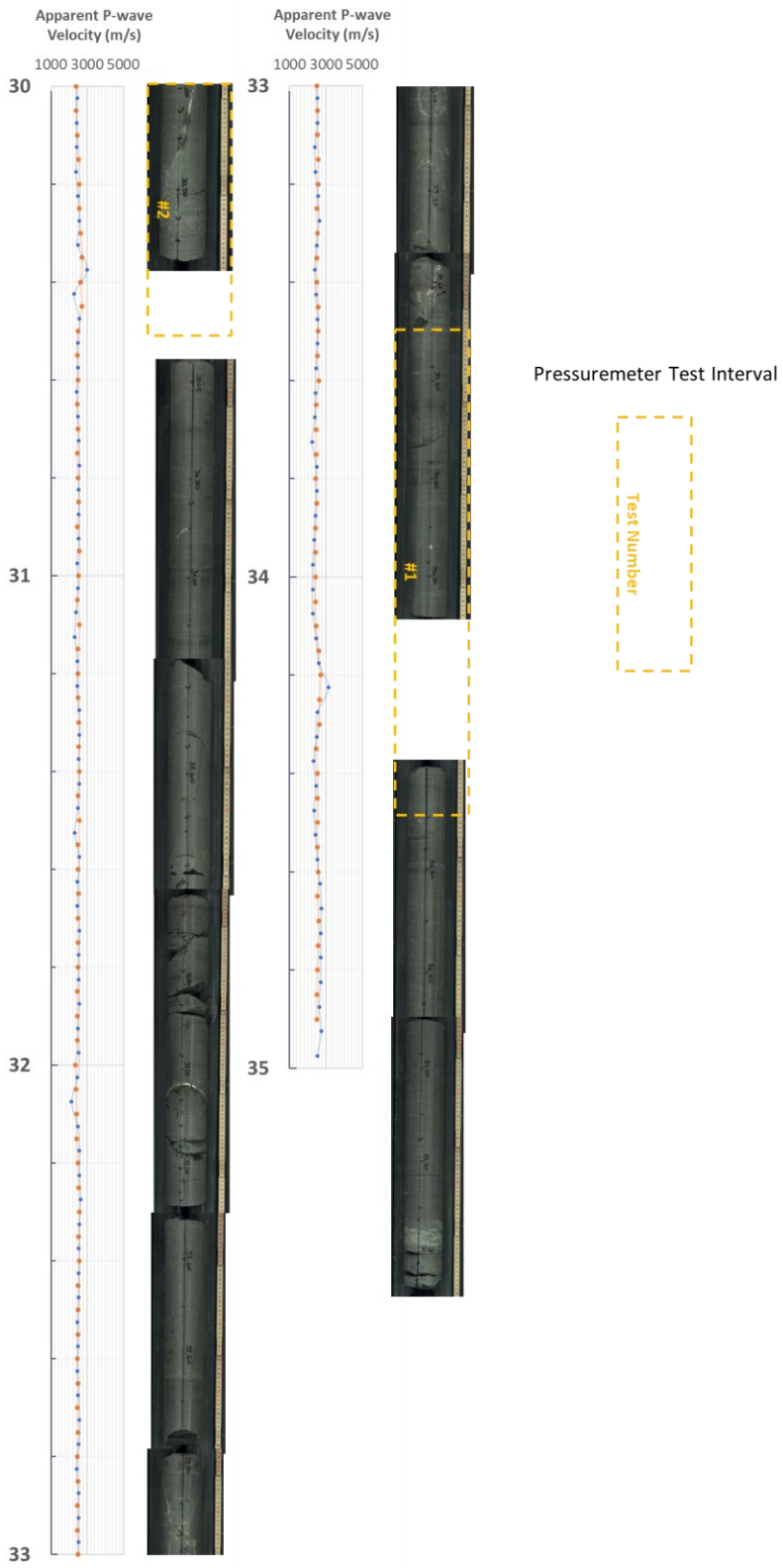

Figure A- 1. Depth variation of apparent P-wave velocity (blue: R1; orange: R4) with core photos at the side for borehole BGC-2

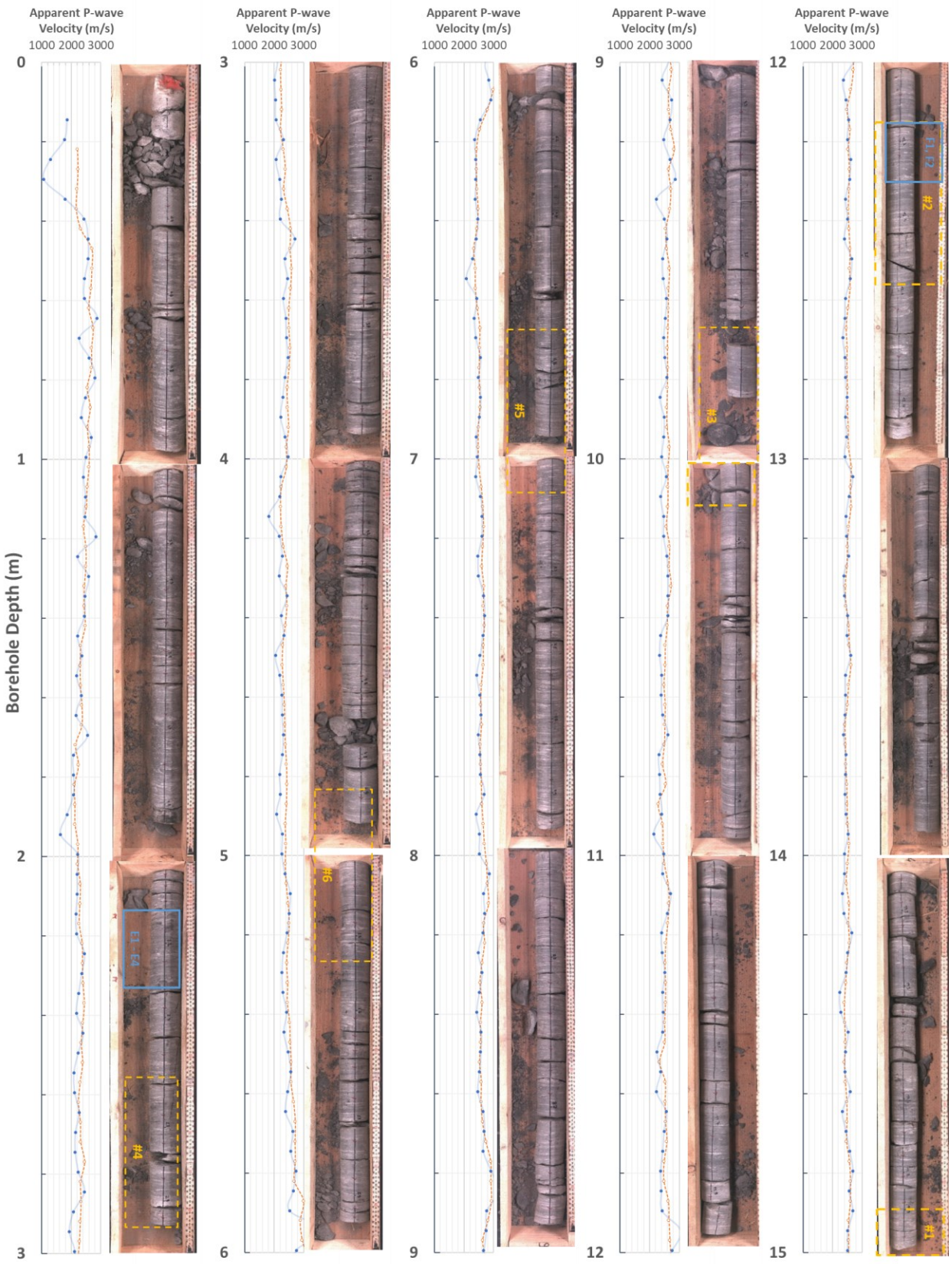
Apparent P-wave Velocity (m/s)
1000 2000 3000
Borehole Depth (m)
0
1
2
3
4
5
6
7
8
9
10
11
12
13
14
15
E1, E4
#4
#6
#5
#3
E1, E2
#2
#1

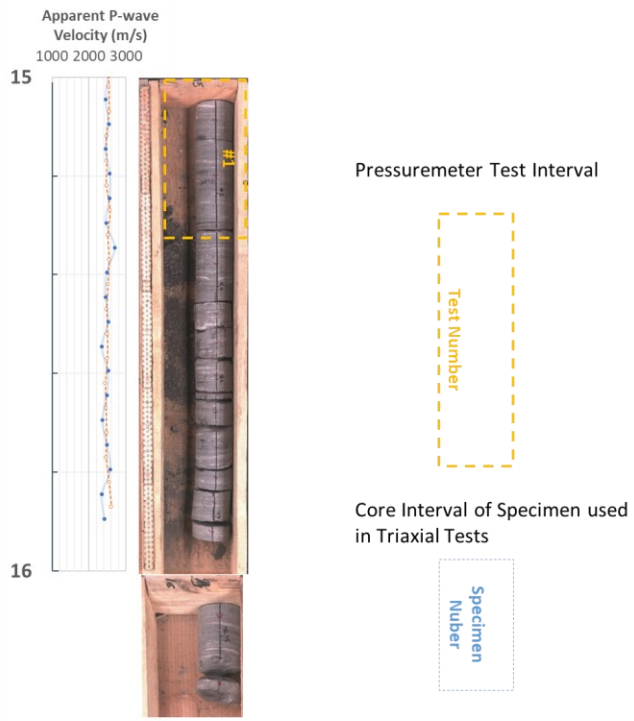

Figure A- 2. Depth variation of apparent P-wave velocity (blue: R1; orange: R4) with core photos at the side for borehole BGC-A4

Appendix II. UofA's Pressuremeter Instrument Calibration and Field Deployment at Mont Terri Site

The 1st test series was completed in borehole BGC-A4 in May 2019, and the 2nd test series included repeat tests in borehole BGC-A4 and tests in a new drilled borehole BGC-A6 in November 2019. UofA's pressuremeter was used in both series of tests. The 1st test (B2T4) in borehole BGC-A4 was aimed to assess the borehole response under a monotonic loading to the maximum allowable pressure, while other tests have unload-reload cycles allowing shear modulus to be evaluated. Another objective of the tests is to examine the anisotropy of borehole deformation. Therefore, the azimuth α_1 of the reference caliper arm, i.e., Arm 1, was determined. Two methods, respectively relying on the internal magnetic sensor and external accelerometer, were used. The α_1 determined from the two methods differed slightly (with a 9~23° discrepancy). The value obtained from the accelerometer is favored because the measurement was more robust in an inclined borehole. Information on the tests (excluding the repeat tests in borehole BGC-A4) for this campaign was summarized in Table 2-2. The following description includes pressuremeter instrument calibration and on-site testing setup.

Instrument Calibrations:

The pressuremeter instrument was designed initially by Cambridge Insitu, Ltd. Calibrations are required for various sensors in the instrument (Figure A- 3).

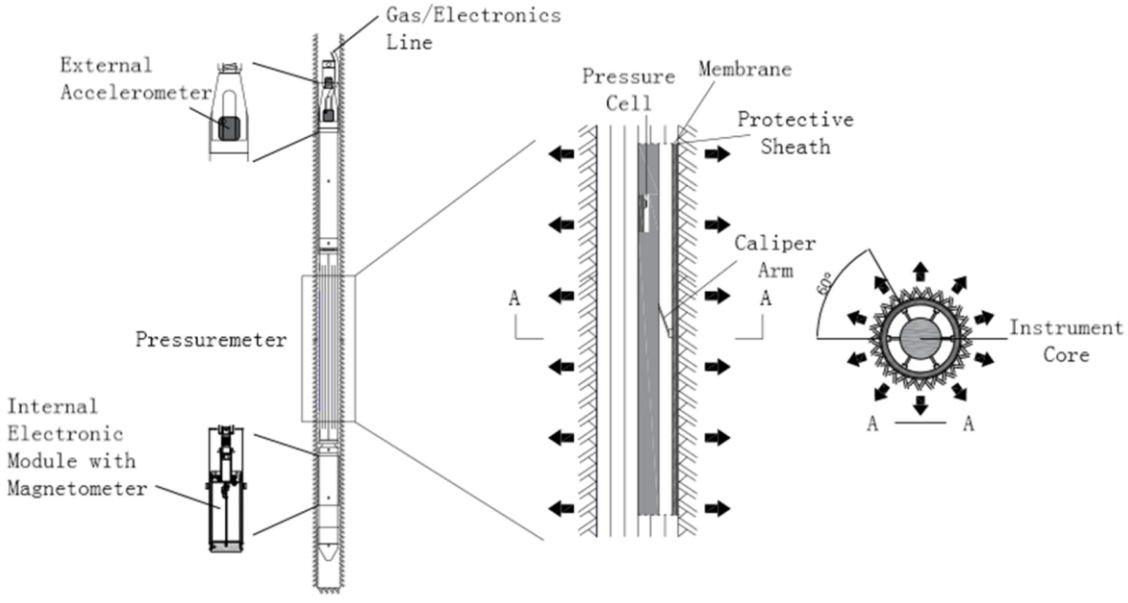

Figure A- 3. Schematic diagram of key instrument components of UofA's pressuremeter

1. Caliper Arms

All the caliper arms are mechanically linked to strain gauges resolving displacements of less than ± 0.5 µm over a range of 16mm. The displacement readings from the caliper arms are calibrated with a micrometer in increments of 1mm (Figure A- 4). The observed repeatable nonlinearity of Arm 5 was fitted by a 2nd order polynomial function as opposed to the linear fits for other arms.

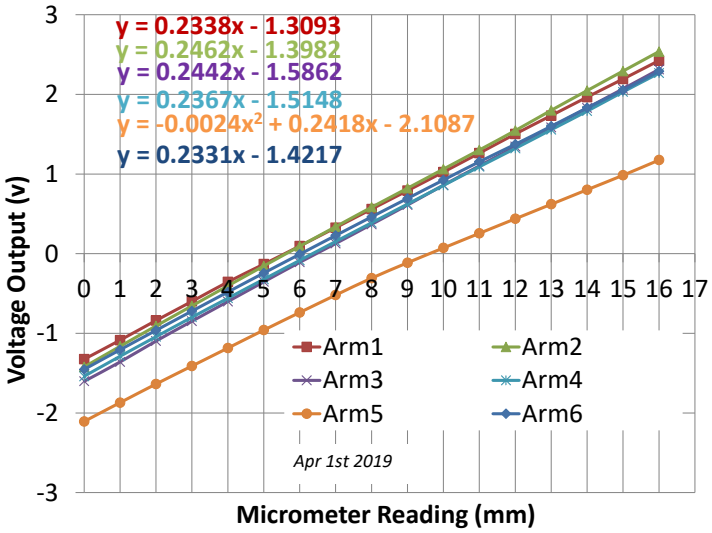

Figure A- 4. Calibration results of caliper arm to maximum radial displacement (16mm)

2. Internal Pressure Cells

Two pressure cells (A & B) are calibrated with a standard pressure gauge during a controlled inflation test (Figure A- 5). The calibrated pressure cells will resolve pressure changes less than 1 kPa.

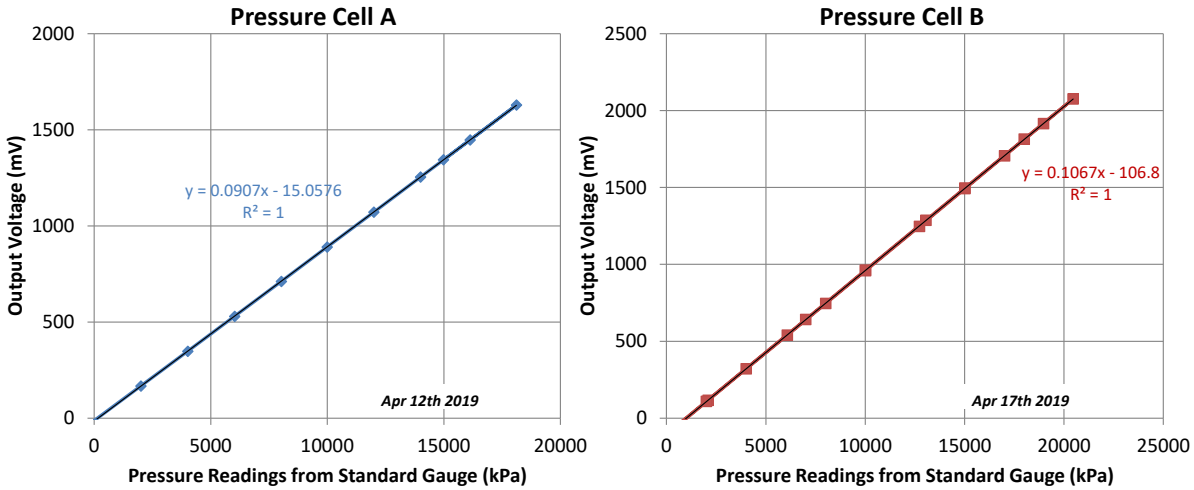

Figure A- 5. Calibration results of internal pressure cells

3. Internal Magnetometer

An internal magnetometer is calibrated with known headings of Arm 1 with respect to the top/bottom of the borehole collar (Figure A- 6). An ellipse is used to fit the data, from which the heading of Arm 1 can be determined with sensor readings when the instrument is deployed.

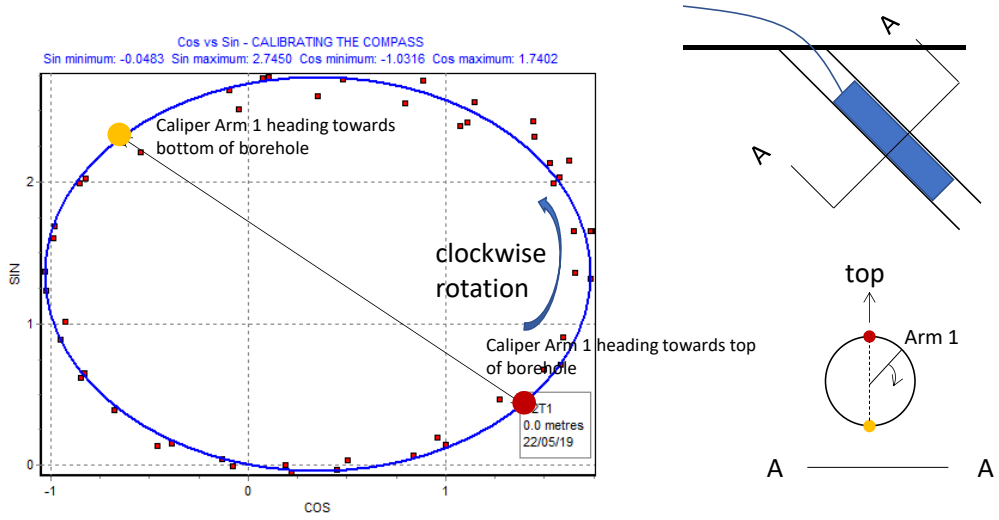

Figure A- 6. Calibration results of internal magnetometer in test borehole BGC-A4

4. System Compliance (Membrane Compression)

The compliance of the testing system is calibrated in an inflation test against a stiff hollow cylinder with known material stiffness (Figure A- 7). Consideration of system compliance over entire expansion pressure is critical for tests in stiff ground. The nonlinearity of instrument deformation in the lower pressure level is captured by a power-law function while the linear part of the curve is fitted by a linear function. The data plotted in Figure A- 7(b) are from multiple calibrations completed in the field campaign. Because the loading portion of the calibration data is sensitive to factors including loading rate and relaxation time from test to test, only the unloading portion is used to derive a system compliance function.

It should also be noted for the shear modulus determination using the unloading step for an expansion pressure less than 5 MPa, only the radial displacement change is used so only the nonlinear term of the calibrated system compliance function matters. According to one calibration test with multiple unload-reload cycles, it is shown that this nonlinear term is invariant of when and where the unloading takes place (Figure A- 8). Therefore, the nonlinearity of the system compliance can be effectively corrected

using a constant system compliance function for the shear modulus determination for all the unloading steps.

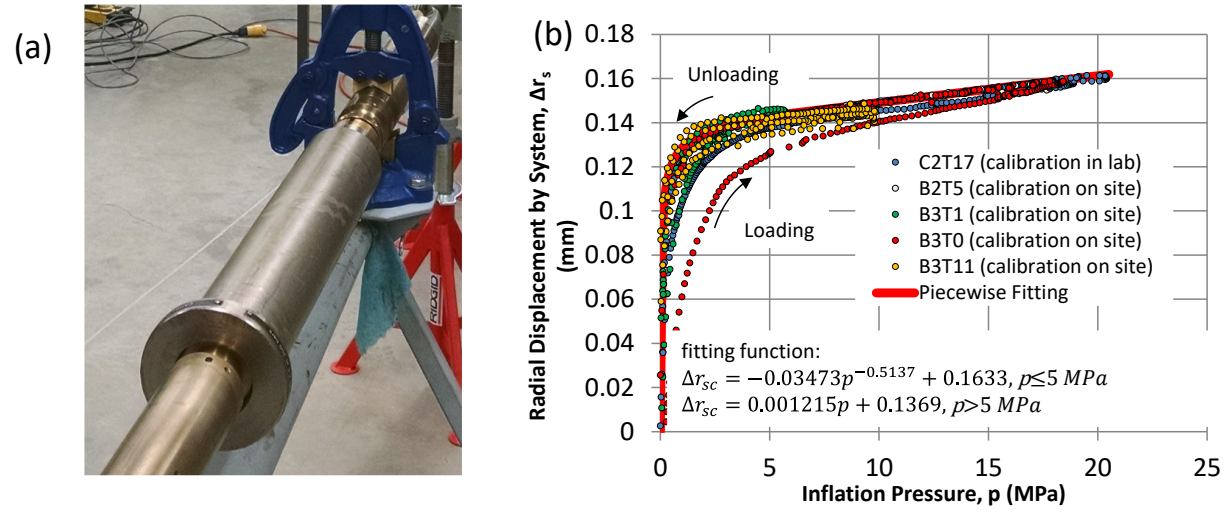

Figure A- 7. (a) Calibration test against hollow steel cylinder (ID=76.2mm, OD=101.6mm) and (b) test data from calibrations using different loading/unloading rates and having different relaxation periods between loadings.

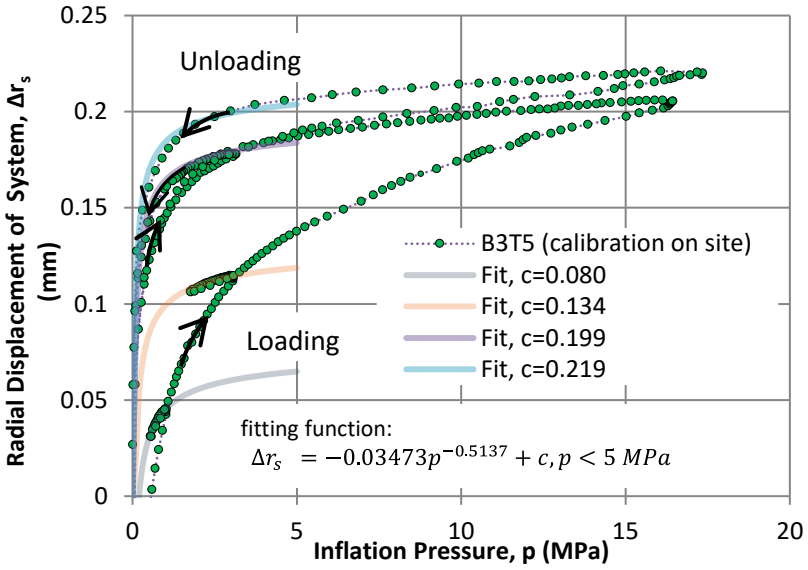

Figure A- 8. Calibration test with multiple unload-reload cycles fitted by the function with the same nonlinear component but different coefficient c.

5. Membrane Stiffness

Membrane stiffness includes the estimates of initial pressure applied to move the membrane and the increasing pressure restraint during membrane expansion. Figure A- 9 shows an example of membrane stiffness calibrated by a linear function in one test.

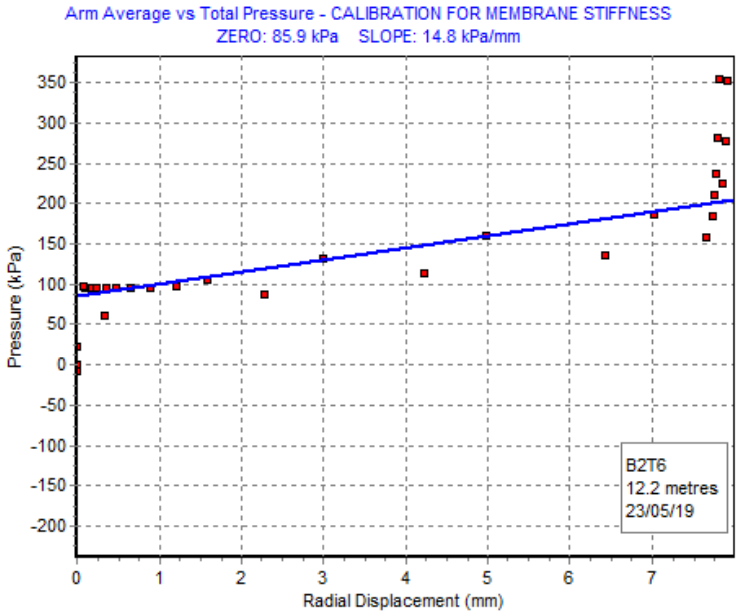

Figure A- 9. Calibrated membrane stiffness for test BGC-A4, #2 (B2T6)

6. External Accelerometer

Calibration of the sensor is not required other than a quick check with vectorial readings from its three axes (i.e., G_{px}, G_{py}, and G_{pz}) – the norm should be close to 1, i.e., $\sqrt{G_{px}^2 + G_{py}^2 + G_{pz}^2} = 1$.

The norms from six tests (#1,#2, #3, #4, #5, and #6) in BGC-A4 are 0.9860, 0.9391, 0.9445, 0.9486, 0.9623, and 0.9528; they are acceptable to represent the gravitational field.

Figure A- 10 shows the sensor attached to the instrument head with its x-axis aligned with the axis of the instrument. When the instrument sits in the downhole, the orientation of the sensor can be characterized by two angles - θ and φ, respectively representing the plunge of the instrument and the angle of the z-axis clockwise from the top of the borehole. These two angles can be determined given the gravitational readings from three axes using,

(A. 1) $$\tan(\varphi) = \frac{G_{py}}{G_{pz}}$$

$$\tan(\theta) = \frac{-G_{px}}{\sqrt{G_{py}^2 + G_{pz}^2}}$$

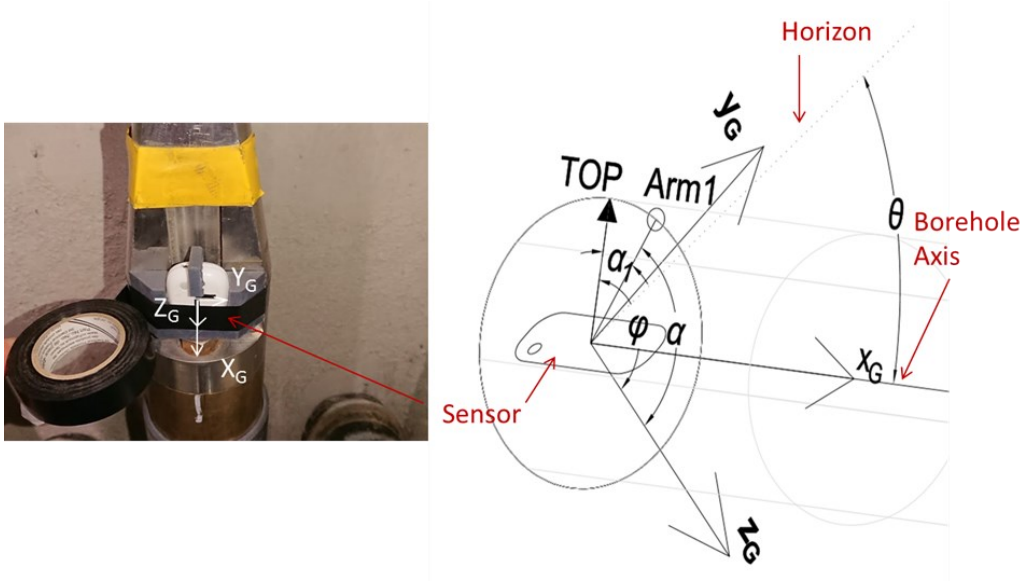

Figure A- 10. Attachment of the accelerometer on the instrument and diagram of its heading with respect to the borehole

Once φ is calculated, the azimuth of Arm 1 α_1 can be determined with the known angle α between the z-axis and Arm 1.

On-site Setup:

Onsite setup mainly consists of equipment for instrument deployment and testing. 20 MPa nitrogen bottles are acquired as the pressure source for all the tests. A complete onsite configuration for tests in BGC-A4 is shown in Figure A- 11. The instrument was slid into the hole by its self-weight and pulled out with wireline to the next test depth. Figure A- 12 shows the deployment of the instrument into BGC-A6 into a horizontal hole drilled into tunnel liners. It was pushed in and pulled out with external forces from onsite tools. Before each test, the location and the orientation of the instrument in the downhole were logged.

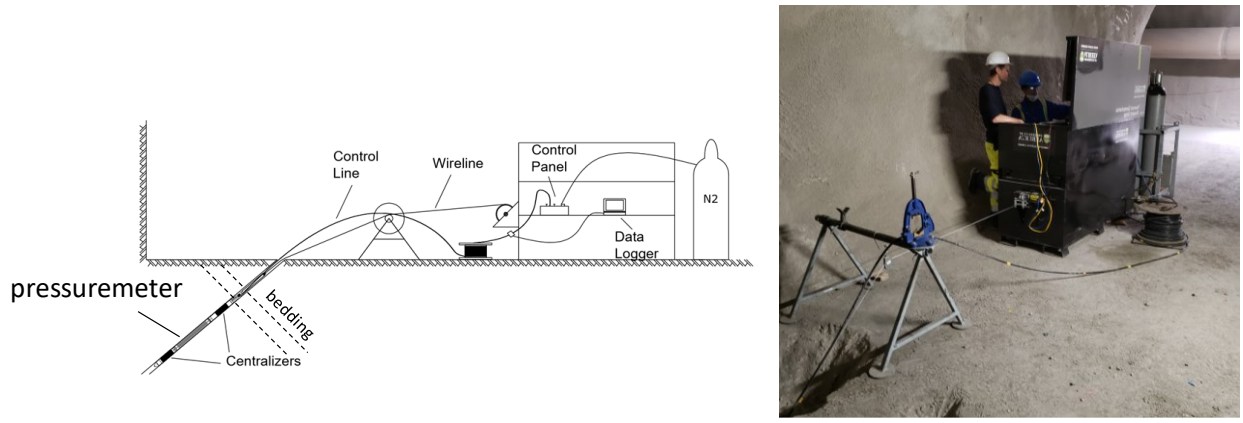

Figure A- 11. Onsite configuration for pressuremeter testing in borehole BGC-A4 (40° dipping into the floor)

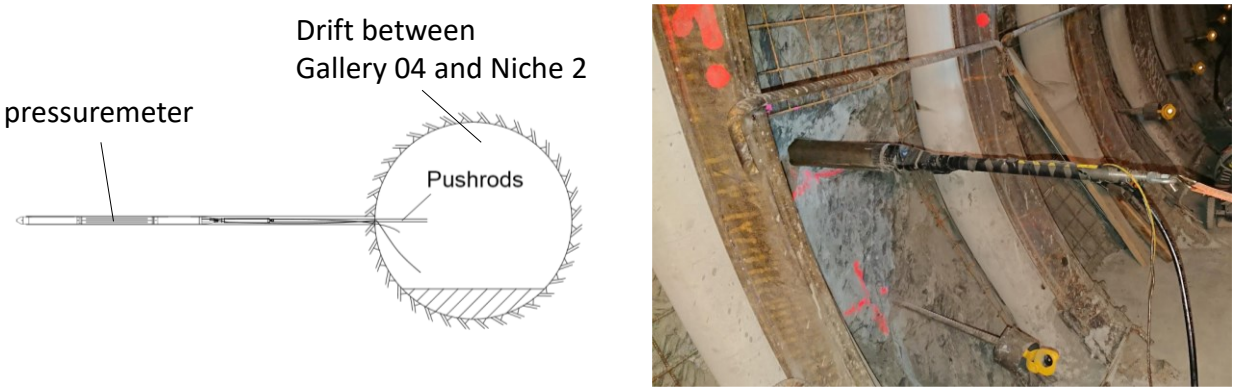

Figure A- 12. Deployment of pressuremeter in borehole BGC-A6 (horizontal)

Appendix III. Summary of Shear Modulus Evaluations Using Unloading Steps

Depth	p_c at the Start of Unloading	Unloading Strain Magnitude		G	Power-law Fit			G_s	
		$\Delta\varepsilon_c$	$\Delta\gamma_s$		α	β	*RMSE* of Δp_c	at $\Delta\gamma_s$= 0.01%	at $\Delta\gamma_s$= 0.1%
(m)	(MPa)	(%)	(%)	(MPa)	(MPa)	-	(MPa)	(MPa)	
Tests in Borehole BGC-2 by SolExperts									
34	1.90	0.023	0.027	2185	622	0.856	0.058	2165	1554
	2.70	0.015	0.018	4357	694	0.799	0.001	3958	2492
	16.01	0.032	0.037	5954	392	0.677	0.011	6410	3050
30	1.91	0.028	0.032	1651	19	0.490	0.035	1591	492
	2.70	0.035	0.040	2204	9	0.358	0.096	2283	520
	3.50	0.046	0.053	2630	42	0.497	0.093	3293	1034
27.5	1.90	0.018	0.021	2590	28	0.504	0.092	2060	657
	2.70	0.034	0.040	2387	26	0.468	0.059	2589	761
	3.50	0.037	0.043	3233	39	0.474	0.163	3676	1095
18	1.90	0.024	0.028	1956	42	0.563	0.008	1838	672
	2.70	0.035	0.041	2426	88	0.604	0.053	2712	1090
	3.50	0.045	0.051	2831	97	0.587	0.138	3486	1347
14.5	1.90	0.026	0.030	1822	76	0.633	0.063	1823	783
	2.71	0.039	0.045	2255	107	0.632	0.020	2591	1110
	3.52	0.051	0.059	2483	142	0.642	0.093	3153	1382
6	1.90	0.031	0.036	1594	155	0.725	0.041	1683	893
	2.70	0.046	0.053	1871	97	0.635	0.030	2298	991
	3.50	0.064	0.074	1997	140	0.658	0.128	2720	1237
2	1.90	0.030	0.034	1603	56	0.607	0.035	1668	675
	2.71	0.060	0.069	1424	36	0.537	0.049	2018	694
	3.50	0.073	0.084	1785	164	0.687	0.141	2474	1203
Tests in Borehole BGC-A4 by UAlberta									
12.2	0.90	0.013	0.015	1525	91	0.700	0.013	1221	612
	1.87	0.010	0.011	3777	163	0.674	0.024	2739	1294

	2.91	0.014	0.016	4174	239	0.688	0.044	3571	1740
	5.90	0.017	0.020	5480	1672	0.866	0.125	5314	3908
	8.40	0.020	0.023	5306	756	0.778	0.035	5149	3092
	11.85	0.021	0.024	5189	1102	0.822	0.026	5159	3422
9.7	0.83	0.012	0.014	955	75	0.717	0.003	872	454
	1.86	0.015	0.017	2388	361	0.790	0.082	2221	1370
	2.86	0.017	0.019	3265	323	0.744	0.019	2965	1644
	5.81	0.016	0.019	4390	827	0.815	0.069	4111	2684
	8.76	0.016	0.019	5159	681	0.775	0.044	4772	2844
	11.92	0.019	0.022	5381	775	0.782	0.057	5131	3104
	13.80	0.023	0.026	5289	793	0.774	0.076	5618	3338
6.7	0.88	0.012	0.014	805	42	0.670	0.008	738	345
	1.84	0.016	0.019	1980	170	0.725	0.031	1841	977
	2.77	0.017	0.020	2999	333	0.755	0.040	2789	1585
	5.82	0.018	0.021	4688	1098	0.835	0.043	4596	3141
	10.78	0.016	0.019	4719	774	0.794	0.035	4629	2877
	15.46	0.014	0.016	4287	812	0.804	0.059	4416	2815
4.9	2.82	0.018	0.021	3343	776	0.855	0.015	2731	1954
	8.96	0.018	0.020	4947	745	0.747	0.027	4674	2868
2.5	0.71	0.021	0.024	1173	82	0.788	0.008	944	494
	2.80	0.021	0.024	2675	265	0.719	0.023	2479	1368
	5.73	0.026	0.030	3865	1362	0.742	0.035	3816	2901
	8.75	0.013	0.015	4162	822	0.881	0.041	4039	2645
	11.70	0.011	0.012	4618	941	0.816	0.030	4399	2919
	13.58	0.017	0.020	4659	368	0.822	0.049	4086	2155
Tests in Borehole BGC-A6 by UAlberta									
9.4	0.98	0.043	0.050	609	31	0.633	0.019	757	325
	1.96	0.040	0.046	1048	230	0.813	0.037	1162	755
	3.10	0.043	0.050	1279	312	0.822	0.050	1459	968
	6.03	0.036	0.042	1691	332	0.798	0.036	1906	1197
	9.93	0.050	0.057	1826	610	0.866	0.041	1940	1426
	15.17	0.072	0.083	1546	310	0.785	0.026	1988	1212
	16.47	0.083	0.095	1638	238	0.738	0.058	2300	1259

7.8	0.93	0.045	0.052	635	69	0.727	0.012	734	391
	2.01	0.035	0.040	1222	96	0.695	0.009	1353	670
	3.10	0.032	0.037	1658	214	0.757	0.030	1757	1004
	6.16	0.034	0.040	2007	401	0.803	0.049	2207	1402
	9.87	0.036	0.041	2390	525	0.814	0.035	2640	1718
	14.91	0.047	0.055	2188	469	0.803	0.093	2586	1642
	18.16	0.055	0.063	1995	455	0.806	0.024	2435	1559
4.5	0.95	0.049	0.056	501	44	0.695	0.010	622	308
	2.06	0.041	0.047	986	83	0.695	0.050	1166	577
	3.00	0.045	0.052	1308	320	0.828	0.016	1423	957
	5.89	0.042	0.049	1709	364	0.807	0.016	1941	1244
	10.03	0.039	0.045	2219	533	0.823	0.013	2462	1639
	13.60	0.047	0.054	2099	1107	0.919	0.015	2234	1854
	17.76	0.104	0.120	2049	674	0.856	0.043	2354	1688
2.9	0.91	0.043	0.050	515	28	0.644	0.009	621	273
	3.06	0.031	0.036	1463	159	0.737	0.006	1559	850
	8.04	0.038	0.044	2067	414	0.803	0.026	2282	1449
	15.30	0.036	0.041	2245	363	0.777	0.078	2494	1494
	17.17	0.085	0.098	2017	604	0.835	0.065	2525	1726
1.4	0.95	0.041	0.048	546	62	0.734	0.007	622	337
	3.16	0.035	0.041	1336	161	0.744	0.031	1479	820
	8.33	0.045	0.052	1876	346	0.788	0.015	2164	1329
	15.00	0.048	0.056	1937	404	0.799	0.038	2308	1452
	16.26	0.057	0.066	2154	423	0.795	0.038	2502	1560

Appendix IV. Elliptical Fitting and Borehole Expansion Curve Correction

In a local coordinate system, as shown in Figure A- 13, the positions of the tips of six caliper arms (x_i, y_i), i = 1,…,6, can be determined with the orientation and measured arm length at the current pressure level. The general equation of the ellipse is

(A. 2) $$F(x,y;\mathbf{p}) = \mathbf{m}\cdot\mathbf{p} = Ax^2 + Bxy + Cy^2 + Dx + Ey = 1$$

where $\mathbf{m} = (x^2, xy, y^2, x, y)$ and $\mathbf{p} = \left(A, B, C, D, E\right)^T$. With six measurements, a system of six linear equations can be established and written as

(A. 3) $$\mathbf{M}\cdot\mathbf{p} = \mathbf{1}$$

where **M** is a 6x5 matrix and $\mathbf{1} = \left(1,1,1,1,1,1\right)^T$. Equation (A. 2) is overdetermined as only five unknown coefficients in **p** need to be solved. This can be solved through a linear least square approach with residuals being minimized.

With the calculated **p**, Equation (A. 2) can be rewritten in a form with geometric parameters as labeled in Fig. A2,

(A. 4) $$F(x,y;\mathbf{p}) = \frac{\left((x-x_0)\cos\alpha_0 + (y-y_0)\sin\alpha_0\right)^2}{a^2} + \frac{\left((x-x_0)\sin\alpha_0 + (y-y_0)\cos\alpha_0\right)^2}{b^2} = 1$$

where $x_0 = \left(2CD - BE\right)/\left(B^2 - 4AC\right)$, $y_0 = \left(2AE - BD\right)/\left(B^2 - 4AC\right)$, $\alpha_0 = 1/2\arctan\left(B/\left(A-C\right)\right)$, $a = \sqrt{2\left(1+F\right)/\left(A+C+B/\sin 2\alpha_0\right)}$ and $b = \sqrt{2\left(1+F\right)/\left(A+C-B/\sin 2\alpha_0\right)}$ with $F = Ax_0^2 + Bx_0y_0 + Cy_0^2$.

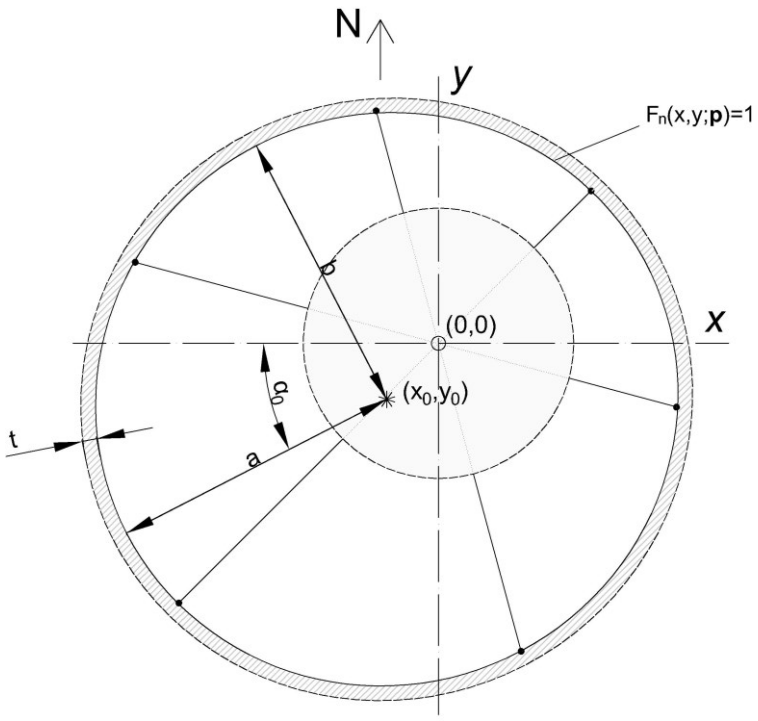

Figure A- 13. Geometry of a fitted ellipse based on the measured lengths of six caliper arms inside the packer membrane

Two corrections need to be made on $F(x, y; \mathbf{p})$ respectively for the thinning effect of the membrane and the shift of the instrument center throughout the test.

Because the fitted ellipse generally has a low eccentricity (< 0.25), it is assumed that the reduction of the membrane thickness is uniform under inflation and the current thickness t for a membrane with negligible compressibility can be determined (Clarke 1995),

$$t = \sqrt{r^2 + t_0(2r_0 + t_0)} - r \tag{A. 5}$$

where the initial radius at the inside of the membrane r_0 and the initial membrane thickness t_0 can be measured before the test, and the averaged radius r is approximated as $(a+b)/2$.

If borehole deformation is presumably symmetric under a biaxial in-situ stress condition, the center of the borehole should have the same position as the center of the fitted ellipse and should not move regardless of inflation. To present all the ellipses in a fixed borehole coordinate system, each fitted ellipse is shifted by $(-x_0, -y_0)$.

Therefore, the elliptical function corrected for the two factors mentioned above is

(A. 6) $$F(x,y;\mathbf{p}^*)=\frac{\left(x\cos\alpha_0+y\sin\alpha_0\right)^2}{(a^*)^2}+\frac{\left(x\sin\alpha_0+y\cos\alpha_0\right)^2}{(b^*)^2}=1$$

where $a^*=a+t+t_{PS}$ and $b^*=b+t+t_{PS}$ with t_{PS} denoted as the thickness of the protective sheath. The borehole radius at any azimuth φ can be derived from the corrected ellipse parameters,

(A. 7) $$r(\varphi)=a^*b^*\sqrt{\frac{\tan\left(\alpha_0+\varphi\right)^2+1}{\left(a^*\right)^2+\left(b^*\right)^2\tan\left(\alpha_0+\varphi\right)^2}}$$

Appendix V. Mineralogical Information of Opalinus Clay Specimens Determined using SEM-based Approach

Table A- 1. Identified mineral compositions in Opalinus Clay samples from borehole BGC-A4

Sample Number		1	2	3	4	5	6	7	8
Sample Type		Plug		Pseudo-cutting					
		perp. to bedding	para. to bedding						
Scanning Method		QEMSCAN				AMICS			
Core depth of samples	Top Depth (m)	500	500	500	436	211	211	1216	1216
	Bottom Depth (m)	512	512	512	450	233	233	1244	1244
	Depth Center (m)	506	506	506	443	222	222	1230	1230
Grain Density (g/cm^3)		2.614	2.592	2.618	2.614	2.800	2.618	2.591	2.592
Lithofacies Unit		Upper Sandy						Upper Shaly	
Quartz		25.75	15.35	28.05	19.53	25.20	33.95	23.50	22.85
K Feldspar		3.11	2.22	3.59	3.18	2.54	3.43	2.40	2.49
Plagioclase		1.50	1.05	1.54	1.21	1.20	1.56	1.14	1.38
Muscovite		7.66	12.07	8.67	11.03	5.08	5.38	7.60	10.36
Biotite		0.97	1.78	1.33	1.85	1.16	1.13	1.72	1.41
Kaolinite		2.98	4.10	3.89	4.28	2.72	2.98	2.75	2.98
Chlorite		1.51	2.10	1.75	2.39	1.97	2.33	3.41	3.22
Illitic Clays		4.57	5.23	4.63	5.33	3.59	3.30	5.83	3.98
Ferroan Illitic Clays		3.79	7.38	4.32	5.98	3.97	3.67	3.30	4.23
Smectitic Clays		28.50	43.28	28.77	37.29	30.51	25.82	39.93	38.87
Calcite		16.57	3.16	10.39	4.48	5.00	13.84	5.60	5.66
Ferroan Calcite		0.97	0.61	0.99	0.58	0.65	1.02	1.61	1.14
Dolomite		0.38	0.27	0.33	0.33	0.21	0.20	0.17	0.22
Ferroan Dolomite		0.24	0.30	0.21	0.21	0.16	0.16	0.21	0.24
Siderite		0.11	0.14	0.26	0.61	0.05	0.04	0.06	0.10
Pyrite		0.44	0.50	0.56	1.04	15.35	0.35	0.23	0.26
Sphalerite		0.02	0.00	0.00	0.00	0.01	0.01	0.00	0.01
Barite		0.01	0.01	0.01	0.01	0.00	0.00	0.00	0.00
Ca Sulphate		0.01	0.00	0.01	0.01	0.00	0.00	0.00	0.00
Ti Oxides		0.28	0.21	0.26	0.33	0.20	0.28	0.17	0.21
Apatite		0.57	0.20	0.36	0.25	0.32	0.43	0.23	0.27
Zircon		0.03	0.02	0.03	0.04	0.03	0.04	0.03	0.02
Tourmaline		0.01	0.01	0.04	0.03	0.04	0.04	0.03	0.04
Undifferentiated		0.00	0.00	0.00	0.00	0.03	0.03	0.07	0.05
Total		100.00	100.00	100.00	100.00	100.00	100.00	100.00	100.00

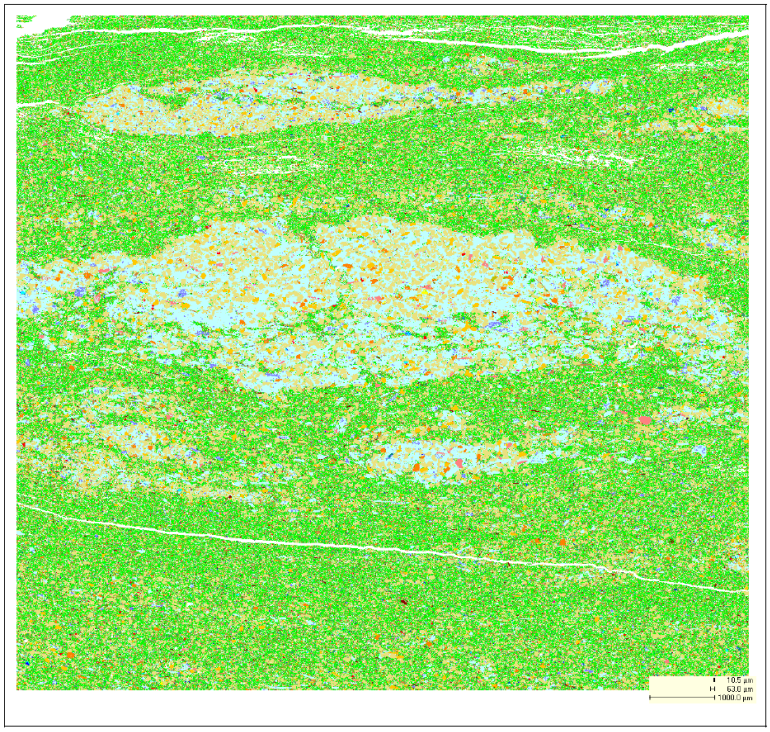

Colour	Mineral	Area %	Mass %	Size µm
	Quartz	25.9	25.7	37
	K Feldspar	3.2	3.1	29
	Plagioclase	1.5	1.5	24
	Muscovite	7.1	7.7	19
	Biotite	0.8	1.0	18
	Kaolinite	3.0	3.0	18
	Chlorite	1.3	1.5	17
	Illite & Illite-smectite	4.4	4.6	17
	Fe-Illite & Illite-smectite	3.5	3.8	17
	Smectitic Clays	30.7	28.5	28
	Calcite	16.1	16.6	46
	Ferroan Calcite	0.9	1.0	23
	Dolomite	0.3	0.4	17
	Ferroan Dolomite	0.2	0.2	16
	Siderite	0.1	0.1	19
	Pyrite	0.2	0.4	20
	Sphalerite	0.0	0.0	62
	Barite	0.0	0.0	18
	Ca Sulphate	0.0	0.0	18
	Ti Oxides	0.2	0.3	20
	Apatite	0.5	0.6	32
	Zircon	0.0	0.0	23
	Tourmaline	0.0	0.0	21
	Undifferentiated	0.0	0.0	0

Well:	BGC-A4
Sample Type:	Core Plug
Formation:	Opalinus Clay
Lab ID:	VL-20029:001
Top Depth (m):	500
Bottom Depth (m):	512
Density (g/cm³):	2.614

Mineralogical image of a selected area of the surface of the sample showing the distribution of the inorganic phases.

Major Minerals:
Quartz, Smectitic Clays, Calcite

Minor Minerals:
K Feldspar, Plagioclase, Muscovite, Kaolinite, Chlorite, Illitic Clays, Ferroan Illitic Clays

Trace Minerals:
Biotite, Ferroan Calcite, Dolomite, Ferroan Dolomite, Siderite, Pyrite, Ti Oxides, Apatite

(a) Upper sandy sample (#1) surface (perpendicular to bedding)

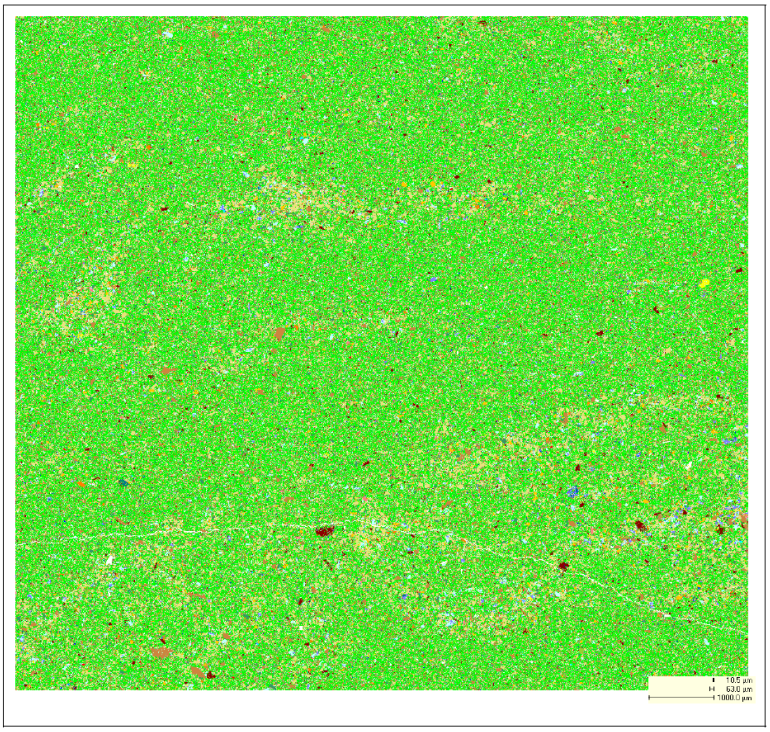

Colour	Mineral	Area %	Mass %	Size µm
	Quartz	15.4	15.3	24
	K Feldspar	2.3	2.2	20
	Plagioclase	1.0	1.1	19
	Muscovite	11.1	12.1	20
	Biotite	1.5	1.8	19
	Kaolinite	4.0	4.1	18
	Chlorite	1.8	2.1	18
	Illite & Illite-smectite	5.0	5.2	17
	Fe-Illite & Illite-smectite	6.9	7.4	17
	Smectitic Clays	46.2	43.3	32
	Calcite	3.1	3.2	20
	Ferroan Calcite	0.6	0.6	20
	Dolomite	0.2	0.3	17
	Ferroan Dolomite	0.3	0.3	16
	Siderite	0.1	0.1	18
	Pyrite	0.3	0.5	18
	Sphalerite	0.0	0.0	16
	Barite	0.0	0.0	16
	Ca Sulphate	0.0	0.0	16
	Ti Oxides	0.1	0.2	18
	Apatite	0.2	0.2	23
	Zircon	0.0	0.0	18
	Tourmaline	0.0	0.0	17
	Undifferentiated	0.0	0.0	16

Well:	BGC-A4
Sample Type:	Core Plug
Formation:	Opalinus Clay
Lab ID:	VL-20029:002
Top Depth (m):	500
Bottom Depth (m):	512
Density (g/cm³):	2.592

Mineralogical image of a selected area of the surface of the sample showing the distribution of the inorganic phases.

Major Minerals:
Quartz, Muscovite, Smectitic Clays

Minor Minerals:
K Feldspar, Plagioclase, Biotite, Kaolinite, Chlorite, Illitic Clays, Ferroan Illitic Clays, Calcite

Trace Minerals:
Ferroan Calcite, Dolomite, Ferroan Dolomite, Siderite, Pyrite, Ti Oxides, Apatite

(b) Upper sandy sample (#2) surface (parallel to bedding)

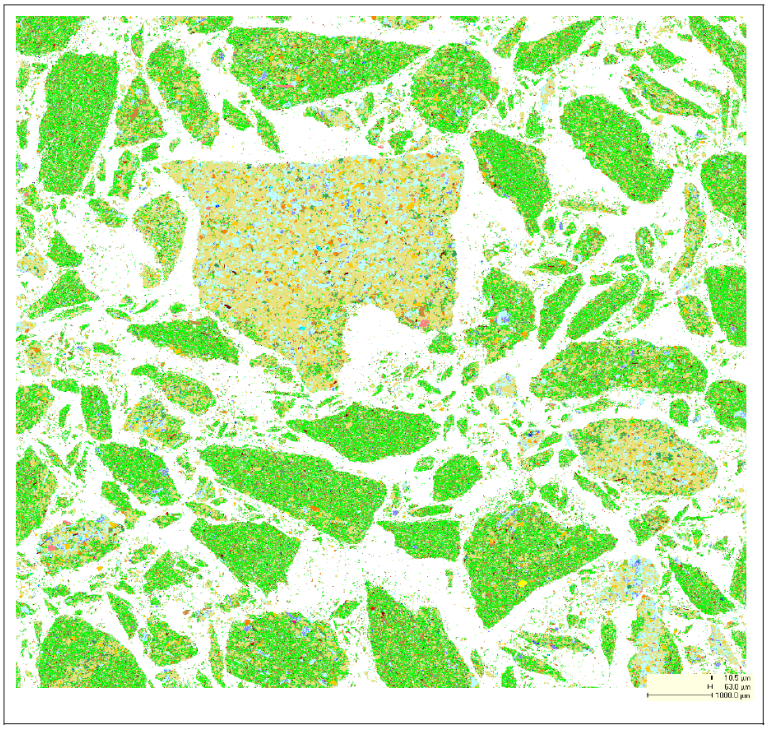

Colour	Mineral	Area %	Mass %	Size µm
	Quartz	28.1	28.0	38
	K Feldspar	3.7	3.6	26
	Plagioclase	1.5	1.5	23
	Muscovite	8.1	8.7	19
	Biotite	1.2	1.3	17
	Kaolinite	3.9	3.9	18
	Chlorite	1.5	1.8	18
	Illite & Illite-smectite	4.5	4.6	17
	Fe-Illite & Illite-smectite	4.0	4.3	17
	Smectitic Clays	31.0	28.8	27
	Calcite	10.1	10.4	32
	Ferroan Calcite	0.9	1.0	23
	Dolomite	0.3	0.3	18
	Ferroan Dolomite	0.2	0.2	16
	Siderite	0.2	0.3	17
	Pyrite	0.3	0.6	19
	Sphalerite	0.0	0.0	17
	Barite	0.0	0.0	16
	Ca Sulphate	0.0	0.0	17
	Ti Oxides	0.2	0.3	19
	Apatite	0.3	0.4	29
	Zircon	0.0	0.0	24
	Tourmaline	0.0	0.0	18
	Undifferentiated	0.0	0.0	17

Well:	BGC-A4
Sample Type:	Pseudocuttings
Formation:	Opalinus Clay
Lab ID:	VL-20029:003
Top Depth (m):	500
Bottom Depth (m):	512
Density (g/cm³):	2.618

Mineralogical image of a selected area of the surface of the sample showing the distribution of the inorganic phases.

Major Minerals:
Quartz, Smectitic Clays, Calcite

Minor Minerals:
K Feldspar, Plagioclase, Muscovite, Biotite, Kaolinite, Chlorite, Illitic Clays, Ferroan Illitic Clays

Trace Minerals:
Ferroan Calcite, Dolomite, Ferroan Dolomite, Siderite, Pyrite, Ti Oxides, Apatite

(c) Upper sandy sample (#3) after pseudo cutting

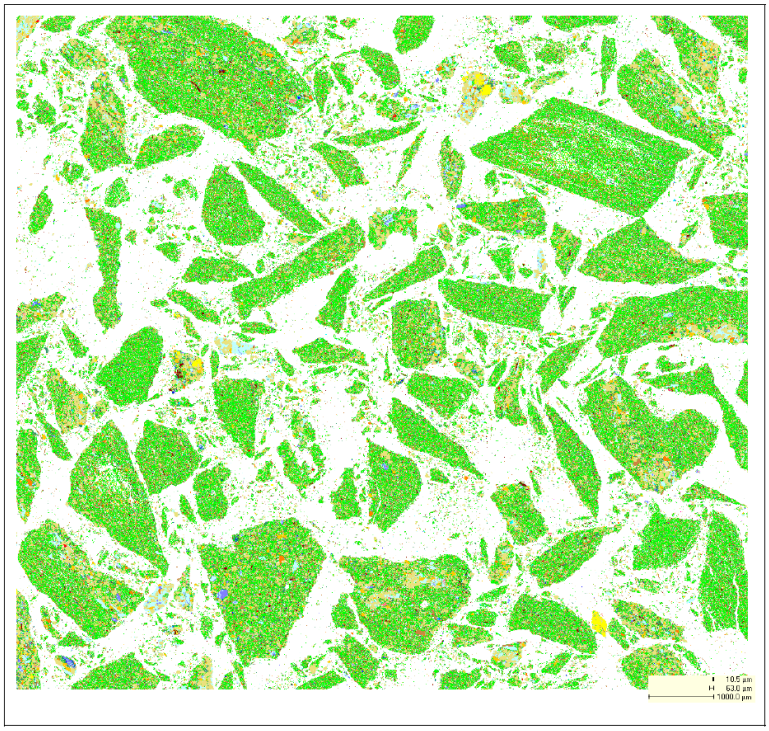

Colour	Mineral	Area %	Mass %	Size µm
	Quartz	19.7	19.5	27
	K Feldspar	3.2	3.2	21
	Plagioclase	1.2	1.2	20
	Muscovite	10.2	11.0	19
	Biotite	1.7	1.9	17
	Kaolinite	4.2	4.3	18
	Chlorite	2.1	2.4	17
	Illite & Illite-smectite	5.1	5.3	16
	Fe-Illite & Illite-smectite	5.6	6.0	17
	Smectitic Clays	40.1	37.3	27
	Calcite	4.4	4.5	25
	Ferroan Calcite	0.5	0.6	21
	Dolomite	0.3	0.3	17
	Ferroan Dolomite	0.2	0.2	16
	Siderite	0.4	0.6	17
	Pyrite	0.6	1.0	23
	Sphalerite	0.0	0.0	17
	Barite	0.0	0.0	16
	Ca Sulphate	0.0	0.0	16
	Ti Oxides	0.2	0.3	17
	Apatite	0.2	0.2	23
	Zircon	0.0	0.0	19
	Tourmaline	0.0	0.0	16
	Undifferentiated	0.0	0.0	16

Well:	BGC-A4
Sample Type:	Pseudocuttings
Formation:	Opalinus Clay
Lab ID:	VL-20029:004
Top Depth (m):	436
Bottom Depth (m):	450
Density (g/cm³):	2.614

Mineralogical image of a selected area of the surface of the sample showing the distribution of the inorganic phases.

Major Minerals:
Quartz, Muscovite, Smectitic Clays

Minor Minerals:
K Feldspar, Plagioclase, Biotite, Kaolinite, Chlorite, Illitic Clays, Ferroan Illitic Clays, Calcite, Pyrite

Trace Minerals:
Ferroan Calcite, Dolomite, Ferroan Dolomite, Siderite, Ti Oxides, Apatite

(d) Upper sandy sample (#4) after pseudo cutting

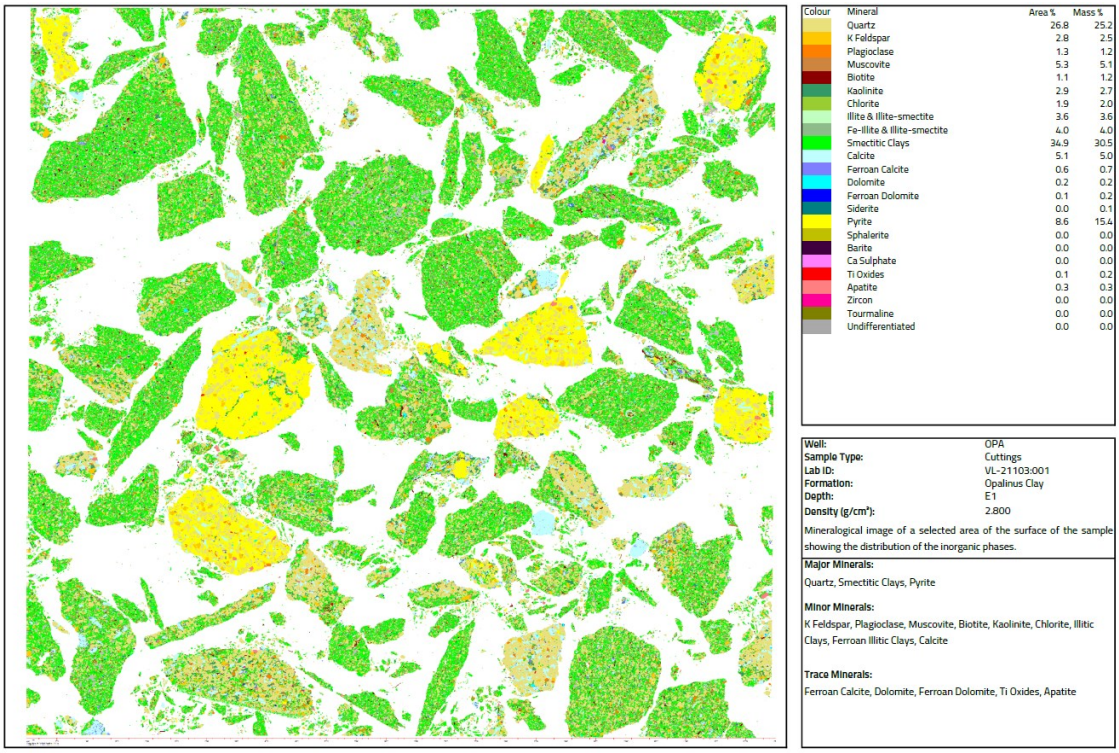

(e) Upper sandy sample (#5) after pseudo cutting

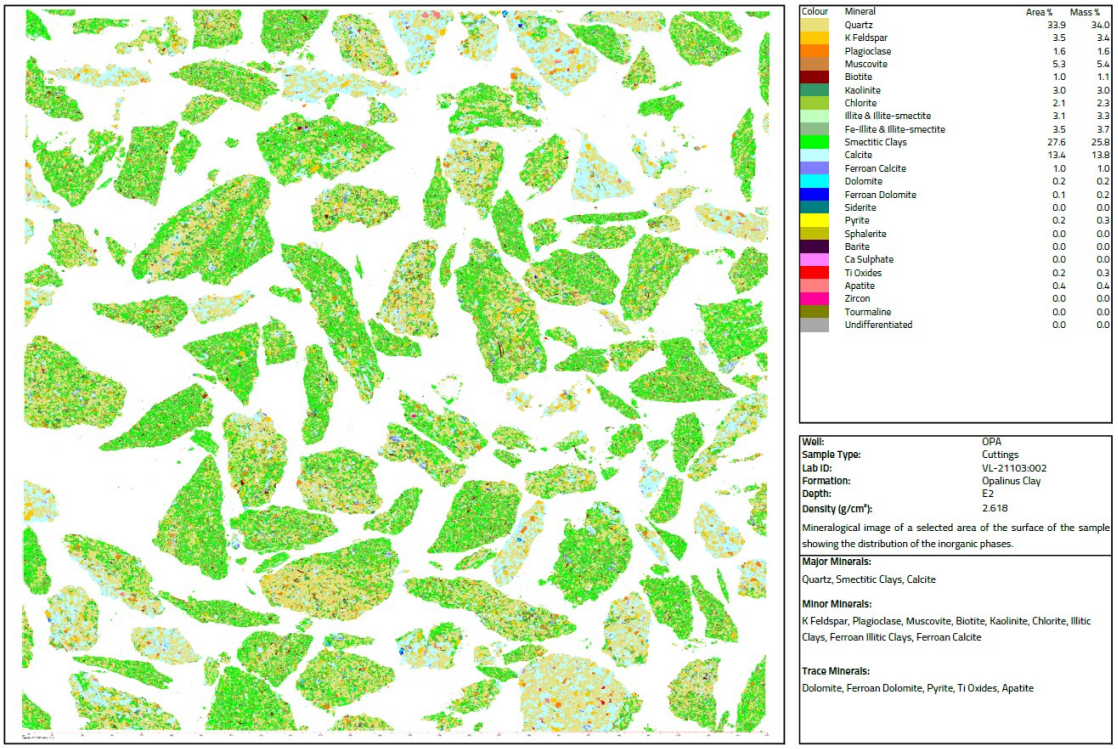

(f) Upper sandy sample (#6) after pseudo cutting

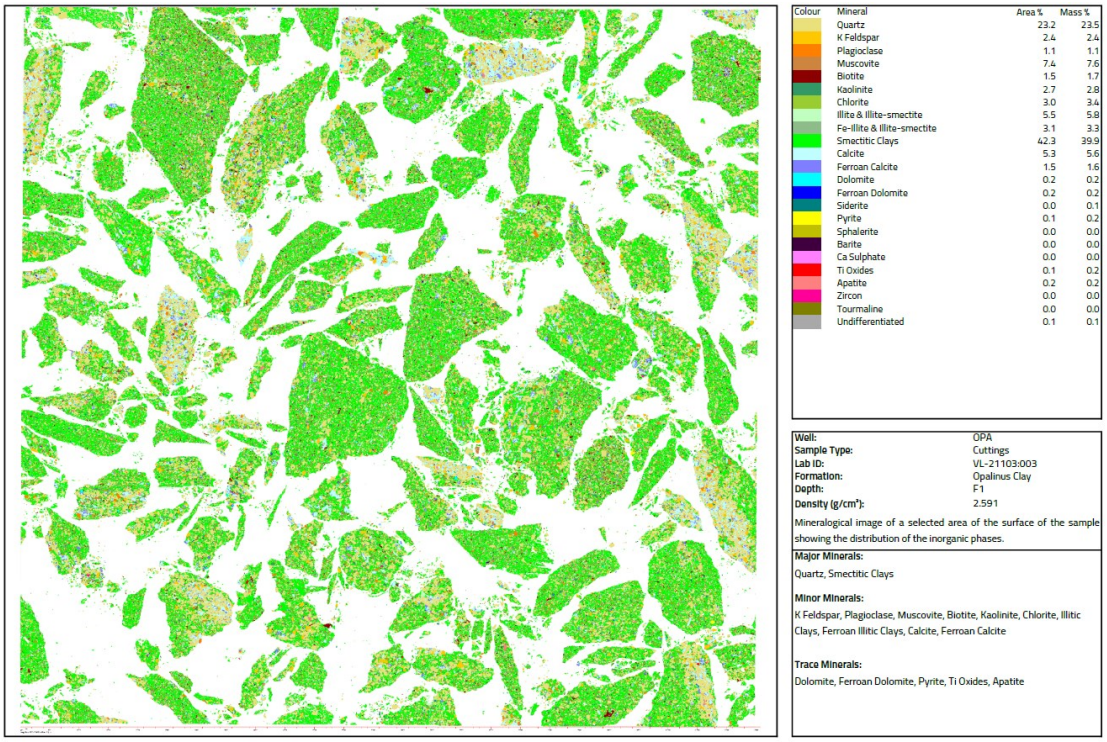

Colour	Mineral	Area %	Mass %
	Quartz	23.2	23.5
	K Feldspar	2.4	2.4
	Plagioclase	1.1	1.1
	Muscovite	7.4	7.6
	Biotite	1.5	1.7
	Kaolinite	2.7	2.8
	Chlorite	3.0	3.4
	Illite & Illite-smectite	5.5	5.8
	Fe-Illite & Illite-smectite	3.1	3.3
	Smectitic Clays	42.3	39.9
	Calcite	5.3	5.6
	Ferroan Calcite	1.5	1.6
	Dolomite	0.2	0.2
	Ferroan Dolomite	0.2	0.2
	Siderite	0.0	0.1
	Pyrite	0.1	0.2
	Sphalerite	0.0	0.0
	Barite	0.0	0.0
	Ca Sulphate	0.0	0.0
	Ti Oxides	0.1	0.2
	Apatite	0.2	0.2
	Zircon	0.0	0.0
	Tourmaline	0.0	0.0
	Undifferentiated	0.1	0.1

Well:	OPA
Sample Type:	Cuttings
Lab ID:	VL-21103:003
Formation:	Opalinus Clay
Depth:	F1
Density (g/cm³):	2.591

Mineralogical image of a selected area of the surface of the sample showing the distribution of the inorganic phases.

Major Minerals:

Quartz, Smectitic Clays

Minor Minerals:

K Feldspar, Plagioclase, Muscovite, Biotite, Kaolinite, Chlorite, Illitic Clays, Ferroan Illitic Clays, Calcite, Ferroan Calcite

Trace Minerals:

Dolomite, Ferroan Dolomite, Pyrite, Ti Oxides, Apatite

(g) Upper shaly sample (#7) after pseudo cutting

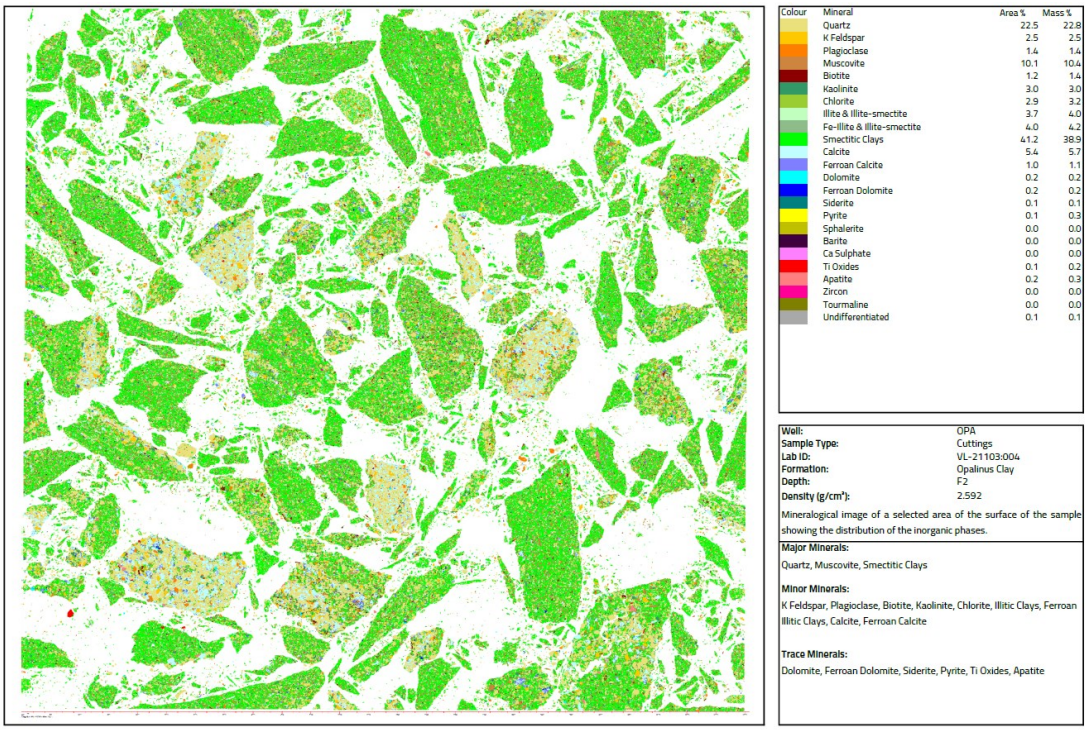

Colour	Mineral	Area %	Mass %
	Quartz	22.5	22.8
	K Feldspar	2.5	2.5
	Plagioclase	1.4	1.4
	Muscovite	10.1	10.4
	Biotite	1.2	1.4
	Kaolinite	3.0	3.0
	Chlorite	2.9	3.2
	Illite & Illite-smectite	3.7	4.0
	Fe-Illite & Illite-smectite	4.0	4.2
	Smectitic Clays	41.2	38.9
	Calcite	5.4	5.7
	Ferroan Calcite	1.0	1.1
	Dolomite	0.2	0.2
	Ferroan Dolomite	0.2	0.2
	Siderite	0.1	0.1
	Pyrite	0.1	0.3
	Sphalerite	0.0	0.0
	Barite	0.0	0.0
	Ca Sulphate	0.0	0.0
	Ti Oxides	0.1	0.2
	Apatite	0.2	0.3
	Zircon	0.0	0.0
	Tourmaline	0.0	0.0
	Undifferentiated	0.1	0.1

Well:	OPA
Sample Type:	Cuttings
Lab ID:	VL-21103:004
Formation:	Opalinus Clay
Depth:	F2
Density (g/cm³):	2.592

Mineralogical image of a selected area of the surface of the sample showing the distribution of the inorganic phases.

Major Minerals:

Quartz, Muscovite, Smectitic Clays

Minor Minerals:

K Feldspar, Plagioclase, Biotite, Kaolinite, Chlorite, Illitic Clays, Ferroan Illitic Clays, Calcite, Ferroan Calcite

Trace Minerals:

Dolomite, Ferroan Dolomite, Siderite, Pyrite, Ti Oxides, Apatite

(h) Upper shaly sample (#8) after pseudo cutting

Figure A- 14. Mineralogy identification by QEMSCAN/AMICS on a selected area (12.5 x 12.5 mm^2)

Appendix VI. Numerical Integration of Constitutive Model

Given $\boldsymbol{\sigma}_n, \boldsymbol{\varepsilon}_n, \boldsymbol{\varepsilon}_n^p, d_n$ from the n^{th} increment and strain increment $\Delta\boldsymbol{\varepsilon}_{n+1}$, determine the nominal stress tensor $\boldsymbol{\sigma}_{d,n+1}$ for the current $n+1^{\text{th}}$ increment.

1. Update damage variable

- $\boldsymbol{\varepsilon}_{n+1} = \boldsymbol{\varepsilon}_n + \Delta\boldsymbol{\varepsilon}_{n+1}$ and calculate $\|\boldsymbol{\varepsilon}_{n+1}^-\|$.
- Evaluate damage loading function $f_{n+1}^d = h(\|\boldsymbol{\varepsilon}_{n+1}^-\|) - d_n$:
  IF $f_{n+1}^d \leq 0$, $d_{n+1} = d_n$; ELSE $d_{n+1} = h(\|\boldsymbol{\varepsilon}_{n+1}^-\|)$.
- $\kappa_{n+1} = (1 - d_{n+1})\kappa$.

2. Update stress-dependent stiffness

- Depending on the stress-dependent stiffness function used, determine stress variable $\sigma_{3,n}, p_n$, or $\sigma_{i,n}$ from $\boldsymbol{\sigma}_n$ and compute stiffness tensor $\mathbf{C}_n$ according to Eqns. (4), (6), or (7), respectively.

3. Update plastic strain

- $\boldsymbol{\varepsilon}_n^e = \boldsymbol{\varepsilon}_n - \boldsymbol{\varepsilon}_n^p$.
- Try $\boldsymbol{\varepsilon}_{\boldsymbol{n+1}}^{\boldsymbol{e}} = \boldsymbol{\varepsilon}_{\boldsymbol{n}}^{\boldsymbol{e}} + \Delta\boldsymbol{\varepsilon}_{\boldsymbol{n+1}}$ and $\boldsymbol{\sigma}_{\boldsymbol{n+1}} = \mathbf{C}_{\boldsymbol{n+1}} : \boldsymbol{\varepsilon}_{\boldsymbol{n+1}}^{\boldsymbol{e}}$. Evaluate plastic yielding function $f_{n+1}^p = q_{n+1} - Bp_{n+1} - \kappa_{n+1}$:
  IF $f_{n+1}^p \leq 0$, $\boldsymbol{\varepsilon}_{n+1}^p = \boldsymbol{\varepsilon}_n^p$; ELSE apply the general return-mapping algorithm (Simo and Hughes 1998) to iterate $\boldsymbol{\varepsilon}_{n+1}^p$ and $\Delta\lambda_{n+1}$ until the plastic flow residual $\mathbf{R}_n$ and yield function f_{n+1}^p both converge to specified tolerance values, where $\mathbf{R}_{n+1} = -\boldsymbol{\varepsilon}_{n+1}^p + \boldsymbol{\varepsilon}_n^p + \Delta\lambda_{n+1}\frac{\partial f_{n+1}^p}{\partial \boldsymbol{\sigma}_{n+1}}$.

4. Update stress

- $\boldsymbol{\varepsilon}_{\boldsymbol{n+1}}^{\boldsymbol{e}} = \boldsymbol{\varepsilon}_{\boldsymbol{n+1}} - \boldsymbol{\varepsilon}_{\boldsymbol{n+1}}^{\boldsymbol{p}}$.
- Update damage effective stress $\boldsymbol{\sigma}_{\boldsymbol{n+1}} = \mathbf{C}_{\boldsymbol{n}} : \boldsymbol{\varepsilon}_{\boldsymbol{n+1}}^{\boldsymbol{e}}$. Evaluate the normalized stress error from iteration, i.e., $\Delta\sigma = \|\boldsymbol{\sigma}_{\boldsymbol{n+1}} - \boldsymbol{\sigma}_{\boldsymbol{n}}\|$:
  IF $\Delta\sigma \leq$ the specified tolerance value, $\boldsymbol{\sigma}_{d,n+1} = (1 - d_{n+1})\boldsymbol{\sigma}_{n+1}$; ELSE $\boldsymbol{\sigma}_n = \boldsymbol{\sigma}_{n+1}$ and repeat from Step 2.

Appendix VII. Explicit Modelling of Stiffness Recovery under Compression on Damaged Solids

Distributed micro-cracking is typically associated with the observed reduction of elastic stiffness (or damage) when materials are under tension. The idea that the elastic stiffness can be recovered upon re-compression is supported by the experimental evidence on damaged concrete specimens (e.g., Reinhardt and Cornelissen (1984) and Mazars et al. (1990)). Because the re-compression does not physically fill the cracks but instead inhibits the degradation effect by closing the cracks, the damage state of the material does not change. Formulations have been proposed to quantify the effect of compression without modifying the damage variable. A common approach is to consider the deactivated part of the damage by introducing the deactivation threshold and deactivation limit (Hansen and Schreyer 1995). The deactivation threshold can be in stress σ_{th} or strain ε_{th}, and an intuitive choice is using the reversal state from the tension to compression, i.e., $\sigma_{th} = 0$ or $\varepsilon_{th} = 0$. The deactivation limit refers to the degree to which elastic stiffness can be recovered after the deactivation threshold is reached. The deactivation process was commonly regarded as an instantaneous process using the Heaviside function $H(\ )$ (Ortiz 1985; Ju 1989; Halm and Dragon 1996), which suggests a full recovery at the deactivation threshold. In their works, due to the tensorial nature of the stress and strain, the Heaviside function was applied to the principal quantities, and the degradation was only partially deactivated unless all three principal quantities reached the threshold at the same time. In this study, for simplification, the deactivation (or recovery) of the degraded stiffness is assumed to be isotropic, and a single scalar variable r can be introduced in the following function,

$$\mathbf{C} = \left(1 - d\left(1 - r\right)\right)\mathbf{C}_0 \tag{A. 8}$$

where $\mathbf{C_0}$ is the initial elastic stiffness and $\mathbf{C}$ is the current elastic stiffness. Instead of the Heaviside function, r is considered to continuously change with the stress (or strain) measure after the deactivation threshold is reached so that the discontinuity of the stress-strain curve at the deactivation threshold can be avoided when plastic deformation is present (Hansen and Schreyer 1995).

$$r = \begin{cases} 0, \sigma \le \sigma_{th} \\ R\left(\sigma\right), \sigma > \sigma_{th} \end{cases} \tag{A. 9}$$

where $R(\chi)$ is a transition function in a stress measure σ. Equivalently a strain measure ε can be considered with the strain deactivation threshold $\varepsilon_{\text{th}} > 0$ at compression, but this would lead to a delayed stiffness recovery when the damage is caused by dilative plastic strain in a formulation. In contrast, using the stress-based transition function, the recovery can occur immediately after the stress reverses from

tension to compression. To demonstrate this, it is proposed that $\sigma = \sigma_3$, $\sigma_{th} = 0$, and the transition function is defined in an exponential form

$$R(\sigma_3) = r_0\left(1 - \exp\left((\sigma_{th} - \sigma_3)/r_1\right)\right) \tag{A. 10}$$

where r_0 and r_1 are two parameters specifying the recovery (or deactivation) limit and the rate of the stiffness recovery, respectively. Eqns. (A. 8), (A. 9), and (A. 10) can be conveniently incorporated into the proposed elastoplastic damage constitutive model in Section 4.4. A numerical integration scheme similar to Appendix VI can be used so that all the internal variables, including r, can be solved for a prescribed strain condition. Newton-Raphson method needs to be applied to solve for the boundary conditions with prescribed stress. An example of the stress-strain curve predicted for a cyclic loading path is shown in Figure A- 15. Plastic yielding is omitted in this case. As specified in Eq. (14), the recovery variable r reduces after a decrease of axial stress at the beginning of axial extension. Once the tensile strain (the axial strain in this case) reaches the damage threshold c_0, the stress-strain curve becomes nonlinear due to inelastic deformation. At this stage, both the variation of r and d play a role in the degradation of Young's modulus, as implied by Eqn. (A. 8). A continued extension would eventually lead the damage to be fully activated and equal to c_1. The reloading stage allows the recovery variable to increase again while the damage variable stays at the same level prior to the stress reversal. Since the recovered stiffness cannot exceed the stiffness of an undamaged material, a reasonable value of r_0 should be < 1. Therefore, in Figure A- 15, when the axial stress or strain returns to the initial level, Young's modulus cannot be fully recovered, i.e., $E_d < E_0$.

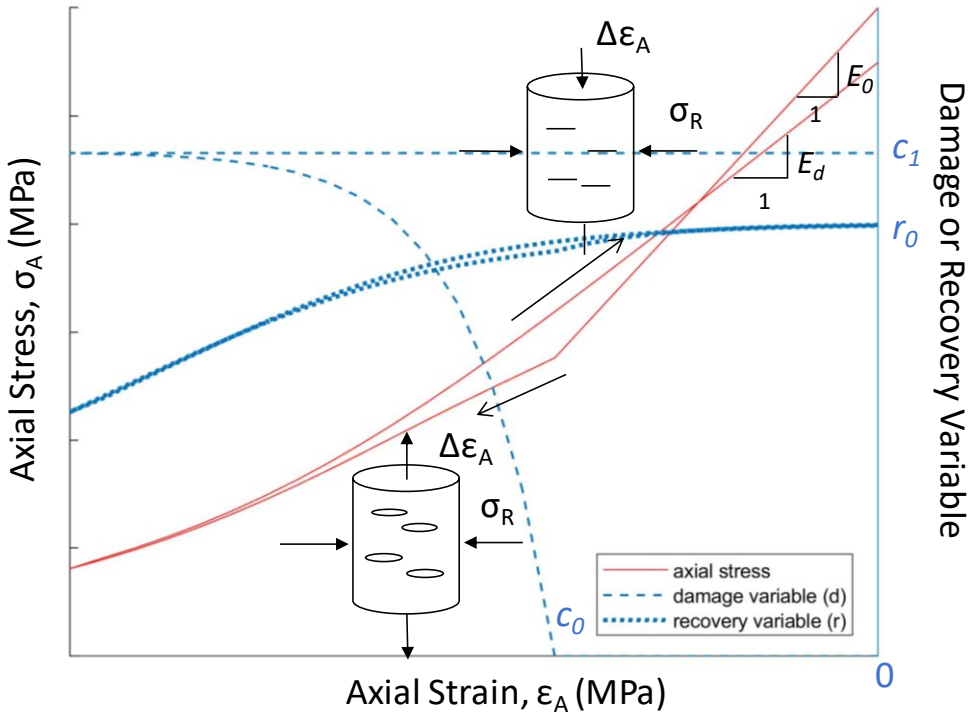

Figure A- 15. Predicted stress-strain curve for triaxial extension-compression test with diagrams illustrating micro-crack opening-closure behavior.

Appendix VIII. Tomographic Inversion of Interval Velocity Measurement (IVM) Data with *rayinvr*

In the waveform measured at each receiver with a given distance x from the emitter, the travel time t of the wave phase of interest can be identified (e.g., Figure 2-4). The objective of the inversion is to find a velocity model that can reproduce the variation of t versus x for the measurements obtained at a total of 7 receivers.

The workflow of the tomographic inversion is demonstrated in Figure A- 16. At the start of the process, an initial velocity model is defined (Figure A- 17). In this study, a few assumptions are imposed to restrict the velocity variation in the near-borehole field: 1) velocity is homogeneous in the longitudinal direction, 2) the model has a fixed number (n) of velocity layers with a uniform gradient in each layer; 3) the velocity is continuous at the layer boundary. Besides, in the initial velocity model, a lower-bound velocity is assigned at the borehole surface ($v_{1,top}$), and an upper-bound velocity is assigned at the approximate outer boundary ($v_{n,btm}$). Since the actual path of wave transmission is greater than the emitter-receiver offset, the average velocity of the path is expected to be higher than the apparent velocity, and the velocity of the layer with the highest stiffness should be even higher than the average velocity. Therefore, a high velocity value is considered for the upper-bound velocity.

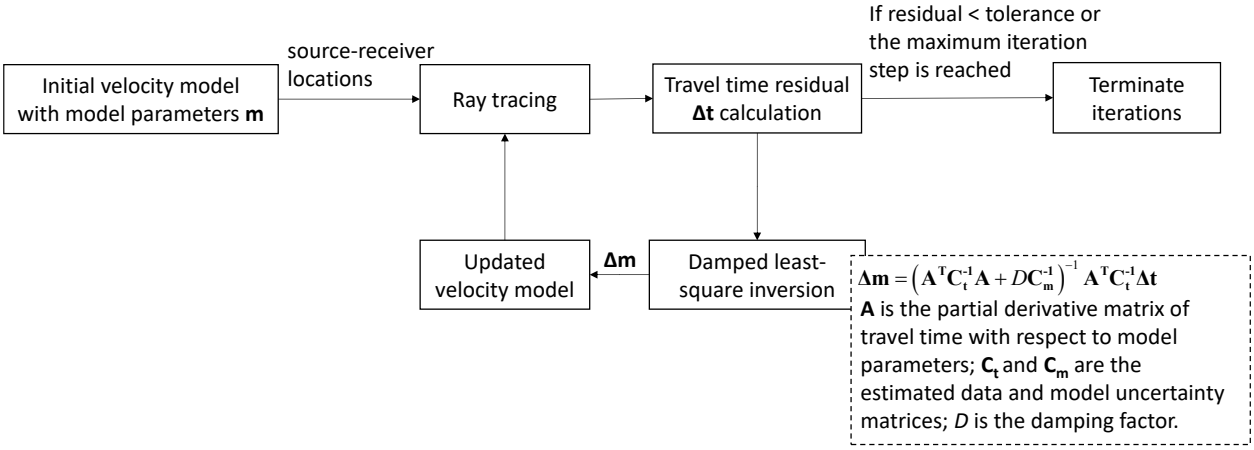

Figure A- 16. Workflow of the tomographic inversion to find the near-borehole velocity structure using IVM data

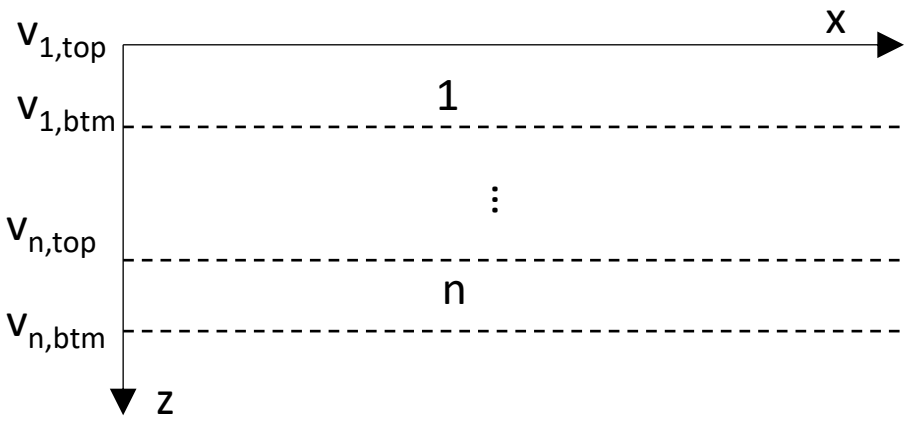

Figure A- 17. Velocity structure considered in the tomographic inversion

Raytracing is performed by solving 2D ray equations over the discretized velocity model with a grid size of 0.5cm by length (x) and 0.1cm by depth (z). Snell's law is applied to account for the refraction at the layer boundary. If any rays return to the surface over the given offsets *x*, the travel time can be calculated using the traced ray path and compared with the measured travel time. In this way, the travel time residual is determined and then used in a damped least-square inversion model to update the parameters of the velocity model, which includes the boundary values and the thickness of velocity layers. This procedure is iterated until the travel time residual drops below the specified tolerance or the maximum iteration step is reached. A final velocity model will be output after the iteration is terminated.

As an example, the data obtained from IVM in borehole BGC-A4 at the borehole depth of 3 ~ 3.4 m is used in the following demonstration. The measured P-wave travel time versus the emitter-receiver offset obtained at R1 ~ R7 is given in Figure A- 18. An initial model with 5 layers with $v_{1,top}$ = 1.5 km/s and $v_{n,btm}$ = 3 km/s is used. Through about four steps of iterations, the travel time has converged to a minimum value (Figure A- 19(a)). Figure A- 19(b) shows the evolution of the velocity model through the iterations. The modification of the velocity structure does not only occur in the defined depth range (0 ~ 0.16m) but also at the boundaries (e.g., $v_{1,top}$ and $v_{n,btm}$). The final velocity model with the rays traced for the given offsets is shown in Figure A- 20. The maximum resolved depth is defined as the outermost depth of the range where the traced rays have covered.

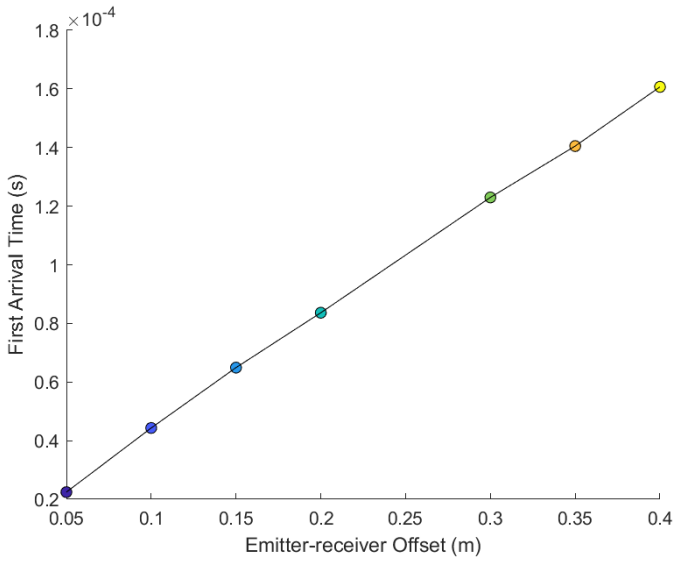

Figure A- 18. Travel time versus the emitter-receiver offset from IVM at 3 ~ 3.4m in borehole BGC-A4

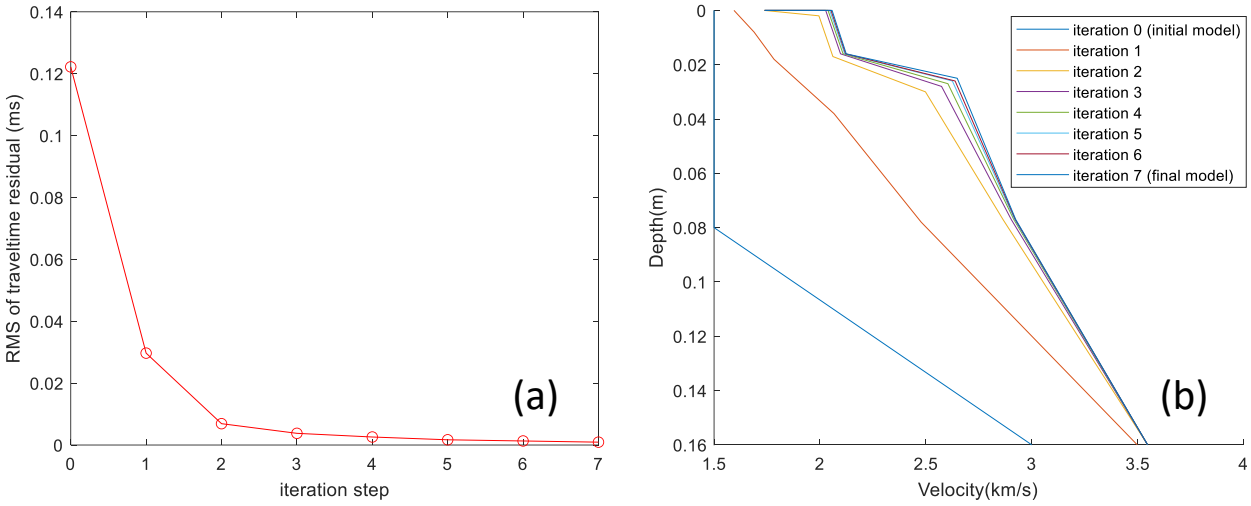

Figure A- 19. (a) Reduction of the travel time residual through iterations and (b) the evolution of the velocity models through iterations

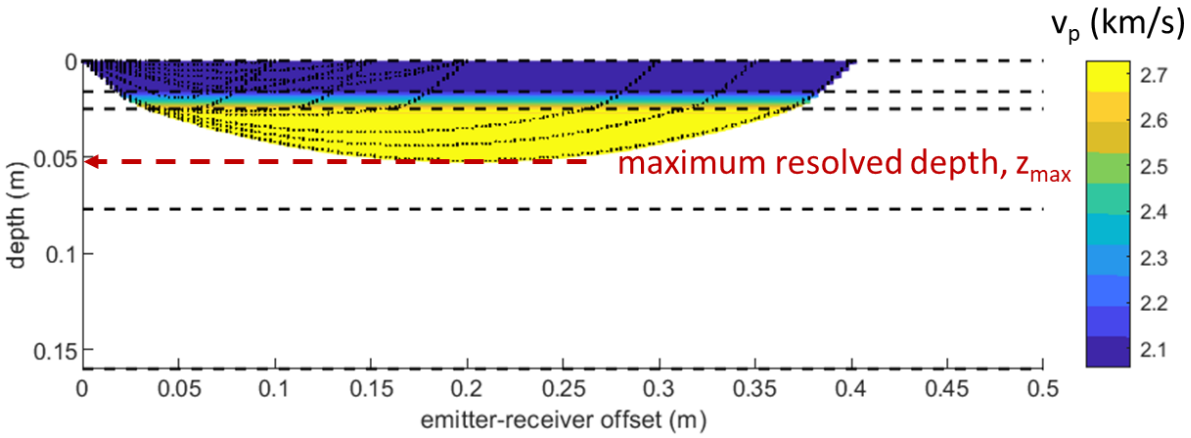

Figure A- 20. Velocity model after the final iteration with the rays traced for all emitter-receiver offsets

The agreement of the inverted travel time with the measured travel time at all emitter-receiver offsets confirms the validity of the inversion results (Figure A- 21). It can be seen from Figure A- 20 that the wave paths arriving at a given offset after propagating through an inverted velocity structure may not be unique, so more than one travel time might be obtained (Figure A- 20). The examination of the ray paths and the corresponding travel time is important after the inversion, as rays may fail to propagate through a particular velocity model over specific emitter-receiver offsets and the travel time residual would be calculated only based on the ray paths that were successfully traced. The output velocity model should be considered invalid if too few data are used.

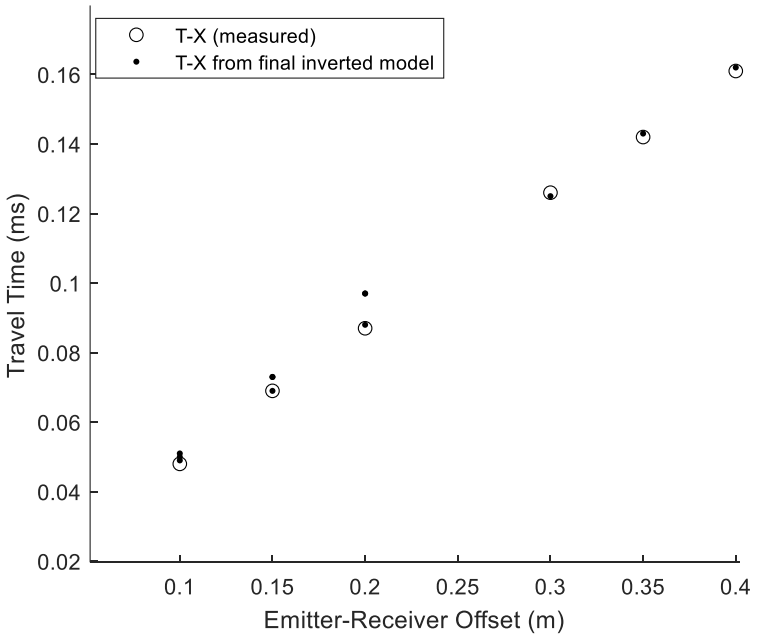

Figure A- 21. Measured and inverted travel times at all emitter-receiver offsets.